SANDIA REPORT
SAND2010-7113
Unlimited Release
Printed October 2010

Metal Fires and Their Implications for Advance Reactors Part 3: Experimental and Modeling Results

Tara J. Olivier, Tom K. Blanchat, Victor G. Figueroa, John C. Hewson, Steven P. Nowlen

Prepared by
Sandia National Laboratories
Albuquerque, New Mexico 87185 and Livermore, California 94550

Sandia National Laboratories is a multi-program laboratory managed and operated by Sandia Corporation, a wholly owned subsidiary of Lockheed Martin Corporation, for the U.S. Department of Energy's National Nuclear Security Administration under contract DE-AC04-94AL85000.

Approved for public release; further dissemination unlimited.

Sandia National Laboratories

Issued by Sandia National Laboratories, operated for the United States Department of Energy by Sandia Corporation.

NOTICE: This report was prepared as an account of work sponsored by an agency of the United States Government. Neither the United States Government, nor any agency thereof, nor any of their employees, nor any of their contractors, subcontractors, or their employees, make any warranty, express or implied, or assume any legal liability or responsibility for the accuracy, completeness, or usefulness of any information, apparatus, product, or process disclosed, or represent that its use would not infringe privately owned rights. Reference herein to any specific commercial product, process, or service by trade name, trademark, manufacturer, or otherwise, does not necessarily constitute or imply its endorsement, recommendation, or favoring by the United States Government, any agency thereof, or any of their contractors or subcontractors. The views and opinions expressed herein do not necessarily state or reflect those of the United States Government, any agency thereof, or any of their contractors.

Printed in the United States of America. This report has been reproduced directly from the best available copy.

Available to DOE and DOE contractors from
U.S. Department of Energy
Office of Scientific and Technical Information
P.O. Box 62
Oak Ridge, TN 37831

Telephone: (865) 576-8401
Facsimile: (865) 576-5728
E-Mail: reports@adonis.osti.gov
Online ordering: http://www.osti.gov/bridge

Available to the public from
U.S. Department of Commerce
National Technical Information Service
5285 Port Royal Rd.
Springfield, VA 22161

Telephone: (800) 553-6847
Facsimile: (703) 605-6900
E-Mail: orders@ntis.fedworld.gov
Online order: http://www.ntis.gov/help/ordermethods.asp?loc=7-4-0#online

SAND2010-7113
Unlimited Release
Printed October 2010

Metal Fires and their Implications for Advanced Reactors

Tara J. Olivier[1]
Thomas K. Blanchat[2]
John C. Hewson[2]
Victor G. Figueroa[3]
Steven P. Nowlen[1]

[1]Risk and Reliability Analysis Department
Sandia National Laboratories
P.O. Box 5800
Albuquerque, NM 87185-1914

[2]Fire and Aerosol Sciences Department
Sandia National Laboratories
P.O. Box 5800
Albuquerque, NM 87185-1914

[3]Transportation and Environmental Safety Department
Sandia National Laboratories
P.O. Box 5800
Albuquerque, NM 87185-1914

Abstract

This report details the primary results of the Laboratory Directed Research and Development project (LDRD 08-0857) Metal Fires and Their Implications for Advance Reactors. Advanced reactors may employ liquid metal coolants, typically sodium, because of their many desirable qualities. This project addressed some of the significant challenges associated with the use of liquid metal coolants, primary among these being the extremely rapid oxidation (combustion) that occurs at the high operating temperatures in reactors. The project has identified a number of areas for which gaps existed in knowledge pertinent to reactor safety analyses. Experimental and analysis capabilities were developed in these areas to varying degrees. In conjunction with team participation in a DOE gap analysis panel, focus was on the oxidation of spilled sodium on thermally massive surfaces. These are spills onto surfaces that substantially cool the sodium during the oxidation process, and they are relevant because standard risk mitigation procedures seek to move spill environments into this regime through rapid draining of spilled sodium.

While the spilled sodium is not quenched, the burning mode is different in that there is a transition to a smoldering mode that has not been comprehensively described previously. Prior work has described spilled sodium as a pool fire, but there is a crucial, experimentally-observed transition to a smoldering mode of oxidation. A series of experimental measurements have comprehensively described the thermal evolution of this type of sodium fire for the first time. A new physics-based model has been developed that also predicts the thermal evolution of this type of sodium fire for the first time. The model introduces smoldering oxidation through porous oxide layers to go beyond traditional pool fire analyses that have been carried out previously in order to predict experimentally observed trends. Combined, these developments add significantly to the safety analysis capabilities of the advanced-reactor community for directly relevant scenarios. Beyond the focus on the thermally-interacting and smoldering sodium pool fires, experimental and analysis capabilities for sodium spray fires have also been developed in this project.

TABLE OF CONTENTS

1 INTRODUCTION 9
2 SODIUM EXPERIMENTS 11
2.1 Experimental Facility Description 11
2.2 Sodium Spray Fire Experiments 13
2.2.1 Overview of Sodium Spray Experimental Results 13
2.2.2 Previous Comparable Sodium Spray Fire Experiments 14
2.3 Sodium Pool Fire Experiments 15
2.3.1 Sodium Pool Fire Experimental Observations 18
2.3.2 Emissivity Measurement 22
2.3.3 Overall Sodium Pool Fire Experimental Data Analysis 22
3 INVERSE HEAT TRANFER CALCULATIONS FOR POOL EXPERIMENTS 29
3.1 Overview of IHCP1D Code 29
3.2 Inverse Heat Flux Results 30
4 Sodium Pool Fire Model Development 37
4.1 Prior sodium pool observations and models 38
4.2 Recent sodium pool observations 38
4.3 Conservation equations for a pool with a porous oxide crust 39
4.3.1 Sodium oxidation chemistry 41
4.3.2 Phase conservation 42
4.3.3 Species conservation 48
4.3.4 Enthalpy conservation 53
4.3.5 Heat flux from reaction zone 54
4.3.6 Numerical details 55
4.3.7 Model Parameters 55
4.3.8 Simplified thermal balances 59
4.4 Results and Discussion 64
4.4.1 Model predictions of sodium pool fire measurements 64
5 SUMMARY AND CONCLUSIONS 69
6 REFERENCES 71
7 APPENDIX A: SODIUM SPRAY FIRE TEST SETUP AND EXPERIMENTAL DATA 74
7.1 Sodium Spray Fire Outdoor Tests 74

7.1.1 Outdoor Spray Test Instrumentation 74
7.1.2 Stainless Steel Spray Nozzles 75
7.2 Sodium Melt Generator 76
7.2.1 Data Acquisition 77
7.2.2 Sodium Outdoor Spray Test 1 Measured Data 79
7.2.3 Sodium Outdoor Spray Test 2 Measured Data 83
7.3 Full-Scale Sodium Spray Fire In-Vessel Tests 87
7.3.1 Full-Scale In-Vessel Instrumentation 87
7.3.2 Sodium In-Vessel Spray Test 3 Measured Data 92
7.3.3 Sodium In-Vessel Spray Test 4 Measured Data 97
7.4 References 104
8 APPENDIX B: SODIUM POOL FIRE TEST SETUP AND EXPERIMENTAL DATA . 105
8.1 Overview of the Outdoor Sodium Pool Fire Test Setup 105
8.2 Outdoor Sodium Pool Fire Test Instrumentation 107
8.3 Sodium Melt Generator 114
8.4 Data Acquisition 114
8.5 Sodium Pool Fire Experimental Data 115
8.5.1 Sodium Pool Test 1 Measured Data 115
8.5.2 Sodium Pool Test 2 Measured Data 121
8.5.3 Sodium Pool Test 3 Measured Data 127
8.5.4 Sodium Pool Test 4 Measured Data 133
8.5.5 Sodium Pool Test 6 Measured Data 139
8.5.6 Sodium Pool Test 7 Measured Data 147
8.5.7 Sodium Pool Test 8 Measured Data 157
8.5.8 Sodium Pool Test 9 Measured Data 166
8.5.9 Sodium Pool Test 10 Measured Data 175
8.5.10 Sodium Pool Test 11 Measured Data 184
9 APPENDIX C: REFERENCE PROPERTIES 192

LIST OF FIGURES

Figure 2-1: The Surtsey Vessel. 12
Figure 2-2: Summary of Sodium Pool Fire Tests 17
Figure 2-3: Sodium Pool Test 3, Pan Bottom TC Trend 19
Figure 2-4: Sodium Pool Test 3, Averaged Pan Bottom TCs' Temperatures versus Time (without Pan TC7) 20
Figure 2-5: Sodium Pool Test 8, Pan Bottom TC Trend 21
Figure 2-6: Sodium Pool Test 8, Averaged Pan Bottom TCs' Temperatures versus Time (without Pan TC24) 22
Figure 2-7: All Sodium Pool Tests Displayed by Liquid to Steel Thickness Ratio: Average Pan Bottom TC Temperatures vs Time 24
Figure 2-8: All Sodium Pool Tests: Measured Peak of Average Pan Bottom Temperature vs Thickness Ratio (Liquid Sodium/Stainless Steel) 25
Figure 2-9: Narrow View Heat Flux Measurements for Pool Tests 1 through 4 26
Figure 2-10: Narrow View Heat Flux Measurements for Pool Tests 6 through 11 27
Figure 2-11: Narrow View Maximum Heat Flux Measured vs Thickness Ratio for Pool Tests 6 through 11 28
Figure 3-1: IHCP problem definition 30
Figure 3-2: Pool Test 2 Calculated Heat Flux and Top Surface Temperatures vs Time 32
Figure 3-3: Pool Test 3 Calculated Heat Flux and Top Surface Temperatures vs Time 33
Figure 3-4: Pool Test 10 Calculated Heat Flux and Top Surface Temperatures vs Time 34
Figure 3-5: Pool Test 3 Calculated Pan Center Temperatures with Estimated Error 35
Figure 3-6: Pool Test 3 Calculated Surface Heat Flux with Estimated Error 36
Figure 4-1: Schematic indicating the layers over which the model will predict heat and mass flux including representative profiles of oxidizer mass fraction and temperature across these various layers. Letters to the right of the upper diagram indicate subscripts applicable to interfaces. 40
Figure 4-2: The ratio of the oxygen mass fraction at the oxide-crust surface to the ambient for $Sh/L = 230$ and $\phi = 0.8$ as a function of the crust thickness. 51
Figure 4-3: Measurements of the l_2-norm error in temperature predictions as a function of the Nusselt number and either $\phi_{\mathrm{Na},lim}$ or ϕ_g. 58
Figure 4-4: The ratio of the effective mass diffusivity to the effective thermal diffusivity through the porous oxide crust, R_Δ, is plotted as a function of the porosity and the bulk thermal conductivity of the oxide. Radiative flux is set to zero. 63
Figure 4-5: The ratio of the effective mass diffusivity to the effective thermal diffusivity through the porous oxide crust, R_Δ, is plotted as a function of the porosity for various oxide bulk conductivities (1 and 20 W/m/K) and using the Bruggemann model for the effective mass diffusivity with an exponent of 2.5. 63
Figure 4-6: Temperature profiles predicted across the insulation, pan, sodium and oxide-crust layers are provided for pan 1 (left panel) and pan 7 (right panel) at various times. 64
Figure 4-7: Temperature predictions (lines) compared with measurements (symbols) for pans 1, 2, 5 and 8. 65
Figure 4-8: Temperature predictions (lines) compared with measurements (symbols) for pans 6, 7 and 9. 66
Figure 4-9: Temperature predictions (lines) compared with measurements (symbols) for pans 3, 4, 10 and 11. 66

Figure 7-1: Nozzle Capacity versus Pressure 76
Figure 7-2: Outdoor Sodium Spray Test Instrumentation Setup and TC Locations..... 78
Figure 7-3: Outdoor Sodium Spray Test 1, Center TC Rake Temperatures vs Time..... 80
Figure 7-4: Outdoor Sodium Spray Test 1, 0.6m (2 ft) Radius TC Rake Temperatures vs Time 81
Figure 7-5: Outdoor Sodium Spray Test 1, Measured Heat Flux (Narrow View Gauge) vs Time 82
Figure 7-6: Outdoor Sodium Spray Test 1, Measured Heat Flux (Wide View Gauge) vs Time.. 83
Figure 7-7: Outdoor Sodium Spray Test 2, Center TC Rake Temperatures vs Time..... 84
Figure 7-8: Outdoor Sodium Spray Test 2, 0.6m (2 ft) Radius TC Rake Temperatures vs Time 85
Figure 7-9: Outdoor Sodium Spray Test 2, Measured Heat Flux (Narrow View Gauge) vs Time 86
Figure 7-10: Outdoor Sodium Spray Test 2, Measured Heat Flux (Wide View Gauge) vs Time 87
Figure 7-11: In-Vessel Sodium Spray Test Instrumentation Layout..... 90
Figure 7-12: In-Vessel Sodium Spray Heat Flux Gauge Locations 91
Figure 7-13: In-Vessel Sodium Spray Test 3, Air TC Rake Temperatures vs Time..... 92
Figure 7-14: In-Vessel Sodium Spray Test 3, Wall TC Rake Temperatures vs Time..... 93
Figure 7-15: In-Vessel Sodium Spray Test 3, Vessel Pressure vs Time 94
Figure 7-16: In-Vessel Sodium Spray Test 3, Measure Heat Flux (Narrow View Gauge) vs Time 95
Figure 7-17: In-Vessel Sodium Spray Test 3, Measure Heat Flux (Wide View Gauge) vs Time 96
Figure 7-18: In-Vessel Sodium Spray Test 3, Measured Pyrometer Temperature vs Time..... 97
Figure 7-19: In-Vessel Sodium Spray Test 4, Air TC Rake Temperatures vs Time..... 98
Figure 7-20: In-Vessel Sodium Spray Test 4, Wall TC Rake Temperatures vs Time..... 99
Figure 7-21: In-Vessel Sodium Spray Test 4, Vessel Pressure vs Time 100
Figure 7-22: In-Vessel Sodium Spray Test 4, Measure Heat Flux (Narrow View Gauge) vs Time 101
Figure 7-23: In-Vessel Sodium Spray Test 4, Measure Heat Flux (Wide View Gauge) vs Time 102
Figure 7-24: In-Vessel Sodium Spray Test 4, Measured Pyrometer Temperature vs Time..... 103

LIST OF TABLES

Table 2-1: Summary of Sodium Spray Tests Experiments..... 14
Table 2-2: Sodium Spray Fire Experiments Compared to the FAUNA Experiments [9] 15
Table 3-1: Material Property Inputs used in IHCP1D 31

1 INTRODUCTION

The research presented here follows the recommendations described in the Laboratory Directed Research and Development (LDRD) proposal (LDRD 08-0857 Metal Fires and Their Implications for Advance Reactors) aimed at establishing a general metal-fires expertise, experimental capability, and analysis capability at Sandia National Laboratories (SNL) to address a key safety issue for the next generation of nuclear reactors. Many Generation IV reactor designs use liquid sodium (Na) as the primary and secondary coolant (as do other advanced reactor concepts). While the use of sodium enhances safety in many aspects related to the high boiling temperature of the sodium coolant, sodium and other materials do pose unique risks in these reactors. In particular, sodium is able to ignite and oxidize (combust) at cooling-loop operating temperatures. At the high temperatures present the reactants, ignition, and combustion of various metals can be a problem but the prevalence of sodium as a coolant and its ease of ignition have led the present LDRD project to focus on sodium fires as a prime example of metal fires. Metal-fires have unique characteristics such as very high temperatures and fire suppression challenges. An enhanced understanding of metal-fire behaviors and the availability of appropriate analysis tools will be needed to achieve and demonstrate the mitigation of metal-fire hazards. This LDRD has advanced SNL expertise in the science and safety/risk aspects of metal-fires, and has established and demonstrate a metal-fires predictive modeling capability to supplement existing SNL fire-modeling capabilities. The work has also established the foundations of a metal-fire experimental capability and has demonstrated that capability through a set of sodium-fire discovery experiments focused on key phenomena of interest [1].

Metal fires can be divided into two broad categories, referred to here as spray fires and pool fires. Spray fires are characterized by the dispersion of metal particles (droplets) through the oxidizing atmosphere as might occur from an elevated leak. Pool fires are characterized by oxidation of the metal on a surface. While metal fires have been studied over the decades, fundamental challenges and unknowns remain. Based on a literature review and a PIRT (phenomenon identification and ranking table) exercise carried out in earlier phases of this project [1-2] a number of research priorities have been identified. The spray fire configuration maximizes the surface-to-volume ratio and this tends to maximize the potential reaction and heat-release rates. However, in the case of sodium fires, the expected droplet size is large enough that the time for a droplet to fall to the ground will often be less than the time to completely oxidize the droplet. This can lead to incomplete combustion of the sodium leaving some fraction of the sodium behind to burn as a pool fire (creating a combined spray/pool scenario). To establish the conditions for the pool fire requires that we understand the completeness of the spray fire combustion process, and therefore the fraction of unburned sodium left behind. Complicating this process is the fact that the particle size distribution is broad, and particles ranging in size over an order of magnitude can be expected. These cause variations in the rate of heat release throughout the plume and in the fraction of sodium that deposits on a surface and burns as a pool. A key aspect of this is the radiative transport of thermal energy to the surroundings. This project has performed some basic investigation on these influences both theoretically and experimentally.

Initially sodium spray fires were the main focus of this program, but after the initial outdoor scoping tests, a sodium pool fire burning mode was observed that differed significantly in its thermal characteristics compared to the pool fire studies that prevailed in the literature. After discussion with an external panel organized by DOE to identify gaps in sodium fire environments, the team reevaluated the experimental plan and designed additional pool fire tests to investigate this new burning regime. For pool fires, it is expected that thermal damage to the surface on which the pool is resting will be most significant, and this project has addressed this challenge. While experimental measurements and models have been developed for deep pools of sodium thermally insulated from their environment, the more likely accident scenario will involve moderately shallow pools that interact thermally with their environment. This can lead to combustion occurring at pool temperatures for which the formation of an oxide crust is important. To the best of the team's knowledge, there are no systematic experimental measurements or physical models to describe pools burning under these conditions. Challenges that were overcome in the development of a sodium pool model include the fact that surface burning for sodium pools is complicated by the formation of an oxide layer (i.e., crust) leading to a different mode of burning than that encountered with other types of pool burning materials; that is, the oxide crust inhibits oxygen transport to the sodium, reducing heat release rates and resulting in lower temperature oxidation. The results of the sodium spray and pool experiments, experimental data analysis, and the model development for this project will be discussed in this report.

2 SODIUM EXPERIMENTS

A series of sodium spray and pool fire experiments were performed at Sandia National Laboratories (SNL) at the Nuclear Energy Work Complex (NEWC) in Albuquerque, NM in 2009 and 2010. The sodium spray fire tests were conducted both outdoor and in-vessel while the sodium pool fire tests were all completed outdoors. Section 2.1 through 2.3 present the general overview of the experimental location, melt generator (container in which sodium is melted), and the details about the sodium metal used for this experimental series. Section 2.4 and 2.5 present the overall experimental results for the spray and pool fire tests respectively. A more detailed explanation and presentation of the experimental setup and data can be found in Appendix A for the spray fire tests and in Appendix B for the pool fire tests.

The main objective for this experimental program was to gain a fundamental understanding of sodium spray and pool fires. Overall the spray fire tests were performed in order to develop SNL's capability with some very important overall phenomenological understanding. Two outdoor spray tests were done in order to understand system performance and instrumentation response. Two in-vessel spray experiments were performed in a controlled atmosphere in order to obtain results with better control of boundary conditions than has been accomplished in the past. Through challenges overcome in carrying out measurements, these tests have advanced our understanding of sodium spray fires.

Eleven sodium pool burns were conducted where molten sodium was poured suddenly into a steel pan at ambient temperatures. Measurements of the thermal evolution in these tests investigated the concept of cooling-induced quenching of the sodium fire. As indicated in the Introduction, these experiments described for the first time the variation of thermal responses as a function of the pools thermal environment (including thermal interactions with the pan). The results show the significance of a smoldering mode of combustion where the oxidation is well within an oxide-crust layer that forms eventually on the surface of the sodium pool. The results from these experiments have been used to develop a sodium pool burning computational model that extends prior models into a regime where the oxide crust causes a transition to what is referred to as the smoldering mode of combustion (Section 4). The results have also been used to carry out inverse heat transfer calculations to enhance our understanding of the thermal loads experienced in sodium leak accidents (Section3).

2.1 Experimental Facility Description

The Surtsey vessel was chosen as the test vessel for the large scale sodium fire spray experiments, following a search of available pressure vessels at Sandia. This vessel was designed and used for similar combustion experiments (high-pressure thermite melt ejection, direct containment heating, hydrogen combustion, etc.) and is well-fitted for the proposed work.

Figure 2-1 displays the Surtsey vessel. The Surtsey vessel is an American Society of Mechanical Engineers (ASME)-approved steel pressure vessel. It has a cylindrical shape with removable, dished heads attached to both ends, and is 3.6 m in diameter by 10.3 m high. The Surtsey vessel has a maximum allowable working pressure of 1 MPa at 533 K, but has a burst diaphragm installed to limit the pressure in the vessel to less than 0.9 MPa.

It is supported approximately 2 m off the ground by a structural steel framework with its longitudinal axis oriented vertically. A total of twenty 30.5-cm and 61-cm instrument penetration ports allow steam, noncondensible gas, water, electrical, instrumentation, and video service into and out of the vessel. The ports are circumferentially arranged on six different levels, evenly spaced 1.22 m apart, with the #1 level near the bottom of the vessel and the #6 level the topmost level. The vessel walls and heads are ~1 cm (3/8 inch) thick mild steel and covered with at least 10 cm of fiberglass, or equivalent material for insulation. A false floor (from a previous experiment) is installed between the lower head and the cylindrical wall section reduces the freeboard volume of the Surtsey vessel to 99 m^3.

The outside of the Surtsey facility (NEWC) at SNL were ideal for the outside spray and pool fire tests. All testing was performed at the NEWC site.

Figure 2-1: The Surtsey Vessel.

2.2 Sodium Spray Fire Experiments

The sodium spray fire experiments were initially the main focus of this research program, however with the initial scoping tests the results switched the focus to the quenching phenomenon with the sodium pool fires. This is the main reason that there were only four sodium spray fire tests all together. From these four tests the team was able to understand the basics of sodium spray fire behavior and identify areas for further research.

There were some challenges with the sodium spray fires including designing the ports to withstand the pressure increase and the ability to obtain better visual during the test due to the large amount of smoke from the fire. Improvements for future tests would be to include more of the advanced diagnostics.

2.2.1 Overview of Sodium Spray Experimental Results

There were two outdoor and two in-vessel sodium spray experiments with this program. The outdoor spray tests varied the droplet diameters while the in-vessel testing varied the initial sodium temperature. Below in
Table **2-1** the overall results for all four spray tests are shown. The details of the experimental setup and experimental data are presented in Appendix A.

For the two outdoor tests (T1 and T2 in
Table **2-1**) the measured plume temperatures vary depending on the median particle diameter. Although for T1 the thermocouple (TC) failed at about 1200ºC. During the experiments T1 spray droplets burned mostly before they reached the catch pan. While in T2 a lot of the droplets burned partially in the catch pan. The heat flux measured for T1 was significantly larger than that measured for T2 but the authors agree this is probably due to gauge location. The middle of the spray height for T1 is where a lot of the burning was taken place while the closer to the catch pan is where most of the burning had taken place for T2.

For the two in-vessel tests (T3 and T4 in
Table **2-1**) the initial sodium temperatures were varied. The measured air temperatures in-vessel were noticeable different for the two tests, cooler for the 200ºC sodium test (T3) than the 500ºC (T4) sodium inlet temperature test. The vessel pressure rose more drastically for the hotter sodium test as well. For the hotter sodium spray test (T4) the initial data is the only relevant data since the vessel experienced a port failure due to the drastic pressure rise. These results demonstrate the strong sensitivity that spray fires will have to the sodium temperature where the leak occurs. With the current results, it is not possible to discern all of the separate influences, but lower temperature droplets are likely to take longer to go through an induction period prior to complete burning, leading the higher-temperature droplets to release a larger fraction of their chemical energy in the rapid-burning spray fire mode (the surface-to-volume ratio drops dramatically after the droplets stick to surfaces).

Table 2-1: Summary of Sodium Spray Tests Experiments

Test #	T1	T2	T3	T4
Location	Outside	Outside	In-Vessel	In-Vessel
Height of Spray (m)	4.6	4.6	5.3	5.3
Nozzle Type	H15	GG15	H15	H15
Amount of Na (kg)	4	4	20	20
Flow rate (kg/s)	1	0.5	1	1
Median Particle Size Diameter (mm)	~6	~10	between 3 and 5	between 3 and 5
Initial Temperature of Sodium (°C)	500	500	200	500
Melt Generator Pressure at System Dump Time (psi)	310.7	28.4	307	307
Measured Peak Air Temperature (TC's 1 foot from vessel wall for in-vessel and center of spray for outdoor tests) (°C)	>1200*	880	480	1200
Measured Peak Vessel Overpressure (MPa)	NA	NA	0.006	0.2**
Measured Peak Narrow View Heat Flux (4.8 ft from center of vessel) (kW/m^2)	250	40	<1	89
Notes	*TC failed around 1200°C			**Instrumentation port failure

2.2.2 Previous Comparable Sodium Spray Fire Experiments

This section will review experiments that were presented in Reference [1] with the initial literature review. Large spray fire experiments were performed at the FAUNA facility which is a 220 m^3 vessel. Comparing this to the Surtsey vessel of 100 m^3, it is about 120% larger. These experiments used 60 kg of sodium which is 200% more than the experiments presented here. The FAUNA facility did have water cooled walls which the Surtsey vessel does not. Another difference is the nozzle used for the FAUNA facility was a nozzle with 271 holes at 4mm each and the facility had three pressure gauges versus Surtsey's one. The initial sodium temperature was 500°C for the FAUNA facility. The two outdoor tests were 500C while the in-vessel tests were at 200°C and 500°C. The table below compares the first outdoor spray test (T1) and the second in-vessel spray test (T4) to the tests performed in the FAUNA facility. T1 and T4 were chosen because they have the most similar initial conditions compared to the FAUNA facility

tests. There is very good agreement with the measured peak air temperatures as well as the vessel pressure measurements [3].

Table 2-2: Sodium Spray Fire Experiments Compared to the FAUNA Experiments [9]

Test #	T1	T4	FAUNA***
Amount of Na (kg)	4	20	60
Flow rate (kg/s)	1	1	40
Initial Temperature of Sodium (°C)	500	500	500
Measured Peak Air Temperature (TC's 1 foot from vessel wall for in-vessel and center of spray for outdoor tests) (°C)	>1200*	1200	1200
Measured Peak Vessel Overpressure (MPa)	NA	0.2**	0.18
Notes	*TC failed around 1200°C	**Instrumentation port failure	***[9]

The handful of sodium spray fire tests presented in [4] by Malet *et al.* were performed in a small enclosed vessel of 3.7 m^3 which is much smaller than the 100 m^3 Surtsey vessel. However the temperature and overpressure ranges that they display in Reference 4's Table 3 are within the same range as the experiments presented here.

2.3 Sodium Pool Fire Experiments

This section presents an overview of the results from the sodium pool experiments. For details on the experimental setup and test specific data please refer to Appendix B. The main objective of these sodium pool fire tests was to investigate the effect of cooling on the oxidation of hot molten sodium being poured onto a cold substrate (in our case a stainless steel pan). The overall setup of the sodium pool fire experiments was as follows. Initially solid sodium was heated to approximately 500ºC in an inert containment vessel referred to here as a melt generator. Once this temperature was reach the discharge valve was opened and the sodium was pushed through 6.35 mm (0.25 in) stainless steel heated pipe. The heated pipe reached the burn pan and the sodium poured out about 0.3 m (12 in) above the pan. The burn pan was equipped with thermocouples on the insulated bottom and sides, as well as inside the pan for most tests. Most of the tests the burn pan thickness was 15.875 mm (0.625 in) and for all of the tests the sidewall thickness was 3.175 mm (0.125 in) as described below in Table 2-3.

Table 2-3: Summary of Sodium Pool Fire Tests

Test Number	Diameter of Pan (m)	Height of Pan (m)	Mass of Sodium (kg)	Base Steel Thickness (mm)	Melt Generator Pressure at System Dump Time (psi)	Average Peak Temperature at Bottom of Pan (deg C)	Thickness Ratio (liquid sodium/stainless steel)
Pool 1	0.6	0.0508	2.6	15.875	2.6	320	0.7
Pool 2	0.6	0.0508	2.6	15.875	2.2	320	0.7
Pool 3	0.3	0.127	4.4	6.35	2.4	800	11.5
Pool 4	0.2	0.1778	1.0	6.35	2.5	780	5.9
Pool 6	0.6	0.0508	4.8	15.875	3.2	480	1.3
Pool 7	0.6	0.0508	7.8	15.875	3.4	600	2.0
Pool 8	0.6	0.0508	1.6	15.875	3.6	220	0.4
Pool 9	0.6	0.0508	6.0	15.875	3.6	490	1.6
Pool 10	0.6	0.1016	11.6	15.875	3.2	746	3.0
Pool 11	0.6	0.1016	9.6	15.875	3.9	648	2.5

2.3.1 Sodium Pool Fire Experimental Observations

As shown above in Table 2-3 the thickness ratio of the liquid sodium to the stainless steel substrate was varied for the sodium pool fire experiments. This goal of this section is to provide detailed experimental observations for two different tests. As described in the next section this thickness ratio affects the overall burning temperature of the sodium pool. This section will detail the experimental observations for a small and large thickness ratio. Pool test 3 with the largest thickness ratio and pool test 8 with the smallest thickness ratio are discussed here.

2.3.1.1 Pool Test 3 Experimental Observations

Pool test 3 was a 0.3 m (12 in) diameter burn pan with a 6.35 mm (0.25 in) thickness which yields a thickness ratio of 11.5 (sodium to stainless steel) assuming the sodium evening spreads throughout the pan with a sodium density of 826.8 kg/m^3. For this test 4.4 kg of sodium was poured into the burn pan at 500ºC and the Pan Bottom temperatures rise to around 300ºC quickly (within 40s). The pan temperature then rose to around 700ºC at about 15 minutes and slowly continued to rise to about 750ºC for the next 24 minutes (the duration of the rigorous burning). The maximum temperature of about 790ºC was reached around 55 minutes into the test and then the pan slowly cooled. All of the Pan Bottom TCs (except TC7) are shown below in Figure 2-2. The intent of showing this figure is to display the overall trend of the TC set and how closely all the TCs trend together. The averaged Pan Bottom TC temperatures versus time graph is displayed in Figure 2-3. The averaged temperatures are shown here because all the Pan Bottom thermocouples basically followed the same trend.

For initial post test observations, the residue in the pan had a bumpy yellow with some reddish hot spots still visible on the surface. The next day post test observations were the same bumpy surface but it had oxidized over night so it was a white surface. The residue was rock-like inside the pan. For past sodium pool experiments, these observations are similar [5,6]. This test observation is also summarized in [7].

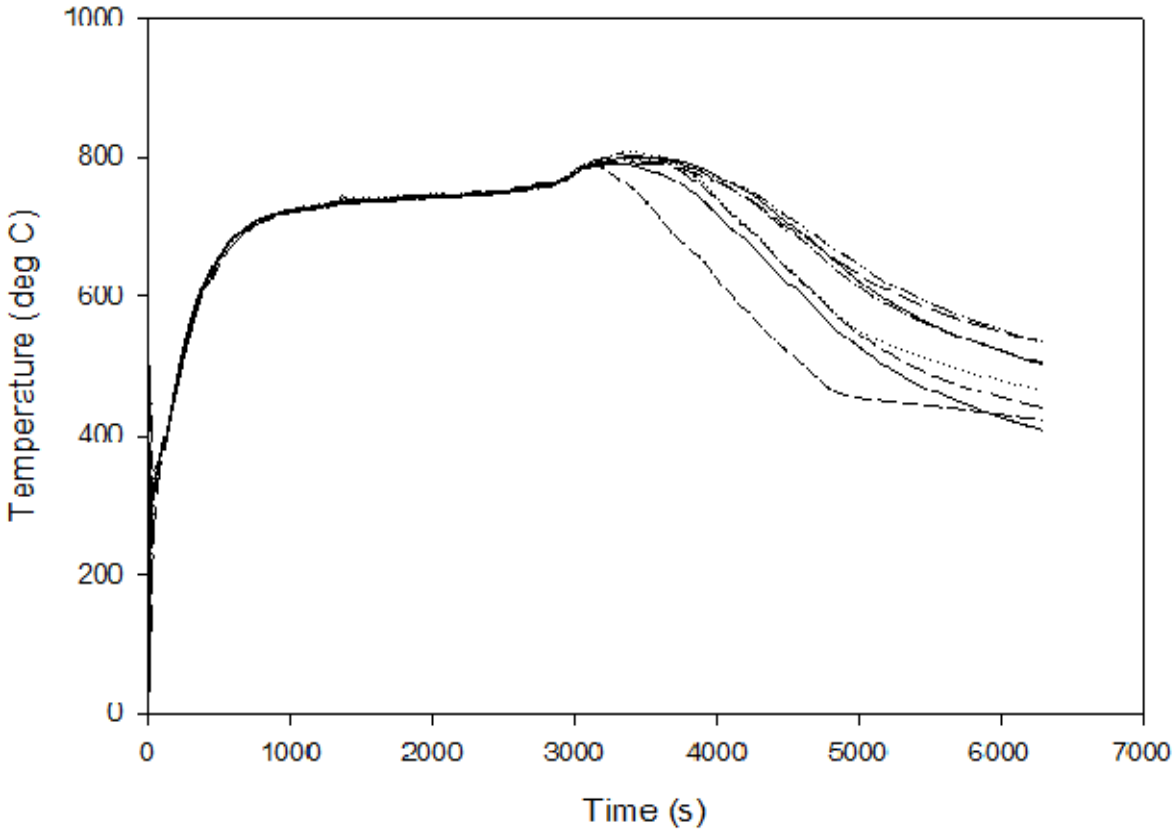

Figure 2-2: Sodium Pool Test 3, Pan Bottom TC Trend

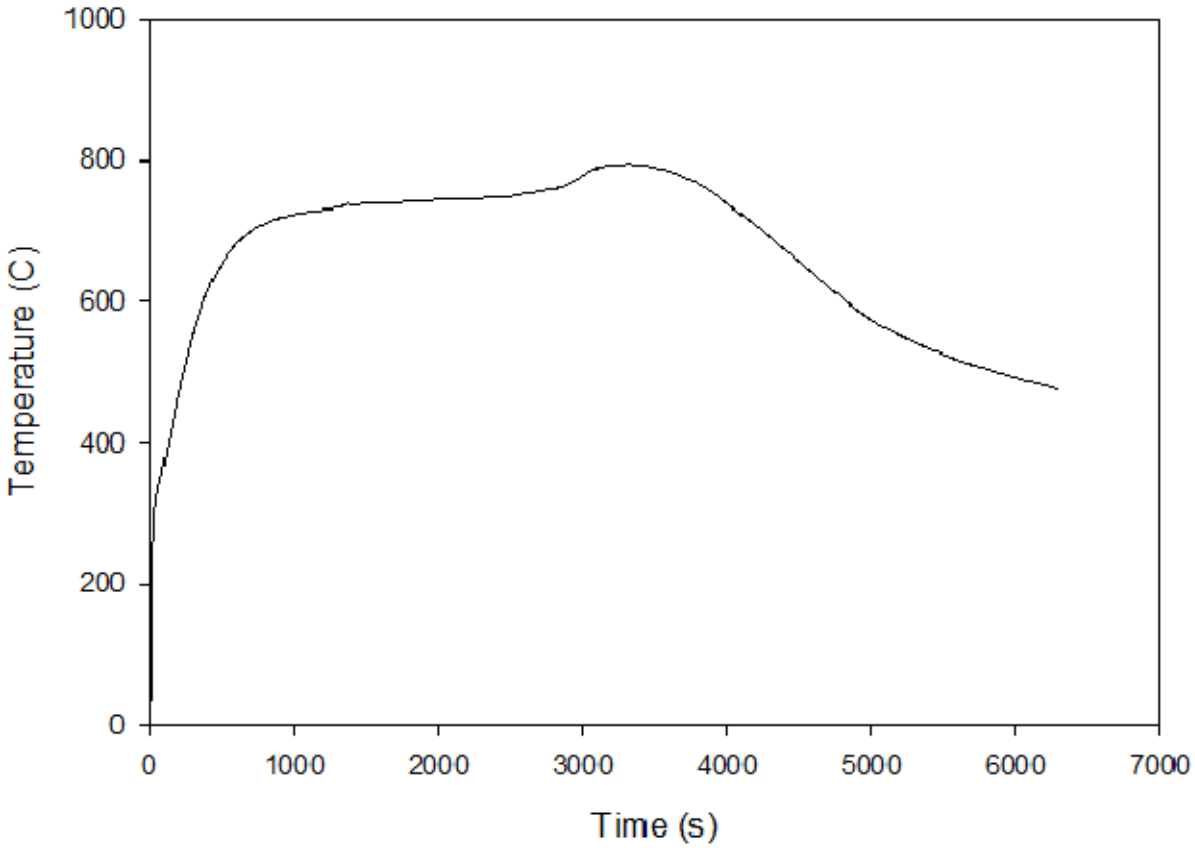

Figure 2-3: Sodium Pool Test 3, Averaged Pan Bottom TCs' Temperatures versus Time (without Pan TC7)

2.3.1.2 Pool Test 8 Experimental Observations

Prior experimental observations in [5,6] differ in significant ways when compared to pool test 8 because the presence of the large heat sink (the steel pan into which the sodium is poured) had a greater impact. Pool test 8 was a 0.6 m (24 in) diameter burn pan with a 15.875 mm (0.625 in) bottom thickness which yields a thickness ratio of 0.4 (sodium to stainless steel) assuming the sodium evenly spreads throughout the pan with a sodium density of 826.8 kg/m^3. The details of the experimental and instrumentation layout are displayed in Appendix B. For this test 1.6 kg of sodium was poured in the steel pan at 500ºC. In brief the Pan Bottom temperatures did not all follow the same trend like that described above for pool test 3. Overall, the measured Pan Bottom temperatures were substantially lower, and there was substantial variation in the measured thermocouple temperatures across the Pan Bottom. The thermocouples on the bottom center of the pan showed much higher temperatures then the outside thermocouples. The center thermocouples quickly rose to around 200ºC but only peaked at 300-325ºC. The thermocouple spread is shown below in Figure 2-4 for reference to spread of the measured temperature evolution. Comparing Figure 2-4 for Pool Test 8 to Figure 2-2 for Pool Test 3, there are notable differences in the TC temperature spread.

The notable difference in the degree of variation for the TC temperature measurements between the two tests is explained by observation of the liquid sodium spreading throughout the pan. Because of the initial heat transfer from the hot liquid sodium to the cool stainless steel substrate, some of the sodium solidifies and forms a ring just outside the center of the spill. Once there is enough sodium to heat up this solid ring of sodium, the sodium spreads further out and forms another solid ring from the same cooling effect as before. Because of this non-uniform spreading behavior the pan was not completely covered with sodium. It was a random pattern with the focus around the more pan center TCs.

Post test observations were conducted on the day of the test at which time the residue in the pan was a powdery yellow surface. Additional observations were conducted the next day and observations indicated the same powdery surface but with both yellow and white powder from the oxidation that occurred overnight. The powdery and soft nature of the residue was distinctly different than the reside from the Pan Test 3 discussed above. These test observations as well as the overall temperature profile for Pan Test 8 have not been described in the literature due to the fact that the previous experimental programs did not have the cold substrate which acts as a heat sink.

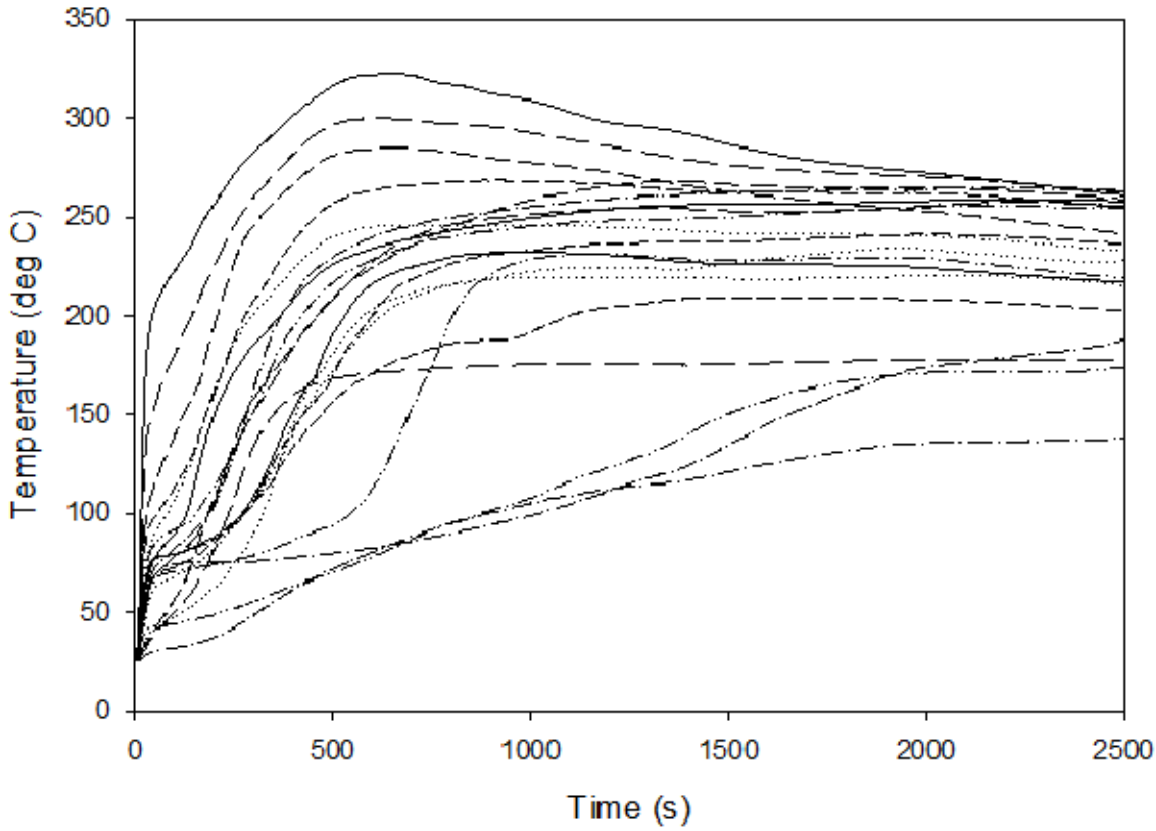

Figure 2-4: Sodium Pool Test 8, Pan Bottom TC Trend

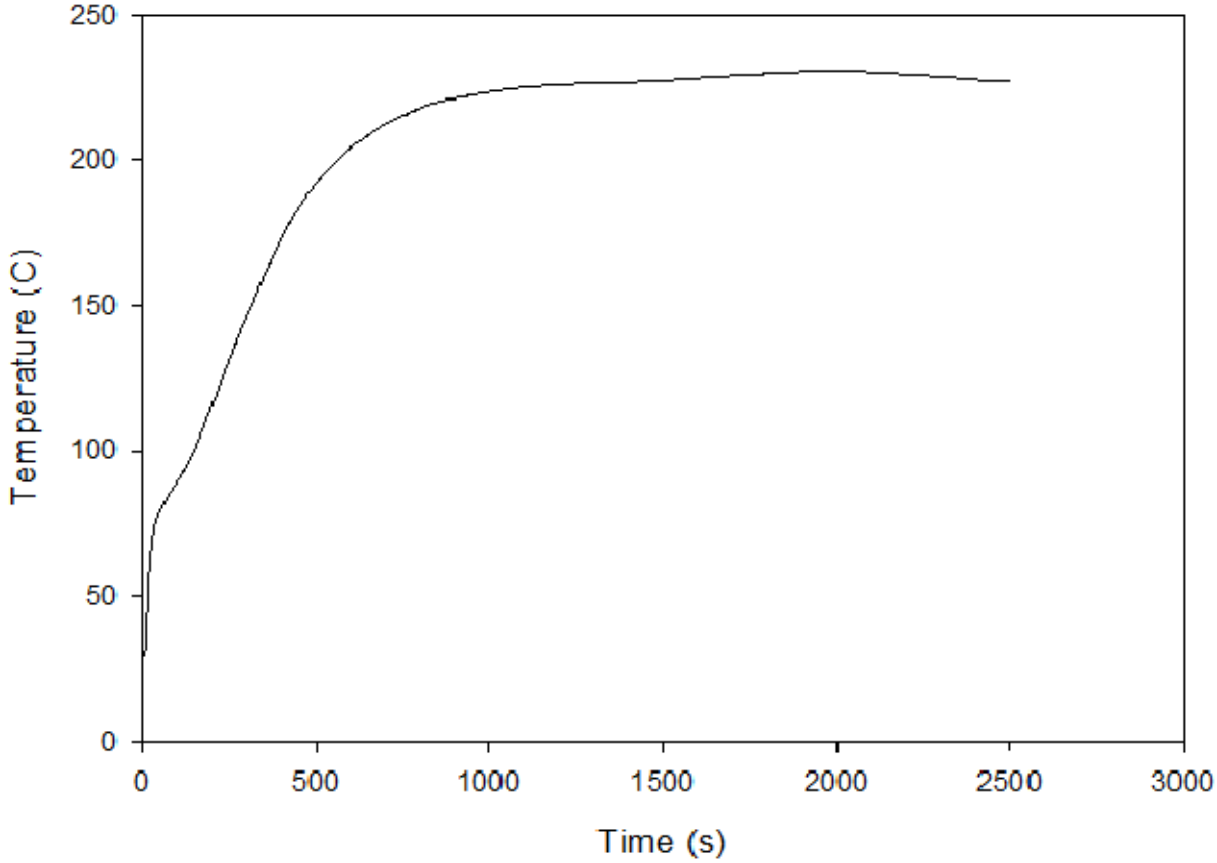

Figure 2-5: Sodium Pool Test 8, Averaged Pan Bottom TCs' Temperatures versus Time (without Pan TC24)

2.3.2 Emissivity Measurement

During Pool Test 6, an optical pyrometer and an IR camera (instrumentation details in Appendix B) were used to obtain an estimate of the surface emissivity of the sodium pool. The basic process is that the temperature of the TC on the top of the burn pan is noted and the emissivity on the IR camera is adjusted until the temperature on the IR camera matches the temperature of the TC. This emissivity is plugged into the pyrometer software. If the pyrometer temperatures match the IR camera temperature and the TC temperature then the estimated emissivity is assumed to be within a reasonable range. This was done for Pool Test 6 and the measured emissivity was 0.58.

2.3.3 Overall Sodium Pool Fire Experimental Data Analysis

When hot sodium is poured onto a cold stainless steel surface (burn pan) there was a significant heat transfer from the hot sodium liquid to the cold pan. Varying the ratio of the thickness of the liquid sodium (assuming an even spread throughout the burn pan) to the thickness of the stainless steel substrate was investigated (see Table 2-3). By varying

this ratio, a significant difference in the measured Pan Bottom peak temperature was observed. Each of the sodium pool burn pans was instrumented with thermocouples on the bottom of the pan. To better understand the effect of the thermal mass of the steel pan, the Pan Bottom below the thermocouples was insulated to reduce the effects of heat loss beyond the pan plus pool system. For each tests these thermocouple temperatures were averaged for each pan and the average temperature evolution over time is shown below in Figure 2-6. The key in this figure is organized by the thickness ratio (liquid sodium/stainless steel). This is to show that by increasing this ratio, the averaged measured temperature also increases. The peaks of each curve from Figure 2-6 are taken and plotted against the thickness ratio in Figure 2-7. There the overall trend of the peak average Pan Bottom temperature increasing with the thickness ratio is indicated.

This overall trend in the data has been qualitatively observed in the literature but to the authors knowledge not been experimentally quantified. This is mainly due to the fact that most of the past experiments use a burn pan that is either externally heated or thermally isolated from its environment (insulated) so the initial heat transfer from the hot liquid sodium to the cold substrate was not the focus of the investigations [1, 8].

In addition to the pan-bottom temperature measurements, heat fluxes from the top surface of the pool have been measured through the use of narrow-angle heat flux gauges. For Pool Tests 1 through 4 only one narrow view heat flux gauge was used for each test and for Pool Tests 6 through 11 there were five narrow view heat flux gauges used (refer to Appendix B for details). As seen below in Figure 2-8 for Pool Tests 1 through 4 the maximum flux reached was about 13 kW/m^2 for Pool Test 2. Gauge location with the higher pan lip heights may explain the measurements for Pool Tests 3 and 4 that differ significantly from other tests. The gauge locations and aiming technique used for these first round of experiments was a lessons learned and changed for the second round of testing.

For Pool tests 6 through 11 Figure 2-9 displays the average measured heat flux from the five gauges. This graph is very difficult to distinguish between tests, but the overall trends can be obtained. Figure 2-10 displays the peak measured heat flux for Pool Test 6 through 11 with respect to the thickness ratio (liquid sodium/stainless steel substrate). This graph displays a clear trend in the measured peak heat flux based on the thickness ratio. This is expected as the same trend is noted with the Pan Bottom temperatures that increase as the thickness ratio is increased.

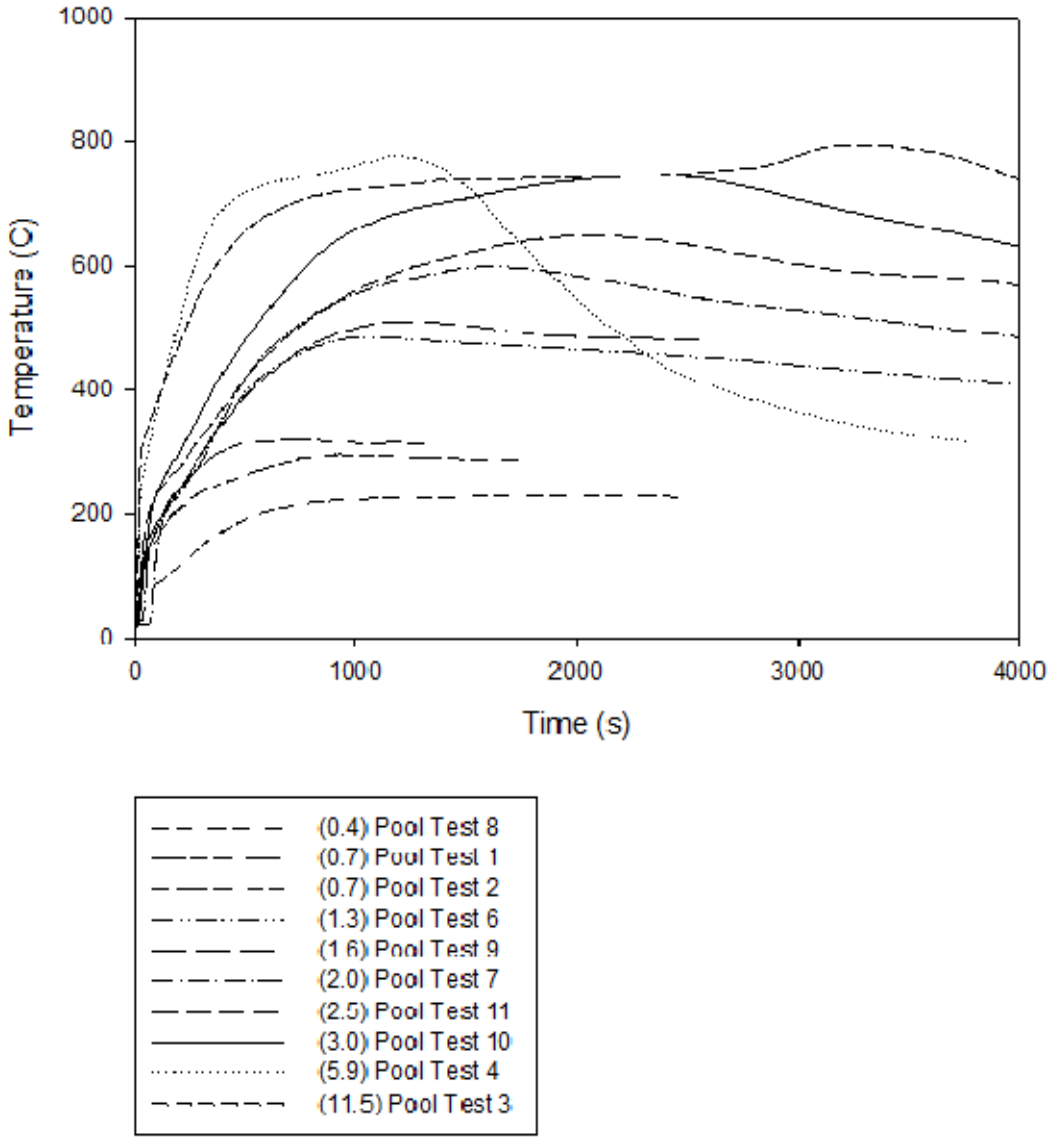

Figure 2-6: All Sodium Pool Tests Displayed by Liquid to Steel Thickness Ratio: Average Pan Bottom TC Temperatures vs Time

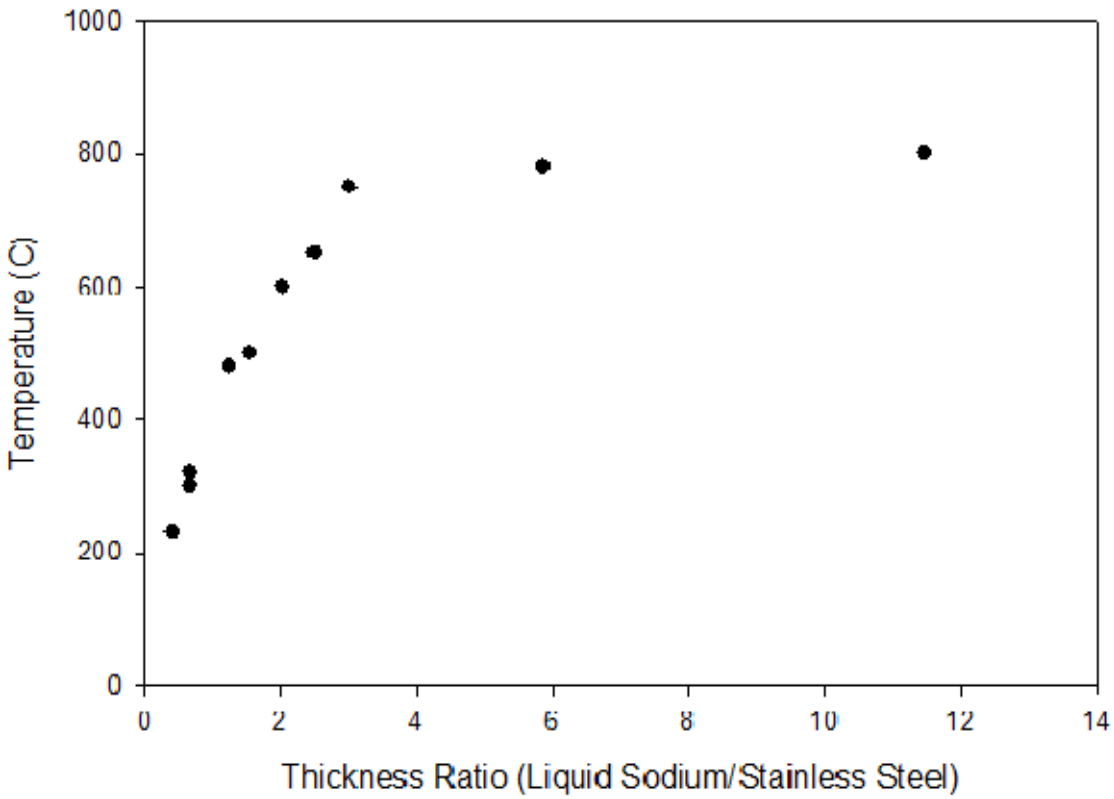

Figure 2-7: All Sodium Pool Tests: Measured Peak of Average Pan Bottom Temperature vs Thickness Ratio (Liquid Sodium/Stainless Steel)

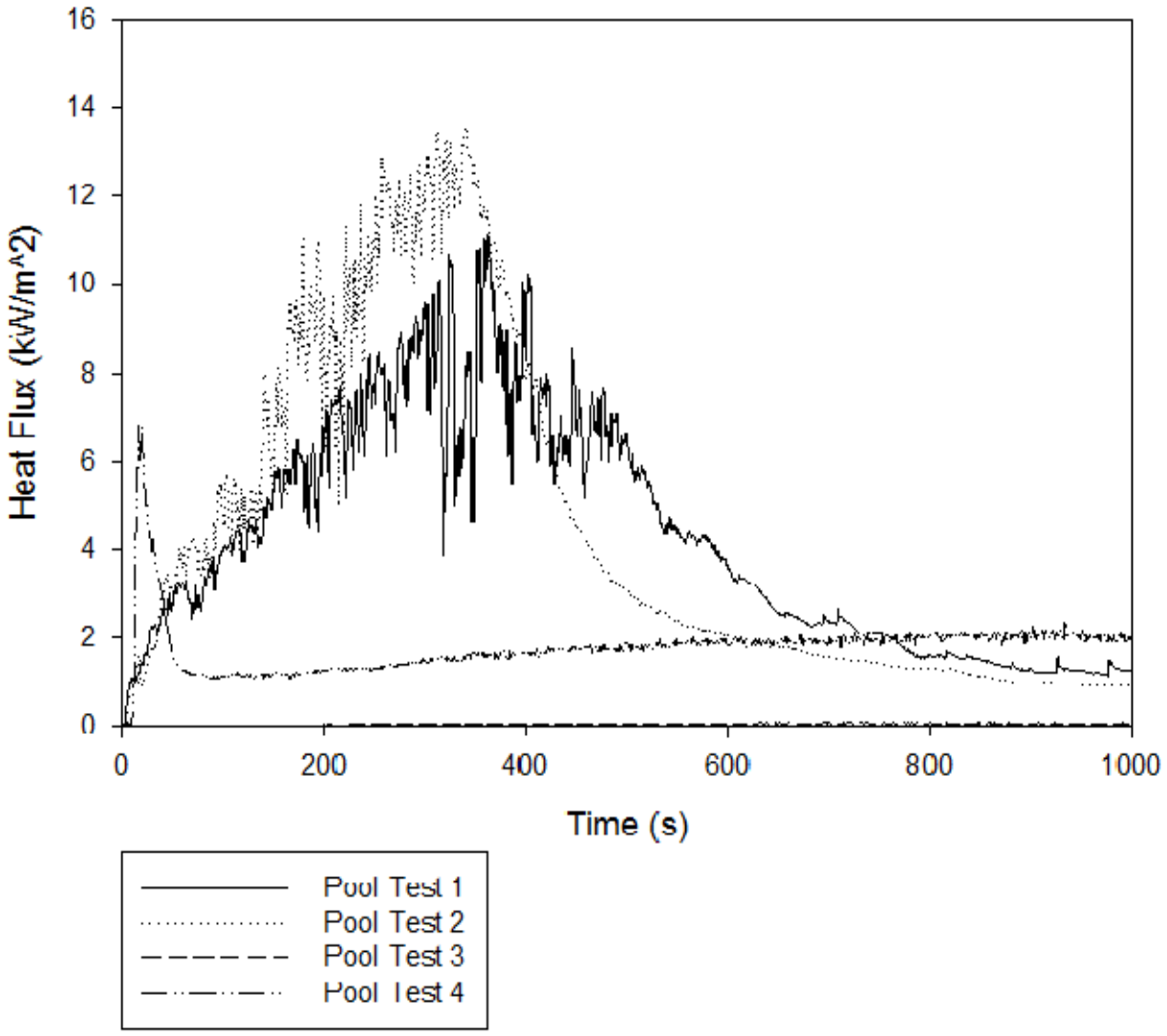

Figure 2-8: Narrow View Heat Flux Measurements for Pool Tests 1 through 4

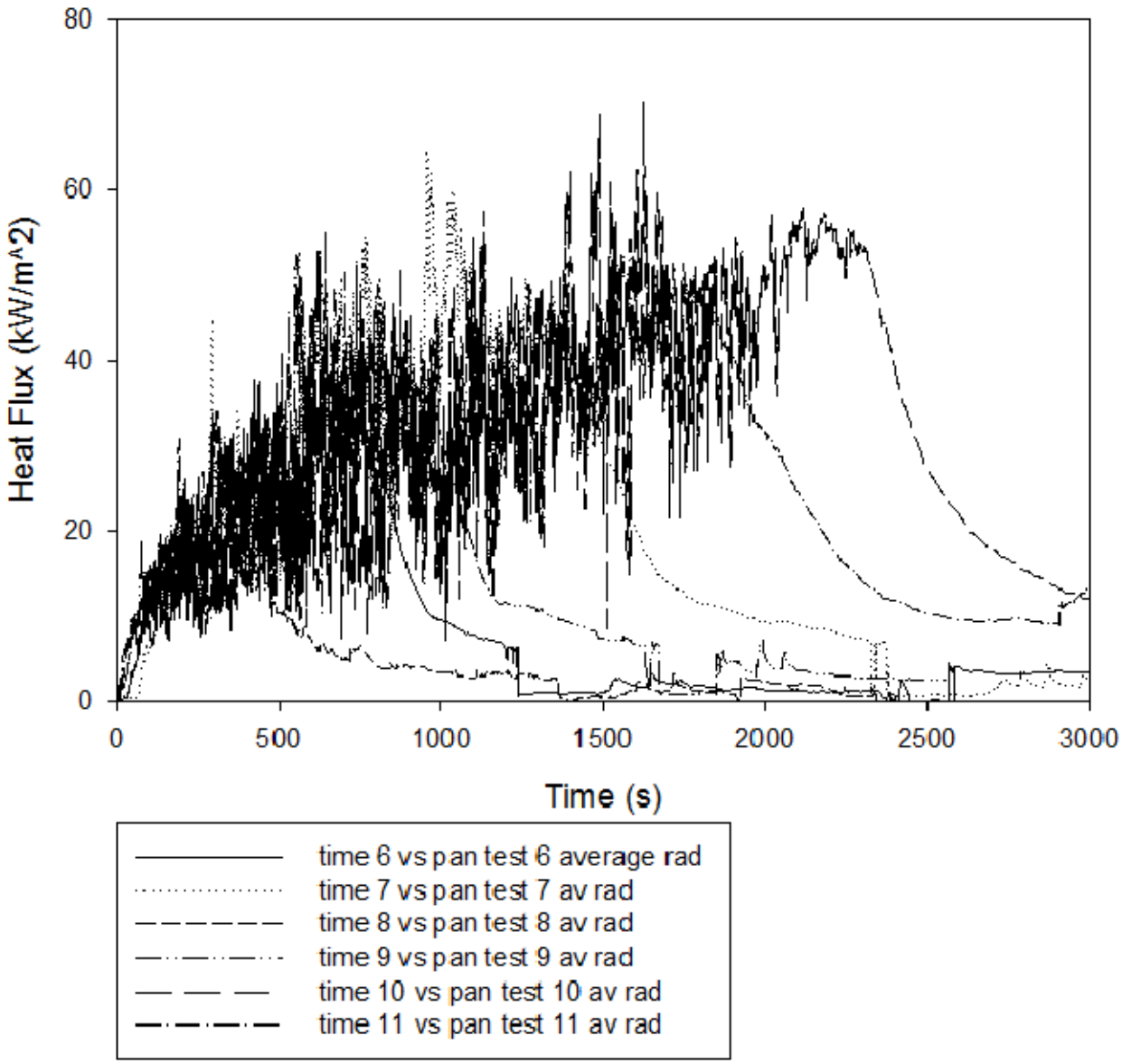

Figure 2-9: Narrow View Heat Flux Measurements for Pool Tests 6 through 11

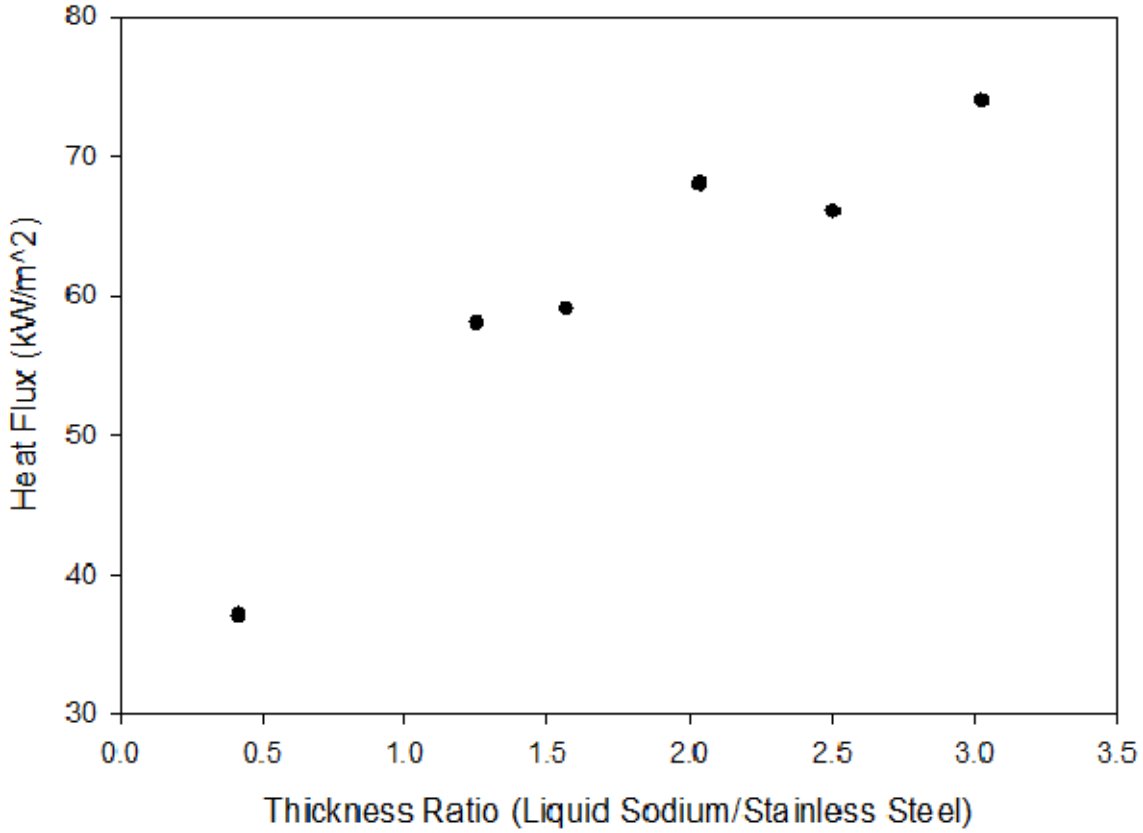

Figure 2-10: Narrow View Maximum Heat Flux Measured vs Thickness Ratio for Pool Tests 6 through 11

3 INVERSE HEAT TRANFER CALCULATIONS FOR POOL EXPERIMENTS

The measurement of heat flux in sodium metal fires is difficult due to the complex surface chemistry as well as the flame being very close to the sodium surface (~5mm). A method for using experimental temperature data to back calculate an estimated surface heat flux that is rugged and relatively inexpensive is based on inverse heat conduction methods. Inverse heat conduction methods estimate absorbed heat flux at specific material interfaces using temperature/time histories, boundary conditions, material properties, and usually an assumption of one-dimensional (1-D) heat flow. This method is commonly used at SNL's fire test facilities.

This section presents the sodium pan absorbed heat flux results obtained from an inverse heat conduction program developed by Beck [9]. These results were used to corroborate the model discussed in Section 4. Other inverse heat-conduction programs are available, e.g., SNL's One Dimensional Direct and Inverse Thermal program (SODDIT) [10], but IHCP1D was chosen because it is commercially available, has a graphical user interface (GUI), and can be used on an IBM-compatible personal computer.

3.1 Overview of IHCP1D Code

In general, the inverse heat conduction methods are very sensitive to TC measurement errors, material properties, thermal-property variations, and two-dimensional effects. Mathematically, inverse methods are "ill-posed," i.e., their solution does not satisfy requirements of existence, uniqueness, and stability under small changes in input parameters [11]. Hence, it is important to understand effects of the changes in input parameters on inverse heat flux calculations.

The effects of temperature measurement random errors (from noise in the data acquisition system digital voltmeter) on inverse heat flux calculations were analyzed in [12] for a flat plate configuration. An analytical solution for a triangular pulse was studied. When controlled random noise was introduced to the temperature history input, error magnitudes in the inverse heat conduction solution increased linearly with the noise level of the input signal. For a ±2°F noise level, the heat flux error was as high as 29% for a low thermal diffusivity material, and as low as 11% for a high diffusivity material. For small noise levels (i.e., ±0.1°F), the errors were 2% for a low diffusivity material, and 1% for a high diffusivity material.

In [13], a sensitivity analysis was performed to quantify the effects of input parameter variations on the estimated heat flux when using the inverse heat conduction method. The approach used was to compare results from a number of cases using modified inputs of a base-case. Some of the input parameters that were varied were the thickness, thermal conductivity, and volumetric heat capacity of the plate and insulation; TC measurement uncertainty; boundary conditions type; data sampling period; and numerical inputs such as number of future times. Results of the analysis show that the use of

constant thermal properties rather than temperature dependent values made a significant difference in the resultant heat flux; therefore, temperature-dependent values were used for this study.
In [14], errors were evaluated when one-dimensional inverse heat flux techniques were applied to problems involving two-dimensional heat-transfer problems using cylindrical geometric configuration. The degree of localized heat flux was controlled using a circumferential heat flux boundary condition. Results were compared against a two-dimensional finite-difference model of the forward problem. Results showed that errors in inverse heat flux calculations ranged between 0.5% and 18%, depending on how localized (i.e., spatially concentrated) the heat flux was on the outer surface of the cylinder.

In summary, results obtained with inverse heat conduction methods should be analyzed carefully given the sensitivity of inverse heat transfer methods to the parameters discussed above.

3.2 Inverse Heat Flux Results

The experimental setup used to obtained the sodium pan, absorbed heat flux is described in detail in Appendix B. Figure 3-1 shows a schematic of the experiment setup with known and unknown quantities. The temperature TC_1 and TC_N were obtained from the TCs installed on the backside of the circular, stainless steel (SS) pan (i.e. at the interface between the pan and the insulation). The temperature on the backside of the insulation was assumed to be at ambient temperature (T_{AMB}). Two-dimensional thermal effects were expected in these tests as depicted in the temperature-depth plot on the left side of the figure and the radial heat flux component Qr through the thickness of the pan. This was expected due to an uneven distribution of the sodium deposition layer across the surface of the pan.

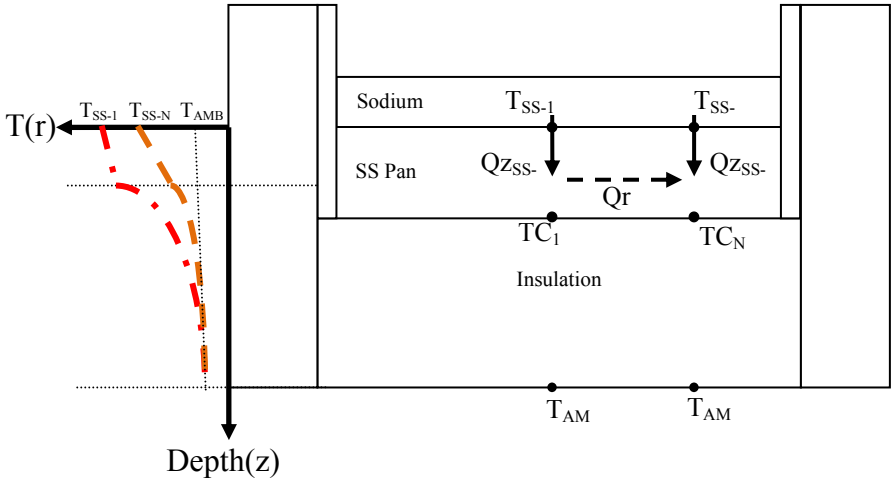

Figure 3-1: IHCP problem definition

Inverse methods, like the one employed by IHCP, use the energy equations, known boundary conditions information (i.e., TC_i and T_{AMB}), and a least-square method with

sensitivity coefficients to calculate a best fit through the known time-dependent boundary conditions. Information gathered from this process is used to determine the unknown temperature, $T_{SS\text{-}I}$, and and the heat flux, $Q_{SS\text{-}i}$, by enforcing an energy balance [10]. The subscript i is an integer from 1 to 9 for Pool Test 1 through 4 and 1 to 25 for Pool Test 6 to Pool Test 11 as described in Appendix B.

In addition to the above considerations, IHCP uses a number future time step values in its input to calculate temperature and heat flux at the surface of interest for the current time step calculation. Undesirable results can be obtained with too small or too large number of future time steps. With small number of future time steps the results are subject to large variations in heat fluxes at the surface of interest due to random errors in the TC temperature measurements errors as suggested by [12]. However, with a large number of future time steps the results are subject to bias errors at the surface of interest due to excess filtering of the data as shown in [13]. The result is that heat fluxes are under-predicted. For this study, Equation 3-1 was used to determine the number of future times needed as suggested by Beck [9]:

$$r = 1 + 0.18\frac{E^2}{\alpha\Delta t} \qquad \text{Equation 3-1}$$

where r is the number of future time steps, E is the thickness of the pan, α is the stainless steel diffusivity and Δt is the temperature measurement frequency. This formula does not take into account the response of the thermocouple. In general ungrounded, 1/16 inch, MgO insulated, metal sheathed thermocouples attached to the bottom of a flat plate, as in this experiments, have response time in the order of two seconds. To take into account this time lag, an additional two seconds were added to the number of future time steps.

IHCP also requires the thickness and material properties of the stainless steel pan and insulation. Table 3-1 shows the material properties that were inputted into IHCP. Figure 3-2 through Figure 3-4 displays the surface temperature and absorbed heat flux results using the actual experimental data taken from the TC measurements at the center, the average TC measurements at half radius, and the average TC measurements at full radius for Pool Tests 2 and 3, and from the TC measurements at the center, averaged TC measurements at quarter radius, averaged TC measurements at three-quarter radius and averaged TC measurements at full radius for Pool Test 10. These tests span the spectrum of sodium-stainless-steel ratios in this test series. As expected, the heat flux increases immediately after the sodium impacts the pan and then decays due to plate-sodium-layer temperature equilibrium.

Table 3-1: Material Property Inputs used in IHCP1D

Temperature (ºC)	Stainless Steel 316		Duraboard® Insulation	
	Conduction Coefficient (W/mºC)	Volumetric Heat Capacity (J/m^{3}ºC)	Conduction Coefficient (W/mºC)	Volumetric Heat Capacity (J/m^{3}ºC)
27	13.4	3855384	0.029	159488
327	18.3	4530900	0.065	
527	21.3	4745088	0.105	
727	24.2	4983990	0.155	

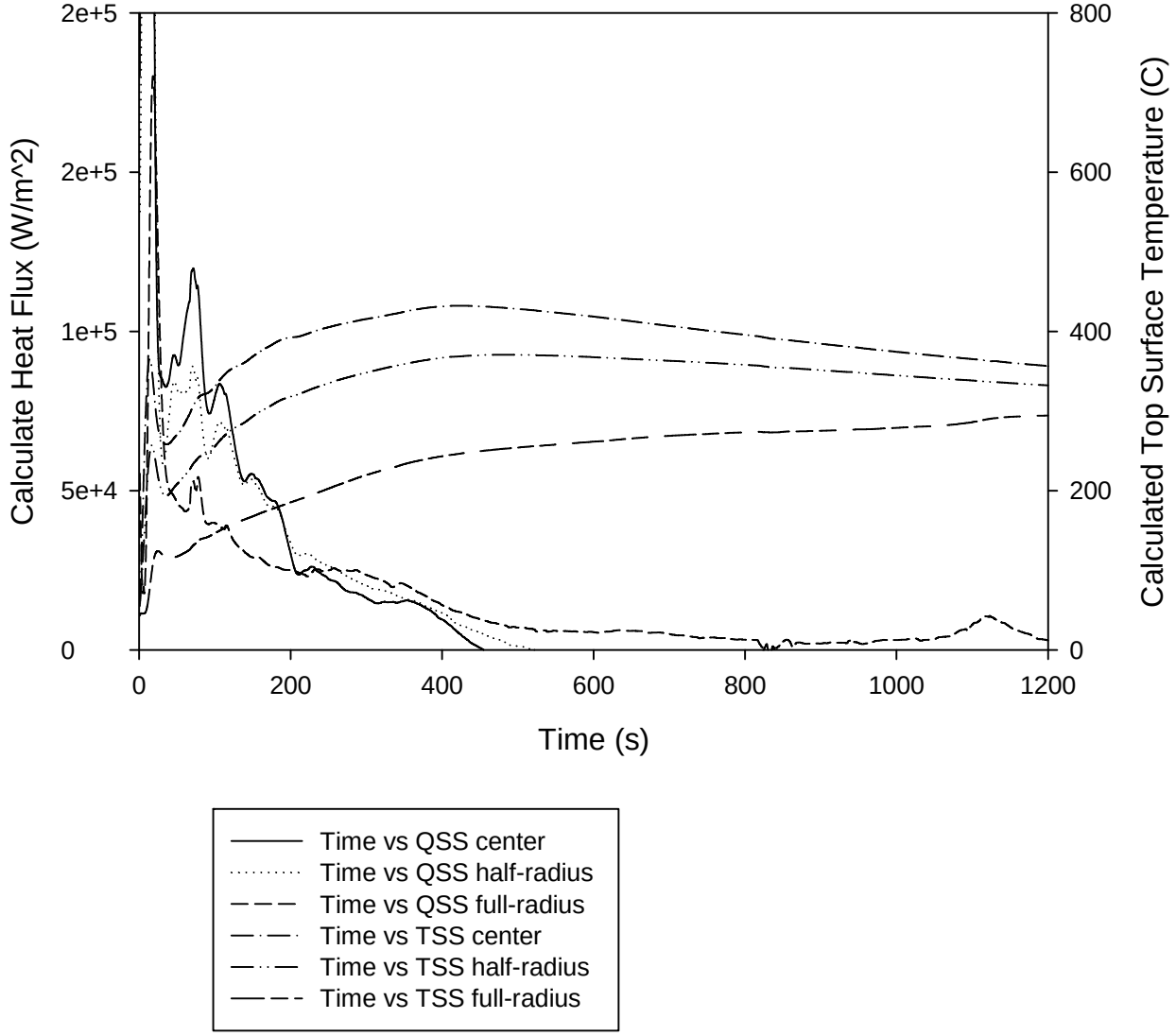

Figure 3-2: Pool Test 2 Calculated Heat Flux and Top Surface Temperatures vs Time

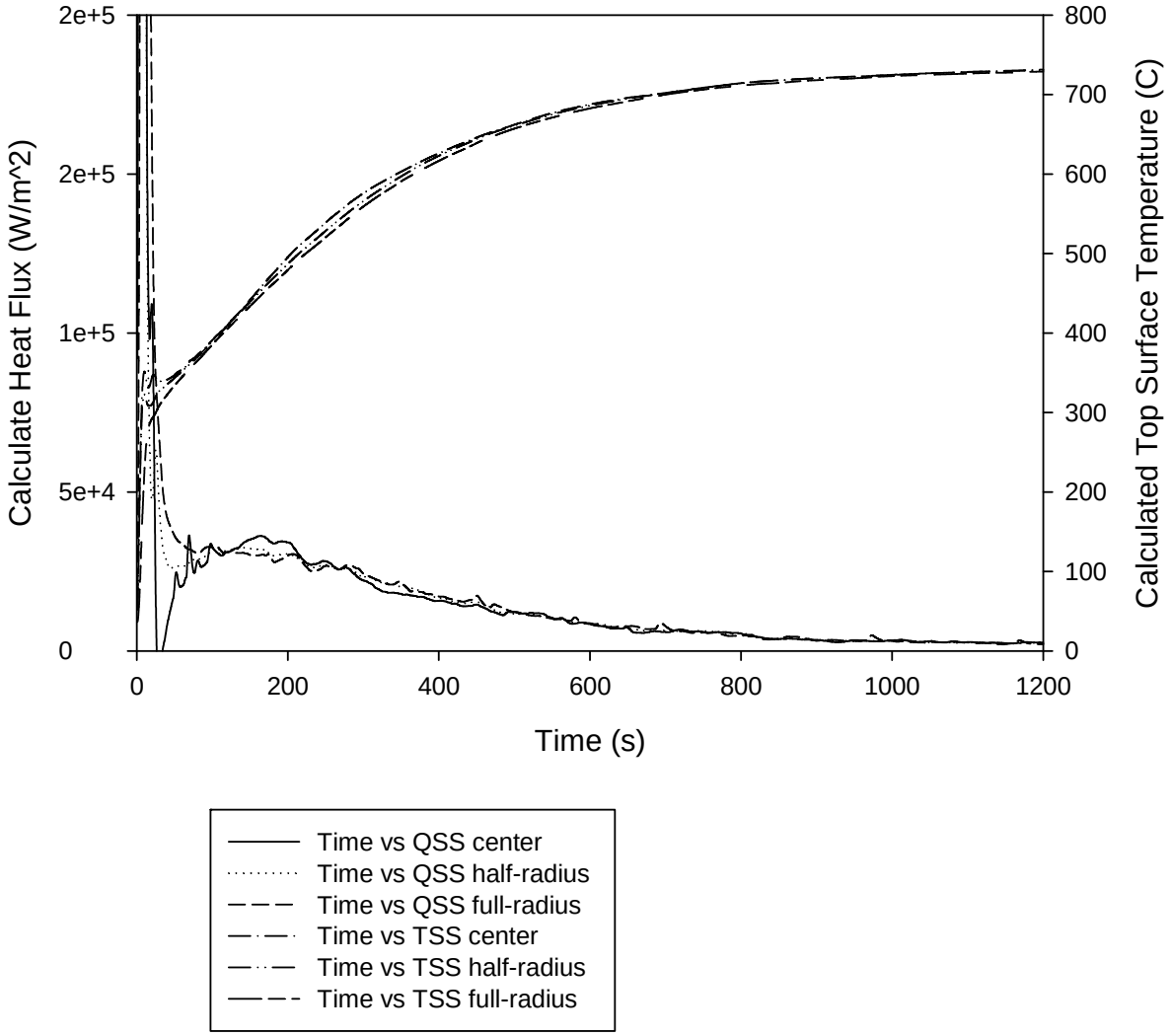

Figure 3-3: Pool Test 3 Calculated Heat Flux and Top Surface Temperatures vs Time

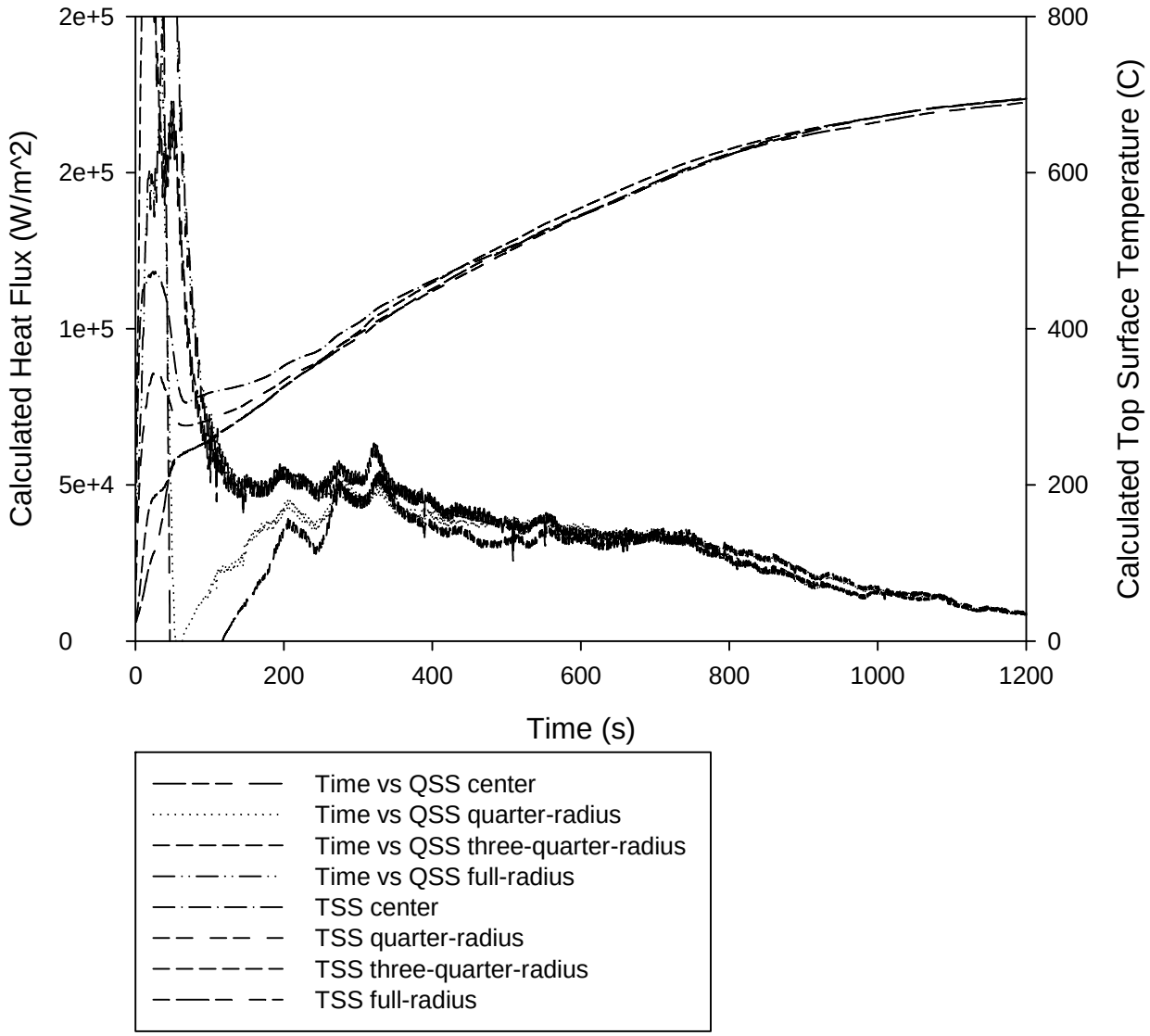

Figure 3-4: Pool Test 10 Calculated Heat Flux and Top Surface Temperatures vs Time

Figure 3-5 and Figure 3-6 present more detail of Pool test 3 to show an example of the error calculation. These figures show results using the center Pan Bottom TC in Pool Test 3. As depicted by the "TC Residual", differences between TC test data and IHCP calculated backside temperature values are large initially. During this time period, errors in the predicted absorbed heat flux are expected to be large (Figure 3-6). After 30 seconds, the differences between TC test data and IHCP calculated backside temperature values begin to decay, giving more confidence in the calculated absorbed heat flux values. These trends were observed initially in all tests and where TC measured temperatures change abruptly during the middle of the experiment. Overall, heat flux trends predicted by inverse heat flux calculations match those of the model shown in Section 4.

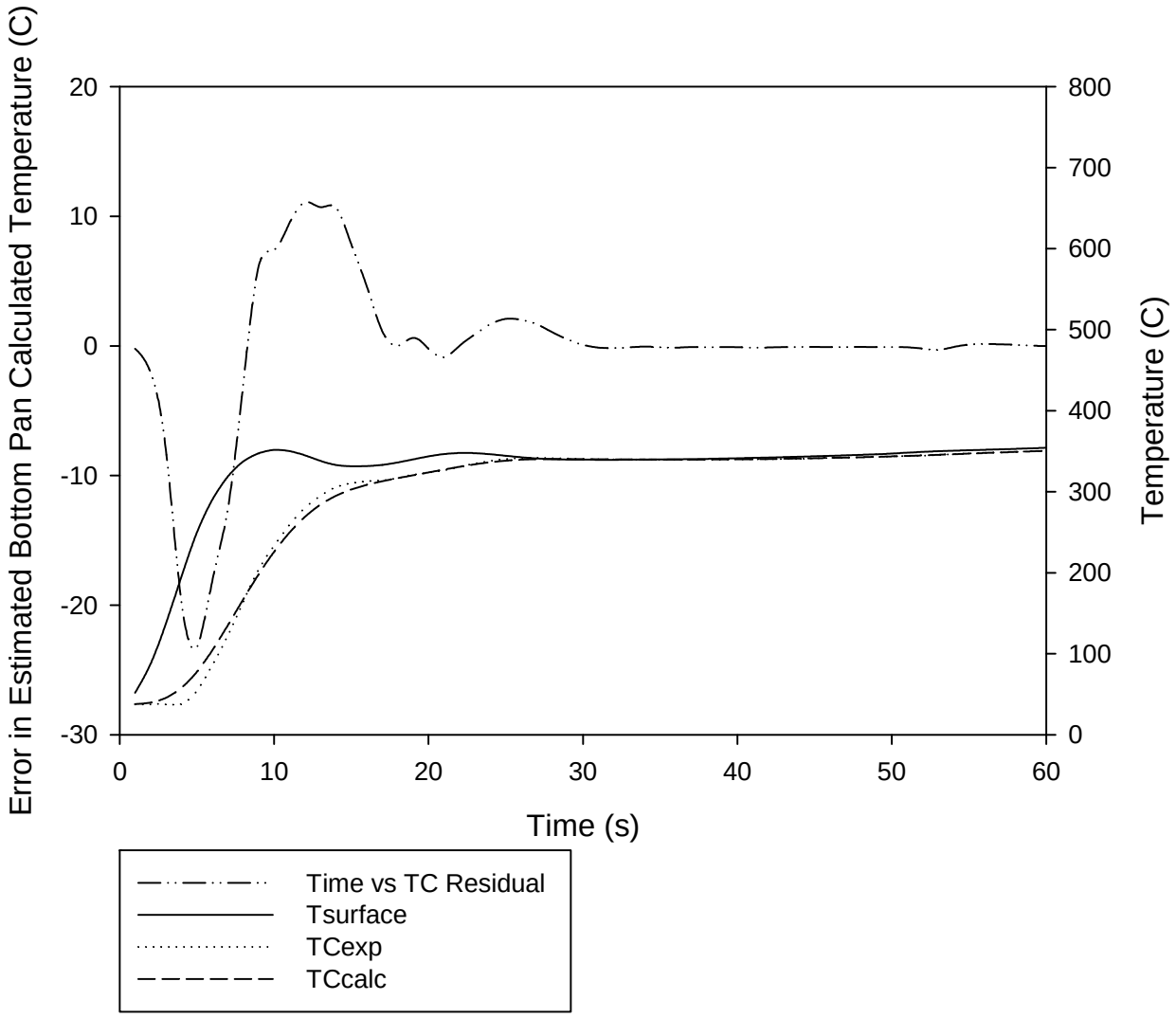

Figure 3-5: Pool Test 3 Calculated Pan Center Temperatures with Estimated Error

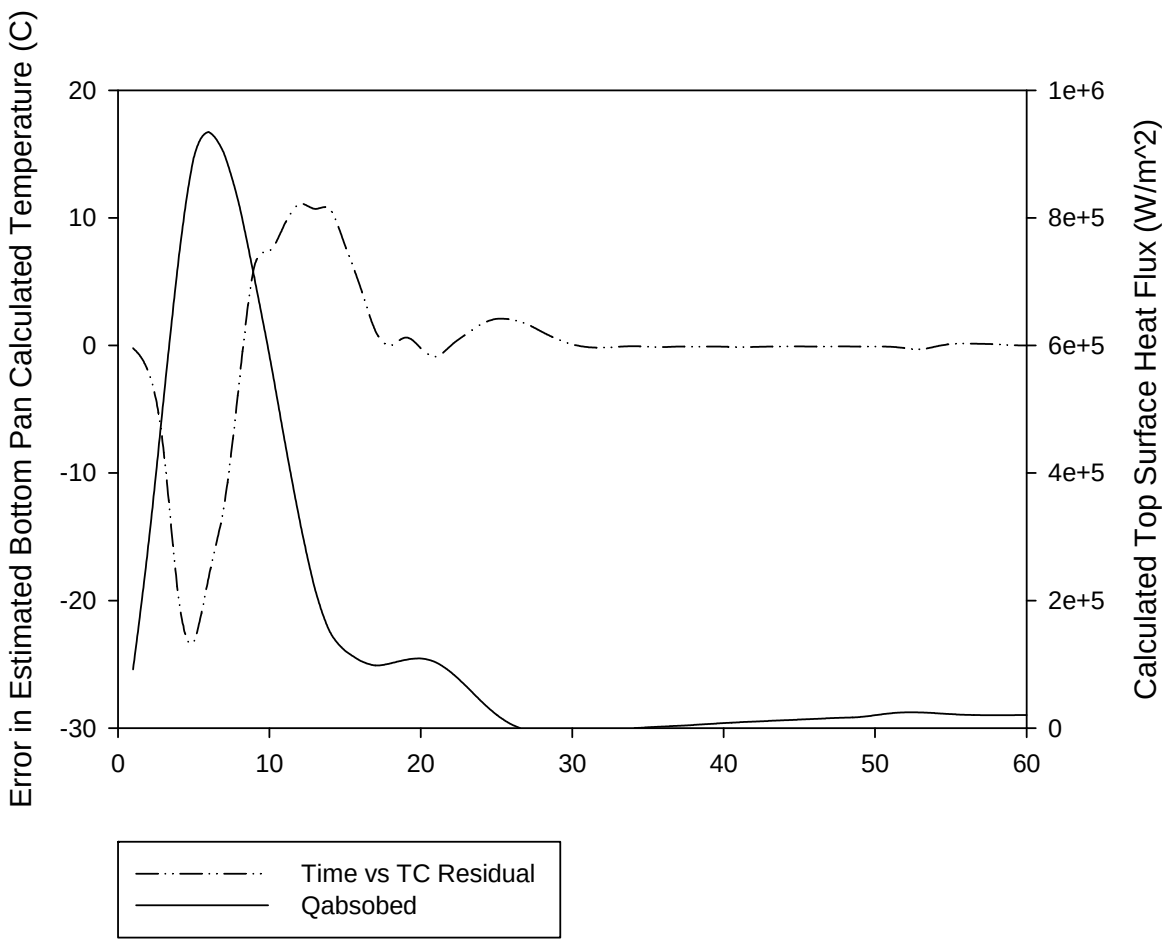

Figure 3-6: Pool Test 3 Calculated Surface Heat Flux with Estimated Error

4 Sodium Pool Fire Model Development

This section addresses model predictions for the oxidation of sodium pools. In light of the results described in Section 2.2 where sodium pool interactions with the steel pan containing the pool led to reduced temperatures, the focus will be on understanding the burning modes in the range of 200°C to 700°C. Key features of the models include (1) the unsteady nature of the thermal evolution because the heating of the pool plus pan system occurs over the same time frame as the sodium oxidation and (2) the role of the sodium oxide crust in altering the burning rate which thus alters the heat release rate. While the section focuses on sodium pools interacting thermally with a substrate, the models described should be generally applicable to sodium oxidation in this temperature range. Prior models for sodium oxidation ignored the formation of an oxide film or crust on the surface and are only accurate for higher temperatures (above 600°C) where this oxide crust appears to melt as will be described below. The present model accounts for the oxide crust and thus extends prediction of sodium oxidation to lower temperatures.

Sodium metal is a solid at room temperature, but melts at 98°C or 371 K. In the liquid phase, sodium has a number of desirable properties associated with its thermal characteristics and its moderation of neutrons that make it desirable as a cooling fluid in certain nuclear reactor designs. In particular, sodium is well-suited for what is referred to as Generation IV reactor technologies that re-burn nuclear fuels to reduce nuclear waste.

While there are a number of desirable thermal characteristics associated with liquid sodium, its propensity to oxidize even at relatively low temperatures presents safety challenges. Sodium ignition measurements suggest ignition temperatures as low as 120°C and as high as 320°C depending on the configuration [5]. The range in these ignition temperatures is better understood by a more recent series of analyses using classical ignition theory, relating chemical kinetic rates to heat loss rates [15-17] although there is little justification for the particular kinetic parameters beyond the empirical fit.

In reactors, sodium coolants might operate in the range from 355°C to 550°C (expected inlet and outlet temperatures) [18-19] so any sodium leak is expected to be ignitable. While every effort is made to prevent leaks, they can occur [21-22] and reactor designs incorporate means of mitigating fires associated with such leaks. One approach to mitigating large sodium-leak fires is to provide gently sloping floors that drain sodium into tanks that are either inerted or have extremely limited ventilation, removing the fuel from the oxidizer [23]. The shear scale of reactor vessels with areas of hundreds of square meters suggests that a substantial quantity of sodium can exist on surfaces before or without draining into such tanks, and experience with small leaks suggests that they do not extend far enough to interact with such tanks. Thus, there is the possibility of a sodium leak leading to a relatively shallow pool on reactor floors that might be subject to an oxidizing environment. It is important to understand the burning rates in this case.

To quantify shallow, we employ the Laplace length, $\delta_L = \sqrt{\sigma_{\mathrm{Na}} / \rho_{\mathrm{Na}} g}$, the length scale obtained from the ratio of the surface forces to the gravitational forces. In the expression

for the Laplace length, σ is the surface tension, ρ is the density, g is the gravitational acceleration and the subscript Na indicates properties evaluated for sodium. The Laplace length is between four and five millimeters in the temperature range of interest and this is a characteristic depth of an unconfined pool (or puddle) on a non-wetting surface.

In the following section, observations relevant to sodium pool fires are summarized based on prior literature. Following that, results from a recent series of pool fire experiments (Section 2.2) that motivate this model are reviewed in a qualitative manner. Conservation equations that describe sodium pool evolution under a broad range of conditions are presented and simplified. The characteristics of the model are presented and then the model is compared with experimental measurements from (Section 2.2). A number of model parameters are not well known, and the final section discusses uncertainties associated with these parameters, identifies sensitivities and suggests further work.

4.1 Prior sodium pool observations and models

If a sodium leak forms a pool at a temperature much above ambient the oxidation of the sodium will release sufficient heat to sustain the reaction. The temperature above which this reaction can be sustained is not the subject of the current analysis but is in the vicinity of 380 – 500 K depending on the environment and the test methods [5]. A model for the ignition of sodium pools has recently been presented by Makino, and reference can be made to that model for ignition conditions [15-17]. One type of boundary condition that is particularly relevant to the occurrence of ignition is the degree to which heat losses to the sides or bottom of a pool affect the thermal balance; in general, test conditions in the sodium pool fire literature have been designed to minimize these heat losses or to control pool temperatures through artificial heating and cooling of pans. In the absence of heat losses, once combustion is sustained the pool will gradually heat until it reaches its own thermal equilibrium temperature at which point the heat transferred to the pool is equal to the enthalpy of vaporization. This heating process goes through a number of phases as described in the literature. These phases include the existence of condensed oxide crust layers on the pool surface up to approximately 600ºC (873 K) when the crust disappears. This last disappearance has been attributed to the melting and subsequent sinking of Na_2O_2 [5].

4.2 Recent sodium pool observations

In recent sodium pool fire experiments (Section 2.2), hot molten sodium was poured into cool (ambient temperature) steel pans that were sufficiently massive to cool the sodium down to temperatures in the range of 70 to 300°C. It is noteworthy that while these temperatures were in the range of observed sodium ignition temperatures or below, the sodium never failed to ignite. In general, the sodium was observed to go through the several phases that were observed and documented elsewhere in the literature. There is an early phase where the surface changes color through grays and whites. Eventually, surface temperatures rise to the point where the surface glows with radiative emissions, but in a mottled manner that indicates some porous solid network through which the

sodium is oxidizing. The porous solid network is presumably comprised of oxide products that are solid up to relevant temperatures. In particular, Na_2O is over the entire range of temperatures while Na_2O_2 has a melting temperature of 675°C. Following this "glowing oxidation through the porous oxide" stage, one of two alternate stages is observed. If the temperatures are sufficiently high, the oxide crust disappears and a clean sodium surface results. This surface oxidizes in a manner than has been described previously through sodium vaporization and gas-phase combustion. Alternately, for lower temperatures, the oxide crust does not disappear (presumably because temperatures do not exceed a phase-change temperature). The oxide crust grows thicker and gradually inhibits the oxidation rate. The focus of this section is on the understanding of this latter burning mode where the oxide crust inhibits oxidation.

The primary data available in the experiments described in Section 2.2 is the time-evolving temperature of the bottom surface of the steel pan within which sodium has been poured. There are several aspects of this temperature evolution that deserve mention prior to describing the model. First, there is a rapid temperature change over tens of seconds while sodium is poured into the pan and the pan and pool temperatures come to an approximate equilibrium [5]. Second, there is a period of roughly linear temperature rise in time that lasts hundreds of seconds, but this period is less for shallower pools. For pools where the temperature rises sufficiently, an equilibrium temperature between 700 and 850°C is reached in these hundreds of seconds. For pools where the temperature rises less in this period, the rate of temperature rise falls off with time and in some cases results in a temperature decline. These aspects of the temperature evolution will be revisited below.

4.3 Conservation equations for a pool with a porous oxide crust

The defining feature of the more recent experimental measurements is the dominance of the oxide crust for scenarios where a sodium pool forms on a thermally massive substrate. As will be seen below (see also [5]) the existing models for sodium pool oxidation neglect the oxide crust and are unable to predict the characteristics of sodium pool oxidation under these conditions. An overall schematic of the model is presented in Figure 4-1 where four layers are indicated. The key aspects of the model are the oxidizer transport to the reaction zone and the distribution of heat transfer from the reaction zone. Oxidizer from the ambient is transported through a boundary layer into the oxide crust and to the sodium pool where it reacts with sodium. In the context of the present model, the reaction zone will be limited to this interface between the sodium pool and the oxide crust, although other options are discussed in later sections. Heat released from this reaction is transported back through the oxide crust to the ambient and through the pool to the substrate (a pan in the experiments). The key difference between the model described here and other models [1, 24] is the influence of the porous oxide crust on both transport processes. In the limit where the oxide crust thickness goes to zero, the model described here transitions to the more traditional models.

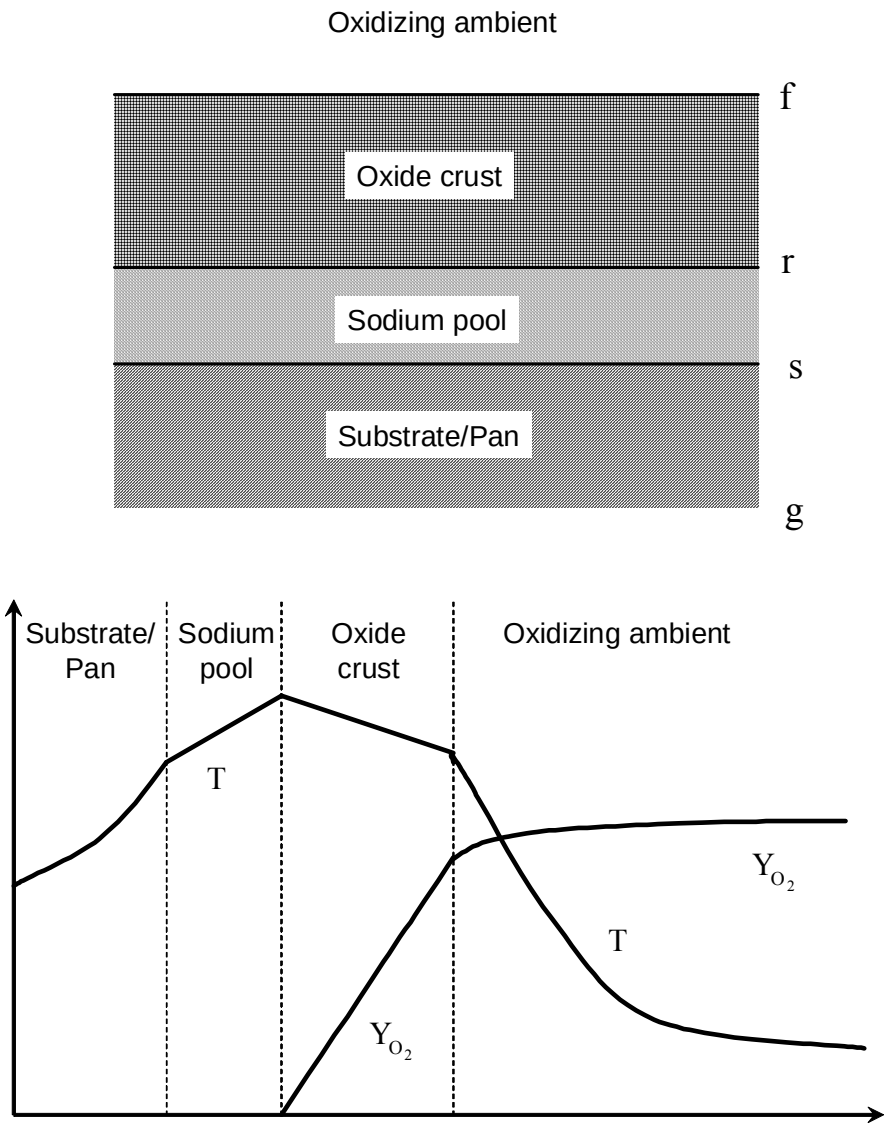

Figure 4-1: Schematic indicating the layers over which the model will predict heat and mass flux including representative profiles of oxidizer mass fraction and temperature across these various layers. Letters to the right of the upper diagram indicate subscripts applicable to interfaces.

Important objectives of the model developed in the following paragraphs are to (1) predict the pool-burning characteristics for the broader range of conditions now measured and (2) aid in the interpretation of the measurements. Of the pool-burning characteristics, it will be important to identify conditions where the sodium oxidizes in the manner described by existing models as opposed to the conditions where the oxide crust is significant. Since the available data is limited to the thermal evolution (temperatures and heat fluxes) of the pool-substrate system, the model predictions will focus on this. Further, the oxide crust is found in the literature to be insignificant for temperatures above approximately 600ºC (873 K) when it disappears [5], making the thermal evolution

significant. It will be found that inhibitions of heat release through reduced transport rates in the oxide crust will lead to situations where heat loss rates, relative to reduced heat release rates, are substantial at lower temperatures. The balance between heat release and heat loss leads to the lower observed temperatures in the experiments.

In the following sections, simplified conservation equations will be developed to describe the evolution of the system shown in Figure 4-1. The most significant issues will generally arise at interfaces between the various layers in Figure 4-1, and these interfaces will be of greater focus. Material properties for the sodium system, especially for the oxides, are not well known in many cases so significant simplifications to the conservation equations are often warranted just because of property uncertainties. In addition, the conservation equations will be given in a single spatial dimension, the *x*-direction, and only the slowly evolving processes will be considered to be unsteady with other processes assumed to be quasi-steady and following the evolution of the slow processes. The processes that are the relevant slowly-evolving processes are:

- The change in thickness of the sodium and oxide-crust layers.
- The thermal evolution of the condensed phases.

Other processes including the mass and thermal evolution of the gas phases can be assumed to be quasi-steady based on faster diffusivity rates.

To develop this predictive capability, the model will be broken down into four components: a review of the oxidation chemistry, a description of mass conservation associated with the conversion of a pool of sodium to an oxide crust, a description of the oxidizer flux to the sodium that determines the reaction rate and a description of the heat transfer that drives the thermal evolution of the system.

4.3.1 Sodium oxidation chemistry

Sodium is readily oxidized by oxygen, and this oxidation is fast relative to other transport processes leading to the assumption that sodium and oxygen do not coexist. This implies that they react in a thin layer to form one of two products, either sodium oxide

$$\mathrm{Na} + \frac{1}{4}\mathrm{O_2} \rightarrow \frac{1}{2}\mathrm{Na_2O} \tag{4-1}$$

or sodium peroxide

$$\mathrm{Na} + \frac{1}{2}\mathrm{O_2} \rightarrow \frac{1}{2}\mathrm{Na_2O_2}\,. \tag{4-2}$$

The latter is favored when there is sufficient oxygen while the former is the product if there is insufficient oxygen. It will be assumed that in regions containing sodium, the only oxide present is sodium oxide, while in regions containing oxygen the only oxide present is sodium peroxide. That is, the shift reactions

$$\mathrm{Na_2O} + \frac{1}{2}\mathrm{O_2} \rightarrow \mathrm{Na_2O_2} \tag{4-3}$$

and

$$\frac{1}{2}\mathrm{Na_2O_2} + \mathrm{Na} \rightarrow \mathrm{Na_2O} \tag{4-4}$$

are assumed to be fast. The oxides Na_2O_2 and Na_2O are generally present in the condensed phase and their melting temperatures are 675°C and 1132°C for Na_2O_2 and Na_2O, respectively. A fraction of these oxides can form aerosols [25], but a fraction also forms a porous oxide layer on a sodium surface as indicated in Figure 4-1. The oxide crust is observed to be stable up to roughly 600°C (873 K); above this temperature, the oxide crust on the surface is observed to disappear, presumably melting and sinking [5, 6].

The oxides Na_2O_2 and Na_2O are generally believed to be porous based on the Pilling-Bedworth ratio [26], the ratio of the oxide volume to the metal volume. For Na_2O_2 and Na_2O.the Pilling-Bedworth ratio is calculated to be 0.58 and 0.57, respectively. Values of this ratio much less than unity are thought to suggest porous oxides, and experimental evidence supports this for Na_2O_2 and Na_2O (Section 2.2). In some instances, varying porosity has been related to ignition observations, as when humid environments favor NaOH oxide layers with a larger Pilling-Bedworth ration of 0.79 [27-28]. It should be noted that Pilling and Bedworth [26] is one of the earliest papers to describe a model for the evolution of porous oxide layers like that described herein, and in the material science community these models are frequently relevant.

4.3.2 Phase conservation

With the oxides believed to be porous, it is possible for air and liquid sodium to permeate the oxide crust. This leads to two multiphase regions, one with air plus oxide and one with sodium plus oxide. With the assumption that the reactions (4-3) and (4-4) are fast, the oxide present with air is assumed to be Na_2O_2, and the oxide present with liquid sodium is assumed to be Na_2O. Then, in the sodium pool and oxide crust regions shown in Figure 4-1, there are no more than two phases with phase volume fractions indicated by ϕ_i. The sodium phase fraction is related to that of sodium oxide by

$$\phi_{\mathrm{Na}} = 1 - \phi_{\mathrm{Na_2O}} \tag{4-5}$$

and the gas-phase volume fraction is related to that of sodium peroxide

$$\phi_{\mathrm{g}} = 1 - \phi_{\mathrm{Na_2O_2}} \,. \tag{4-6}$$

In multi-phase flow considered here, separate continuity equations are required for each phase and these include source terms associated with inter-phase conversion

$$\frac{\partial\left(\rho_i\phi_i\right)}{\partial t} + \frac{\partial\left(\phi_i\rho_i v_i\right)}{\partial x} = \phi_i W_i \omega_i \,. \tag{4-7}$$

where the phase i moves with a displacement velocity v_i relative to the frame of reference, which is the reacting surface of the sodium. The density and molecular weights of phases i are given by ρ_i and W_i, respectively; the molar production rate (per volume of phase i) is given by ω_i. As indicated above, the reactions are limited to the interface between the sodium pool and the oxide crust. Integrating Eq. (4-7) over this reaction zone gives the mass production rate of species I per unit area

$$\dot{m}_i = \int \phi_i W_i \omega_i dx \,. \tag{4-8}$$

Here x is the direction normal to the oxidation front and the mass production rate is per total area (not per phase area). The actual mass production rates, $\dot{m}_i$, will be given in Section 4.3.3.1, but they are related by the stoichiometry of the reactions.

With the phase volume fractions and densities assumed to be constant, integrating Eq. (4-7) away from the reaction zone along this normal coordinate gives $\rho_i \phi_i v_i =$ constant so that v_i is related to the mass production rate by

$$v_i = \frac{\dot{m}_i}{\phi_i \rho_i}. \tag{4-9}$$

The total thickness of the layers will be given by the time integral of Eq. (4-9) for the relevant phases

$$\delta_i - \delta_i^0 = \frac{1}{\phi_i \rho_i} \int_0^t \dot{m}_i dt \tag{4-10}$$

where δ_i^0 is the initial thickness of the layer (nonzero for the sodium pool, for example).

With the volume fractions assumed, the phase conservation equations give the one-dimensional velocity of each phase including the vapor phase. For the present purposes, no momentum equation will be considered; instead a balance between a pressure gradient and viscous loss is assumed for the fluid phases. If there is sufficient porosity, buoyancy may drive convection within the porous layer, but at the present there is insufficient evidence to consider such a complication.

At the present, there is little information regarding the phase volume fractions. An oxide crust is clearly observed on the surface of the pool under certain conditions. Experimental observations of continued heat release with this visible oxide crust suggest that there is sufficient gas-phase void fraction to allow oxygen transport through the oxide crust, but the actual porosity will remain a parameter in the problem. The extent to which sodium oxide exists within the sodium pool is also uncertain. As the peroxide sinks below the surface and reaction (4-4) takes place, the resulting Na_2O will be solid and presumably porous. The solid Na_2O matrix will provide some support for the porous Na_2O_2 oxide crust that can exist above the sodium pool surface. At the present, the mechanics of the oxide matrices within the sodium pool and above the pool surface are not well understood. Based on the experimental observations (Section 2.2), one possible model is suggested here. Observations suggest the continual presence of an oxide crust, but that the crust does not become thick until some time after the burning has been initiated. If one observes the timing at which the oxide crust appears to thicken, it is evident that a non-negligible fraction of the sodium pool has oxidized. This *fraction oxidized* before the crust becomes thick may be relatively constant since the timing increases approximately linearly (this is a very qualitative measurement at this point) as the depth of the pool increases. It is suggested here that once some relatively small quantity of porous (Na_2O) oxide framework forms beneath the sodium pool surface, it supports the growth of a visible (Na_2O_2) peroxide crust above the pool surface. After this point in time, any sodium oxidation will result in the peroxide product as the sodium recedes through the porous (Na_2O) oxide and the (Na_2O_2) oxide crust thickens.

This suggests two distinct periods in the sodium oxidation where the distinction is in the products formed. In the first period, the oxide that remains on the pool surface will be Na_2O since it is assumed to be in contact with molten sodium. (A fraction of the oxide forms an aerosol, assumed to be Na_2O_2, and is observed as white smoke.) This period is referred to as the *oxide-sinking period* and it is characterized by an increase in the volume fraction of Na_2O within the sodium pool. This will be expressed in terms of a decrease in the sodium void fraction, ϕ_{Na}. During this period, there will be no reduction in the oxidation rate and the temperature continues to rise nearly linearly (until heat losses become significant). This period will end when $\phi_{Na} = 0.95$ as discussed below if the temperature remains below the observed oxide crust disappearance temperature of 600°C. If the temperature during the oxide-sinking period rises above 600°C before $\phi_{Na} = 0.95$ then this period continues until the sodium is depleted at which time the pool is filled with Na_2O. The second period begins when the Na_2O within the pool is assumed to support the growth of a Na_2O_2 peroxide crust above the sodium pool. This period will be referred to as the *oxide-crust period*. Several observations motivate the description of this period: As the oxide crust forms, the rate of observed temperature rise is reduced, the burning surface is no longer observed to glow red and the quantity of aerosol smoke is reduced to near zero. The phase-volume evolution during each of these periods is described in the following paragraphs.

Since there is redundancy (linear dependence) in reactions (4-1) to (4-4), we will make simplifying assumptions regarding which reactions occur under various conditions based on the above reasoning. First, for the direct oxidation of sodium, reaction (4-2) will always be preferred for expedience. When conditions suggest that the proper product is Na_2O, as should occur in the excess of Na, then reaction (4-4) will occur. When conditions suggest that Na_2O should be consumed, this would be described through the addition of oxygen as in reaction (4-3), though this is equivalent to the reverse of reaction (4-4) plus reaction (4-2). Note that reaction (4-1) has not been used explicitly in this sequence, but has been used implicitly since it is a linear combination of reactions (4-2) and (4-4) (or equivalently a linear combination of reactions (4-2) and (4-3)). The occurrence of reactions (4-3) and (4-4) in the above sequence will depend on a set of rules described in the following paragraphs. First for conditions where the oxide crust is found to exist stably on the surface for temperatures below about 600°C and second for conditions where the oxide crust is experimentally observed to sink below the surface for temperatures above about 600°C.

For temperatures below approximately 600°C, the oxide crust formed on the surface is found to be stable. Note that the melting point of Na_2O_2 is approximately 675°C so the lack of stability of the oxide crust at these high temperatures can readily be explained by a melting or dissolution of the crust and this process is described in a following paragraph[1].

---

[1] What is not clear to the present authors is what happens to the Na_2O_2 once it melts or dissolves. Under the conditions where the oxide layer disappears above 600°C, a clean metal surface is generally observed suggesting that Na_2O_2 sinks as has been suggested in

4.3.2.1 Oxide-sinking period

As discussed above, the oxide can exist in two forms: Na_2O in the presence of excess Na and Na_2O_2 in the presence of excess O_2. There is an observed fraction of the oxide that forms an aerosol and this fraction is presumed to form Na_2O_2 since it exists in the ambient oxidizing flow where there is an excess of oxygen. The fraction of oxide that sticks will form Na_2O if it comes into contact with sodium. It will be assumed that the sticking oxide comes into contact with sodium and sinks into the sodium pool *unless* the already deposited Na_2O has reached a suitable density that provides support for the growth of an oxide layer above the pool surface. This density is expressed in terms of the volume fraction so that when $\phi_{\mathrm{Na}} > \phi_{\mathrm{Na},lim}$ reaction (4-4) is assumed to proceed at the rate of reaction (4-2) times F_{st}, the fraction of the sodium that is associated with the sticking oxide,

$$\dot{m}_{\mathrm{Na_2O}} = -\frac{F_{st}}{2}\frac{W_{\mathrm{Na_2O}}}{W_{\mathrm{Na}}}\dot{m}_{\mathrm{Na}} . \tag{4-11}$$

The fraction of oxide that does not stick is released to the atmosphere as the peroxide

$$\dot{m}_{\mathrm{Na_2O_2}(aerosol)} = -\left(\frac{1-F_{st}}{2}\right)\frac{W_{\mathrm{Na_2O_2}}}{W_{\mathrm{Na}}}\dot{m}_{\mathrm{Na}} . \tag{4-12}$$

The oxygen consumption is the limiting factor in the oxidation process and the sodium consumption is related to the oxygen consumption via

$$\frac{\dot{m}_{\mathrm{Na}}}{W_{\mathrm{Na}}} = \left(\frac{4}{2-F_{st}}\right)\frac{\dot{m}_{\mathrm{O_2}}}{W_{\mathrm{O_2}}} . \tag{4-13}$$

This dependence on F_{st} arises because of the difference in the ratio of Na to O atoms in the sticking product, Na_2O, and the aerosol product, Na_2O_2. We can rewrite Eqs. (4-11) and (4-12) in terms of the oxygen consumption

$$\dot{m}_{\mathrm{Na_2O}} = -\left(\frac{2F_{st}}{2-F_{st}}\right)\frac{W_{\mathrm{Na_2O}}}{W_{\mathrm{O_2}}}\dot{m}_{\mathrm{O_2}} \quad \text{and} \quad \dot{m}_{\mathrm{Na_2O_2}(aerosol)} = -2\left(\frac{1-F_{st}}{2-F_{st}}\right)\frac{W_{\mathrm{Na_2O_2}}}{W_{\mathrm{O_2}}}\dot{m}_{\mathrm{O_2}} \tag{4-14}$$

As the sodium oxide is deposited in the sodium pool, the phase volume fraction of sodium and sodium oxide in the pool layer will vary along with its depth. From the combined phase conservation equations these are expressed as

$$\frac{d\delta_{\mathrm{Na}}}{dt} = \frac{\dot{m}_{\mathrm{Na}}}{\rho_{\mathrm{Na}}} + \frac{\dot{m}_{\mathrm{Na_2O}}}{\rho_{\mathrm{Na_2O}}} \quad \text{and} \quad \frac{d\phi_{\mathrm{Na}}}{dt} = \frac{1}{\delta_{\mathrm{Na}}}\left[\left(1-\phi_{\mathrm{Na}}\right)\frac{\dot{m}_{\mathrm{Na}}}{\rho_{\mathrm{Na}}} - \phi_{\mathrm{Na}}\frac{\dot{m}_{\mathrm{Na_2O}}}{\rho_{\mathrm{Na_2O}}}\right]. \tag{4-15}$$

Here the thickness of the sodium oxide layer is taken to be the same as the thickness of the sodium pool and the volume fraction is assumed to vary. This process occurs until

---

the past. In contact with molten Na, it is presumed that reaction (4-4) would be fast leading to Na_2O, a solid at the relevant temperatures that will sink into the sodium pool. Alternately, if the level of the sodium pool is low relative to the Na_2O, that is the Na_2O matrix protrudes above the sodium pool, the melting Na_2O_2 might fill in pores in any solid Na_2O matrix reducing oxygen mixing with sodium. The former (Na_2O formation followed by Na_2O sinking) results in the clean metal pool fire that is observed. It remains to be seen whether the other condition occurs for other regimes.

ϕ_{Na} is reduced to $\phi_{Na,lim}$, at which point additional oxide deposited remains above the pool surface if the temperature is below the 600°C transition temperature. This parameter, $\phi_{Na,lim}$, is the volume fraction of the Na when the oxide crust growth is supported; this value will be estimated as described in later Section 4.3.3.1.

4.3.2.2 Oxide-crust period

Once the sodium oxide layer builds up to the point where $\phi_{Na} = \phi_{Na,lim}$, then the oxide-crust layer is assumed to rise above the sodium pool surface. This is in agreement with experimental observations discussed in Section 2.2 and 4.2. It is also experimentally observed that, once the oxide crust protrudes substantially above the surface of the sodium, the aerosol release becomes negligible so that F_{st} approaches unity. Since the oxidation process occurs very close to the sodium surface inside the oxide layer, the oxide product will remain trapped in the porous matrix as the porous matrix rises above the reaction zone. Further, the oxide product is assumed to remain as Na_2O_2 since it is remains above the receding Na pool layer. As the Na pool recedes, it will expose Na_2O to additional air.[2] In this case, reaction (4-3) is assumed to occur at the rate

$$\dot{m}_{Na_2O} = \dot{m}_{Na}\frac{\rho_{Na_2O}}{\rho_{Na}}\left(\frac{1-\phi_{Na}}{\phi_{Na}}\right) \quad \text{or} \quad \omega_3 = \omega_2\frac{W_{Na}}{W_{Na_2O}}\frac{\rho_{Na_2O}}{\rho_{Na}}\left(\frac{1-\phi_{Na}}{\phi_{Na}}\right), \tag{4-16}$$

which is equivalent to matching

$$\frac{d\delta_{Na}}{dt} = \frac{d\delta_{Na_2O}}{dt}$$

with a fixed ϕ_{Na}. That is, both the oxidation of Na and Na_2O lead to the production of Na_2O_2 during this phase since the product remains in contact with the air. The relevant reaction occurring are reactions (4-2) and (4-3). Using Eq. (4-16) to relate the rates for reactions (4-2) and (4-3) yields expressions for the rates of production

$$\begin{aligned}
\dot{m}_{Na} &= 2\dot{m}_{O_2}\frac{W_{Na}}{W_{O_2}}\left[\frac{\rho_{Na}\phi_{Na}W_{Na_2O}}{\rho_{Na}\phi_{Na}W_{Na_2O}+\rho_{Na_2O}(1-\phi_{Na})W_{Na}}\right] \\
\dot{m}_{Na_2O} &= 2\dot{m}_{O_2}\frac{W_{Na_2O}}{W_{O_2}}\left[\frac{\rho_{Na_2O}(1-\phi_{Na})W_{Na}}{\rho_{Na}\phi_{Na}W_{Na_2O}+\rho_{Na_2O}(1-\phi_{Na})W_{Na}}\right] \\
\dot{m}_{Na_2O_2} &= -\dot{m}_{O_2}\frac{W_{Na_2O_2}}{W_{O_2}}\left[\frac{\rho_{Na}\phi_{Na}W_{Na_2O}+2\rho_{Na_2O}(1-\phi_{Na})W_{Na}}{\rho_{Na}\phi_{Na}W_{Na_2O}+\rho_{Na_2O}(1-\phi_{Na})W_{Na}}\right]
\end{aligned} \tag{4-17}$$

in terms of the limiting rate of oxygen consumption. During the oxide crust period it will be assumed in the present work that the ratio of reaction rates in Eq. (4-18) is fixed allowing the introduction of the parameter

---

[2] The exposure of Na_2O is an assumption. An alternate assumption is that the Na_2O sinks to the pool bottom and is not exposed until the sodium is fully oxidized. The assumption of Na_2O exposure is made here because we have invoked Na_2O as playing a role to support the Na_2O_2 oxide crust. In the Discussion below, it is suggested that Na_2O may also dissolve into the sodium and sink. The present experimental evidence is insufficient to discriminate between these fates of Na_2O.

$$F_e = \frac{W_{\mathrm{Na}}}{W_{\mathrm{Na_2O}}} \frac{\rho_{\mathrm{Na_2O}}}{\rho_{\mathrm{Na}}} \left(\frac{1-\phi_{\mathrm{Na}}}{\phi_{\mathrm{Na}}} \right) \tag{4-18}$$

representing the fraction of Na_2O exposure relative to Na consumption. This allows the simplification of Eq. (4-17) to

$$\begin{aligned} \dot{m}_{\mathrm{Na}} &= \dot{m}_{\mathrm{O_2}} \frac{W_{\mathrm{Na}}}{W_{\mathrm{O_2}}} \left[\frac{2}{1+F_e} \right] \\ \dot{m}_{\mathrm{Na_2O}} &= \dot{m}_{\mathrm{O_2}} \frac{W_{\mathrm{Na_2O}}}{W_{\mathrm{O_2}}} \left[\frac{2F_e}{1+F_e} \right] \\ \dot{m}_{\mathrm{Na_2O_2}} &= -\dot{m}_{\mathrm{O_2}} \frac{W_{\mathrm{Na_2O_2}}}{W_{\mathrm{O_2}}} \left[\frac{1+2F_e}{1+F_e} \right] \end{aligned} \tag{4-19}$$

4.3.2.3 Characteristics of the oxide crust

The porous nature of the oxide-crust layer will have a significant effect on the heat and mass transfer through that layer. To account for this effect, expressions for effective transport coefficients are developed here. The sodium-peroxide component of the crust is able to conduct heat but not to diffuse species at any relevant rates. The vapor-phase or porous component of the crust is able to transport species (oxygen being the relevant species) and heat. It is noted that there are substantial uncertainties regarding the properties of the porous oxide crust as will be discussed below so that only the most rudimentary approaches to porous media transport are required. One approach to developing transport coefficients in porous media that works reasonably well was provided by Maxwell [29]. For heat transfer in which both phases conduct, an effective conductivity would be written

$$\frac{\lambda_{eff}}{\lambda_g} = \frac{3\lambda_{\mathrm{Na_2O_2}} - 2\phi_g \left(\lambda_{\mathrm{Na_2O_2}} - \lambda_g \right)}{3\lambda_g + \phi_g \left(\lambda_{\mathrm{Na_2O_2}} - \lambda_g \right)} \approx \frac{3-2\phi_g}{\phi_g} \tag{4-20}$$

with the second approximate inequality coming from the limit where $\lambda_{\mathrm{Na_2O_2}} \gg \lambda_g$. For diffusive transport, the oxide-phase contribution is zero so that Maxwell's effective diffusivity is

$$\frac{\phi_g D_{eff}}{D} = \frac{2\phi_g}{3-\phi_g} . \tag{4-21}$$

In the above expressions λ_g and λ_{Na2O} are the thermal conductivities of the gas and oxide phases respectively, while D is the appropriate gas-phase diffusivity (oxygen in nitrogen). Equations. (4-20) and (4-21) are used below to describe heat and mass transfer rates through the oxide crust.

The expression derived by Maxwell, given in Eqs. (4-20) and (4-21), is formally correct only for small mass fractions of the dispersed phase, although it has been found to work well over a much broader range than its formal applicability. For this reason, a comment is made here regarding alternate approaches to effective transport coefficients in porous

media, of which there are many possibilities. When a single phase conducts, as for oxygen diffusion, effective transport coefficients are sometimes described in terms of a tortuosity factor, $D_{eff} = D/\tau^2$, that represents the increased path length over which diffusion occurs in porous media. The tortuosity can be related to the void fraction through an empirical expression by Bruggemann characterized by a power-law dependence, $D_{eff} = D\,\phi^{m-1}$, through the Bruggemann exponent, m, [30]. A Bruggemann exponent of 1.5 is typical and agrees well with Maxwell's expression in Eq. (4-21), but larger exponents are also recommended in the literature. Alternate approaches also include percolation theory [31]. In the present absence of data supporting one approach or another, the expressions from Maxwell in Eqs. (4-20) and (4-21) are employed here with a comment made below (Figure 4-4) on the magnitude of the influence.

4.3.3 Species conservation

In each of the condensed phases only a single species will exist for thermodynamic reasons. In the vapor phase, oxygen or sodium vapors exist with nitrogen and satisfy the porous-media species conservation equation

$$\frac{\partial\left(\phi_g \rho_g Y_i\right)}{\partial t} + \frac{\partial\left(\phi_g \rho_g u_g Y_i\right)}{\partial x} = \frac{\partial}{\partial x}\left(\phi_g \rho_g D_{eff} \frac{\partial Y_i}{\partial x}\right) + W_i \omega_i \,. \tag{4-22}$$

Here the species mass fraction within a phase is denoted Y_i and that species has an effective diffusion coefficient of D_{eff}. In the single-phase oxidizing-ambient region (Figure 4-1) the effective diffusion coefficient is simply the binary diffusion coefficient between O_2 and N_2, D. In porous regions, the effective diffusion coefficient is given by Eq. (4-22). The gas-phase will be assumed to be quasi-steady based on the diffusivity relative to the thermal evolution.

There are two levels at which the gas-phase chemistry will be treated. At lower temperatures where the oxide crust is present, the sodium vapor pressure is negligible (vapor pressure at 600°C is 0.02 atmospheres). Under these conditions, the sodium oxygen reaction can be assumed to occur at the pool surface so that there are essentially no chemical reactions of significance in the gas phase. This low temperature limit will be considered first in the following subsection. Following that, higher sodium pool surface temperatures will be analyzed allowing sodium vapors to react in the gas phase. The latter treatment will be required to obtain the equilibrium burning conditions at high temperatures.

4.3.3.1 Low-temperature oxidation

In the low temperature regime, the reaction occurs at the sodium-pool interface identified with the subscript r. Integrating the quasi-steady version of Eq. (4-22) over the reacting sodium-oxidizer interface as for Eq. (4-8), an expression for the species flux is obtained

$$\phi_g \rho_g u_g Y_i - \phi_g \rho_g D_{eff} \frac{dY_i}{dx} = \dot{m}_i \,. \tag{4-23}$$

The right-hand side source term of Eq. (4-23) is zero for N_2 and nonzero for O_2. Further, the mass flux of each species is fixed by the quasi-steady and one dimensional nature assumed here so that Eq. (4-23) holds not only at the sodium-oxidizer interface but

throughout the oxide crust and into the ambient flow region. Equation (4-9) can be used to obtain $\phi_g \rho_g u_g = \dot{m}_{O_2}$, a relation that also holds throughout the oxide crust and into the ambient flow region. The oxygen diffusive flux is also related to $\dot{m}_{O_2}$

$$\dot{m}_{O_2} = -\phi_g \rho_g D_{eff} \left. \frac{dY_{O_2}}{dx} \right|_r = -\phi_g \rho_g D_{eff} \frac{Y_{O_2,f}}{\delta}. \tag{4-24}$$

The second equality in Eq. (4-24) arises with the assumption that the oxygen gradient is constant throughout the oxide crust (equivalent to ignoring density variations). This last relationship is noteworthy because it relates the oxygen mass fraction at the interface *f* with the oxidation rate.

For consistency, Eq. (4-23) is also evaluated for nitrogen under similar assumptions. As indicated above, the net nitrogen flux is zero and the net advective flux is related to the oxygen consumption rate

$$\dot{m}_{N_2} = 0 = \dot{m}_{O_2} Y_{N_2} - \phi_g \rho_g D_{eff} \frac{dY_{N_2}}{dx}. \tag{4-25}$$

Evaluating this at the sodium-oxidizer interface where $Y_{N_2,r} = 1$ and assuming a constant gradient with $Y_{N_2,f} = 1 - Y_{O_2,f}$ so that

$$\frac{dY_{N_2}}{dx} = \frac{\left(Y_{N_2,r} - Y_{N_2,f}\right)}{\delta} = -\frac{Y_{O_2,f}}{\delta} \tag{4-26}$$

and Eq. (4-24) is confirmed.

The above paragraphs evaluated the oxygen mass flux in the oxide-crust region. This flux must be matched at the interface between the oxidizing-ambient region and the two-phase oxide-crust region. Evaluating Eq. (4-23) across this interface yields

$$\phi_g \rho_g D_{eff} \left. \frac{dY_i}{dx} \right|_{f-} = \rho_g D_i \left. \frac{dY_i}{dx} \right|_{f+} \tag{4-27}$$

where Eq. **Error! Reference source not found.Error! Reference source not found.** is used to eliminate the advective terms and the gradients need to be evaluated in each of the regions. In the oxide-crust region, the gradient from Eq.
Error! Reference source not found.Error! Reference source not found. is

$$\left. \frac{dY_{O_2}}{dx} \right|_{f-} = \frac{Y_{O_2,f}}{\delta} \tag{4-28}$$

In the oxidizing-ambient region, a boundary layer flow will develop. Resolution of the gas-phase boundary layer gradients at *f*+ in Eq. (4-27) in conjunction with resolution of engineering or device-scale features is computationally expensive, and it is beneficial if a model for these gradients can be obtained. The typical practice is to express the flux using an effective transport coefficients using a Sherwood number defined as

$$Sh = \frac{L \left. \frac{\partial Y_{O_2}}{\partial x} \right|_{f+}}{Y_{O_2,\infty} - Y_{O_2,f}}. \tag{4-29}$$

where L is the characteristic length scale associated with the Sherwood number. If one is conducting a computational fluid dynamics (CFD) study, expressions for the Sherwood number are generally available through various wall models. For the present purposes, correlations for heat and mass transport from a horizontal heated plate will be used to describe oxidizing ambient mass transfer. This approach has been used successfully in the past for predicting sodium pool fires when the oxide crust was not present [5,6]. For a circular pool (or circular hot plate) the transfer coefficient is [32]

$$Sh = 0.16(GrSc)^{1/3} \tag{4-30}$$

for turbulent flow regimes and

$$Sh = 0.7(GrSc)^{1/4} \tag{4-31}$$

for laminar flow regimes; here Sc is the Schmidt number for air, estimated to be 0.7. The Grashof number is defined as

$$Gr = \left(\frac{T_f - T_\infty}{T_\infty}\right)\left(\frac{g}{\nu^2}\right)L^3 \tag{4-32}$$

where T_f is the oxide crust surface temperature, T_∞ is the ambient temperature, L is the pool diameter, ν is the air viscosity and g is the gravitational acceleration. In the turbulent regime, the ratio Sh/L will be independent of the pool diameter. For the circular buoyant surface this results in a Nusselt or Sherwood number divided by pool diameter of order 100 times the pool diameter for the conditions of relevance here (lesser transport numbers for lower surface temperatures). The experiments described in the previous sections were conducted out-doors and were subject to winds that visibly affected the gas-phase transport, so a correlation for turbulent boundary layers is also considered. Such a correlation is [33][3]

$$Nu / L = 0.016 Re_L^{4/5} Pr^{1/3} \quad \text{and} \quad Sh / L = 0.016 Re_L^{4/5} Sc^{1/3}, \tag{4-33}$$

and this results in a Nusselt or Sherwood number that can exceed that for pure buoyant convection given in Eq. (4-30) for moderate wind speeds on the order of five to ten meters per second. Because accurate wind velocities were not measured (measurements were made on site but away from the actual pool), there is substantial uncertainty in the transport coefficients. This is amplified by effects of the pan rim and other clutter so that the appropriate transfer rates are considered to be substantially uncertain. While further work might clarify this uncertainty, for the present purposes the quotients Nu/L and Sh/L will be estimated using Eq. (4-30) and adjusted as noted below according to the experimental observations. Substantial uncertainties in these quantities are assumed.

Combining Eqs. (4-28) and (4-29) in (4-27) yields

$$\frac{\phi_g D_{eff}}{D}\frac{Y_{O_2,f}}{\delta} = Sh\frac{Y_{O_2,\infty} - Y_{O_2,f}}{L}. \tag{4-34}$$

The quantities $\delta D/\phi_g D_{eff}$ and L/Sh can be interpreted as effective transport resistances. The drop in the oxygen potential (oxygen mass fraction) across each of the two regions depends on the magnitude of the resistance in each region with greater drops in the oxygen potential corresponding to greater resistances in that region. In the turbulent pool

[3] Note that Eq. (4-33) was obtained from the integral of local transfer numbers having expressions of the form $Nu = 0.0296 Re_x^{4/5} Pr^{1/3}$ and $Sh = 0.0296 Re_x^{4/5} Sc^{1/3}$.

regime where *Sh* is given by Eq. (4-30) the oxide-crust surface temperature is the primary determining factor of the effective transport resistance in the oxidizing-ambient region. As the pool burns and the oxide crust thickness increases, the effective transport resistance will increase from the initial resistance given by the boundary layer in the oxidizing ambient. At sufficient thicknesses, the oxide-crust resistance will be predominant. Equation (4-34) can be solved to obtain the oxidizer mass fraction at the interface between the air and oxide layer

$$Y_{O_2,f} = \frac{Y_{O_2,\infty}}{1 + \frac{L}{Sh}\frac{\phi D_{eff}}{\delta D}}. \tag{4-35}$$

This is plotted in Figure 4-2 as a function of the oxide-layer thickness and provides an indication of the significance of the resistance of the separate regions.

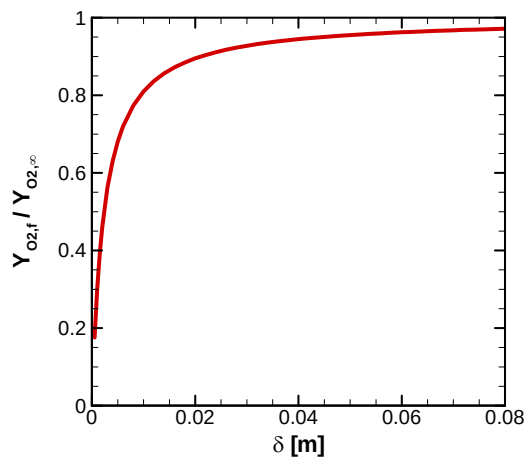

Figure 4-2: The ratio of the oxygen mass fraction at the oxide-crust surface to the ambient for *Sh/L* = 230 and ϕ = 0.8 as a function of the crust thickness.

Combining Eqs. (4-24) and (4-35) gives an expression for the combustion rate in terms of the oxygen flux

$$\dot{m}_{O_2} = -\left(\frac{Sh}{L}\right)\left(\frac{\rho_g D Y_{O_2,\infty}}{1 + \delta / \Delta_1}\right) \tag{4-36}$$

where the oxide layer thickness is normalized by the characteristic length scale

$$\Delta_1 = \left(\frac{D_{eff}}{D}\right) \Big/ \left(\frac{Sh}{L}\right). \tag{4-37}$$

4.3.3.2 The oxide layer growth equation

We are primarily interested in the evolution of δ, the oxide layer thickness. Combining equations (4-10) and (4-36) we get an evolution equation for δ,

$$\frac{d\delta}{dt} = -\left(\frac{W_{Na_2O_2}}{W_{O_2}}\right)\left(\frac{\rho_g D Y_{O_2,\infty}}{\rho_{Na_2O_2}\phi}\right)\left(\frac{Sh}{L}\right)\left(\frac{1}{1+\delta/\Delta_1}\right). \tag{4-38}$$

Normalizing the layer thickness by Δ_1

$$\delta = \Delta_1 \hat{\delta} \tag{4-39}$$

and the time by the remaining rate expression

$$t = \hat{t}\left(\frac{W_{O_2}}{W_{Na_2O_2}}\right)\left(\frac{\rho_{Na_2O_2}\phi}{\rho_g D Y_{O_2,\infty}}\right)\left(\frac{L}{Sh}\right)^2\left(\frac{\phi D}{D_{eff}}\right). \tag{4-40}$$

This normalization of time is largely based on the rate of oxidation in the absence of the oxide crust, but terms related to the oxide crust appear. Using the normalizations in Eqs. (4-39) and (4-40), Eq. (4-38) is rewritten in simplified form

$$\frac{d\hat{\delta}}{d\hat{t}} = \frac{1}{1+\hat{\delta}} \tag{4-41}$$

that has a solution

$$\hat{\delta} = \left(2t + \hat{\delta}_0^2 + 2\hat{\delta}_0 + 1\right)^{1/2} - 1. \tag{4-42}$$

Here $\hat{\delta}_0$ is the initial condition for $\hat{\delta}$. Equations (4-41) and (4-42) indicate that the oxide crust growth is linear in time when the resistance across the oxide crust is small relative to the resistance across the boundary layer (when $\hat{\delta} \ll 1$) and follows the quadratic growth model (Pillings and Bedworth) where $\hat{\delta}^2 \propto t$ when the oxide crust resistance is much greater than that of the boundary layer (when $\hat{\delta} \gg 1$).

4.3.3.3 High-temperature oxidation

At higher temperatures the sodium vapor pressure is non-negligible and oxidation chemistry is assumed to occur in the gas phase. In order to treat the reacting gas-phase flow in the same manner as above, it is useful to express the gas-phase mixing in terms of conserved scalars, combinations of Eq. (4-22) for which the source terms are zero. Using reaction (4-2) a conserved scalar is

$$\beta_{FO} = \frac{1}{2}\frac{Y_{Na}}{W_{Na}} - \frac{Y_{O_2}}{W_{O_2}} \tag{4-43}$$

where the factor of 1/2 appears because of the reaction stoichiometry. Following the same process as for Eqs. (4-23) through
Error! Reference source not found.Error! Reference source not found. for β_{FO} in lieu of Y_{O2} the mass burning rate in terms of oxygen consumption is written

$$\begin{aligned}\dot{m}_{O_2} &= \left(\frac{Sh}{L}\right)\left(\frac{\rho_g D W_{O_2}}{1+\delta/\Delta_1}\right)\left(\beta_{FO,\infty} - \beta_{FO,r}\right) \\ &= -\left(\frac{Sh}{L}\right)\left(\frac{\rho_g D}{1+\delta/\Delta_1}\right)\left(Y_{O_2,\infty} + \frac{1}{2}\frac{W_{O_2}}{W_{Na}}Y_{Na,r}\right)\end{aligned} \tag{4-44}$$

where the sodium mass fraction associated with the sodium vapor pressure at the pool surface is added to that of oxygen when this is compared with Eq. (4-36).

At this point, a comment regarding other models of sodium pool oxidation is warranted. Typically, prior approaches have ignored the contribution of sodium vapor pressure appearing in Eq. (4-44) and in all cases they have ignored the additional resistance of the oxide layer appearing in Eqs. (4-36) and (4-44). Ignoring the sodium vapor contribution to the oxidation potential is generally a small contribution, but it is required if one wishes to identify the equilibrium burning temperature as will be described in the following section. As will be found in the results of this paper, the resistance associated with the oxide crust is significant for the low temperature burning mode.

4.3.4 Enthalpy conservation

In the previous section, the oxygen flux was determined. Through the stoichiometry and enthalpy of Reaction (4-2), this determines the heat release occurring in the sodium oxidation process. In the Introduction it was noted that for temperatures exceeding 600°C (873 K) the oxide crust is observed to be eliminated (presumably through melting and sinking) [5], and thus the net temperature rise associated with the oxidation is important. If the temperature rise is sufficiently great, the oxide crust will be eliminated and the pool will proceed to burn in a manner analogous to that described previously where oxygen flux is assumed to limit the rate of combustion [6, 24]. On the contrary, if the dissipation of the enthalpy of reaction is sufficiently fast, the additional resistance to oxidation associated with the oxide crust increasingly reduces the heat release rate leading to a situation where heat release rates continually decline and the net temperature rise is limited. In this section, the salient physics that determines the temperature evolution are described.

Enthalpy conservation determines the temperature profile through the various layers indicated in Figure 4-1. A generic expression for sensible enthalpy conservation where there are no significant composition gradients (in the condensed phases) or where the unity Lewis number approximation is appropriate (in the gas phase) is

$$\frac{\partial\left(\phi\rho c_p T\right)}{\partial t}+\frac{\partial\left(\phi\rho v c_p T\right)}{\partial x}=\frac{\partial}{\partial x}\left(\phi\lambda_{eff}\frac{\partial T}{\partial x}\right)+\sum_i\sum_j\phi\hat{h}_i^r\upsilon_{i,j}\omega_j+\nabla\cdot Q_{rad}\,. \qquad (4\text{-}45)$$

Here the enthalpies of the individual species have been brought into the right hand side along with the reaction rate. In this context, $\hat{h}_i^r$ is the molar enthalpy of formation for species i at T_r, $\upsilon_{i,j}$ is the stoichiometric coefficient of species i in reaction j, ω_j is the reaction rate of reaction j and Q_{rad} is the radiative flux. The radiative flux from the surface is

$$Q_{rad}=\varepsilon\left(\sigma T_f^4-G_{in}/4\right) \qquad (4\text{-}46)$$

where G_{in} is the incident radiative flux, σ is the Stefan-Boltzmann constant and ε is the emissivity of the surface. The source terms will only be relevant at discrete interfaces with the reaction term assumed to occur at the interface between the sodium layer and the oxide crust (or boundary layer if there is no oxide crust) and the radiative source term only considered at the interface adjacent to the boundary layer. Radiative flux is often

significant within porous media, but the current uncertainties in the nature of the porous oxide crust do not warrant a consideration of that contribution to heat flux; any radiative flux contribution to the heat flux in the porous oxide layer is absorbed into the uncertainties in the heat conduction characteristics. Solution of Eq. (4-45) is generally straightforward and only the specific forms within the oxide crust layer and at the two boundaries of that layer require further comment given in the following paragraph.

Unlike species conservation, energy conservation encompasses both the condensed and vapor phases. While it is possible to describe separate temperatures for separate phases in a porous mixture, the fine scale porosity expected of the oxides suggests temperature equilibration between the phases in the porous oxide crust, and the combined conservation equation is given here. To bring conciseness to the equation, the advective terms are replaced with the mass fluxes according using Eq. (4-9), and the thermal mass of the oxide crust

$$\left(\rho c_p\right)_{oc} = \phi_g \rho_g c_{p,g} + (1-\phi_g)\rho_{Na_2O_2} c_{p,Na_2O_2} \tag{4-47}$$

is introduced. As with diffusive transport, porosity affects the thermal conductivity so that the effective porous-media conductivity defined in Eq.
Error! Reference source not found.Error! Reference source not found. is employed Using this notation, the porous-media enthalpy equation in the oxide crust is

$$\left(\rho c_p\right)_{oc} \frac{\partial T}{\partial t} + \left(\dot{m}_{O_2} c_{p,g} + \dot{m}_{Na_2O_2} c_{p,Na_2O_2}\right)\frac{\partial T}{\partial x} = \frac{\partial}{\partial x}\left(\lambda_{eff}\frac{\partial T}{\partial x}\right) + \sum_i \sum_j \hat{h}_i^r \upsilon_{i,j}\omega_j + \frac{\partial Q_{rad}}{\partial x}. \tag{4-48}$$

The source terms have been left in Eq. (4-48) to help in evaluating the boundary conditions where those source terms will be relevant; within the oxide crust the source terms are zero. The mass flux of oxygen was determined in Eq. (4-44) and the mass flux of the crust is related to that in Eq. (4-17).

4.3.5 Heat flux from reaction zone

The reaction zone at the interface between the sodium pool and the oxide surface (or the ambient if there is no oxide surface), denoted with the subscript *r*, is the location of heat release. A fraction of the heat released is transferred through the oxide layer to the ambient while the remainder is transferred through the sodium to the substrate. The fractional heat transfer in each direction is approximated in the present section. To do so, the reaction zone is considered to be infinitesimally thin and thus represents a jump condition across which heat flux changes by the rate of sodium-oxidation heat release. It is helpful to express the enthalpy of reaction explicitly in terms of the rate of oxygen consumption, and because the fraction of oxide that sticks or sinks back into the sodium pool yields varying reaction products, these expressions are unusually complicated. During the oxide-sinking period, this enthalpy of reaction can be written

$$q_1 = \frac{-1}{W_{O_2}}\left[\frac{2-2F_{st}}{2-F_{st}}\hat{h}^r_{Na_2O_2} + \frac{2F_{st}}{2-F_{st}}\hat{h}^r_{Na_2O} - \hat{h}^r_{O_2} - \frac{4}{2-F_{st}}\hat{h}^r_{Na}\right] \tag{4-49}$$

while during the oxide-crust period it is written

$$q_2 = \frac{-1}{W_{O_2}} \left[\frac{1+2F_e}{1+F_e} \hat{h}^r_{Na_2O_2} - \hat{h}^r_{O_2} - \frac{2}{1+F_e} \hat{h}^r_{Na} - \frac{2F_e}{1+F_e} \hat{h}^r_{Na_2O} \right]. \quad (4\text{-}50)$$

Both or these expressions are written per mass of oxygen consumption.

Formally integrating Eq. (4-48) across this thin reaction zone and using Eq. (4-9) for the advective terms gives

$$\left(\dot{m}_{O_2} c_{p,g} + \dot{m}_{Na_2O_2} c_{p,Na_2O_2} - \dot{m}_{Na_2} c_{p,Na} \right) T_r = \left(\lambda_{eff} \frac{\partial T}{\partial x} \right)_{r+} - \left(\lambda_{Na} \frac{\partial T}{\partial x} \right)_{r-} - \dot{m}_{O_2} q_{eff} \quad (4\text{-}51)$$

Where the effective heat of combustion, q_{eff}, is given by either Eq. (4-49) or (4-50) as appropriate. The advective terms on the left hand side of Eq. (4-51) are easily evaluated to be roughly 5% of the magnitude of the enthalpies of reaction. While they will be retained in the numerical simulation, they are safely ignored in understanding the results.

4.3.6 Numerical details

The unsteady energy conservation equations are solved in one-dimension using the control-volume formulation. The mass, phase and species transport is assumed to be in quasi steady state so that the source terms at the reaction zone (subscript *r*) are computed using the expressions in Eqs. (4-14), (4-15), (4-17), (4-44), and (4-51).

The sodium and oxide layer both change thickness so that the heat and mass transfer within these regions is carried out within the context of a moving boundary on the domains of each of those layers. In moving boundary problems, the numerical solution must include the flux of control volume faces in the advective term. The velocity of the control volume faces is related to the thickness of the various layers linearly. For the sodium layer the control volume face adds the advective velocity

$$u_{face,Na} = \left(\frac{x - x_s}{\delta_{Na}} \right) \frac{d\delta_{Na}}{dt} = \left(\frac{\text{distance to left face of sodium layer}}{\delta_{Na}} \right) \frac{d\delta_{Na}}{dt}. \quad (4\text{-}52)$$

Similarly, the control volume faces of the oxide layer move according to

$$u_{face,ox} = \left(\frac{x - x_f}{\delta} \right) \frac{d\delta}{dt} = \left(\frac{\text{distance to right face of sodium layer}}{\delta} \right) \frac{d\delta}{dt}. \quad (4\text{-}53)$$

Here it is recognized that the moving boundaries are at the reaction interface (subscript *r*) and so that the positive face of the sodium domain moves and the negative face of the oxide domain moves. Also the control volume faces move relative to the control volume so that these velocities appear with the opposite sign in the advective terms. The advective velocities in Eqs. (4-52) and (4-53) are combined with the bulk flow velocities; the bulk flow velocities are only relevant in the sense of oxygen transport through the oxide crust layer since other motions are included in the above moving grid expression.

4.3.7 Model Parameters

A number of parameters appearing in the equations described above are not well known. These are briefly discussed here. The most significant unknowns are related to the

porosities of the oxide crust, ϕ_g, and the limiting porosity at which the oxide crust builds up, $\phi_{\mathrm{Na},lim}$. These have been estimated through gradient-based parameter optimization methods by attempting to minimize the mean-square error in the temperature predictions for the experiments

$$l_2 = \sqrt{\sum_{i=1}^{n} \frac{\left(T_i^{pred} - T_i^{meas}\right)^2}{n}} \tag{4-54}$$

where the summation is over the temperature measurements and predictions at one second intervals. In general, the range of experiments suggested similar, though not identical optimum values for these parameters. The exact optimum parameters were not selected, but rather values that also limited the maximum error. For reference, two-dimensional parameter studies between the Nusselt number and either $\phi_{\mathrm{Na},lim}$ or ϕ_g are shown in Figure 4-3. This shows the general regimes of favorable values. Nusselt numbers for buoyant flow are in the vicinity of 50 (varying with temperature).

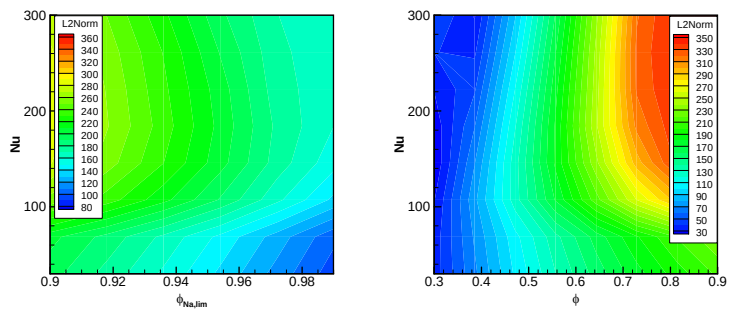

Pan01

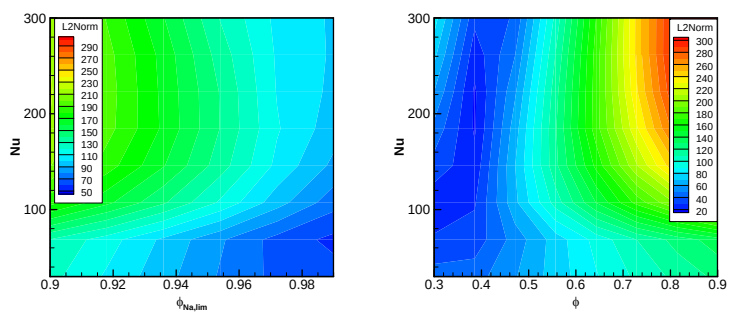

Pan02

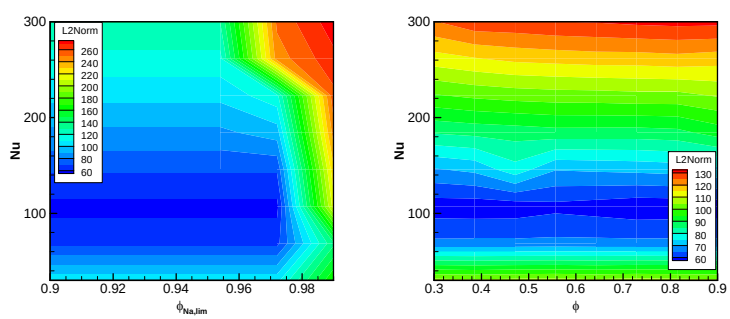

Pan03

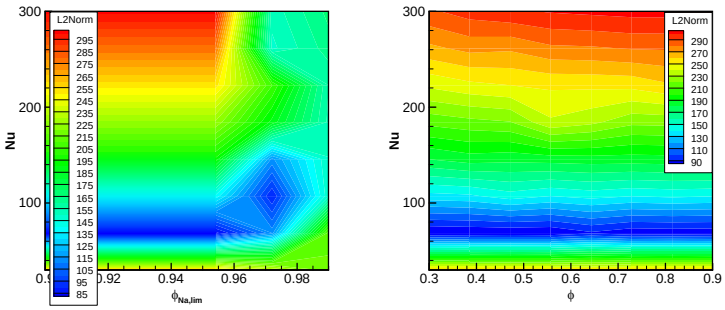

Pan04

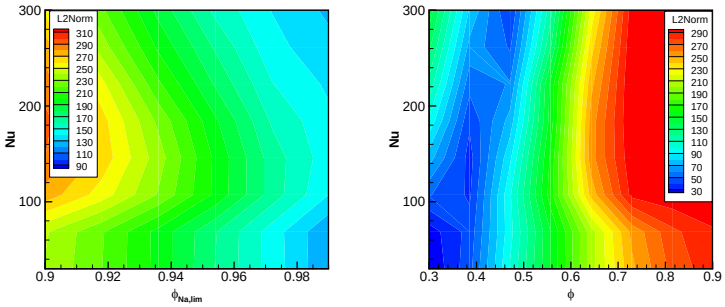

Pan05

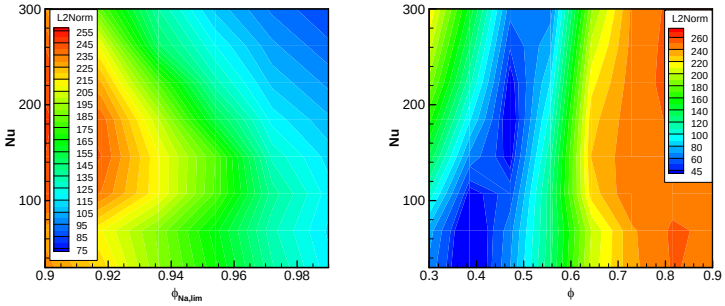

Pan06

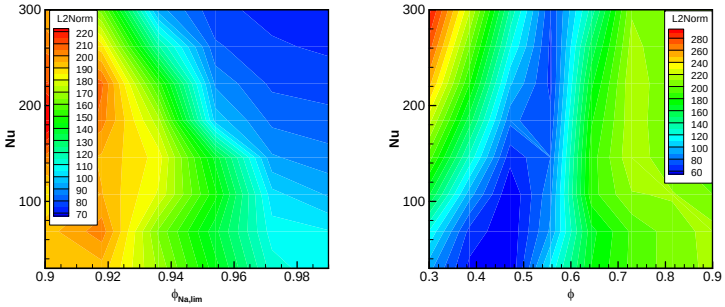

Pan07

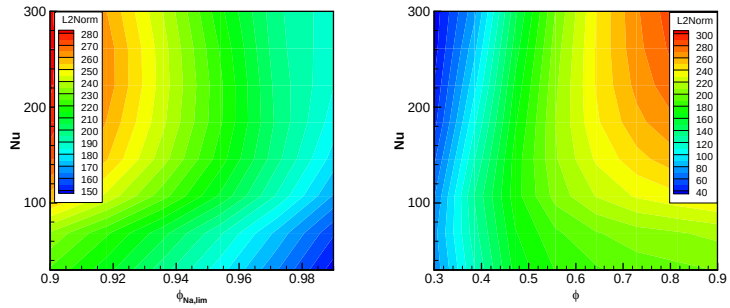

Pan08

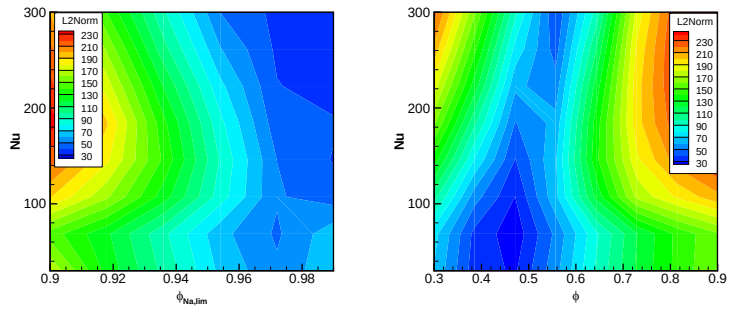

Pan09

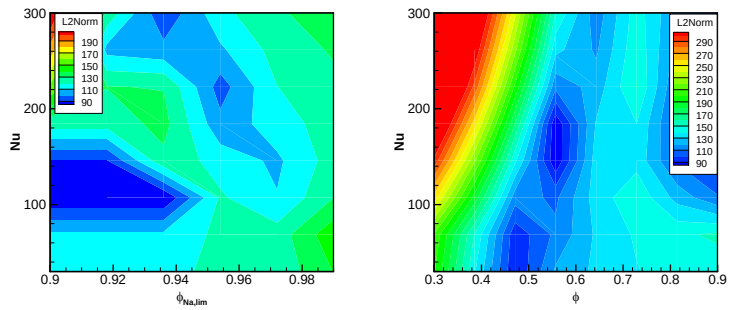

Pan10

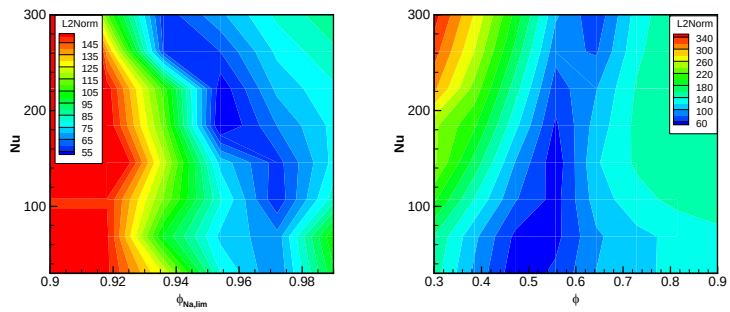

Pan11

Figure 4-3: Measurements of the l_2-norm error in temperature predictions as a function of the Nusselt number and either $\phi_{Na,lim}$ or ϕ_g.

For the oxide crust porosity, the value is set to 0.4 or 40% void fraction by volume. This is a reasonable value in light of the theory of porous oxides put forth by Pilling and Bedworth [26] for oxides that are volumetrically smaller than the metals they replace. The degree to which the sodium peroxide is smaller is estimated to be just under 60% (0.57) suggesting that a porosity of 0.4 is reasonable (and not feeling that more than a single significant digit is appropriate).

For the limiting porosity at which the oxide crust builds up, the optimal results are obtained in the vicinity of 0.95. This corresponds to approximately 5% Na_2O by volume before the oxide crust builds up. This value is interpreted as corresponding to the solubility of Na_2O in sodium which is indicated to be no more than a couple percent at these temperatures [34]. That is, Na_2O deposited in the molten sodium will dissolve until it saturates the pool at which point deposited oxide will remain solid and support the oxide crust. The 5% Na_2O volume fraction probably requires assuming that some Na_2O solidifies below the surface, and oxide is generally found within the remnants of the pool supporting such a viewpoint. In fact, the results suggest that $\phi_{\mathrm{Na},lim}$ should be somewhat lower when the sodium pool burns hot and should be somewhat higher when the sodium pool does not reach high temperatures as will be discussed in the Results. This supports the expected increase in solubility with increasing temperature.

Another set of parameters that is uncertain is the transfer coefficients described by the Nusselt and Sherwood numbers. The results show a high sensitivity to these transfer coefficients because they determine the rate of heat release and thus the rate of heating. In general, the buoyant disk values given in Eq. (4-30) are used. In comparison with certain experiments, a higher rate of heating in the early stages of the experimental measurement, the approximately linear period occurring over hundreds of seconds discussed in Section 4.2 and where heat losses and the oxide crust are less significant. In two of the tests (Pool Tests 3 and 4) when this higher rate of heating suggested a higher transfer coefficient, these were employed to mimic potential forced convection enhancements.

The thermal conductivity of the sodium peroxide in the oxide crust is also not well known, but the results will be shown to have little sensitivity to this parameter below.

4.3.8 Simplified thermal balances

Equation (4-51) will be solved numerically and the solutions described below. To aid in the interpretation of the results, simplifications can be made to the system from a thermal point of view. Heat released through the various reactions at the sodium pool surface is conducted down into the sodium pool or up into the ambient boundary layer (through the oxide crust if it is present). The heat conducted down into the sodium pool proceeds to heat the pool plus pan system (and whatever is insulating this over sufficient time scales) while heat transmitted upward is lost to the sodium pool plus pan system but possibly affects surroundings through advective or radiative transport. The purpose of this section is to provide a rough estimate of the heating of the pool plus pan system through

simplifications to the energy equation leading to an equation that is analogous to Eq. (4-36) developed for the rate of oxidation.

In this simplified approach, linear temperature profiles through the oxide crust will be assumed and the small contribution of the advective terms in Eq. (4-51) will be neglected. The quantity of interest is the pool plus pan heating rate equated here to the heat conduction at *r*- in Eq. (4-51) leading to a simplification of that equation

$$Q_{heat} = \left(\lambda_{\mathrm{Na}} \frac{\partial T}{\partial x} \right)_{r-} = \lambda_{eff} \left(\frac{T_f - T_r}{\delta} \right) - \dot{m}_{\mathrm{O}_2} q_{eff} \tag{4-55}$$

The temperature T_f is not known a priori. It can be obtained in the quasi-steady limit by matching heat fluxes across the interface at *f*

$$0 = \left(\lambda_{\mathrm{O}_2} \frac{\partial T}{\partial x} \right)_{f+} - \left(\lambda_{eff} \frac{\partial T}{\partial x} \right)_{f-} + Q_{rad} \tag{4-56}$$

To do this, the assumption of a linear temperature profile across the oxide layer is continued, the radiative flux term is linearized such that

$$Q_{rad} = \varepsilon \left(\sigma T_f^4 - G_{in}/4 \right) = \varepsilon\sigma \left(T_f^4 - T_\infty^4 \right) \approx \varepsilon\sigma T_f^3 \left(T_f - T_\infty \right) \tag{4-57}$$

and the convective heat flux in the ambient boundary layer is estimated in directly the same manner as for mass flux in Eqs. (5-29) through (4-32) introducing the Nusselt number for the turbulent regime

$$Nu = 0.16(GrPr)^{1/3} \tag{4-58}$$

where *Pr* is the Prandtl number. Using these assumptions in Eq. (5-56)**Error! Reference source not found.Error! Reference source not found.** leads to an expression for T_f

$$T_f \approx \frac{\dfrac{\lambda_{eff}}{\delta} T_r + \dfrac{\lambda_g Nu}{L} T_\infty + 4\varepsilon\sigma T_\infty^4}{\dfrac{\lambda_{eff}}{\delta} + \dfrac{\lambda_g Nu}{L} + 4\varepsilon\sigma T_\infty^3} = \frac{T_r + \left(\delta / \Delta_2 \right) T_\infty}{1 + \delta / \Delta_2} \tag{4-59}$$

where the parameter

$$\Delta_2 = \frac{\lambda_{eff}}{\dfrac{\lambda_g Nu}{L} + 4\varepsilon\sigma T_\infty^3} \tag{4-60}$$

is introduced to indicate the relative resistance to heat transfer through the oxide layer compared to the ambient. When most of the thermal resistance is in the oxide layer, T_f is close to T_∞, and when the thermal resistance of the oxide layer is small, T_f approaches T_r. Making the assumption that the Sherwood and Nusselt numbers are equalallows the introduction of the parameter

$$R_\Delta = \frac{\Delta_1}{\Delta_2} = \left(\frac{D_{eff}}{D} \right) \left(\frac{\lambda_g}{\lambda_{eff}} \right) \left[1 + \frac{4\varepsilon\sigma T_\infty^3}{\lambda_g} \left(\frac{L}{Nu} \right) \right]. \tag{4-61}$$

The parameter R_Δ will prove to be important in that it indicates the ratio of the resistances of the oxide layer to heat and mass flux respectively. It can be broken into the three terms indicated by parentheses and brackets: the change in the mass diffusivity through

the porous oxide crust, the change in the thermal conductivity through the oxide crust and the relative contribution of radiative transport to heat transfer. It will be further discussed at the end of this subsection.

With the expression for T_f in Eq. (4-59)**Error! Reference source not found.Error! Reference source not found.**, it is possible to use Eq. (4-55) to describe the pool heating. The thermal mass per unit area of the substrate plus pool can be defined

$$M_{layer} = \rho_{layer} c_{p,layer} \delta_{layer} \tag{4-62}$$

where ρ_{layer}, $c_{p,layer}$ and δ_{layer} are effective properties (density, specific heat and thickness, respectivley) of the combined pool and substrate layer. An effective temperature for the layer, T_{layer}, then evolves according to the conservation equation

$$\begin{aligned} M_{layer} \frac{dT_{layer}}{dt} = Q_{heat} \approx & \left(\frac{\lambda_g Nu}{L} + 4\varepsilon\sigma T_\infty^3 \right) \left(\frac{T_\infty - T_r}{1 + \delta / \Delta_2} \right) \\ & + \left(\rho_g D \frac{Sh}{L} \right) \left(\frac{Y_{O_2,\infty} q_{eff}}{1 + \delta / \Delta_1} \right) - Q_{loss} \end{aligned} \tag{4-63}$$

where the oxygen consumption rate was expressed using Eq. (4-36) and a final Q_{loss} term is introduced to account for any additional heat losses (through the insulation to the ground, for example). If the normalizations for δ and t from Eqs. (4-39) and (4-40) are introduced into Eq. (4-63),**Error! Reference source not found.Error! Reference source not found.** and the temperature is normalized using the heat release term in Eq. (4-63) scaled by the time normalization

$$T = \hat{T} \left(\frac{W_{O_2}}{W_{Na_2O_2}} \right) \left(\frac{\rho_{Na_2O_2} \phi}{M_{layer}} \right) \left(\frac{D_{eff}}{D} \right) \left(\frac{L}{Sh} \right) q_{eff} = \hat{T} \left(\frac{W_{O_2}}{W_{Na_2O_2}} \right) \left(\frac{\rho_{Na_2O_2} \phi}{M_{layer}} \right) \Delta_1 q_{eff} \tag{4-64}$$

then an additional parameters arises associated with the first term on the right-hand side of Eq. (4-63) **Error! Reference source not found.Error! Reference source not found.**

$$\hat{h} = \left(\frac{W_{O_2}}{W_{Na_2O_2}} \right) \left(\frac{\rho_{Na_2O_2} \phi}{M_{layer}} \right) \left[\frac{\lambda_g \left(\frac{Nu}{L} \right) + 4\varepsilon\sigma T_\infty^3}{\rho_g D \left(\frac{Sh}{L} \right) Y_{O_2,\infty}} \right] \Delta_1 \tag{4-65}$$

With a unity Lewis number approximation, the combination $\lambda_g/\rho_g D$ can be replaced by $c_{p,g}$ and the Nusselt and Sherwood numbers can be equated yielding

$$\hat{h} = \left(\frac{W_{O_2}}{W_{Na_2O_2}} \right) \left(\frac{\rho_{Na_2O_2} \phi c_{p,g}}{M_{layer} Y_{O_2,\infty}} \right) \left[1 + \frac{4\varepsilon\sigma T_\infty^3}{\lambda_g} \left(\frac{L}{Nu} \right) \right] \Delta_1 . \tag{4-66}$$

Using Eqs. (4-39), (4-40),
Error! Reference source not found.Error! Reference source not found. and
Error! Reference source not found.Error! Reference source not found. in Eq.
Error! Reference source not found.Error! Reference source not found., a normalized expression for the layer heating rate is obtained

$$\frac{d\hat{T}_r}{d\hat{t}} \approx \hat{h}\left(\frac{\hat{T}_\infty - \hat{T}_r}{1+R_\Delta\hat{\delta}}\right) + \left(\frac{1}{1+\hat{\delta}}\right) - \hat{Q}_{loss} \tag{4-67}$$

From Eq. (4-67)**Error! Reference source not found.Error! Reference source not found.**, it is evident that the thermal evolution is parameterized by the dimensionless heat transfer coefficient, $\hat{h}$, the ratio of thermal to mass resistances, R_Δ, and the normalized temperatures, $\hat{T}$. Of the temperatures, the boundary condition temperature $\hat{T}_\infty$ and the initial condition for $\hat{T}_r$ are relevant.

The first term on the right-hand side of Eq. (4-67)**Error! Reference source not found.Error! Reference source not found.** represents heat losses to the environment and the second term represents heat release associated with oxidation (and oxide layer growth). If the heat loss term is negligible, then the temperature evolves in a manner identical to the oxide layer thickness, increasing with time. With an increase in δ, both the oxide layer growth rate and the heat release rate are reduced. When the heat loss term is not negligible, the increase in δ also tends to reduce the heat loss rate, but at a rate that differs according to the parameter R_Δ. In general R_Δ is less than unity since the solid oxide phase reduces mass diffusivity relative to gas-phase diffusivities but enhances thermal diffusivities relative to the gas-phase. It is also evident from Eq. (4-67)**Error! Reference source not found.Error! Reference source not found.** that for $R_\Delta <$ 1, there can be a set of conditions where the right-hand side of Eq. (4-67)**Error! Reference source not found.Error! Reference source not found.** changes from positive to negative. This happens at the temperature

$$\hat{T}_{max} = \hat{T}_\infty + \frac{1}{\hat{h}}\left(\frac{1+R_\Delta\hat{\delta}}{1+\hat{\delta}}\right). \tag{4-68}$$

The parameter R_Δ introduced in Eq. (4-61)**Error! Reference source not found.Error! Reference source not found.** is the ratio of the resistances of the oxide layer to heat and mass flux respectively. Because the conductivity of the solid oxide is greater than the gas phase and because the mass diffusivity of the solid oxide (non-pore) is essentially zero, R_Δ will be less than unity. Ignoring the radiative enhancement (the $\varepsilon = 0$ limit in Eq.**Error! Reference source not found.Error! Reference source not found.**) R_Δ is plotted in Figure 4-4**Error! Reference source not found.Error! Reference source not found.** as a function of the porosity and the oxide thermal conductivity. There it is seen that except for very small oxide thermal conductivities, the ratio of effective transport coefficients is independent of the oxide conductivity as suggested by the limiting case (second approximate equality) in Eq. (4-20). Slices from this same set of parameter values for λ_{ox} = 1 and 20 W/m/K are plotted in Figure 4-5**Error! Reference source not found.Error! Reference source not found.**.

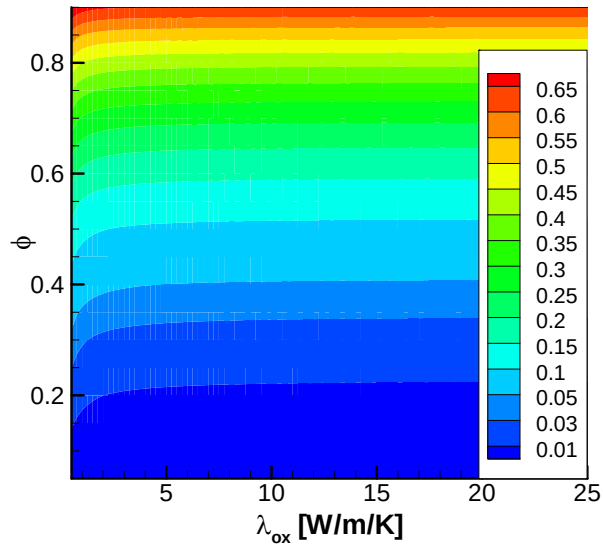

Figure 4-4: The ratio of the effective mass diffusivity to the effective thermal diffusivity through the porous oxide crust, R_Δ, is plotted as a function of the porosity and the bulk thermal conductivity of the oxide. Radiative flux is set to zero.

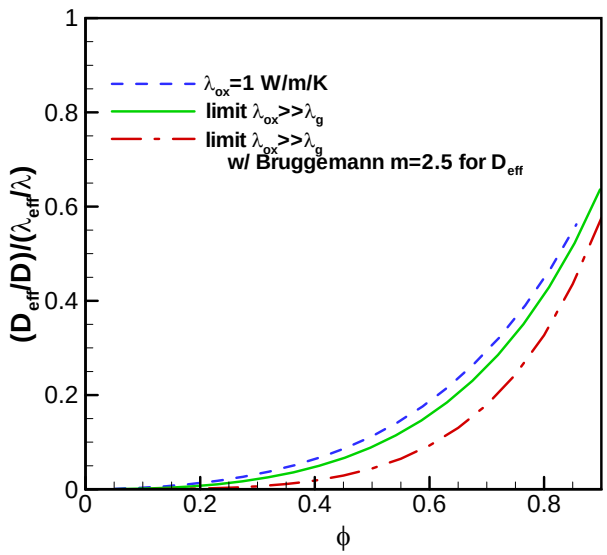

Figure 4-5: The ratio of the effective mass diffusivity to the effective thermal diffusivity through the porous oxide crust, R_Δ, is plotted as a function of the porosity for various oxide bulk conductivities (1 and 20 W/m/K) and using the Bruggemann model for the effective mass diffusivity with an exponent of 2.5.

4.4 Results and Discussion

In this section, the pool fire model developed in the previous sections is exercised and evaluated.

4.4.1 Model predictions of sodium pool fire measurements

The primary measurements available from the experimental measurements described in Section 2.2 are temperatures at the Pan Bottom. These temperatures represent an integral of the heating rate associated with the sodium oxidation, reduced by heat losses. Simulations were carried out by evolving Eq. (4-45) forward in time for the various layers to predict the temperature distribution through the oxide crust, the sodium pool, the steel pan and the insulation. The heat release rate appearing in Eq. (4-45) at the interface between the sodium pool and the oxide crust or ambient was obtained using Eq. (4-51) with the oxygen consumption rate from Eq. (4-36). A representative series of temperature profiles is indicated in Figure 4-6 for a set of conditions that corresponds to pan 1 and pan 7. The sodium and oxide crust regions exist in these figures for coordinates greater than zero. The steel pan with its relatively large conductivity occupies the region from zero to -0.016 m and the insulation with its relatively low conductivity occupies the bulk of the domain at more negative coordinates. The temperature profiles are shown for two early times, 10 and 30 s, to show the relatively rapid equilibration of temperatures across the sodium. After an intermediate time of 300 s during the oxide-sinking period, later times show the existence of the oxide crust in these cases. The oxide crust is evident in the sharp drop in temperature at the right of the domain associated with its lower thermal diffusivity than the sodium and steel. Naturally, the insulation also exhibits sharp temperature gradients. The discontinuity in the temperature gradient that occurs at -0.016 m corresponds to this transition from the high-conductivity steel pan to the insulation and it is at this point that the temperature predictions are compared with measurements.

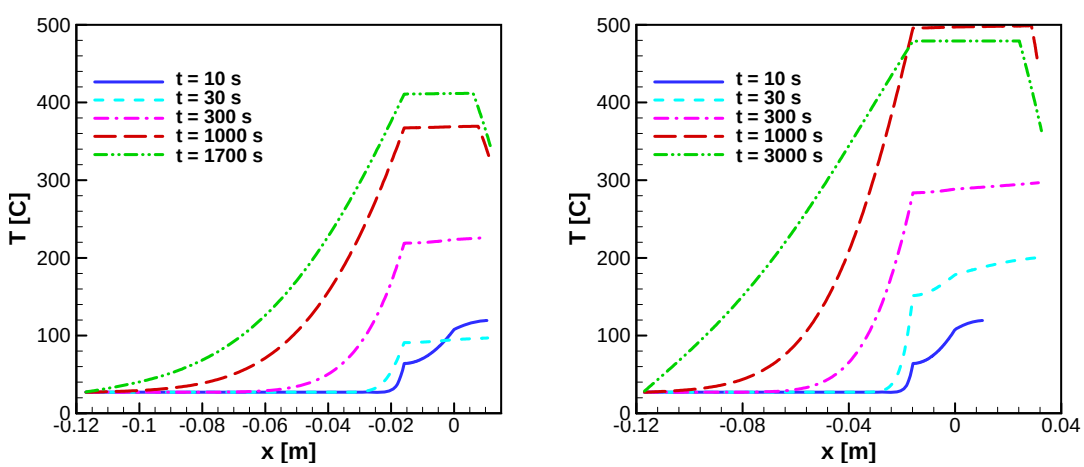

Figure 4-6: Temperature profiles predicted across the insulation, pan, sodium and oxide-crust layers are provided for pan 1 (left panel) and pan 7 (right panel) at various times.

In the following, predictions of the Pan Bottom temperature evolution with time are compared with the experimental measurements. Comparisons are grouped according to the relative mass of the sodium to the pan. In Figure 4-7comparisons are made with pans 1, 2, 5 and 8. These pans have the smallest masses of sodium and the temperatures rise the least. In Figure 4-8 comparisons are made with pans 6, 7 and 9 containing intermediate masses of sodium. In Figure 4-9 comparisons are made with pans 3, 4, 10 and 11. Pans 3 and 4 contained the greatest masses of sodium relative to the mass of their respective pans and these are the two that pass the 600°C temperature limit for the disappearance or non-occurrence of the oxide crust. These pans are also the only two pans that required an alteration of the Nusselt and Sherwood numbers from the buoyant flow values to larger values associated with forced convection; the Nusselt numbers were only set for Pan 3 to 80. For Pan 4 it was set to 50, which is less than the buoyant Nusselt number which is from 50-70.

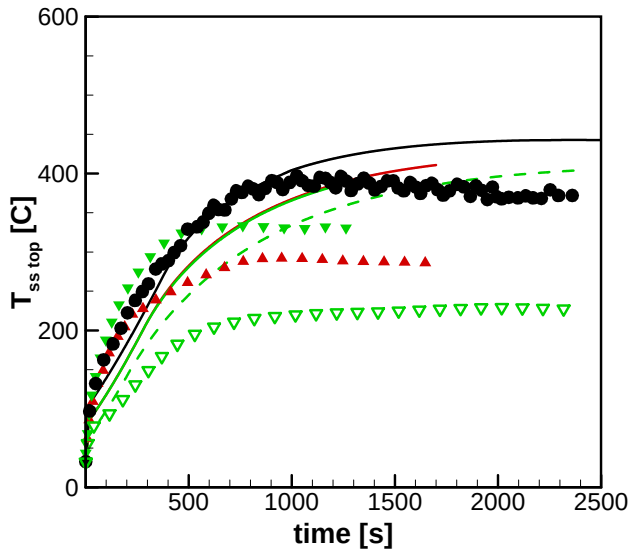

Figure 4-7: Temperature predictions (lines) compared with measurements (symbols) for pans 1, 2, 5 and 8.

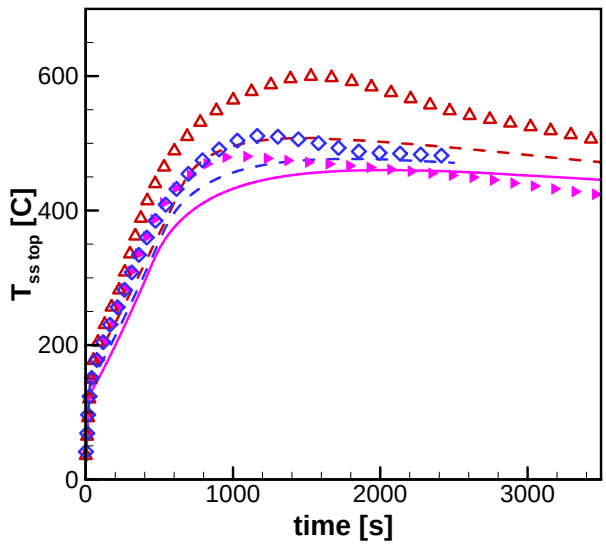

Figure 4-8: Temperature predictions (lines) compared with measurements (symbols) for pans 6, 7 and 9.

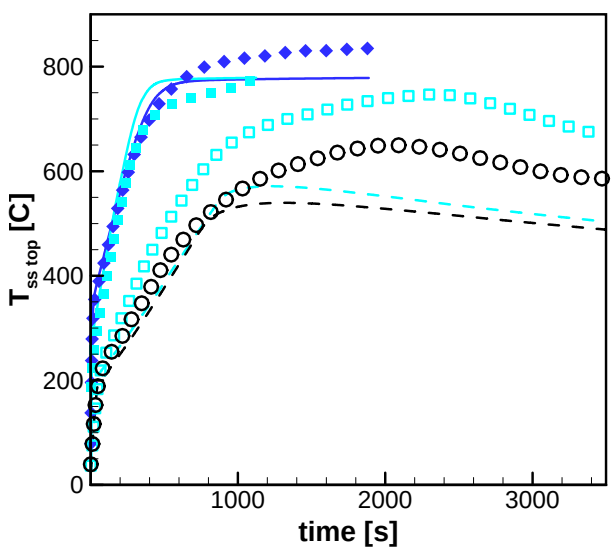

Figure 4-9: Temperature predictions (lines) compared with measurements (symbols) for pans 3, 4, 10 and 11.

In general, predictions are reasonable in light of the variability in the individual thermocouple measurements shown in Appendix B. In particular, the predictions are a substantial improvement over the prior models that ignored the presence of the oxide crust. For models that ignored the presences of the oxide crust, all temperature trajectories approximately follow those of pans 3 and 4 where no significant oxide crust was observed. The reason for the improved prediction is the role of the oxide crust in

reducing the mass flux of oxygen to the surface. The oxide crust acts as an additional resistance. Considering the oxygen mass fraction at ambient as an oxidizing potential, the boundary layer provides a resistance to the flux of oxygen to the surface and the oxide crust provides an additional resistance. This additional resistance appears in Eq. (4-36) through the factor $1/(1+\delta/\Delta_1)$ that shows these resistances to be in series. Another factor in the different predictions with the present models is that the similar additional thermal resistance associated with the oxide crust, through the factor $1/(1+\delta/\Delta_2)$ in Eq. (4-63). Since the ratio of the characteristic scaling for the oxide thickness, R_Δ, is small, the thermal resistance is small relative to the oxygen flux resistance.

There is one notable trend in the discrepancies between the experiments and predictions over those experiments where oxide crusts were significant (all but pans 3 and 4). This trend is that the model does not predict as much variation in peak temperatures as the experimental results. We note here that in an earlier version of the model where there was no oxide-sinking period this discrepancy is exacerbated. When there is no oxide-sinking period the temperatures peak with values that depend primarily on the thermal mass of the system, M_{layer}, as can be seen by examining Eq. (4-68). This leads to the understanding that the oxide crust is instrumental in dramatically reducing the peak temperatures through the reduced oxidation rates, but that this is not enough to reproduce the richness of the experimental results.

As implied in the previous paragraph, the introduction of the oxide-sinking period during which the oxide layer did not grow was instrumental in improving the results. At the present, the authors have considered only the simplest of oxide-sinking regime models where the parameter $\phi_{\mathrm{Na},lim}$ was fixed at 0.95. In the Model Parameters subsection above this parameter was interpreted as the sodium volume fraction when there was sufficient oxide saturation in the liquid phase to give a solid oxide crust supporting the further growth of that crust. A fixed solubility with varying temperature is not physical as solubility is expected to increase [34]. Allowing $\phi_{\mathrm{Na},lim}$ to decrease with increasing temperature would tend to improve results, but this has not been pursued at this point in the interest of minimizing model complexity. Introducing a variable limiting value for the oxide solubility would introduce a mechanism for the oxide crust to sink after it is formed since increasing solubility with increasing temperature would suggest gradual dissolution of the crust while the temperature is rising. There is much additional richness in the physics since solute-rich sodium will be denser and potentially advect to the bottom of the pan setting up solute concentration gradients within the pool. This leads to seamless transitions between oxide-crust smoldering modes and the higher temperature burning mode where the oxide crust has dissolved, but there is too little known about the nature of the oxide crust in the pool at this point to pursue this approach.

The discussion in the previous paragraphs suggest that sodium pool experiments that independently varied the depth of the sodium pool and the overall thermal mass of the pan plus pool system might help validate or refute the above ideas and other aspects of the present model. In addition, inerting and quenching oxidation in such experiments followed by analyzing the frozen composition and structure of the sodium pools would provide guidance as to the evolution of the pool. Measurement of the oxide crust

characteristics in an inerted environment (where further hydrolysis and conversion to sodium carbonate would be inhibited) will help identify the appropriate structures of that layer in terms of porosities.

For very shallow pools, the model was observed to over predict the temperature in Figure 4-7. Observation of the actual pool fires upon which the data is based reveals that the pools did not spread over the entire pan surface. This will be in part due to surface tension effects, but a substantial fraction of the sodium, or perhaps most of it, freezes upon contact with the pan since the thermal mass of the sodium is relatively small in these cases. The thermally averaged temperature for these tests in pans 1, 2, 5 and 8 are all below the sodium freezing temperature. In these cases, the model may be more applicable if corrections are made for the limited spreading and the reduced surface area. Reduced surface area reduces oxygen transport rates (though not linearly because boundary layers are thinner), leading to reduced heat release rates. At the same time, the thermal mass of the pan is unchanged so that the temperatures are expected to be lower as measured. Other effects would include heat losses from parts of the pan that are uncovered. The analysis quickly becomes multi-dimensional and goes beyond the current scope. Spreading of sodium pools has been studied recently [35-36] but these ignored any freezing of the sodium.

It is interesting to discuss the present model in the context of agents employed to extinguish metal fires (class D fires). In general, the approach to extinguishing such fires is to employ a powder that is thermodynamically stable in the presence of the metal and oxidizer and employ that powder to smother the fire through inhibition of fuel-air mixing. Examples of such powders include G-1 powder (a graphitized-coke powder), Met-L-X (a sodium-chloride based powder) and Na-X (a sodium-carbonate based powder) [37-38]. Each of these commercial products contain additives to facilitate fluidization and to render them nonhygroscopic. These powders dispersed on the surface will inhibit fuel-oxidizer mixing as described with the models here. In addition, they are generally designed to either release inert gases into the vapor-phase void fraction in the case of G-1 powder or to partially fuze or cake to reduce porosity in the case of Met-L-X or Na-X. Both of these actions serve to further reduce the ability of the oxidizer to penetrate the porous mixture. Typical suggested coverage is on the order of a couple centimeters of depth. At such depths, even the sodium oxide crust, using the current models, provides substantial inhibition to the oxidation rate. The fact that these suppressants are designed to fuze would naturally lead to reduced porosities and better inhibition of the oxidation rate, but thermally inhibited sodium (by cooling it on a thermally massive surface) provides its own inhibition of oxygen transport through the thick oxide crust. This is not meant as a recommendation for self-extinguishment of sodium, in particular because of the strongly corrosive nature of the oxides and subsequent products, but just to point out similarities.

5 SUMMARY AND CONCLUSIONS

The results of sodium spray and pool fire experiments as well as the development of a sodium pool fire model have been presented in this paper. Appendix A and B present additional details of the sodium spray and pool fire experimental results respectively. These appendices include the details of the experimental setup, instrumentation, and the detailed data for each experiment.

The sodium spray fire experiments have shown some interesting conceptual results including the high temperatures and heat fluxes off of the spray. SNL has established a knowledge base for sodium spray fire experimentation and modeling. The improvement for future sodium spray tests would include the elimination of the sodium vapor formation before the start of the test. The piping system was not inerted so there is some speculation that there was a decent amount of sodium vapor formation as the sodium passed through the piping system to the nozzle tip. Other advanced diagnostics for future tests would include floor vessel temperatures, aerosol characterization, oxygen consumption, and spray characterization.

A focus of this project has been a series of pool fire experiments. These measurements demonstrate temperature-evolution trends in more relevant regimes than previous available. In particular, when the thermal mass associated with a pool plus pan system is significant, temperatures may be kept within a range where oxide crusts are significant. When this happens, reduced temperatures are observed when compared with the standard suggested peak pool temperatures in the 700 - 800 C range [5].

This paper has also introduced a model for sodium oxidation that adds several features to prior models. Of greatest importance is the presence of the oxide crust that inhibits the oxygen transport to the molten sodium. This porous oxide crust inhibits oxygen transport to a greater degree than it inhibits heat transfer, and this inhibition can be interpreted as an additional resistance to mass and heat transfer that is in series with the boundary layer. That is, an analogy is introduced to the well-known scenario where an electric current is proportional to the potential divided by the sum of series resistances. The oxygen mass fraction is the potential in the mass transport case and the boundary layer and oxide crust are series resistances that limit the rate of flux. The same analogy holds for the thermal transport but the thermal resistance of the oxide crust is relatively small and there is a parallel path of low resistance into the pool.

This oxide crust is observed to occur for temperatures below approximately 600°C and after a duration that is related to the mass of the sodium. The model has been set to allow oxide products to sink into the pool until the concentration in the pool approaches 5% by volume at which time the oxide crust forms. This concentration is suggested to be related to the solubility of the oxide in the pool, although at this point only the roughest association is possible.

This research is important to the Generation IV advanced reactor concepts. Model predictions can greatly influence risk/hazard estimates for Nuclear Power Plant applications.

6 REFERENCES

[1] Olivier, T.J., et al., *Metal Fire Implication for Advanced Reactors, Part 1, Literature Review.* 2007, Sandia National Laboratories, SAND2007-6332.

[2] Olivier, T.J., et al., *Metal Fire Implication for Advanced Reactors, Part 2: PIRT Results* 2008, Sandia National Laboratories, SAND08-6855.

[3] Cherdron, W. & J. Charpenel, 1985a, *Thermodynamic Consequences of Sodium Spray Fires in Closed Containments, Part 1-Experiments*. Laboratorium für Aerosolphysik und Filtertechnik, Kernforschungszentrum, Karlsruhe.

[4] Malet, J.C. et al., 1981, *Potential Results of Spray and Pool Fires. Nuclear Engineering and Design* , North-Holland Publishing Company (68:195-206).

[5] Newman, R.N., *The Ignition and Burning Behavior of Sodium Metal in Air.* Prog. Nucl. Energy, 1983. **12**(2): p. 119-147.

[6] Newman, R.N. and J.F.B. Payne, *Burning Rates of Sodium Pool Fires* Combust. Flame, 1978. **33**(3): p. 291-297.

[7] Olivier, T.J., J.C. Hewson, T.K. Blanchat, S.P. Nowlen, "Understanding Thermal Consequences of Liquid Sodium Fires", Proceedings of the International Heat Transfer Conference, IHTC-14-23268, August 8-13, 2010, Washington, DC, USA.

[8] Johnson, R.P. *et al*., 1968, *Characterization of Sodium Pool Fires*. Proceedings of the International Conference on Sodium Technology and Large Fast Reactor Design, Part I, Sessions on Sodium Technology, Argonne National Laboratory,ANL-7520, pp. 195-205.

[9] J. V. Beck, "Users Manual for IHCP1D," a Program for Calculating Surface Heat Fluxes from Transient Temperatures Inside Solids, Beck Engineering Consultants Co., Okemos, Michigan, 48864, January 12, 2010.

[10] B. F. Blackwell, R.W. Douglass, and H. Wolf, "A Users Manual for the Sandia One-Dimensional Direct and Inverse Thermal (SODDIT) Code," Sandia National Laboratories report SAND85-2478, UC-32, Printed May 1987, Reprinted December 1980.

[11] M.N. Ozisik, "Heat Conduction," 2nd ed., John Wiley & Sons Inc., New York, 1993.

[12] J. J. Gregory, "Sensitivity Analysis for Noisy Temperature Data in Inverse Heat Conduction Calculations," Sandia National Laboratories memorandum, to N.R. Keltner, 1987.

[13] V.G. Figueroa and J.T. Nakos, Uncertainty Analysis of Heat Flux Measurements Estimated Using a One-Dimensional, Inverse Heat-Conduction Program, Sandia National Laboratories report SAND2005-0339, Printed February 2005

[14] C. Lopez, J.A. Koski, and A. Razani, "Estimate of Error Introduced When One-Dimensional Inverse Heat Transfer Techniques Are Applied to Multi-Dimensional Problems," in *Proceedings of Numerical Heat Transfer Conference*, (Pittsburgh, Pennsylvania, August 2000), NHTC2000-12037.

[15] Makino, A., *Ignition delay and limit of ignitability of a single sodium droplet: theory and experimental comparisons.* Combust. Flame, 2003. **134**(1-2): p. 149-152

[16] Makino, A. and H. Fukada. *Ignition and combustion of a falling, single sodium droplet*. in *30th International Symposium on Combustion*. 2004. Chicago, IL: Combustion Inst.
[17] Makino, A., *Ignition delay and limit of ignitability for sodium pool (Theory and experimental comparisons).* Jsme International Journal Series B-Fluids and Thermal Engineering, 2006. **49**(1): p. 92-101.
[18] Chang, Y.I., P.J. Finck, and C. Grandy, *Advanced Burner Test Reactor Preconceptual Design Report, ANL-ABR-1 (ANL-AFCI-173)*, Argonne National Laboratory: Argonne, IL, 2006.
[19] Ichimiya, M., T. Mizuno, and S. Kotake, *A Next Generation Sodium-Cooled Fast Reactor Concept and its R&D Program.* Nuclear Engineering and Technology, 2007. **39**(3): p. 171-186.
[20] Mikami, H., A. Shono, and H. Hiroi. *Sodium Leak at Monju (I)-Cause and Consequences*. in *Technical Committee Meeting on Evaluation of Radioactive Materials Release and Sodium Fires in Fast Reactors*. 1996. O-aria, Ibaraki, Japan: International Atomic Energy Agency, Vienna, Austria.
[21] Buksah, Y.K., *Operation Experience of the BN-600 Fast Reactor.* Nuclear Engineering and Design, 1997. **173**: p. 67-79.
[22] Luster, V.P. and K.F. Freudenstein. *Feedback from Practical Experience with Large Sodium Fire Accidents*. in *Technical Committee Meeting on Evaluation of Radioactive Materials Release and Sodium Fires in Fast Reactors*. 1996. O-aria, Ibaraki, Japan: International Atomic Energy Agency, Vienna, Austria.
[23] Huber F, *Investigation of Sodium Area Conflagrations and Testing of a Protective System Nuclear Engineering and Design and Design* 35: 155, 1975.
[24] Yamaguchi, A. and Y. Tajima, *Sodium pool combustion phenomena under natural convection airflow.* Nuclear Engineering and Design, 2009. **239**(7): p. 1331-1337.
[25] Jordan, S., et al., *Sodium Aerosol Behavior in Liquid-Metal Fast Breeder Reactor Containments.* Nuclear Technology, 1988. **81**(2): p. 183-192.
[26] Pilling NB, Bedworth RE (1923) J Inst Met 29: 529
[27] Yuasa, S., *Spontaneous Ignition of Sodium in Dry and Moist Air Streams.* Proc. Combust. Instit., 1984. **20**: p. 1869-1876.
[28] Richard, J.B., R. Delbourgo, and P. Laffitte, *Spontaneous Ignition and Combustion of Sodium Droplets in Various Oxidizing Atmospheres at Atmospheric Pressure.* Proc. Combust. Instit., 1969. **12**: p. 39-48.
[29] Maxwell, J. C. *A Treatise on Electricity and Magnetism*; Dover Publications: New York, 1954; Vol. 1
[30] Bruggemann, D.A.G., Ann. Phys., 1935. **24**: p. 636.
[31] Hunt, A., *Percolation Theory for Flow in Porous Media*. Lect. Notes Phys., ed. C. Caron. Vol. 674. 2005, Berlin: Springer.
[32] Fujii, T. and H. Imura, *NATURAL CONVECTION HEAT-TRANSFER FROM A PLATE WITH ARBITRARY INCLINATION.* International Journal of Heat and Mass Transfer, 1972. **15**(4): p. 755-&.
[33] Incropera, Frank P., David P. DeWitt, *Introduction to Heat Transfer*, Fourth Edition. John Wiley & Sons, Inc., New York, 2002.

[34] H. A. Wriedt, Na-O (Sodium-Oxygen), Binary Alloy Phase Diagrams, II, Editor: T. B. Massalski, vol. 3, 1990, pp 2718-2722.
[35] "Dynamics of liquid sodium pool spreading under sodium fire conditions" Author(s): Subramani, A; Jayanti, S; Shet, USP, et al. Source: NUCLEAR ENGINEERING AND DESIGN Volume: 239 Issue: 7 Pages: 1354-1361 Published: 2009
[36] "Development of mathematical model for optimization of sodium leak collection tray" Author(s): Diwakar, SV; Sundararajan, T; Das, SK, et al. Source: NUCLEAR ENGINEERING AND DESIGN Volume: 238 Issue: 10 Pages: 2684-2692 Published: 2008
[37] Brzustowski, T.A. and I. Glassman, *Vapor-phase diffusion flames in the combustion of magnesium and aluminum: I. Analytical developments*, in *Heterogeneous Combustion*. 1964, Academic Press: New York. p. 75-116.
[38] *DOE Handbook: Primer on Spontaneous Heating and Pyrophoricity, DOE-HDBK-1081-94*, U.S.D.o. Energy, Editor. 1994: Washington, D.C.

7 APPENDIX A: SODIUM SPRAY FIRE TEST SETUP AND EXPERIMENTAL DATA

This Appendix focuses on the sodium spray fire tests. There were two outdoor sodium spray experiments and two in-vessel sodium spray experiments performed. Overall the spray fire tests were performed in order to develop SNL's capability with some very important overall phenomenological understanding. The two outdoor spray tests were done in order to understand system performance and instrumentation response. The two in-vessel spray experiments were performed in a controlled atmosphere in order to obtain better boundary conditions than in the past. **Table 7-1** displays the general information about all four sodium spray fire tests.

Table 7-1: Overview of Sodium Spray Fire Tests

Test #	T1	T2	T3	T4
Location	Outside	Outside	In-Vessel	In-Vessel
Height of Spray (m)	4.6	4.6	5.3	5.3
Nozzle Type	H15	GG15	H15	H15
Amount of Na (kg)	4	4	20	20
Flow rate (kg/s)	1	0.5	1	1
Median Particle Size Diameter (mm)	~6	~10	between 3 and 5	between 3 and 5
Initial Temperature of Sodium (°C)	500	500	200	500
Melt Generator Pressure at System Dump Time (psi)	310.7	28.4	307	307

7.1 Sodium Spray Fire Outdoor Tests

Below is a detailed explanation of the setup and instrumentation used during the outdoor sodium spray fire experiments and the data obtained specific to each test. The difference between the two outdoor spray tests was the median particle size of the spray. The first test was at a much higher pressure creating smaller spray droplets. The second outdoor test was performed with a larger nozzle and a lower pressure to obtain bigger spray droplets than the first test.

7.1.1 Outdoor Spray Test Instrumentation

This section will present the instrumentation used for the outdoor sodium spray fire testing. **Figure 7-2** displays the overall outdoor setup with instrumentation and systems locations.

1. Spray Plume Temperature

For the sodium outdoor scoping experiment, four type-K thermocouple (1 m (3.3 ft) spacing) were installed in a vertical array at center and at 0.6m (24 in) radius (shown below in **Figure 7-2**). The temperature range of the thermocouples is from 273 K to 1533 K. The maximum error using the manufacturer's calibration is ±25.9 K with a 0.9-s time constant.

2. Heat Flux
A narrow-angle radiometer and a total heat flux gauge were used to measure the radiation intensity at mid level of the sodium spray. The pair of gauges, a narrow-angle radiometer (Medtherm model NVRW-15-5-360-2183, 5º view angle) and a total heat flux gauge (Medtherm model 64-2-18 with a view angle of 180º) were mounted together at a distance of approximately 2.3 m (7.5 ft) from the spray centerline. The spot diameter for the narrow-angle gauges (at 2 m) is about 0.15 m (0.5 ft). The gauge pair was at a height of 2.3m (7.5 ft), midpoint of the height of the sodium spray. The line of sight for each gauge will pass through the centerline of the fire at the height of the gauge. All of the heat flux gauges were water-cooled. The radiative heat flux measured by the narrow angle radiometers and total heat flux gauges have a manufacturer's stated uncertainty of ±3%.

3. Visual
Three high-resolution color video cameras – views from the east, north, and above the large catch pan. One IR camera will be focused on the entire height of the spray.

7.1.2 Stainless Steel Spray Nozzles

The spray nozzles that were used for these experiments are narrow angle, full solid cone nozzles that were manufactured by Spraying Systems, Co., Wheaton, IL. **Table 7-2** provides the nozzle inventory that was obtained from Spraying System, Co.

Table 7-2: Nozzles Obtained from Spraying Systems, Co.

Nozzle Model Number	Nozzle Orifice Diameter (in)	Spray Angle (°)
1590 (G-15)	0.219	15
15430 (H-15)	0.484	15

These nozzles were chosen for the uniform, round, full spray pattern with a narrow spray angle. The outdoor scoping tests utilized both of the nozzles listed in Table 2-2 while the in-vessel tests only ysed the H-15 nozzle. The nozzle flow data versus pressure is shown in Figure 7-1 for all four nozzles. The nozzles were supplied from Spraying Systems, Co., and were characterized at their laboratory using water. The data from the characterizations can be found in two different laboratory reports by Spraying Systems, Co. [1].

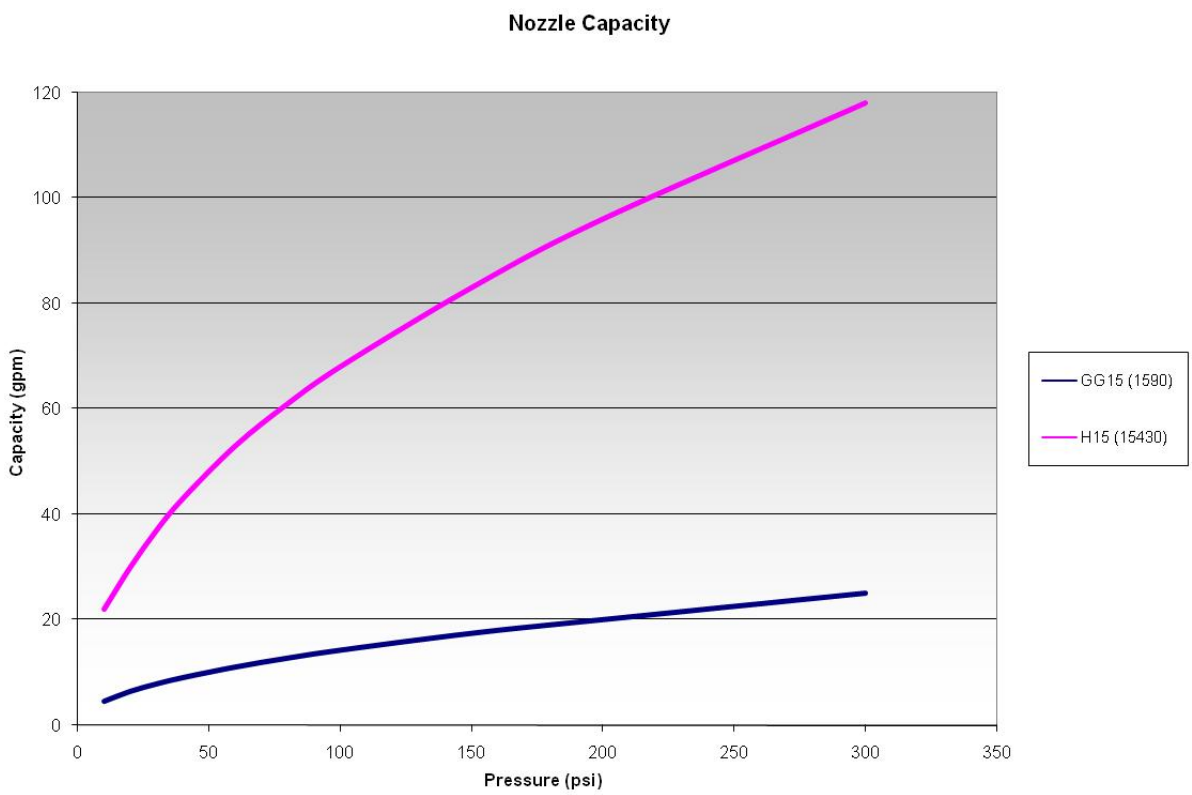

Figure 7-1: Nozzle Capacity versus Pressure

7.2 Sodium Melt Generator

The melt generator is a stainless steel pressure vessel designed to hold 36 kg of Na (150% of the theoretical amount for complete combustion), yielding a liquid volume of about 0.039 m^3 (1.37 ft^3), based on the density of 0.968 g-cm^3. Assuming the generator is designed to have the same amount of free gas space, the melt generator empty volume is about 0.078 m^3 (2.75 ft^3).

The vessel was wrapped with heat tape and insulation capable of bring the melt to a temperature of 500°C within a reasonable amount of time. Stainless steel tubing (1.27 cm, 0.5 inch diameter) connects the melt generator to the vessel, either directly to the burn pan or to a stainless steel spray nozzle. All tubing and components through which liquid sodium passed through was wrapped in heat tape, insulated, and brought to the same temperature as the melt to prevent freezing in the lines.

To perform an experiment, solid sodium was placed in the melt generator via the top head. After loading and securing the head, the vessel was be purged with nitrogen. Nitrogen gas was also used to drive (by pressure) the sodium to the burn pan or to a stainless steel nozzle.

7.2.1 Data Acquisition

The data acquisition system (DAS) consists of a PC with a 16-bit data acquisition card connected to a National Instruments (NI) SCXI-1001 chassis. It has NI SCXI-1102 cards with NI SCXI-1303 blocks for TCs and NI SCXI-1104 cards with NI SCXI-1300 blocks for analog signals. This provides the ability to increase either analog signals or TC signals. The data acquisition system can acquire temperature, heat flux, and pressure data. The integrity of all thermocouple channels is evaluated prior to each experiment with an Ectron thermocouple simulator, which inputs a controlled signal into each channel at the thermocouple device connection point and provides a check on the integrity of the channel hardware and software from that point to the final magnetic storage location. Data are sampled simultaneously for all channels, typically at 1000 Hz with an average value recorded at a rate of at least one sample per second. The spectrometer is a stand-alone instrument and data is recorded independent of the DAS.

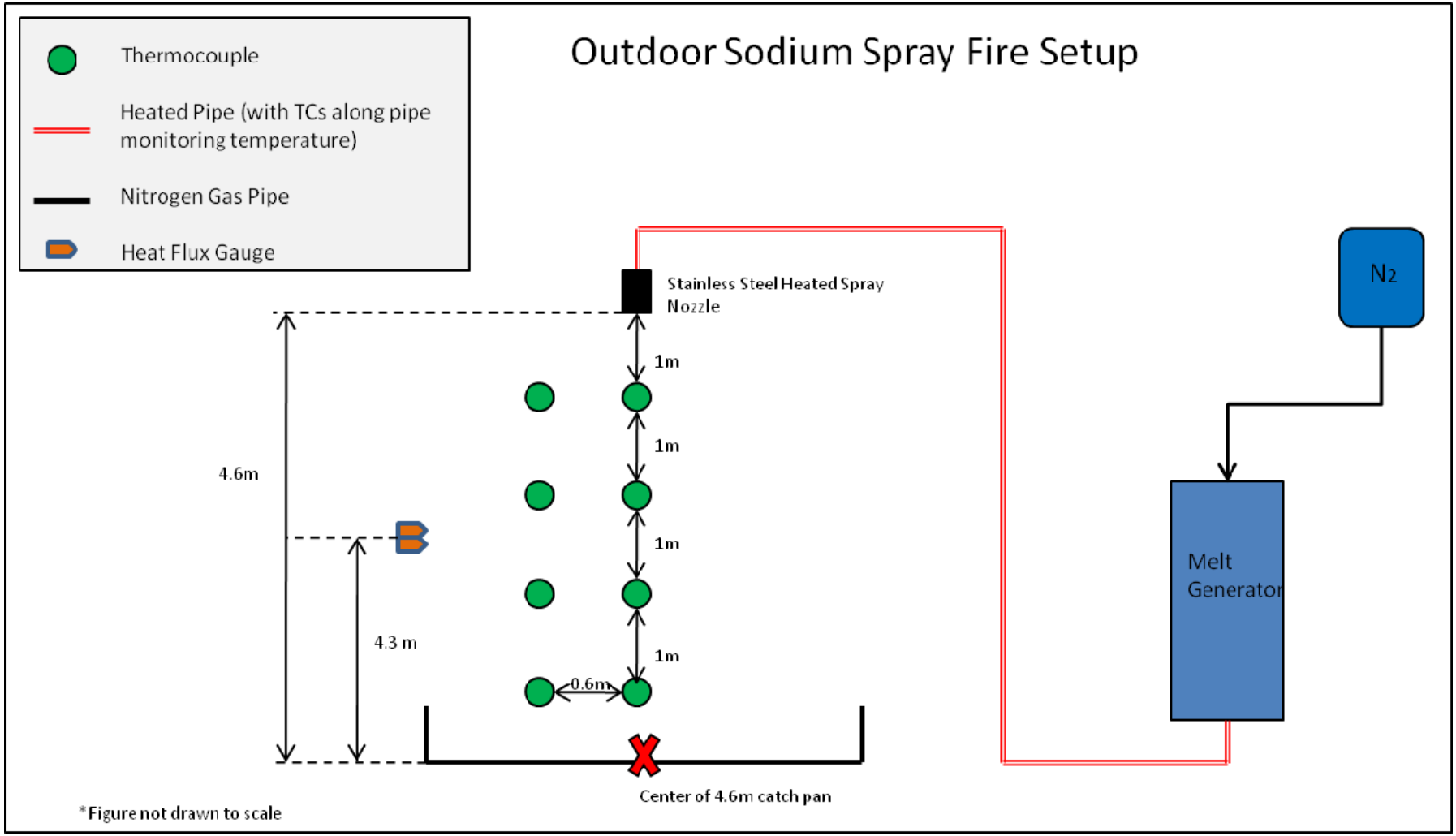

Figure 7-2: Outdoor Sodium Spray Test Instrumentation Setup and TC Locations

7.2.2 Sodium Outdoor Spray Test 1 Measured Data

This section displays the measured data from the first outdoor sodium spray test (Test 1). For instrumentation locations and specifications referred to in the figures of this section please reference Section 7.1.1. There was intention to utilize pyrometers for these tests, but they had gotten damaged from the outside environments in between testing series. Instead they were sent off for repair in order to use them during the larger in-vessel spray tests. The load cell data is also not presented, there was issues with the amount of noise the instrument saw from the intense heating of the melt generator in order to melt the sodium to such high temperatures. The figures below are the actual measured experimental data.

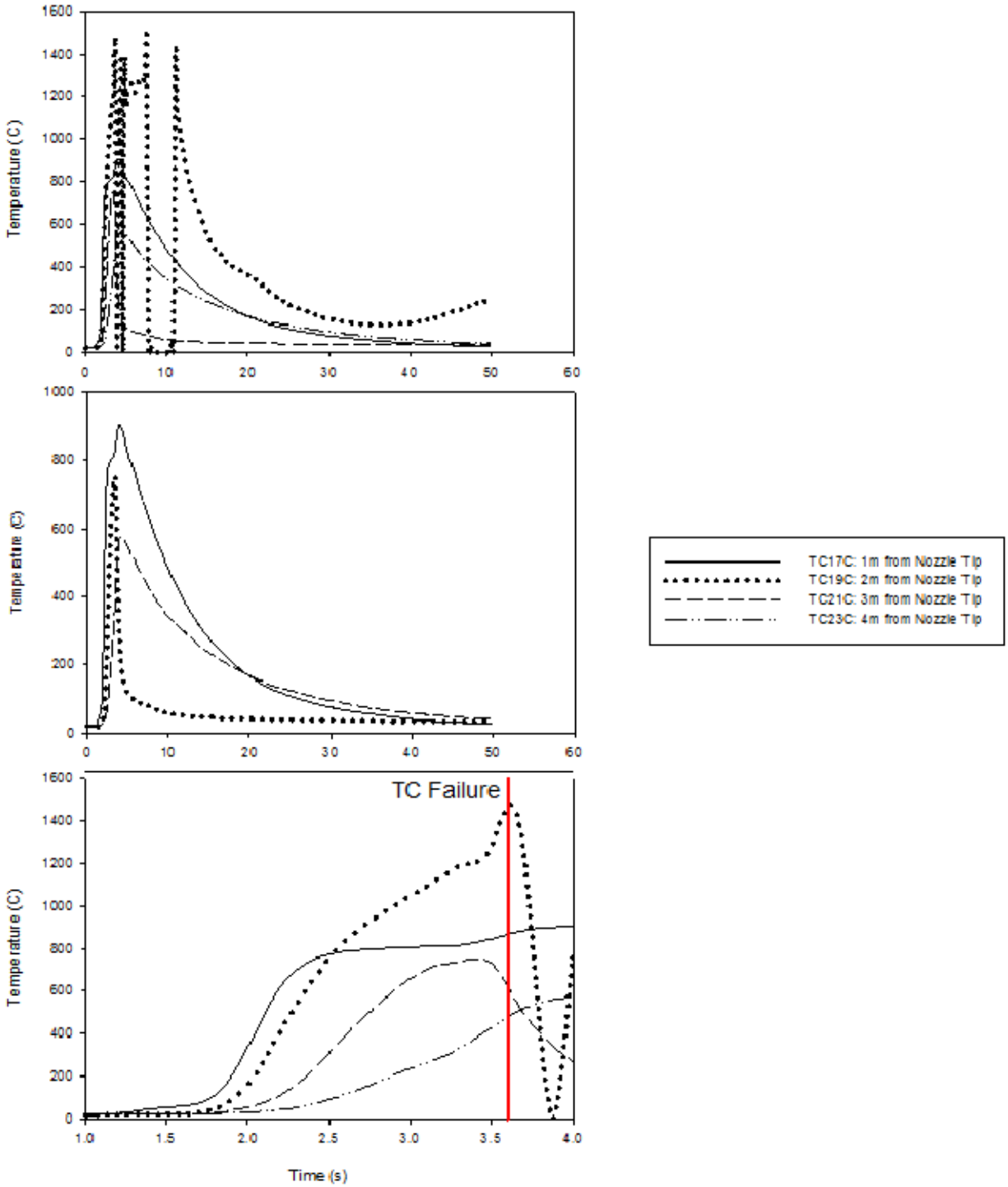

Figure 7-3: Outdoor Sodium Spray Test 1, Center TC Rake Temperatures vs Time

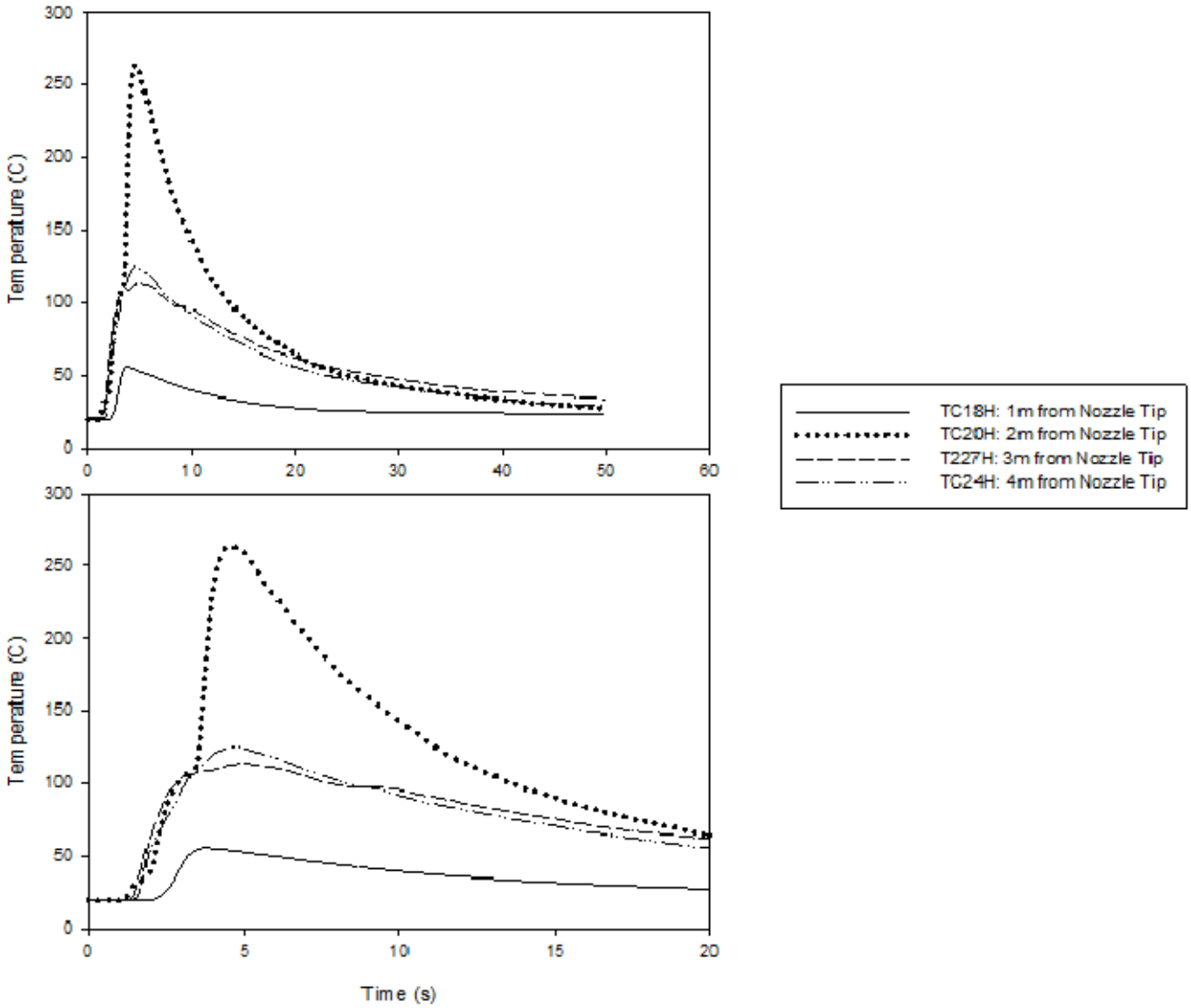

Figure 7-4: Outdoor Sodium Spray Test 1, 0.6m (2 ft) Radius TC Rake Temperatures vs Time

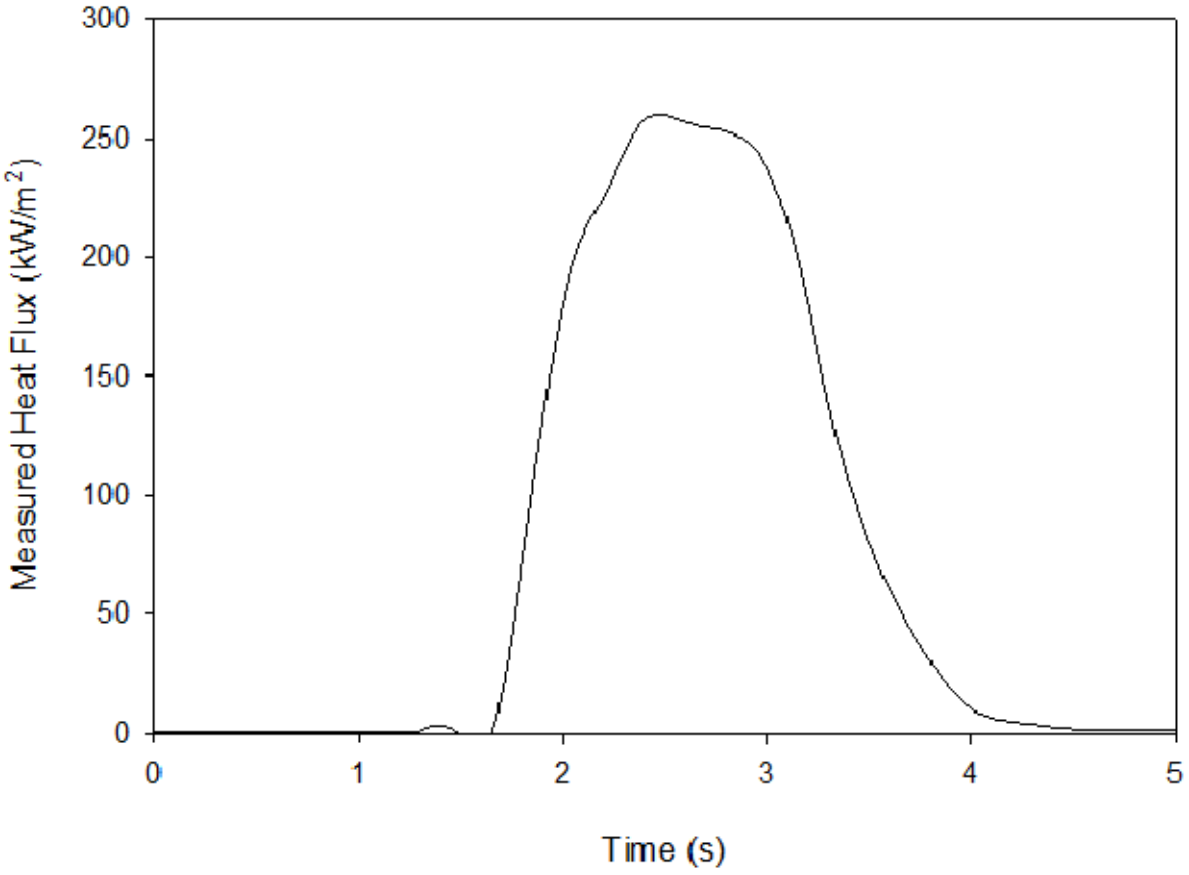

Figure 7-5: Outdoor Sodium Spray Test 1, Measured Heat Flux (Narrow View Gauge) vs Time

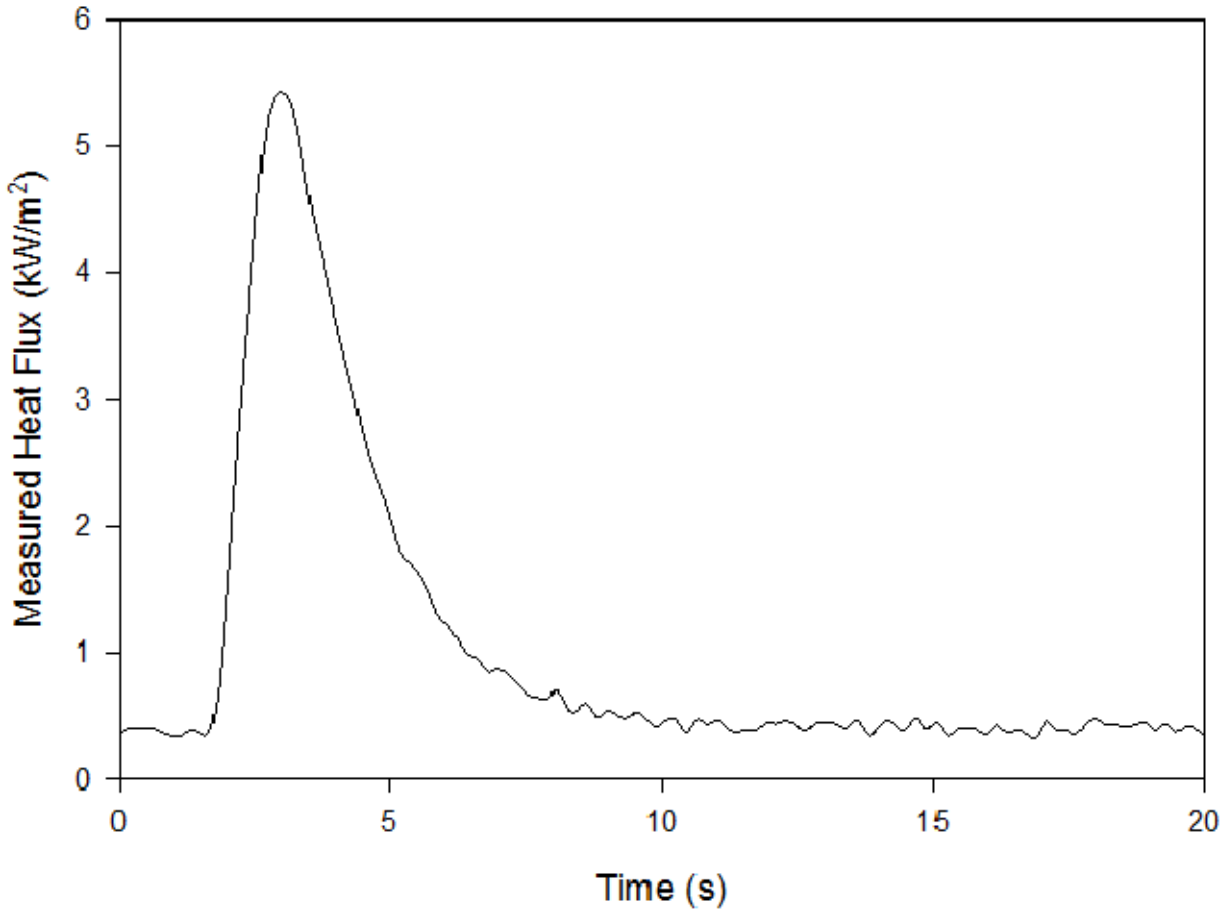

Figure 7-6: Outdoor Sodium Spray Test 1, Measured Heat Flux (Wide View Gauge) vs Time

7.2.3 Sodium Outdoor Spray Test 2 Measured Data

This section displays the measured data from the second outdoor sodium spray test (Test 2). For instrumentation locations and specifications referred to in the figures of this section please reference Section 7.1.1. Again the pyrometers and load cell data will not be displayed based on the discussion in Section 7.2.2. The figures below are the actual measured experimental data.

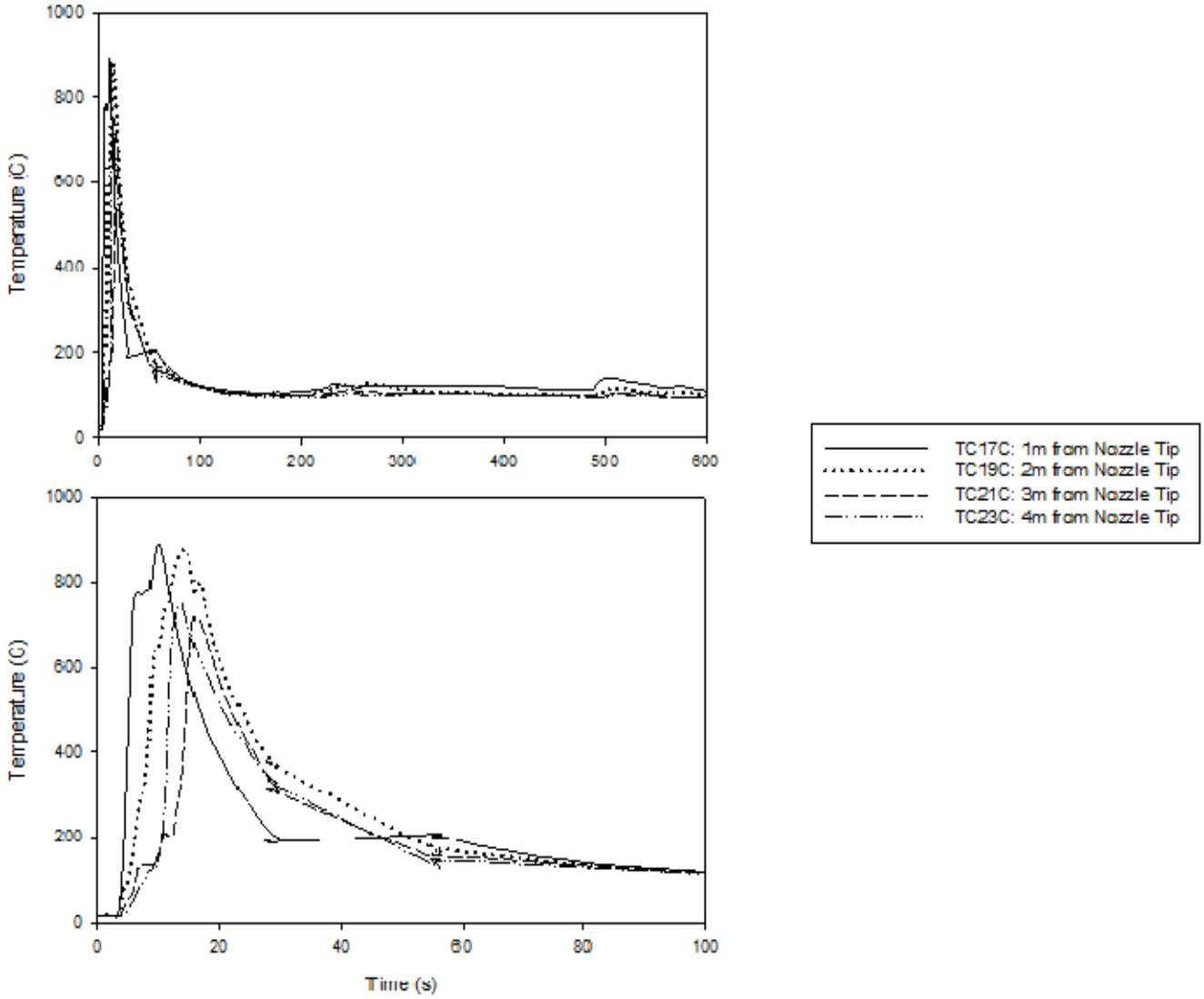

Figure 7-7: Outdoor Sodium Spray Test 2, Center TC Rake Temperatures vs Time

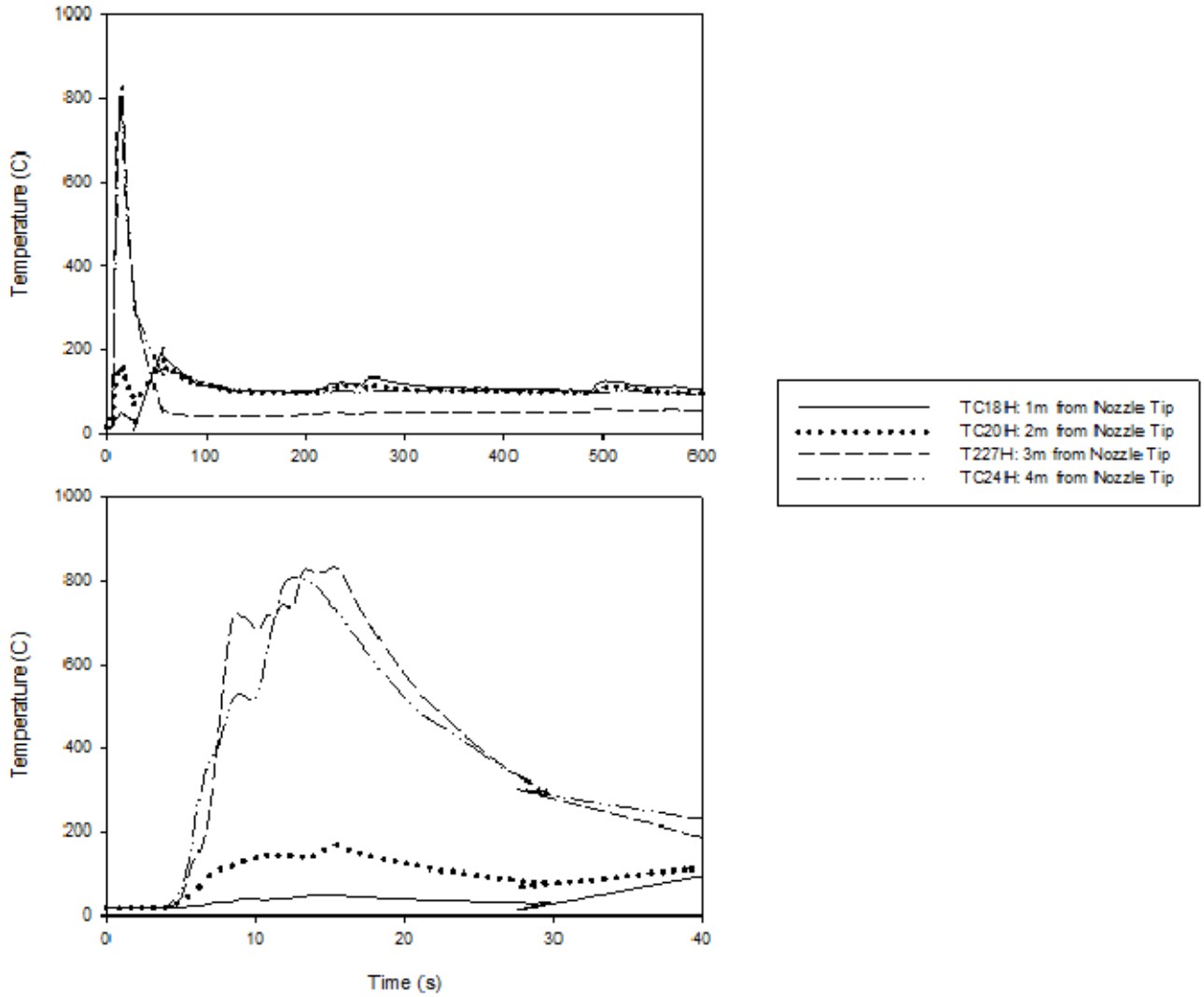

Figure 7-8: Outdoor Sodium Spray Test 2, 0.6m (2 ft) Radius TC Rake Temperatures vs Time

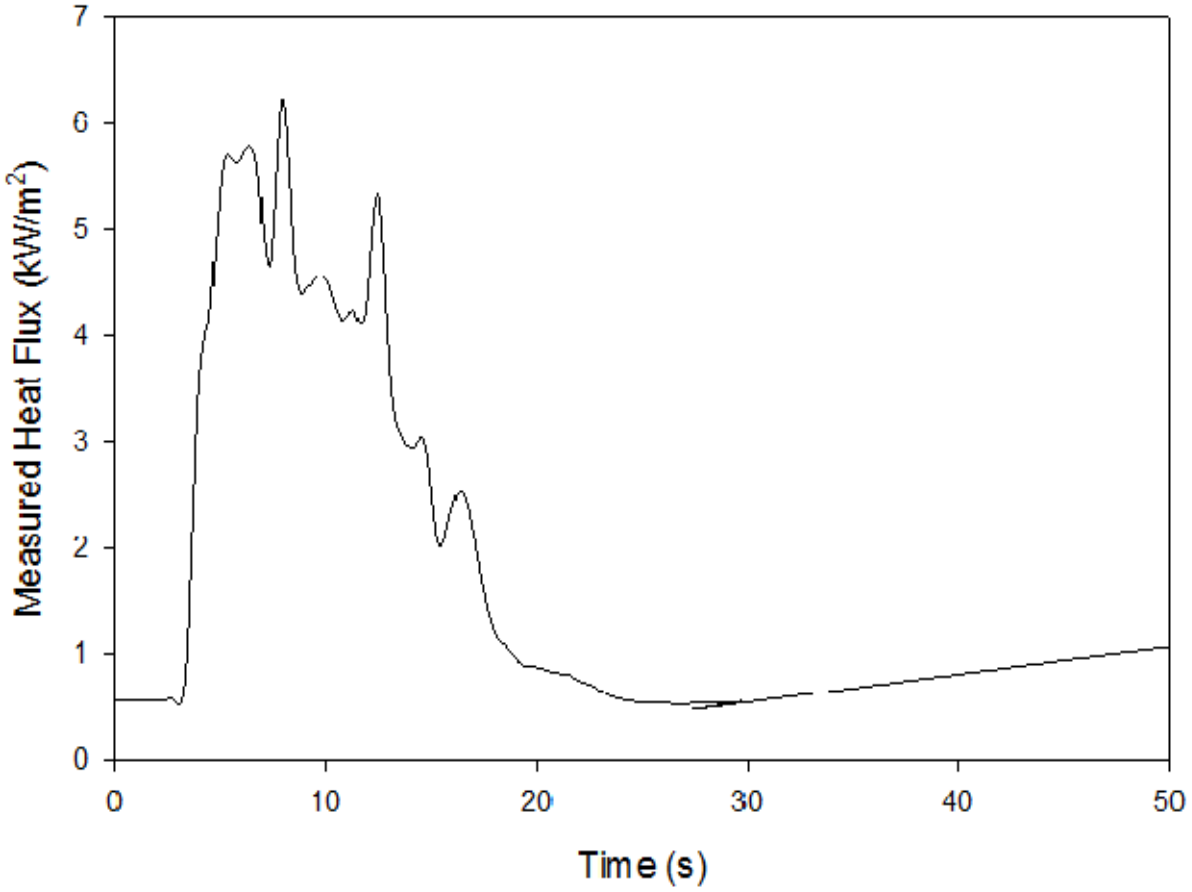

Figure 7-9: Outdoor Sodium Spray Test 2, Measured Heat Flux (Narrow View Gauge) vs Time

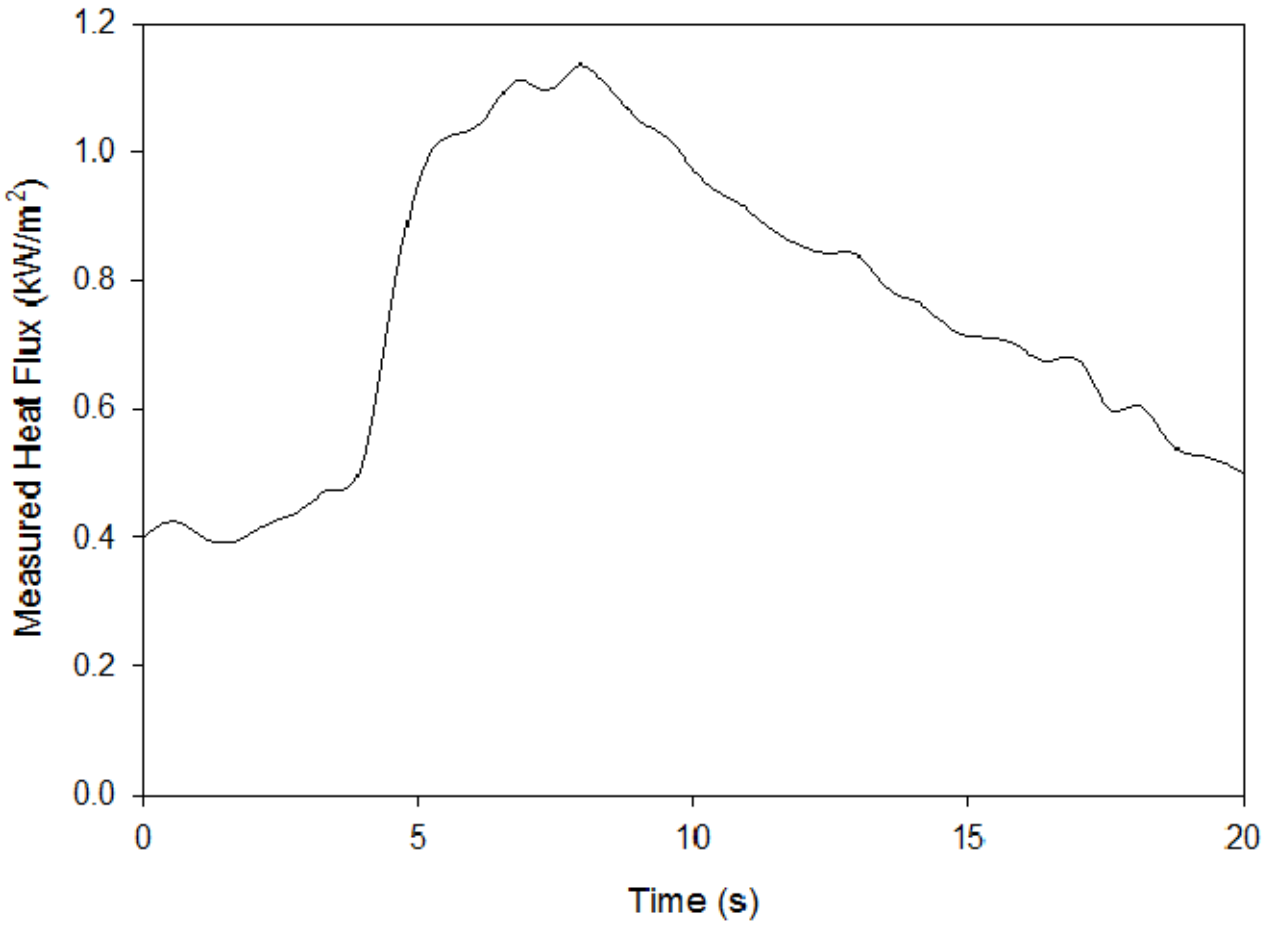

Figure 7-10: Outdoor Sodium Spray Test 2, Measured Heat Flux (Wide View Gauge) vs Time

7.3 Full-Scale Sodium Spray Fire In-Vessel Tests

Below is a detailed explanation of the setup and instrumentation used during the in-vessel sodium spray fire experiments and the data obtained specific to each test. The spray nozzles and the DAQ were the same for the in-vessel testing as mentioned for the outdoor spray tests.

7.3.1 Full-Scale In-Vessel Instrumentation

The most significant variables to be measured and the instrumentation for the sodium spray fire full-scale in-vessel experiments are described below.

1. Melt generator pressure

For the melt generator pressure both a low pressure and high pressure transducer were used. Depending on the test specifications both transducers were used throughout different parts of the test series. A calibrated low pressure transducer with a range of 0-100 psi was used. The specified accuracy from the manufacturer for the pressure transducer is less than ± 0.25 percent

at full-scale output. A calibrated high pressure transducer with a range of 0-500 psi was used. The specified accuracy from the manufacturer for the pressure transducer is less than ± 0.25 percent at full-scale output.

2. Surtsey vessel pressure

In order to measure the pressure change inside the Surtsey vessel during the spray fire experiments, a calibrated pressure transducer with a range of 0 to 100 psi located on the south wall at level 4 (4.75m above vessel floor) was used. The specified accuracy from the manufacturer for this pressure transducer is less than ± 0.25 percent at full-scale output.

3. Surtsey wall temperature

For the Surtsey wall temperatures three type-K thermocouples (2 m spacing, starting at 1 m from the bottom of the vessel) were installed in a vertical array along the northwest vessel wall. The temperature range of the thermocouples was from 273 K to 1533 K. The maximum error using the manufacturer's calibration is ±25.9 K with a 0.9-s time constant. These are shown below in Figure 7-11.

4. Spray droplet characteristics (mean size, velocity) and visual

In order to attempt to obtain spray droplet characterization and visual images in-vessel, one black and white high speed camera, one high definition camera, and one low speed camera was used. The high speed black and white camera was used to estimate droplet size and velocities. The high definition camera and low speed camera was used to determine time to ignition.

Note that all cameras are installed outside port windows besides the one low speed camera which was inside the vessel. The cameras looked through a 2.5-cm-thick tempered glass window.

5. Spray temperature

In order to obtain spray temperatures, an array of seven type-K thermocouples (0.5 m spacing, first thermocouple installed 0.5 m from the vessel floor) installed in a vertical array 0.3 m (1 ft) away from the vessel wall as shown in Figure 7-11. The temperature range of the thermocouples is from 273 K to 1533 K. The maximum error using the manufacturer's calibration is ±25.9 K with a 0.9-s time constant.

An optical pyrometer was used to measure the temperature of the sodium spray fire. They were located at a distance of 1.75 m (69 in) from center of the vessel aimed 2 m (6.6 ft) below the spray nozzle at the horizontal center of the spray (as shown in **Figure 7-11**). A pyrometer similar to type 11x30, Ircon Inc., Niles, IL was located outside the vessel and focused through a window into the Surtsey vessel. The optical pyrometer had a response time of 1.5 ms to 95 percent of its full range. A low-to-mid range signal conditioner was installed on the 11x30 pyrometer to yield temperature measurements between 723 K and 1573 K with a specified accuracy of 1% of the full-scale temperature. In a transient event, the accuracy of the pyrometer measurement is expected to be no better than ±25 K.

6. Heat flux

One cluster of five narrow-angle heat flux gauges were used to measure the radiation intensity as a function of height (as shown in Figure 7-11). Three of the narrow view heat flux gauges were aimed at 1m, 2m, and 3m at center from the tip of the spray nozzle. The other two will be aimed at 2m in height below the spray nozzle tip, but will be 0.3 m (1 ft) east and west of center. All gauges will be located 1.5 m (58 in) from the center of the vessel. This resembles a cross pattern of the five narrow view heat flux gauges. A detailed drawing of this is shown below in Figure 7-12. The narrow-angle radiometers are model, Medtherm model NVRW-15-5-360-2183, 5º view angle. The spot diameter for the narrow-angle gauges (at 2 m) is about 0.5 ft (0.16 m). All of the heat flux gauges are water-cooled. The radiative heat flux measured by the narrow angle radiometers and total heat flux gauges have a manufacturer's stated uncertainty of ±3%.

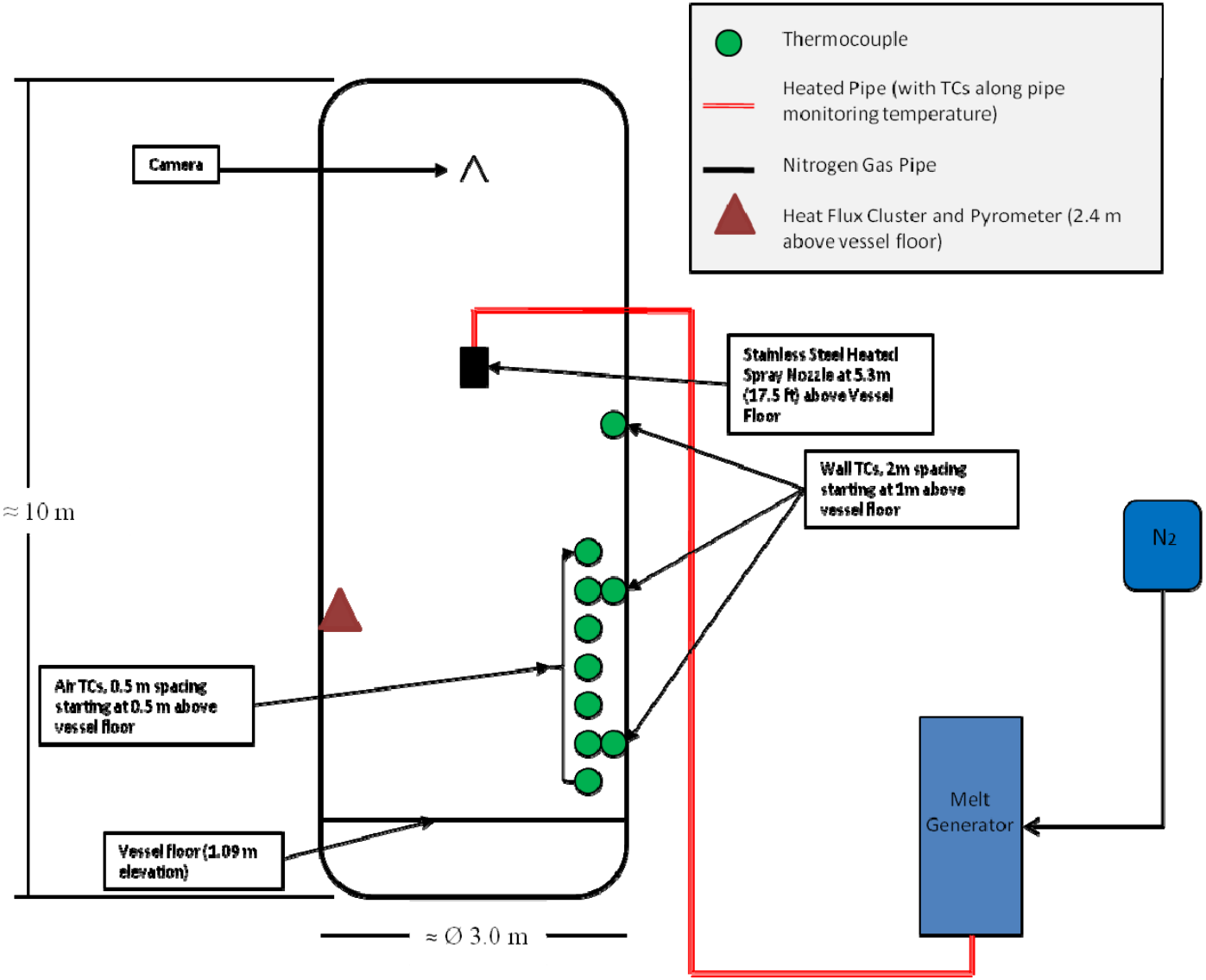

Figure 7-11: In-Vessel Sodium Spray Test Instrumentation Layout

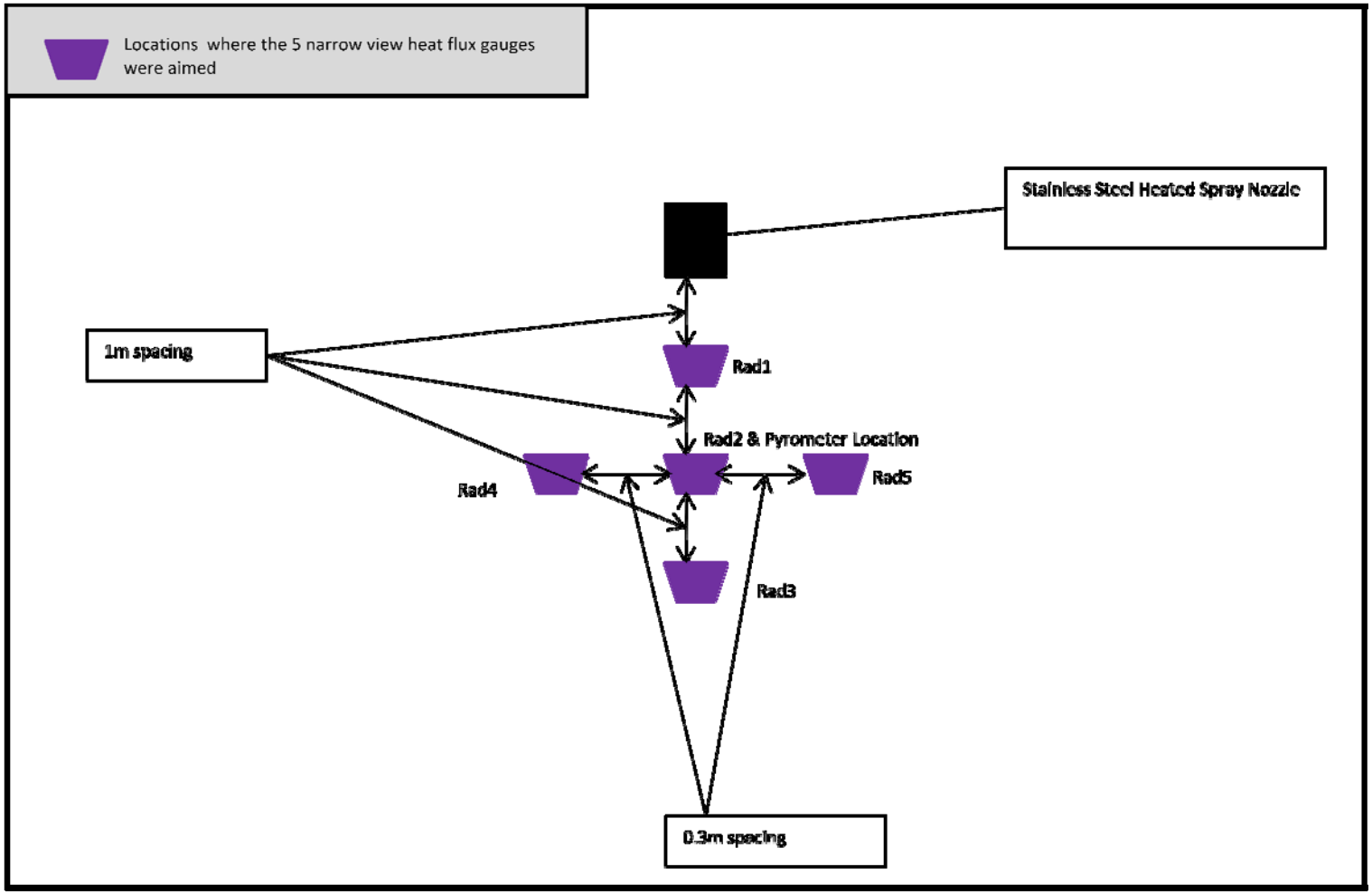

Figure 7-12: In-Vessel Sodium Spray Heat Flux Gauge Locations

7.3.2 Sodium In-Vessel Spray Test 3 Measured Data

This section displays the measured data from the first in-vessel sodium spray test (Test 3). For instrumentation locations and specifications referred to in the figures of this section please reference Section 7.3.1. The melt generator heaters broke during the beginning of this experiment so the test was performed with the sodium only at 200°C instead of the desired 500°C. This however in the end provided important comparisons for two sprays at different temperatures. The figures below are the actual measured experimental data.

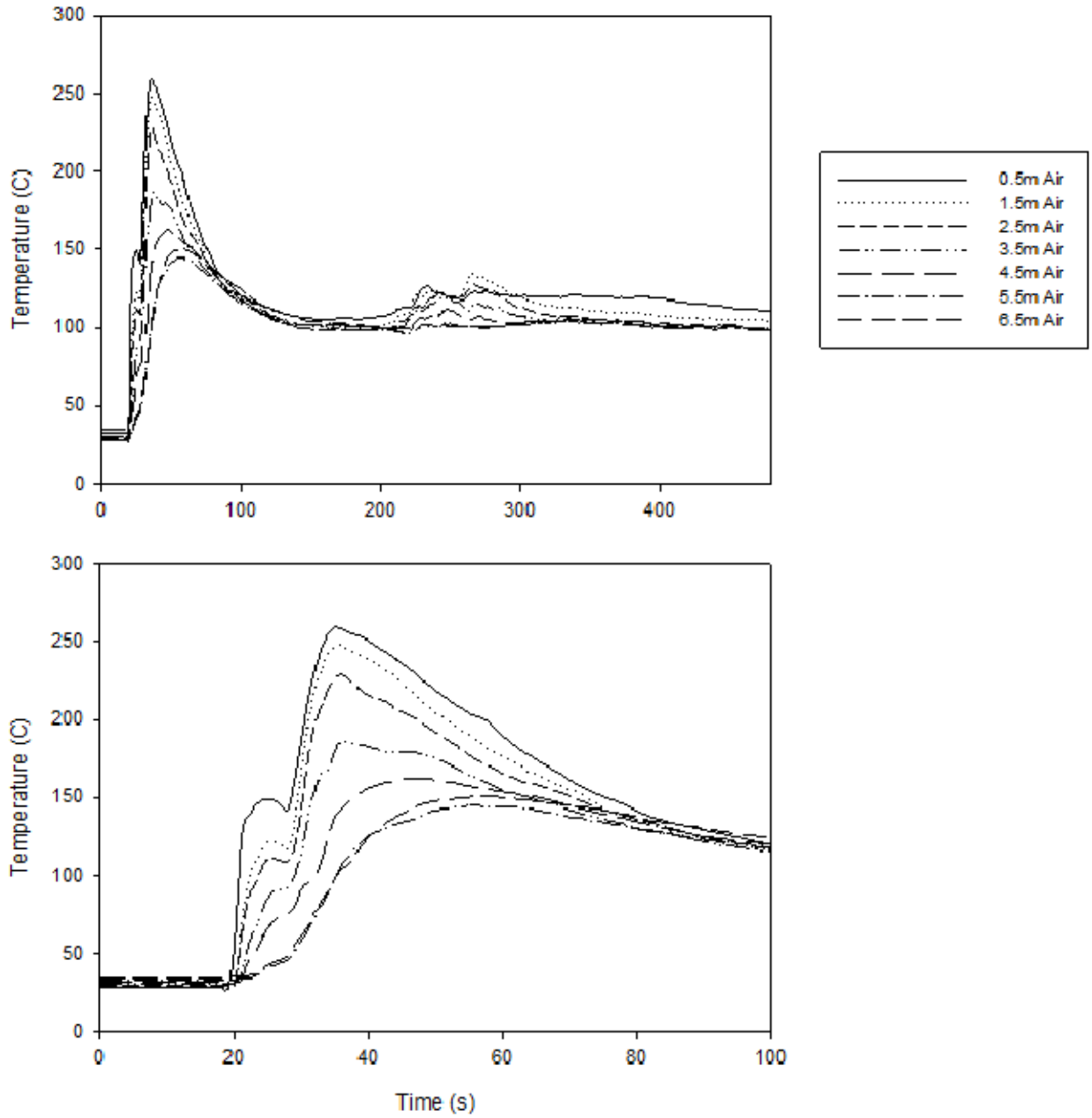

Figure 7-13: In-Vessel Sodium Spray Test 3, Air TC Rake Temperatures vs Time

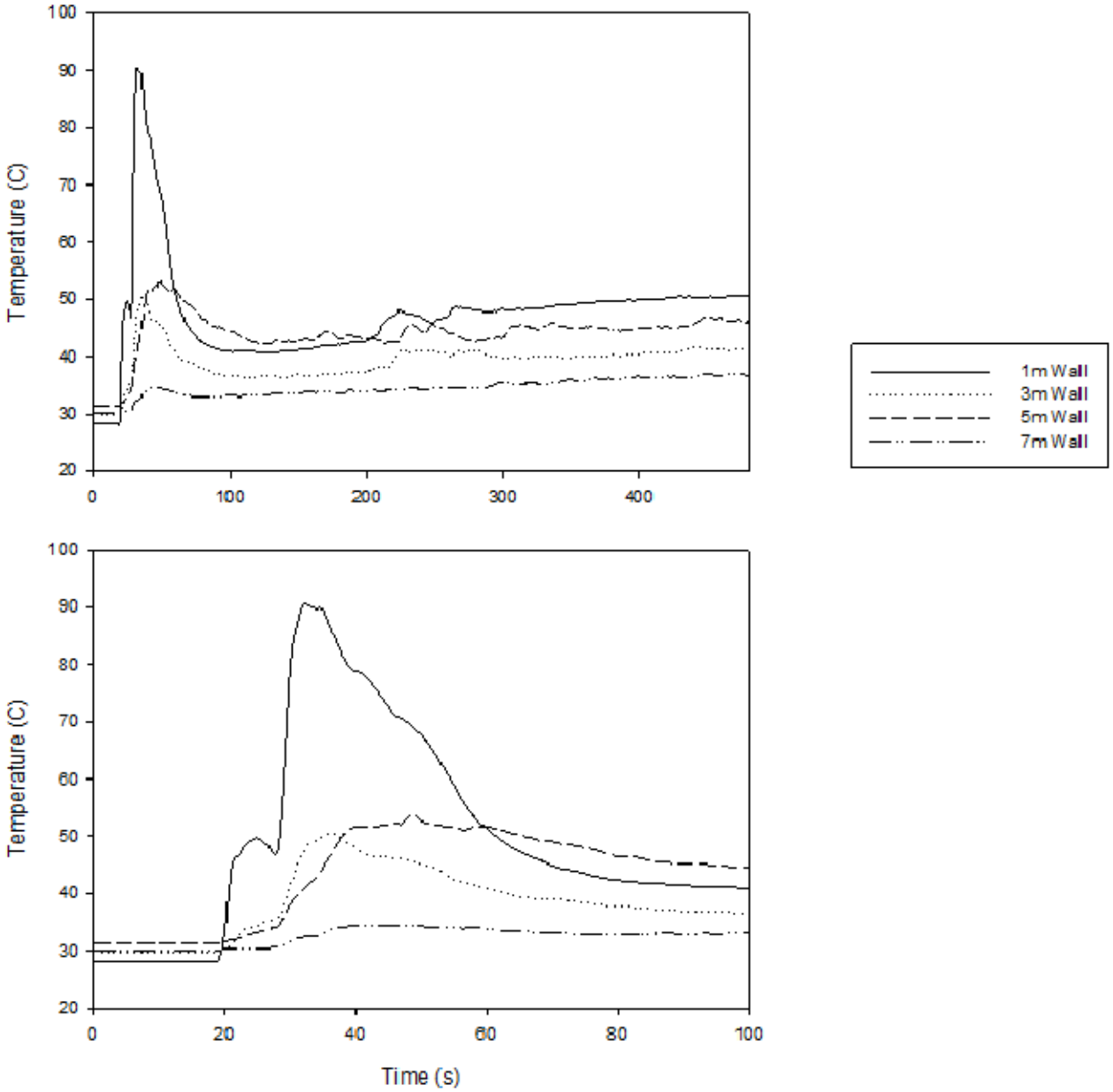

Figure 7-14: In-Vessel Sodium Spray Test 3, Wall TC Rake Temperatures vs Time

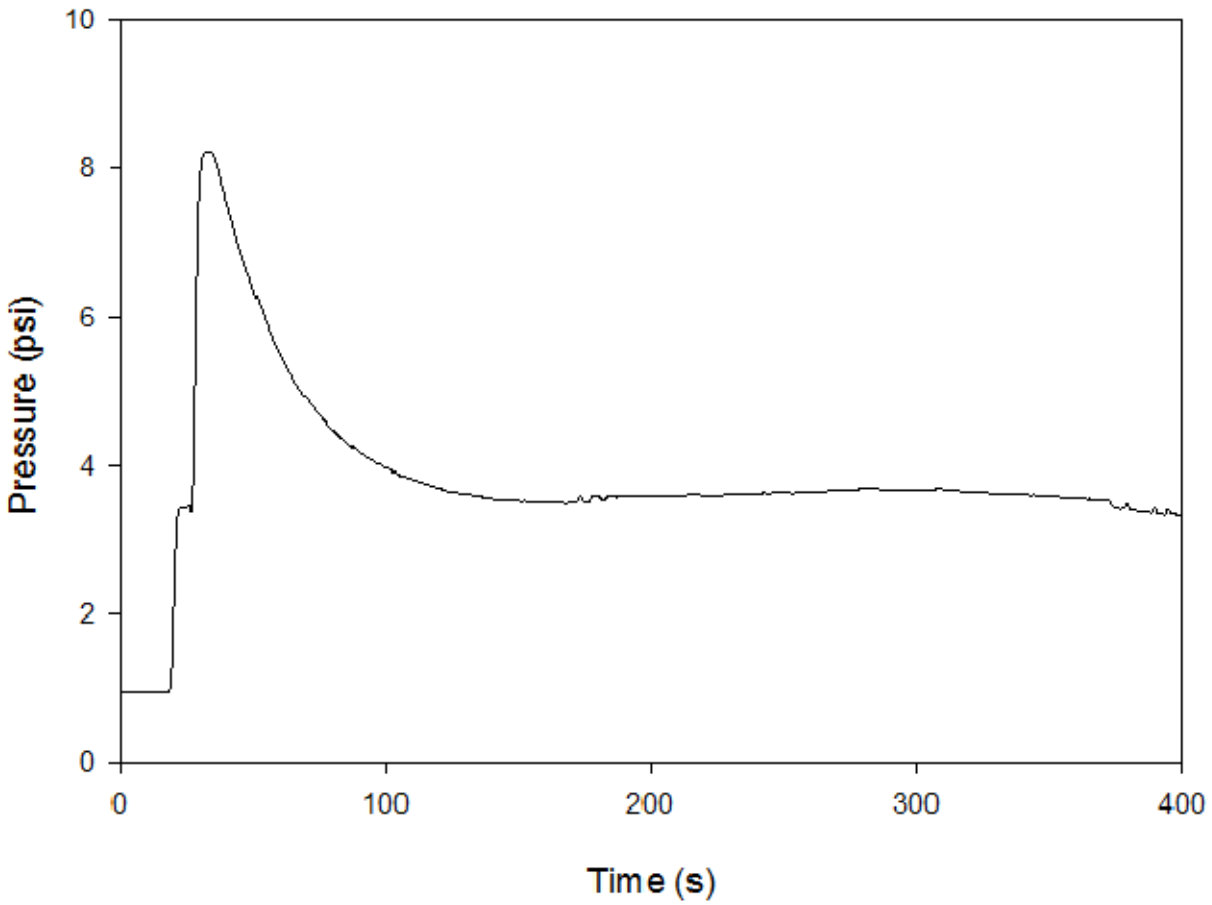

Figure 7-15: In-Vessel Sodium Spray Test 3, Vessel Pressure vs Time

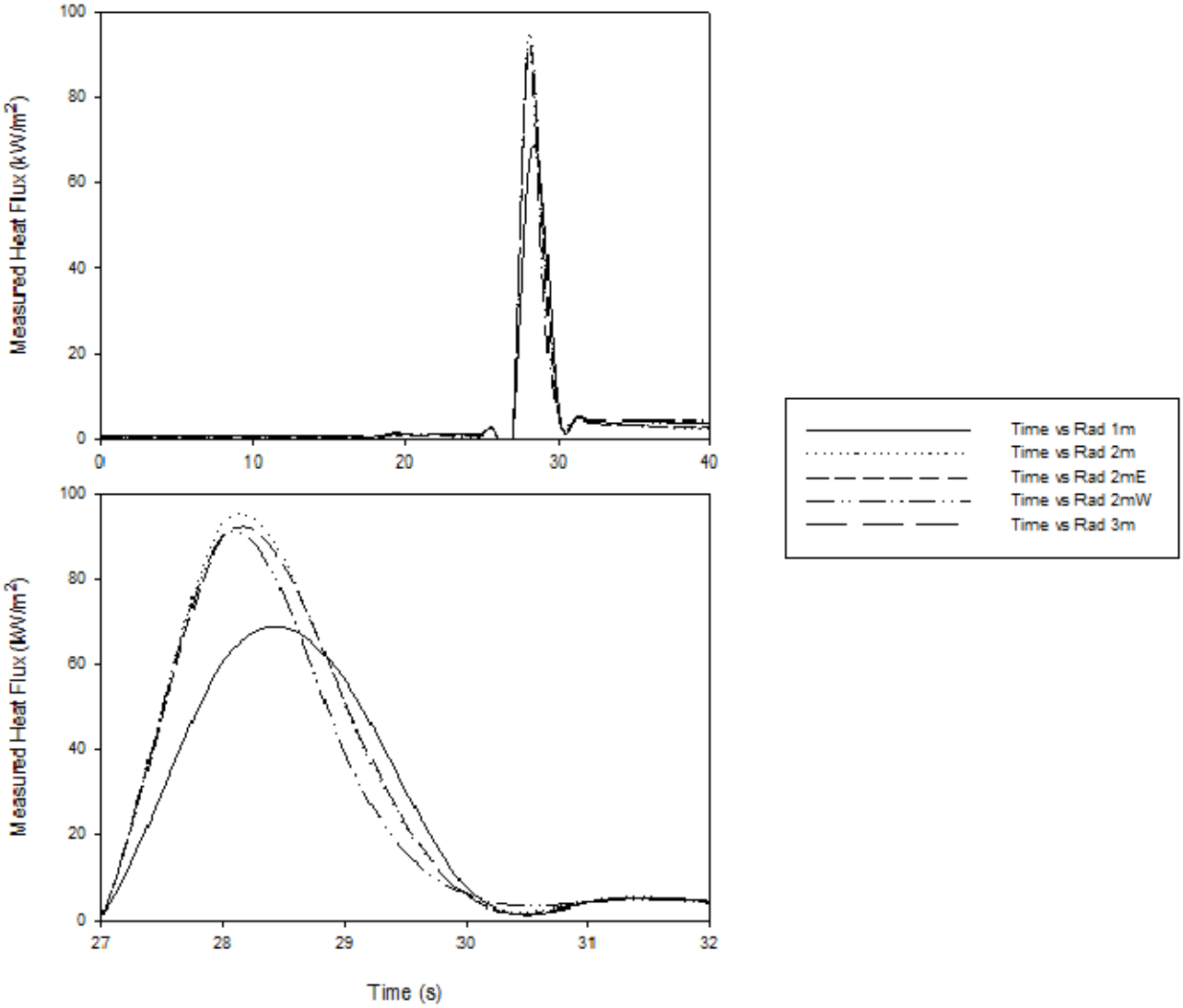

Figure 7-16: In-Vessel Sodium Spray Test 3, Measure Heat Flux (Narrow View Gauge) vs Time

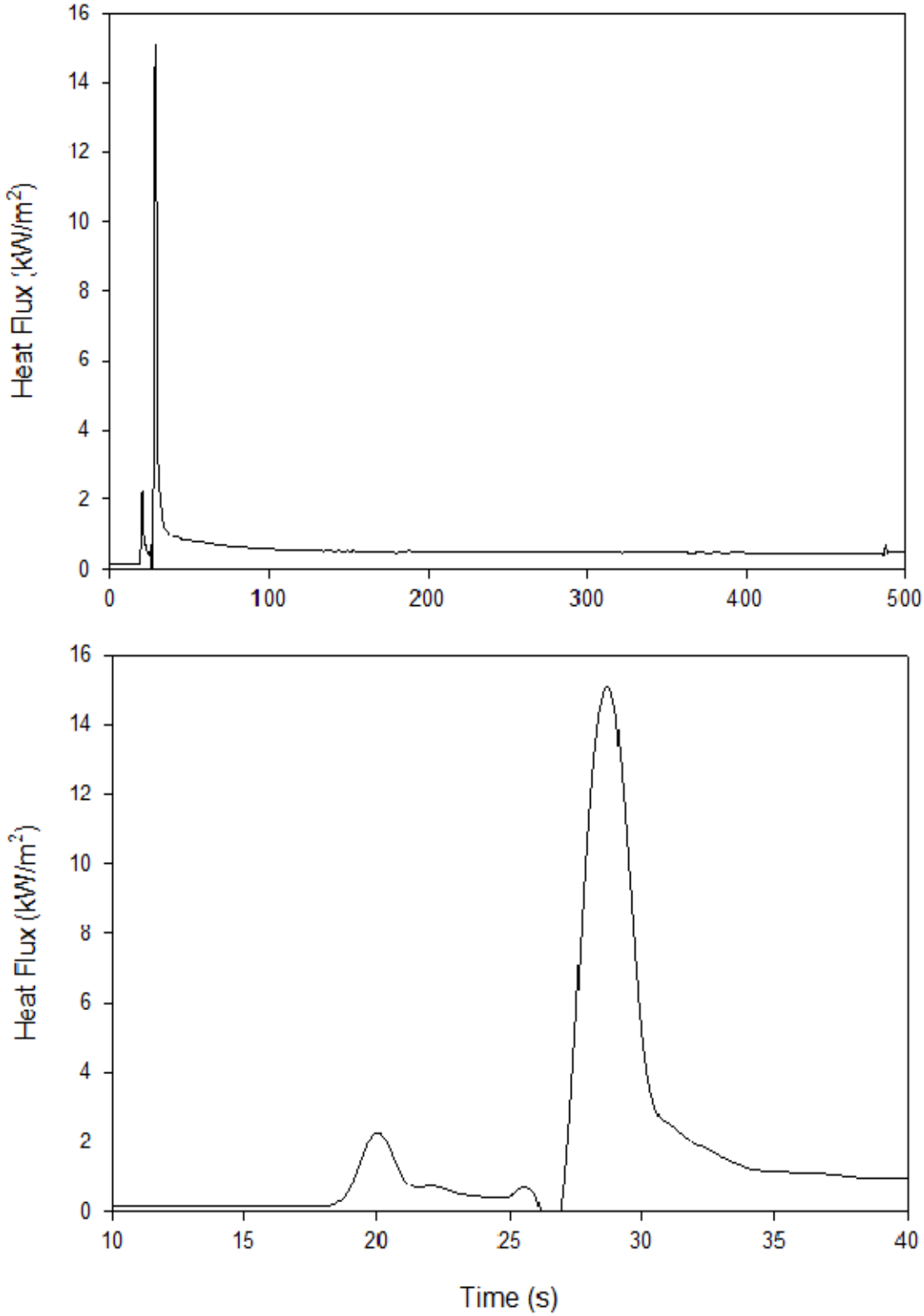

Figure 7-17: In-Vessel Sodium Spray Test 3, Measure Heat Flux (Wide View Gauge) vs Time

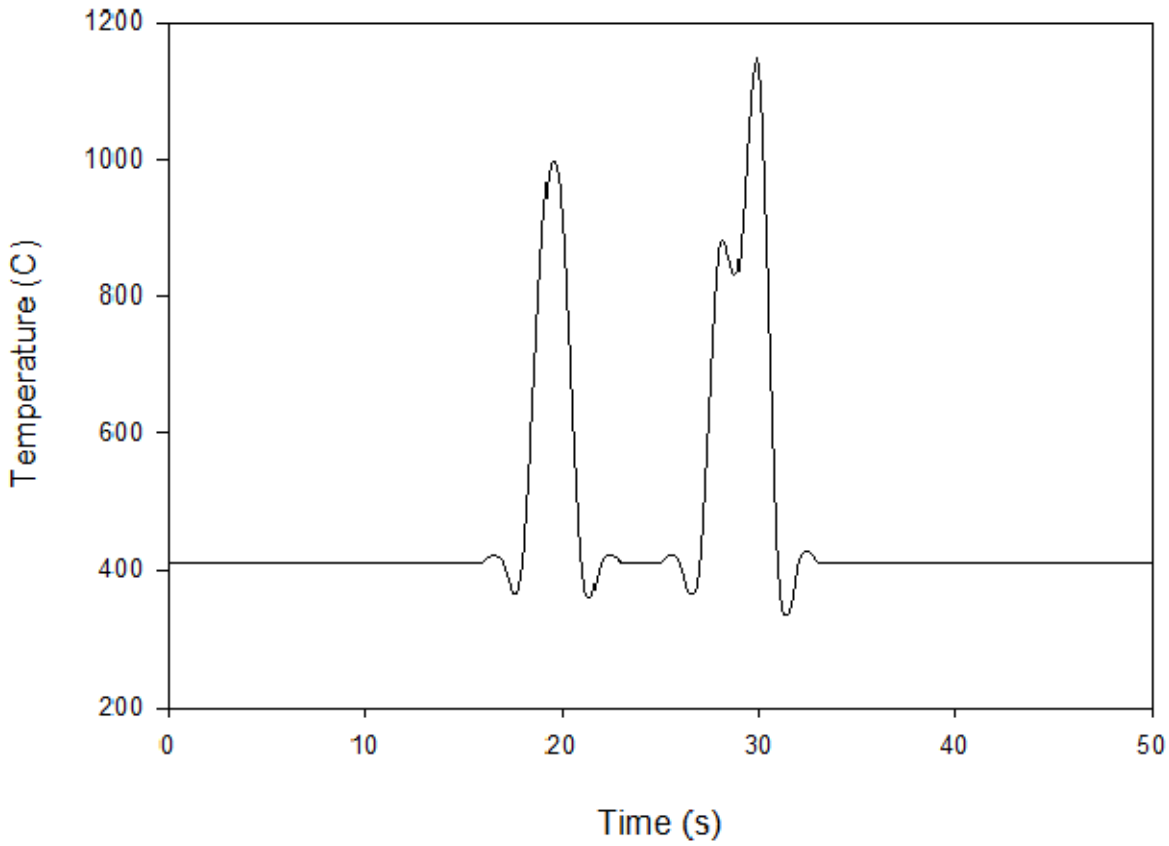

Figure 7-18: In-Vessel Sodium Spray Test 3, Measured Pyrometer Temperature vs Time

7.3.3 Sodium In-Vessel Spray Test 4 Measured Data

This section displays the measured data from the second in-vessel sodium spray test (Test 4). For instrumentation locations and specifications referred to in the figures of this section please reference Section 7.3.1. For this test one of the vessel ports failed at about 0.2MPa, there is still relevant data obtained from this test. Comparing the initial phase of the two sodium sprays at different temperatures is what the analysis has focused on. The figures below are the actual measured experimental data.

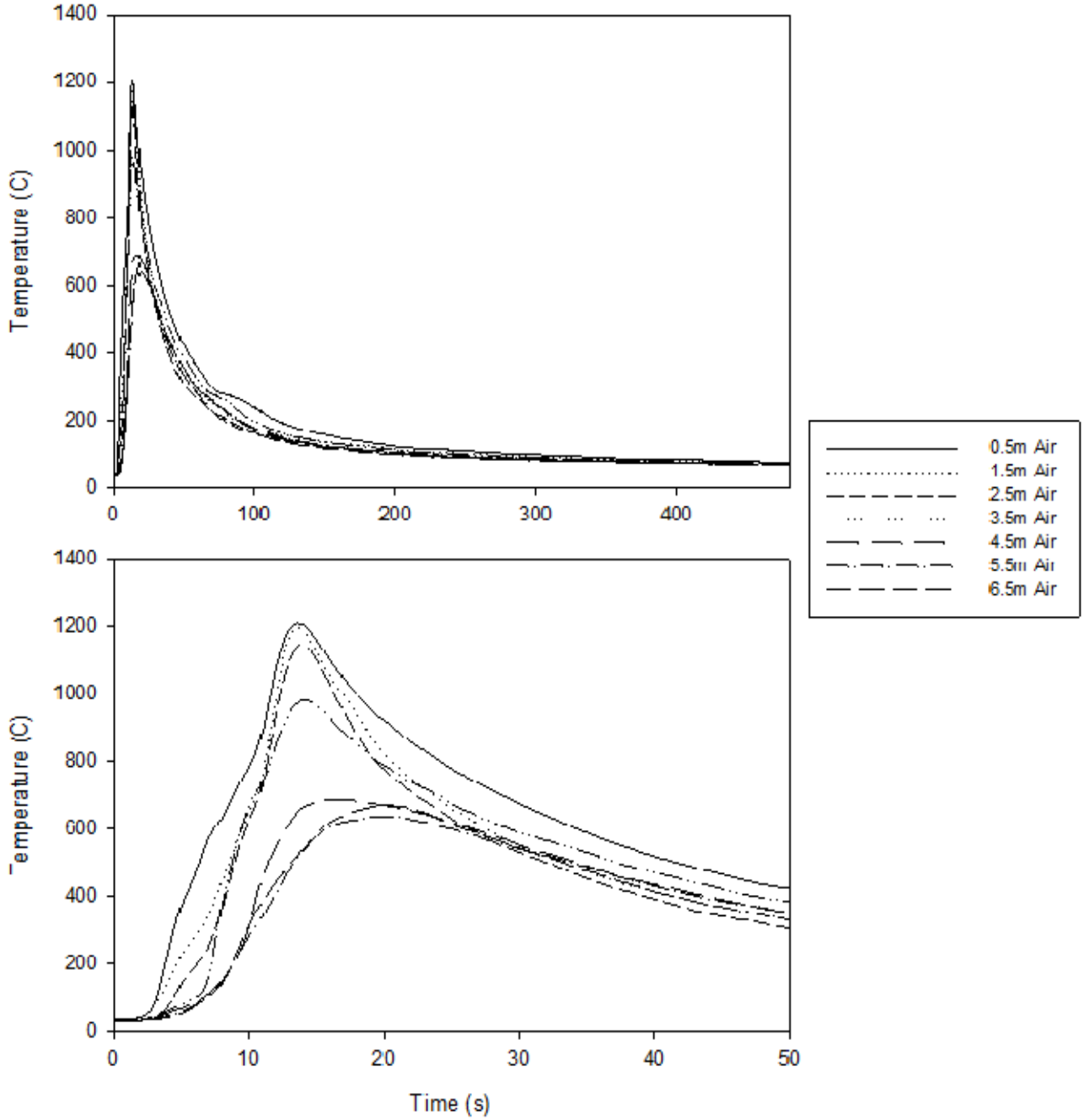

Figure 7-19: In-Vessel Sodium Spray Test 4, Air TC Rake Temperatures vs Time

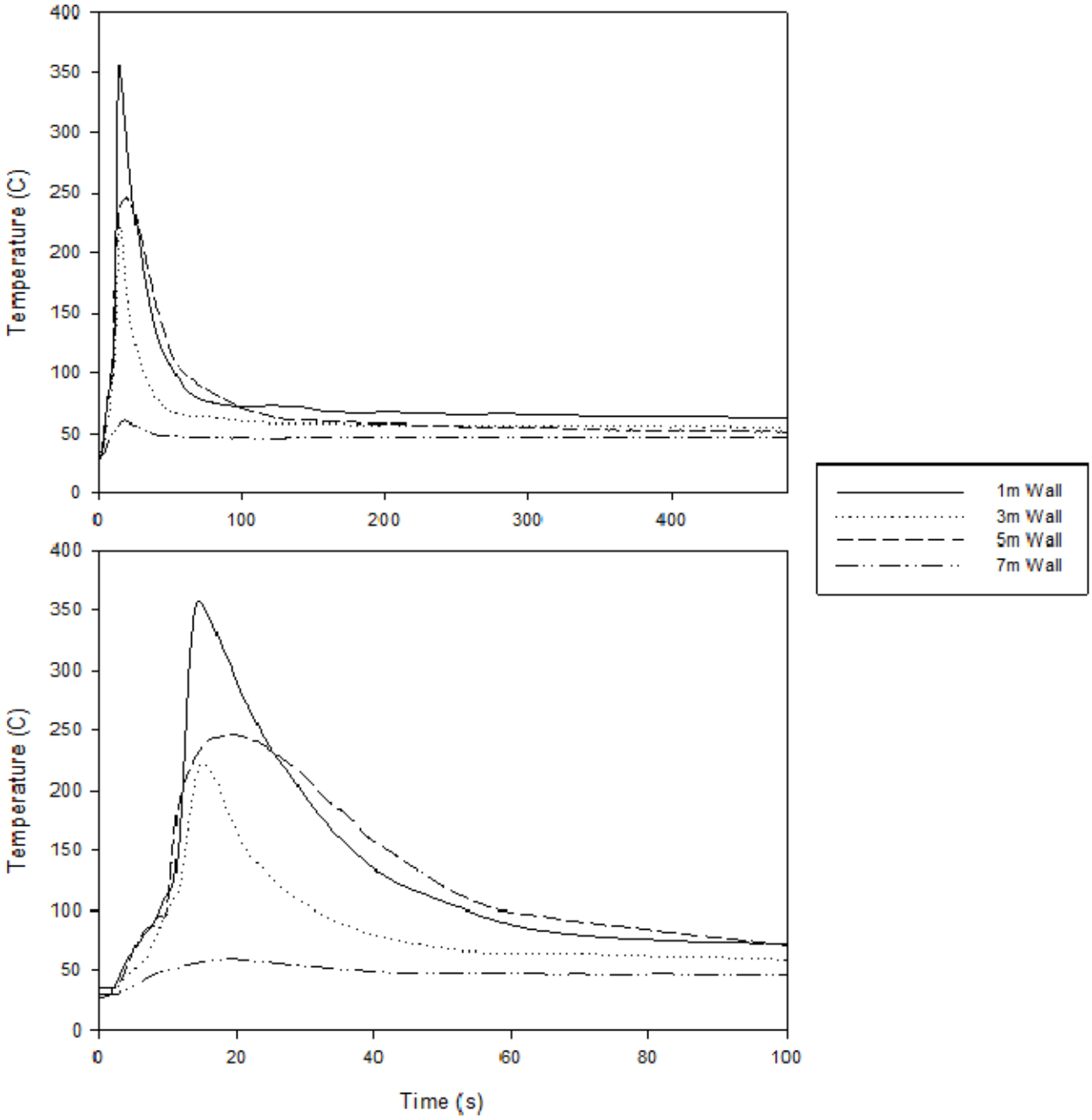

Figure 7-20: In-Vessel Sodium Spray Test 4, Wall TC Rake Temperatures vs Time

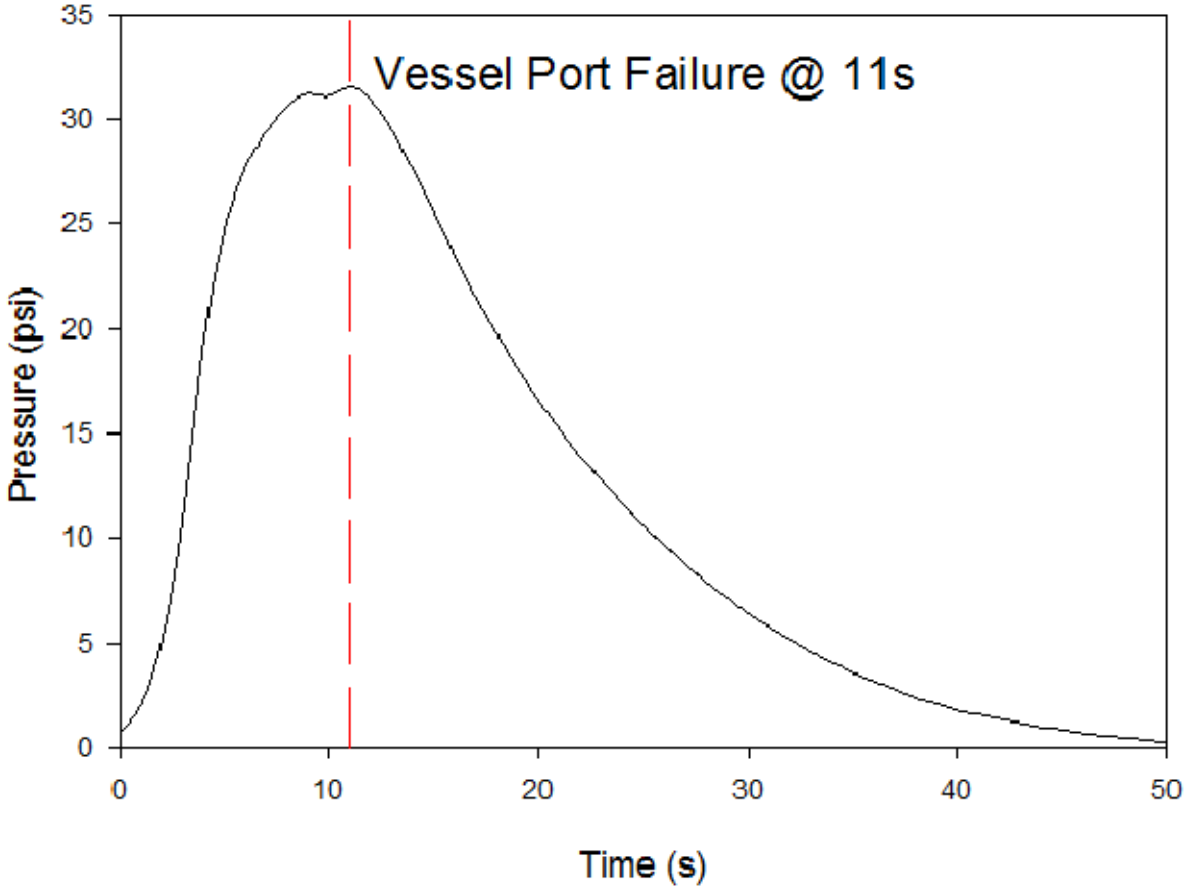

Figure 7-21: In-Vessel Sodium Spray Test 4, Vessel Pressure vs Time

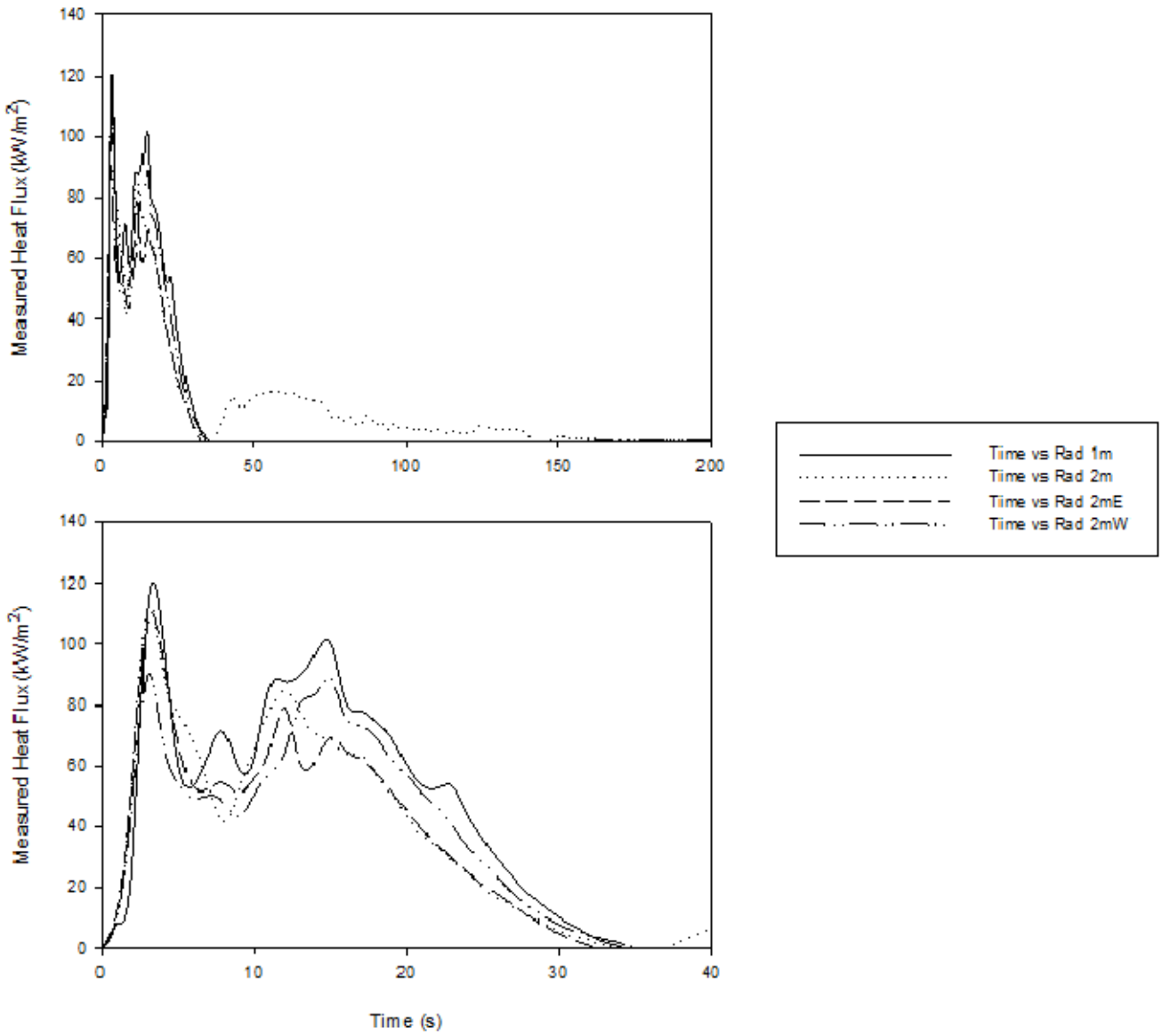

Figure 7-22: In-Vessel Sodium Spray Test 4, Measure Heat Flux (Narrow View Gauge) vs Time

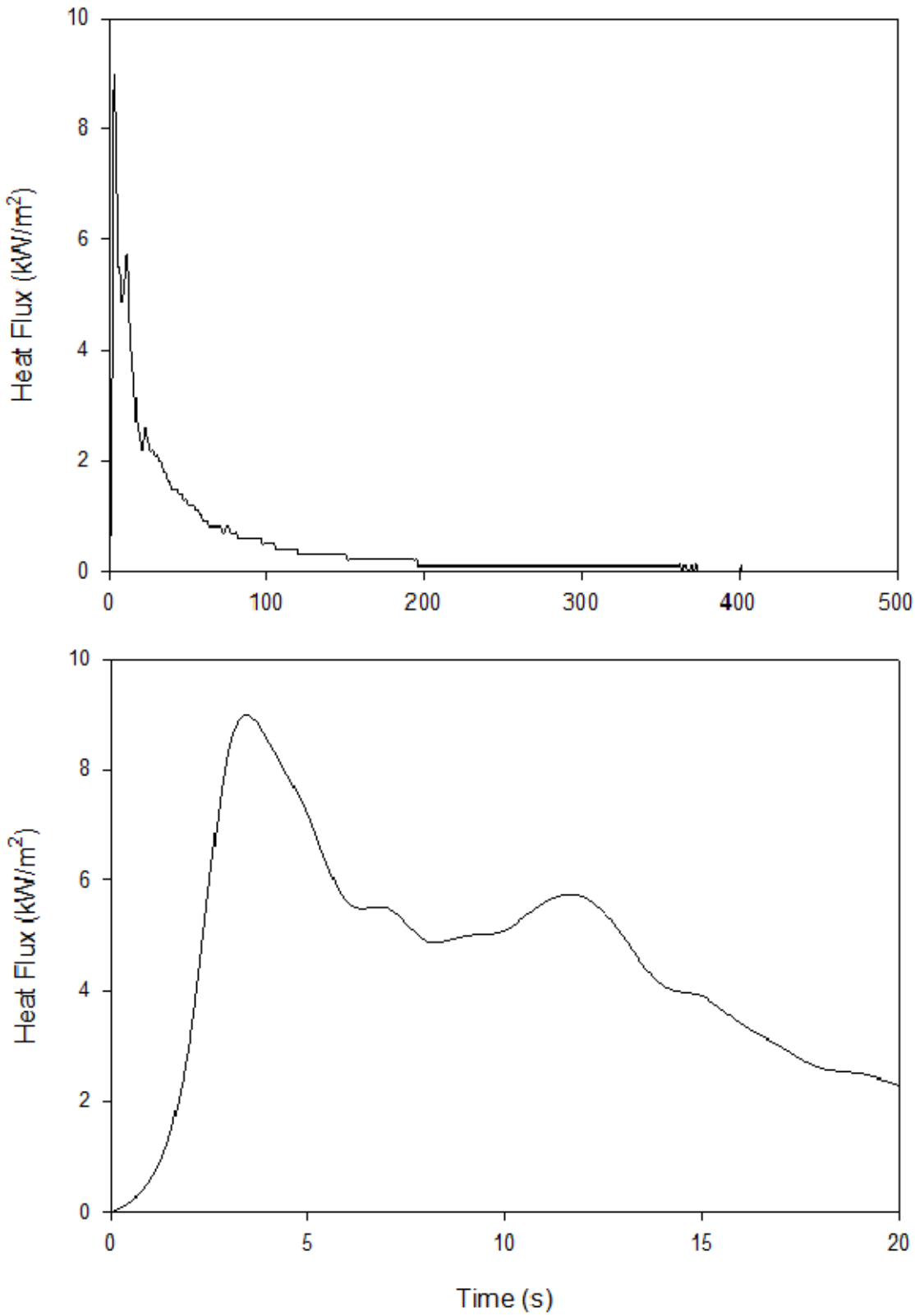

Figure 7-23: In-Vessel Sodium Spray Test 4, Measure Heat Flux (Wide View Gauge) vs Time

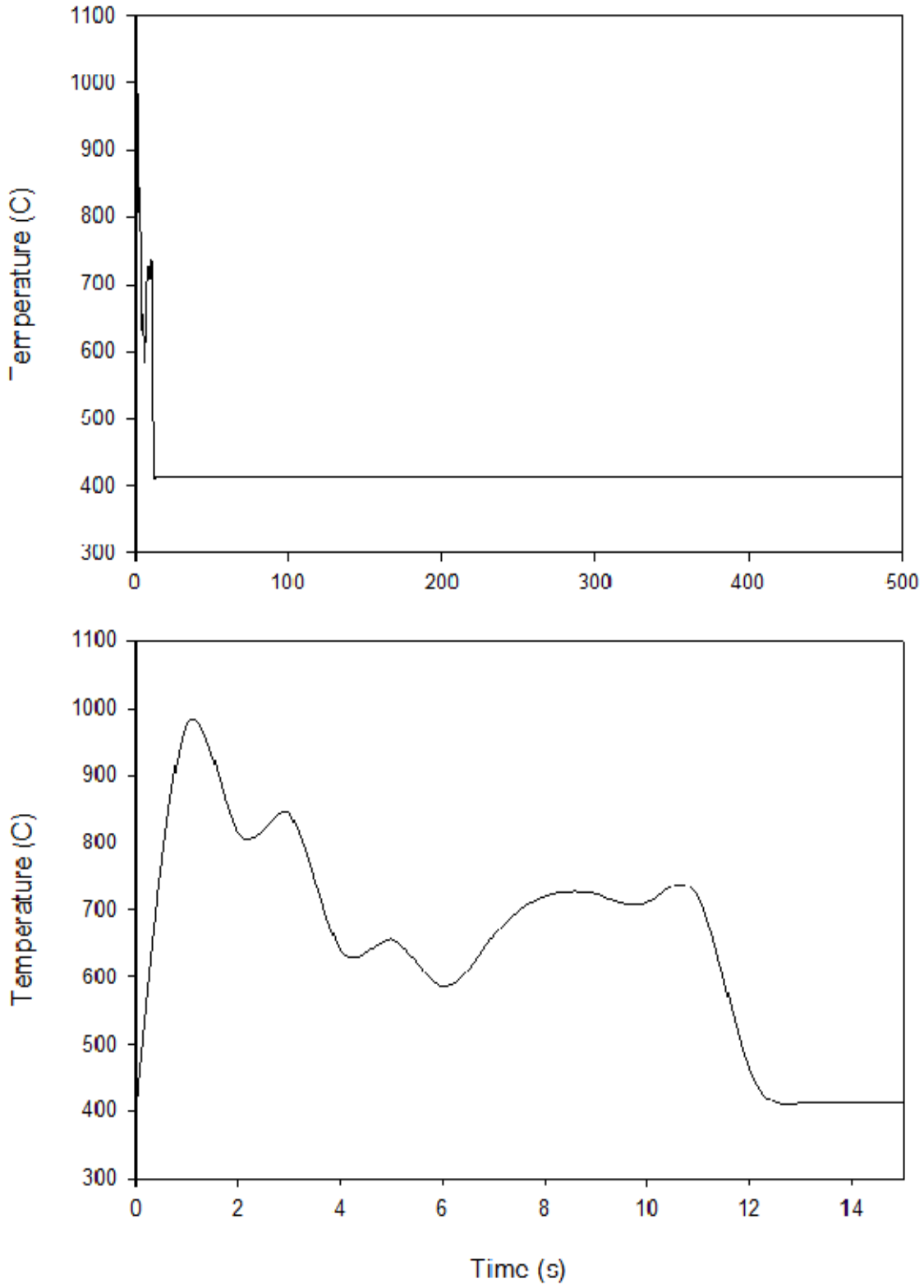

Figure 7-24: In-Vessel Sodium Spray Test 4, Measured Pyrometer Temperature vs Time

7.4 References

[1] *Laboratory Test Report. Test Number 2005T17 and 2009T17.* 2009, Spray Analysis and Research Services, Spray Systems Co.

8 APPENDIX B: SODIUM POOL FIRE TEST SETUP AND EXPERIMENTAL DATA

This Appendix focuses on the sodium pool fire tests. There were initially 4 outdoor sodium pool burns when the focus of the research brought on 6 more outdoor pool tests. These 10 sodium pool burns investigated the concept of quenching the sodium fire on a stainless steel surface. The results from these experiments have been used to develop a sodium pool burning computational model and used for inverse heat transfer calculations. Again the overall objectives of these pool fire tests were performed to obtain a fundamental understanding for sodium pool combustion as well as advancing the current state of knowledge at SNL. This included investigated the burning rates and heat transfer characteristics of cooled sodium pools. Below is a detailed explanation of the setup and instrumentation used during the sodium pool fire experiments and the data obtained specific to each sodium pool tests.

8.1 Overview of the Outdoor Sodium Pool Fire Test Setup

A total of 10 sodium pool tests were performed. A summary of these tests can be found in Table 8-1. The theory behind these tests was to investigate whether the pool would burn or quench by varying the sodium liquid thickness to that of the stainless steel pan thickness. Depending on this ratio a different equilibrium temperature would be reached which results in two categories of sodium pool burning. This will be explained in more detail in the data analysis section.
To perform these experiments, solid sodium was melted to 500°C inside an inert chamber. This sodium was carried through heat pipes (1.3 cm in diameter) and discharge from an orifice approximately 30 cm above the burn pan surface. As mentioned before the details are in Table 8-1 and all the tests sidewall thickness was 3.175 mm (0.125 in). These tests were performed outdoors. The next section describes the instrumentation setup to measure significant variables during these experiments.

Test Number	diameter of pan (m)	height of pan (m)	mass sodium (kg)	base steel thickness (mm)	Melt Generator Pressure at System Dump Time (psi)	average peak temperature at bottom of pan (deg C)	thickness ratio (liquid sodium/stainless steel)
Pool 1	0.6	0.0508	2.6	15.875	2.6	320	0.7
Pool 2	0.6	0.0508	2.6	15.875	2.2	320	0.7
Pool 3	0.3	0.127	4.4	6.35	2.4	800	11.5
Pool 4	0.2	0.1778	1.0	6.35	2.5	780	5.9
Pool 6	0.6	0.0508	4.8	15.875	3.2	480	1.3
Pool 7	0.6	0.0508	7.8	15.875	3.4	600	2.0
Pool 8	0.6	0.0508	1.6	15.875	3.6	220	0.4
Pool 9	0.6	0.0508	6.0	15.875	3.6	490	1.6
Pool 10	0.6	0.1016	11.6	15.875	3.2	746	3.0
Pool 11	0.6	0.1016	9.6	15.875	3.9	648	2.5

Table 8-1: Sodium Pool Test Summary

8.2 Outdoor Sodium Pool Fire Test Instrumentation

This section will present the instrumentation used for the outdoor sodium pool fire testing. Figure 8-1 displays the setup for the outdoor sodium pool experiments. The most significant variables to be measured and the instrumentation for the sodium pool fire experiments are described below.

1. Mass flow of Na discharged into Surtsey

Load cells on the melt generator obtained a transient mass flow rate into the vessel, with a range of 0-500lbs. The specified accuracy from the manufacturer for the scale is less than ± 0.03 percent at full-scale output (FSO).

2. Melt generator pressure

For the melt generator pressure both a low pressure and high pressure transducer were used. Depending on the test specifications both transducers were used throughout different parts of the test series. A calibrated low pressure transducer with a range of 0-100 psi was used. The specified accuracy from the manufacturer for the pressure transducer is less than ± 0.25 percent at full-scale output. A calibrated high pressure transducer with a range of 0-500 psi was used. The specified accuracy from the manufacturer for the pressure transducer is less than ± 0.25 percent at full-scale output.

3. Pour Pan Temperature

Type-K TCs were installed at the bottom of the tests pans. For the first 4 the TCs on the bottom of the pan were located at center, half radius and full radius (6.35 mm (1/4 in) from sidewall) at 4 locations 90 degrees apart (Figure 8-2). For tests 6-11 the TCs on the bottom of the pan were located at center, 1/3 radius, 2/3 radius, and full radius (6.35 mm (1/4 in) from sidewall) at 8 locations 45 degrees (starting at 0 degrees) (Figure 8-3). For tests 8 through 11 the 1/3 radius TCs were 4 locations every 90 degrees apart (TC5, TC11, TC17, and TC23 were excluded). The side wall TCs are the same for all tests, and they were located at bottom just above the bottom plate, half height, and full height at 2 locations 90 degrees apart. The bottom and side of the pan were insulated with 4 inch Duraboard and 3 inches Durablanket insulation respectively.

For Pool Tests 6-11 there were type-K TCs added inside the top part of the pan at 0° at center, half radius and full radius (6.35 mm (1/4 in) from the edge of the pan) as shown **Figure 8-4**.There was also a TC rake added 0.1 m (4 in) off center inside the pan to obtain liquid temperatures while the experiment was taking place (details show in Table 8-3 and **Figure 8-4**). Note that in Section 8.5, only the rake TCs that survived the test are shown in the figures. There were problems with these TCs being able to handle the hot, corrosive environment.

The temperature range of all the TCs is from 273 K to 1533 K. The maximum error using the manufacturer's calibration is ±25.9 K with a 0.9-s time constant. The TC location for each burn pan will be center, half and full along the diameter of the bottom of the pan (9 total). For the pan walls there will be thermocouples at center, half, and full along the height of the pan at two locations 90 degrees apart (6 total).

For Pool Tests 6-11, a pyrometer similar to type 11x30, Ircon Inc., Niles, IL was located outside the vessel and focused through a window into the Surtsey vessel. The optical pyrometer had a response time of 1.5 ms to 95 percent of its full range. A low-to-mid range signal conditioner was installed on the 11x30 pyrometer to yield temperature measurements between 1323 K and 1773 K with a specified accuracy of 1% of the full-scale temperature. In a transient event, the accuracy of the pyrometer measurement is expected to be no better than ±25 K.

Infrared data was acquired using FLIR System TM model S-60 infra-red camera. This camera has a 640 x 480 pixel array, measures temperature form -40ºC to 1500ºC and is sensitive to the wavelength band of 7.5 -13 micrometers.

4. Heat Flux

For the first four Pool Tests (1-4) a narrow-angle and a total heat flux gauge was setup to measure the radiation intensity at the edge of the catch pan. The pair of gauges, a narrow-angle heat flux gauge (Medtherm model NVRW-15-5-360-2183, 5º view angle) and a total heat flux gauge (Medtherm model 64-2-18 with a view angle of 180º) were be mounted together at a horizontal distance of approximately 2.3 m (7.5 ft) from the pool centerline at a height of 2.3 m (7.5 ft). All of the heat flux gauges are water-cooled. The radiative heat flux measured by the narrow angle radiometers and total heat flux gauges have a manufacturer's stated uncertainty of ±3%.

For Pool Tests 6 through 11, five narrow-angle gauges (Medtherm model NVRW-15-5-360-2183, 5º view angle) were used. The gauges were setup with a horizontal distance of 2.3 m (7.5 ft) from the center of the burn pan. The narrow view gauges were aimed along the pan's 0.10 m (4 in) radius at 0°, 90°, 180°, 270° as well as the center of the pan (shown in Figure 8-). The diagonal distances for each gauged and its target point were measured and recorded for each test as shown in Table 8-1.

5. Visual

Three high-resolution color video cameras were installed with views from the east, west, and above the large catch pan for Pool Tests 1 through 4. For tests 6 through 11, one high speed black and white camera and one high definition color camera were focused on a mirror looking down at the surface of the sodium pool. These two cameras were used to estimate ignition time, pool spreading rate, when the fire went out, and to obtain visual stills of the unmanned experiment. Also for tests 6 through 11, there was a high definition camera view from the east looking at the entire catch pan to see the smoke plume formation.

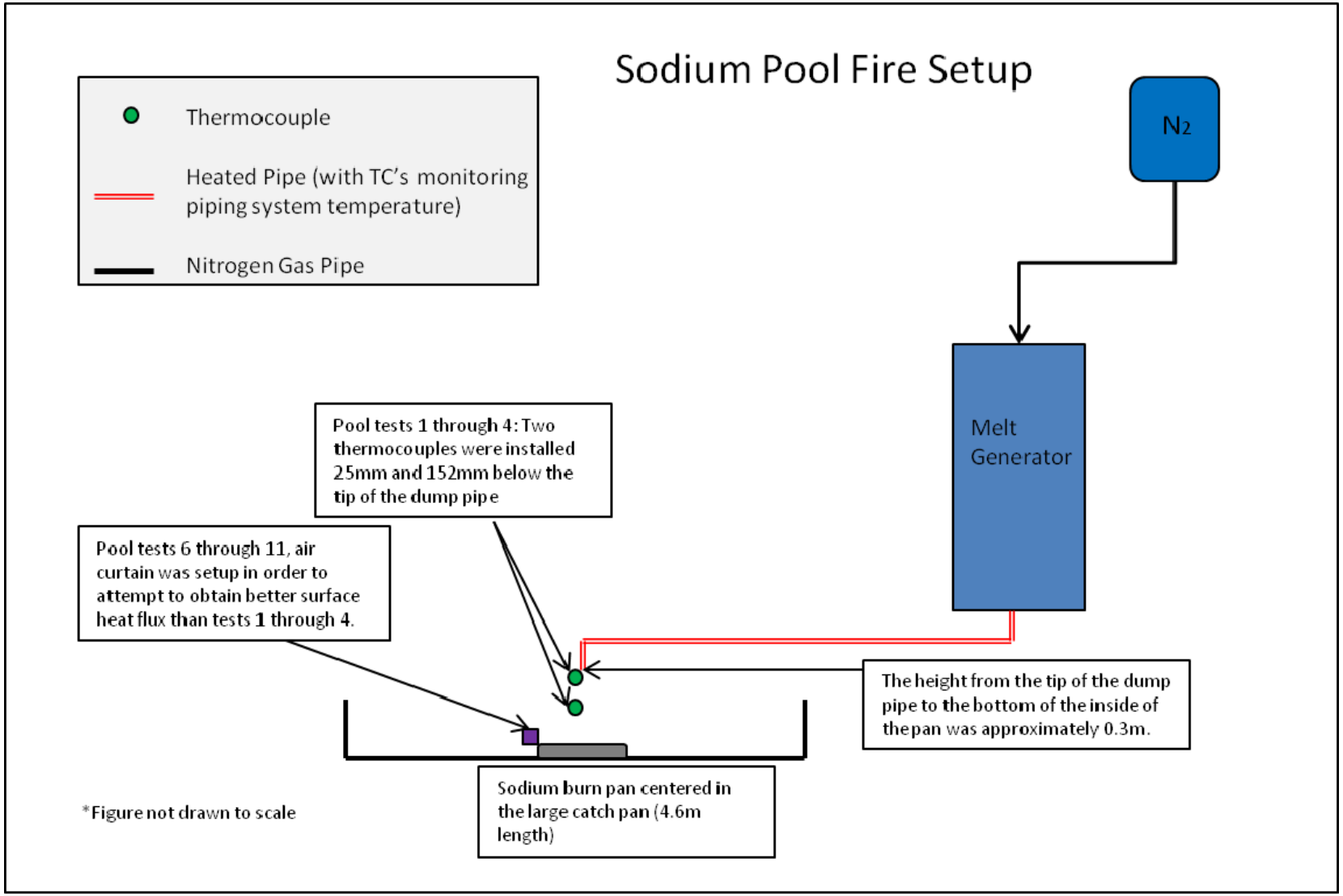

Figure 8-1: Outdoor Sodium Pool Fire Tests Instrumentation Setup

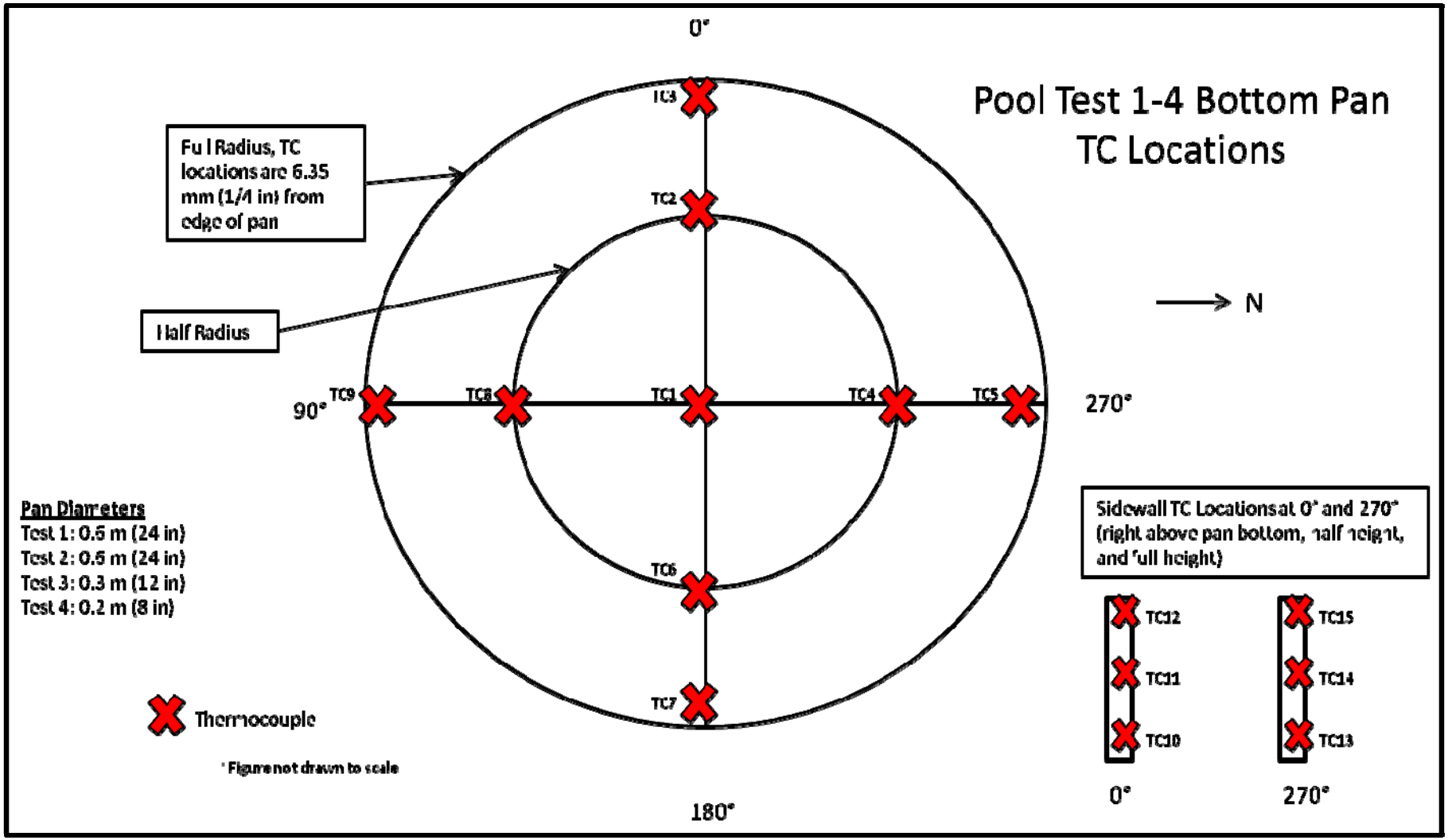

Figure 8-2: Outdoor Sodium Pool Fire Tests 1-4 Pan Bottom TC Locations

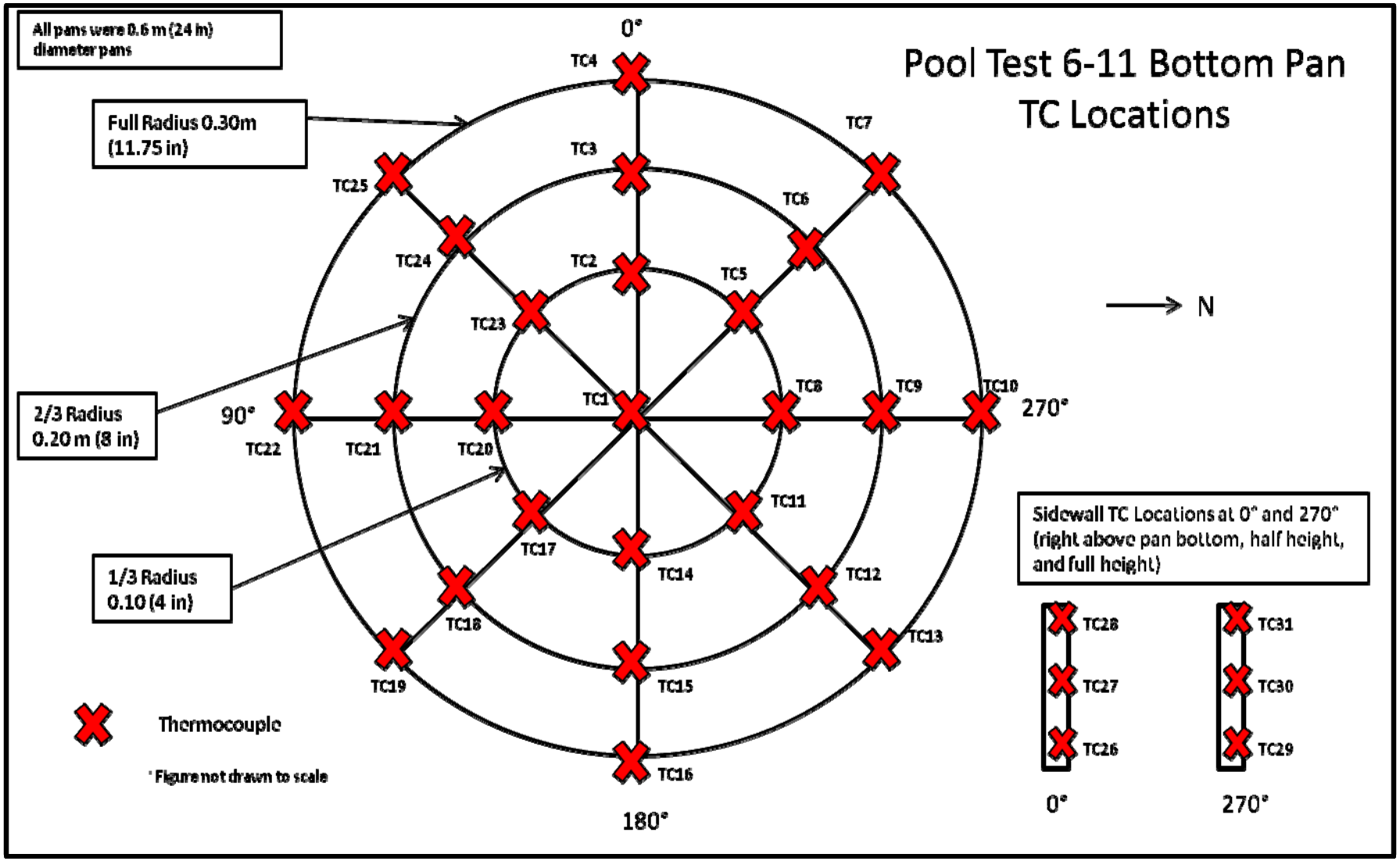

Figure 8-3: Outdoor Sodium Pool Fire Tests 6-11 Pan Bottom TC Locations

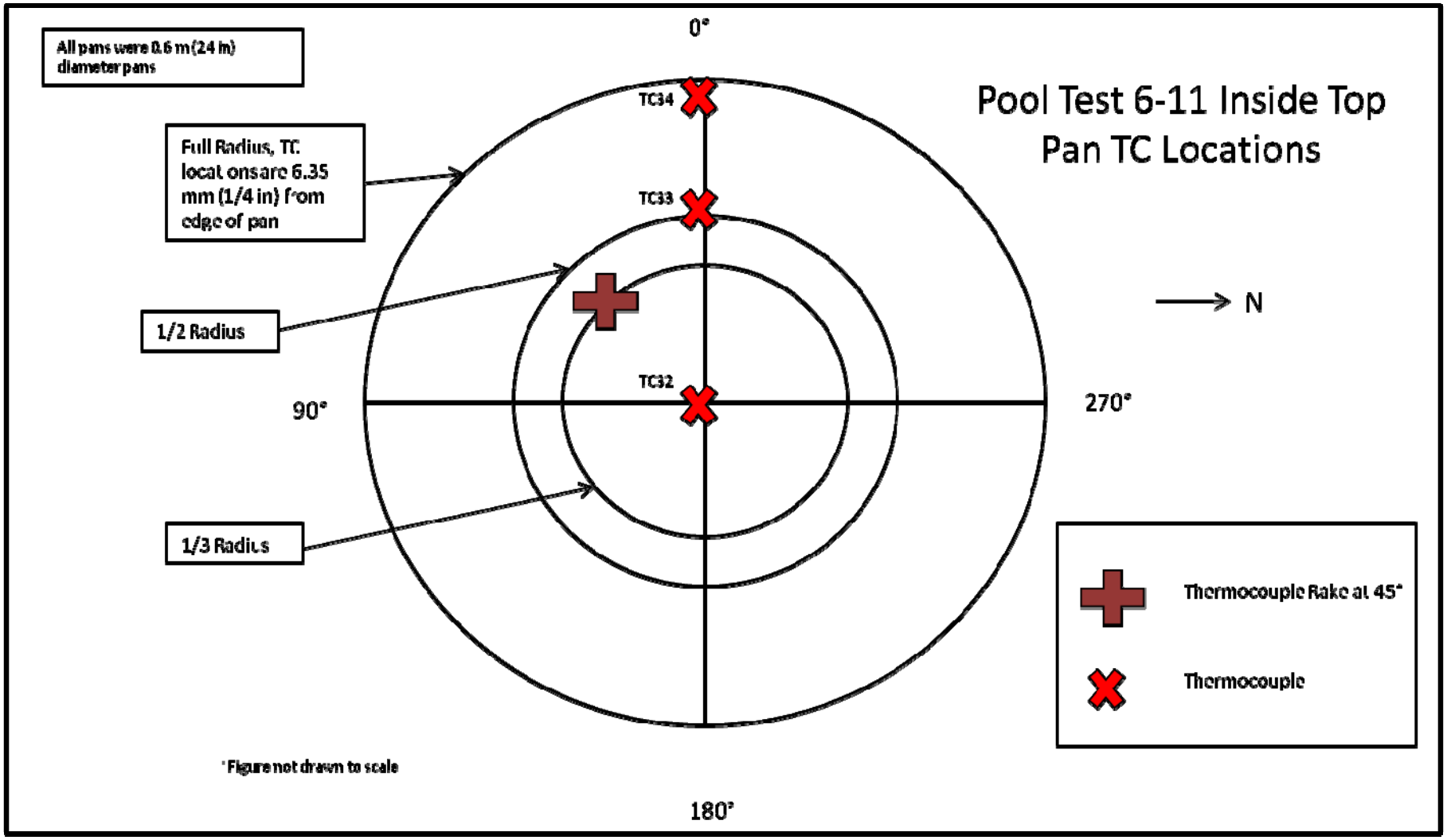

Figure 8-4: Outdoor Sodium Pool Fire Tests 6-11 Inside Top Pan TC Locations

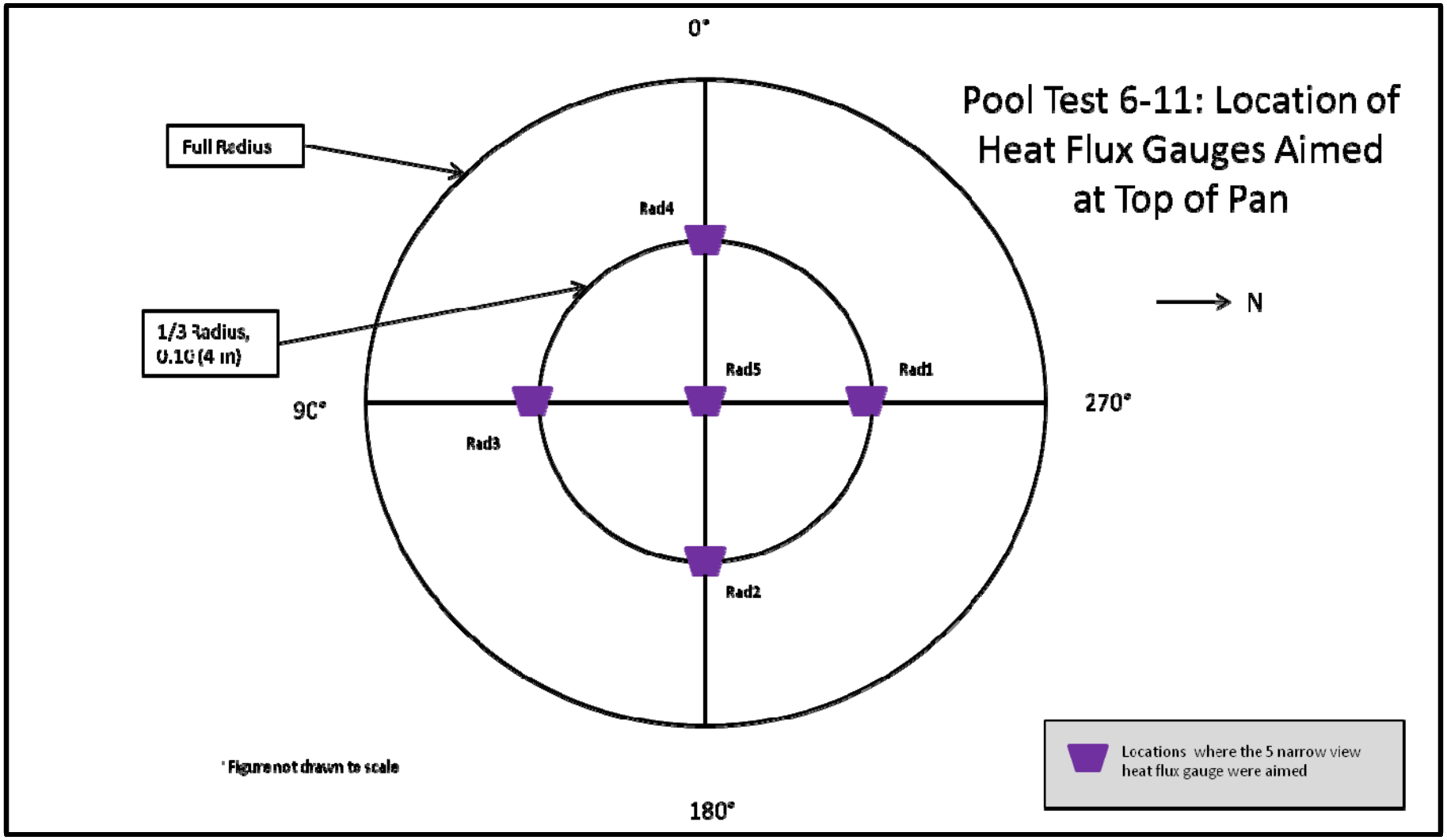

Figure 8-6: Outdoor Sodium Pool Fire Tests 5-11 Locations of Heat Flux Gauges Aimed at Top of Pan

Measured Diagonal Distance from Heat Flux Gauges, Pyrometer, and IR Camera to Aimed Location in Pan							
Test Number	Rad 1 (m)	Rad 2 (m)	Rad 3 (m)	Rad 4 (m)	Rad 5 (m)	Pyrometer	IR Camera
Pool 6	2.4	2.5	2.6	2.8	2.9	2.9	2.9
Pool 7	2.3	2.6	2.6	2.9	2.9	2.9	2.9
Pool 8	2.4	2.5	2.6	2.8	2.9	2.7	2.8
Pool 9	2.5	2.5	2.6	2.8	2.9	2.7	2.7
Pool 10	2.5	2.5	2.6	2.8	2.9	3.0	2.8
Pool 11	2.5	2.4	2.6	2.9	2.8	3.0	2.8

Table 8-2: Measured Distances for Instrumentation for Outdoor Pool Tests 6-11

Sodium Pool Test	TC Spacing	Number of TCs, note TC1starts at the spacing above the pan
1,2,3,4	N/A	N/A
5	3.175mm (0.125 in)	6.0
6	3.175mm (0.125 in)	6.0
7	3.175mm (0.125 in)	8.0
8	3.175mm (0.125 in)	4.0
9	3.175mm (0.125 in)	8.0
10	6.35mm (0.25 in)	15.0
11	6.35mm (0.25 in)	15.0

Table 8-3: Inside Test Pan Rake (0.1 m (4 in) from center) TC Details

8.3 Sodium Melt Generator

The melt generator is a stainless steel pressure vessel designed to hold 36 kg of Na (150% of the theoretical amount for complete combustion), yielding a liquid volume of about 0.039 m3 (1.37 ft3), based on the density of 0.968 g-cm3. Assuming the generator is designed to have the same amount of free gas space, the melt generator empty volume is about 0.078 m3 (2.75 ft3).
The vessel was wrapped with heat tape and insulation capable of bring the melt to a temperature of 500°C within a reasonable amount of time. Stainless steel tubing (1.27 cm, 0.5 inch diameter) connects the melt generator to the vessel, either directly to the burn pan or to a stainless steel spray nozzle. All tubing and components through which liquid sodium passed through was wrapped in heat tape, insulated, and brought to the same temperature as the melt to prevent freezing in the lines.

To perform an experiment, solid sodium was placed in the melt generator via the top head. After loading and securing the head, the vessel was be purged with nitrogen. Nitrogen gas was also used to drive (by pressure) the sodium to the burn pan or to a stainless steel nozzle.

8.4 Data Acquisition

The data acquisition system (DAS) consists of a PC with a 16-bit data acquisition card connected to a National Instruments (NI) SCXI-1001 chassis. It has NI SCXI-1102 cards with NI SCXI-

1303 blocks for TCs and NI SCXI-1104 cards with NI SCXI-1300 blocks for analog signals. This provides the ability to increase either analog signals or TC signals. The data acquisition system can acquire temperature, heat flux, and pressure data. The integrity of all thermocouple channels is evaluated prior to each experiment with an Ectron thermocouple simulator, which inputs a controlled signal into each channel at the thermocouple device connection point and provides a check on the integrity of the channel hardware and software from that point to the final magnetic storage location. Data are sampled simultaneously for all channels, typically at 1000 Hz with an average value recorded at a rate of at least one sample per second. The spectrometer is a stand-alone instrument and data is recorded independent of the DAS.

8.5 Sodium Pool Fire Experimental Data

For each sodium pool test this section will display the details of the measured data. For details about the experimental data analysis please refer to the main body of this report. This section will start with test number "Pool 1" from Table 8-1 and end with "Pool 11" from the same table. For Pool Tests 1 through 4 the Pan Bottom TCs, pan sidewall TCs, and heat flux data will be presented. For tests pan 6-11 the Pan Bottom TCs, pan sidewall TCs, inside top pan TCs, inside pan rake TCs, and heat flux data will be presented. The data presented here are the measured values during the experiment.

8.5.1 Sodium Pool Test 1 Measured Data

For instrumentation locations and specifications referred to in the figures of this section please reference Section 8.2. This section displays the measured data from sodium pool test 1.

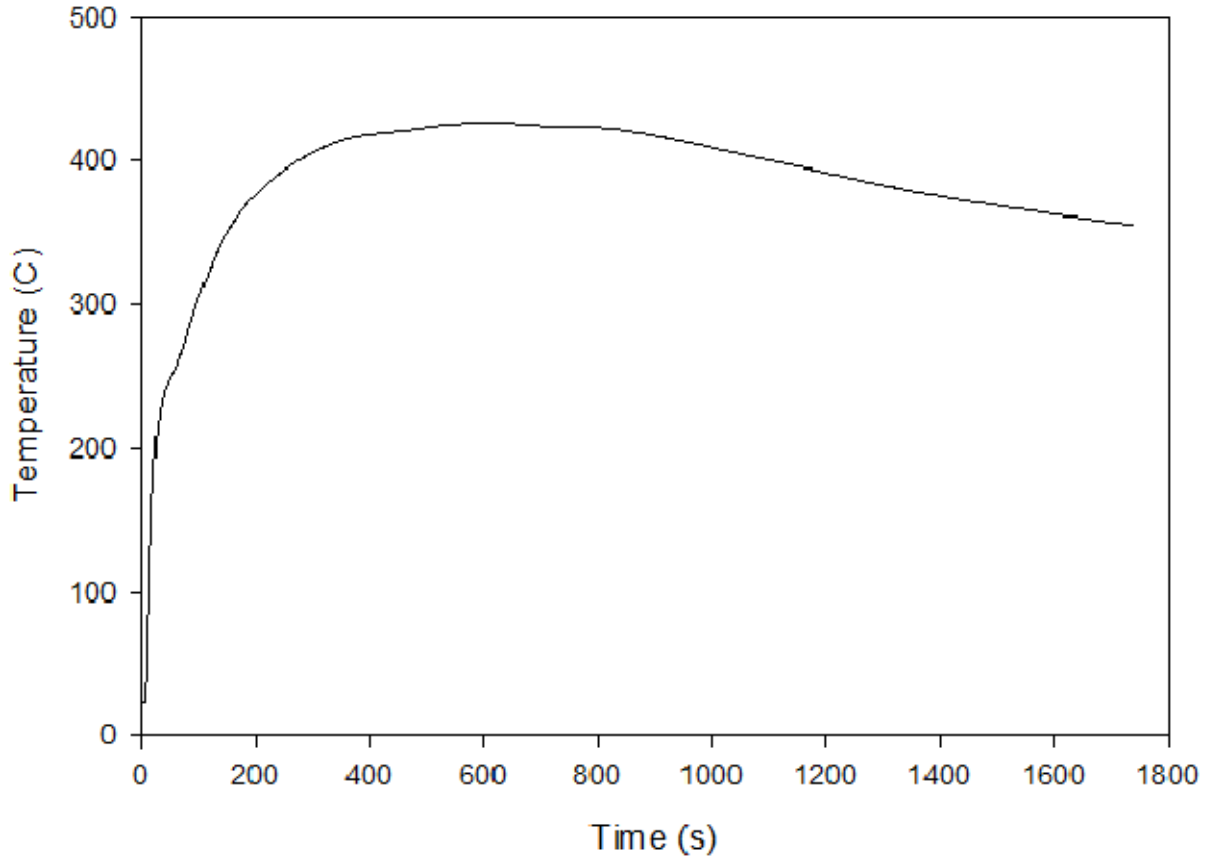

Figure 8-5: Sodium Pool Test 1, Bottom PoolCenter TC Temperature versus Time

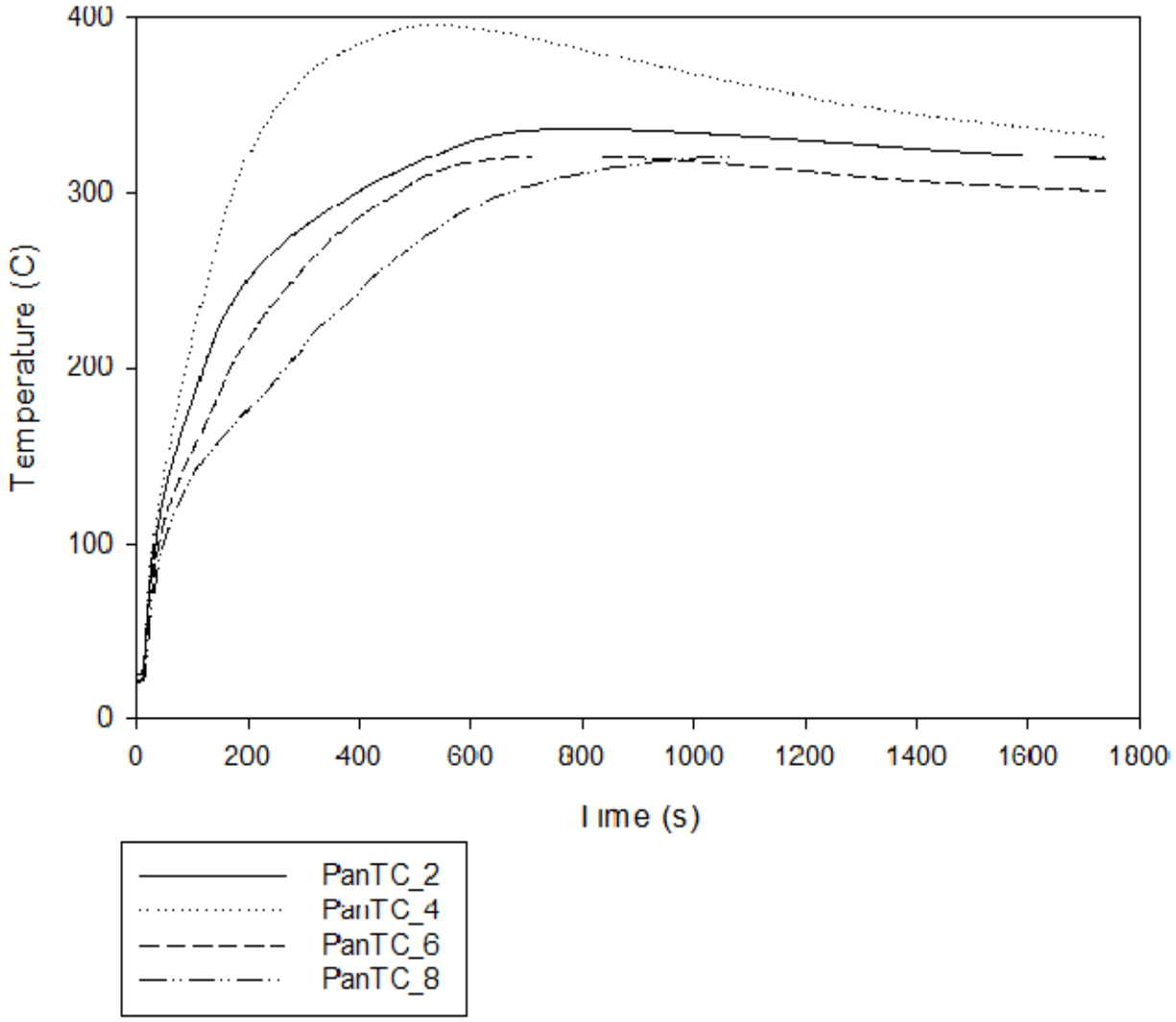

Figure 8-6: Sodium Pool Test 1, Pan Bottom ½ Radius TC Temperatures versus Time

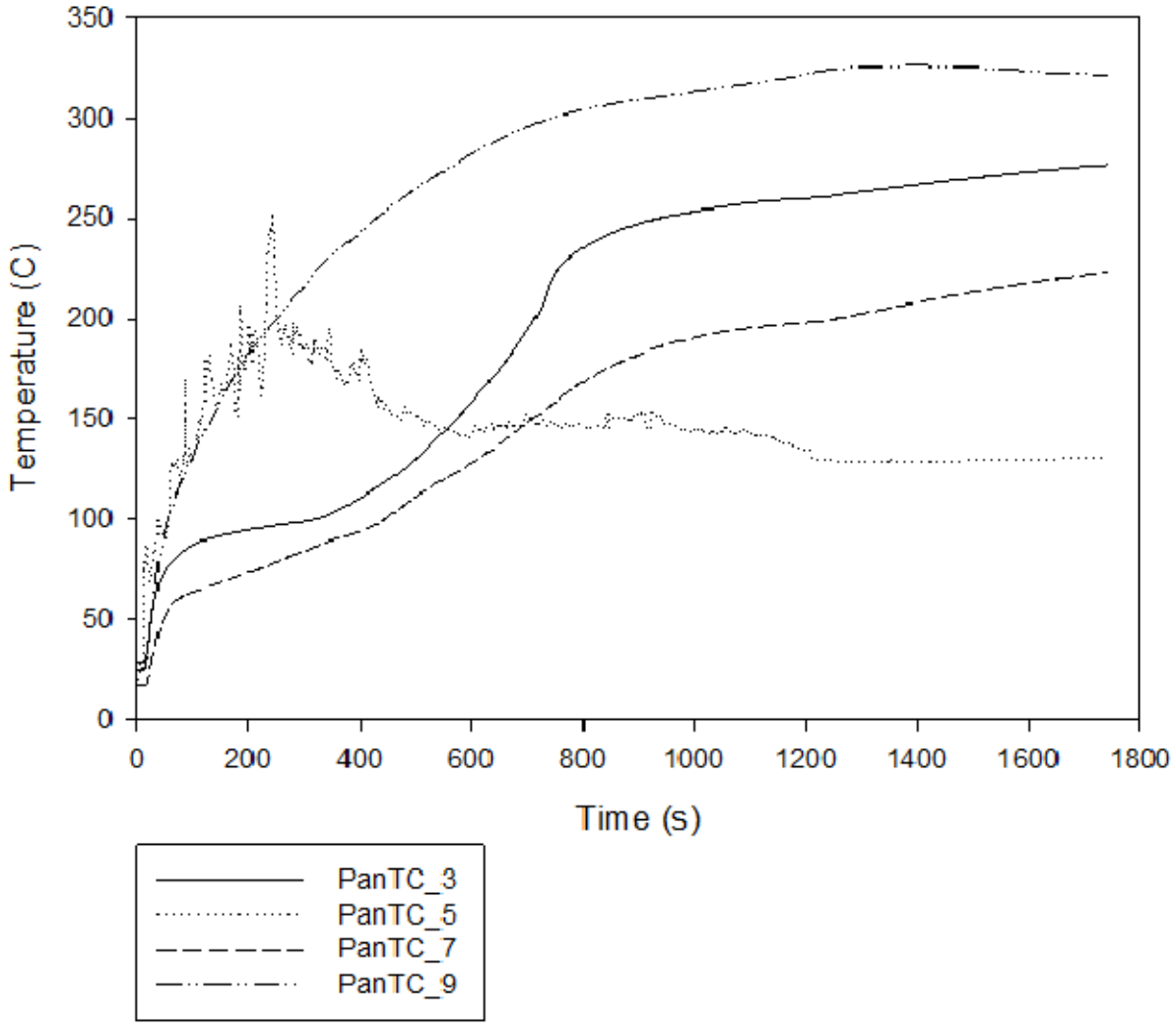

Figure 8-7: Sodium Pool Test 1, Pan Bottom Full Radius TC Temperatures versus Time

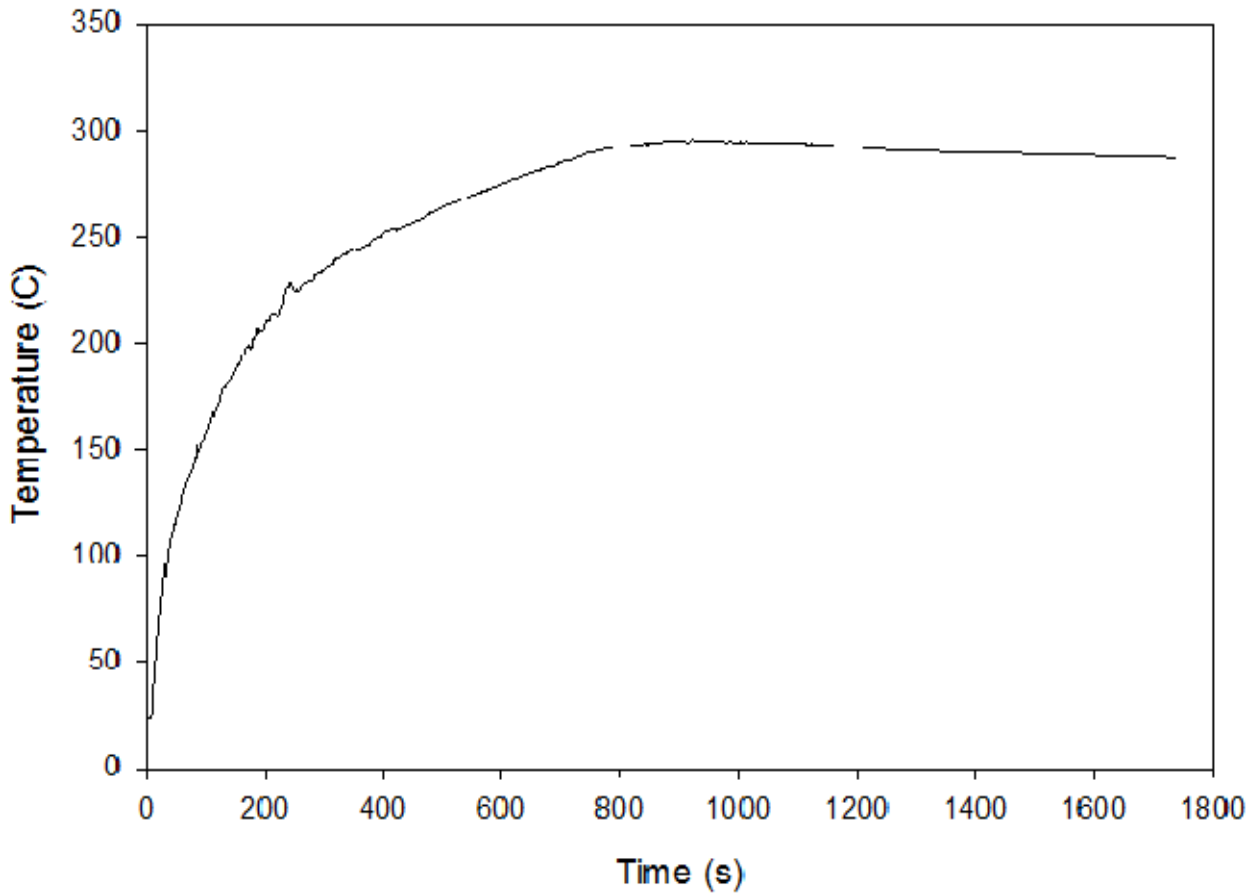

Figure 8-8: Sodium Pool Test 1, Averaged Pan Bottom TCs' Temperatures versus Time

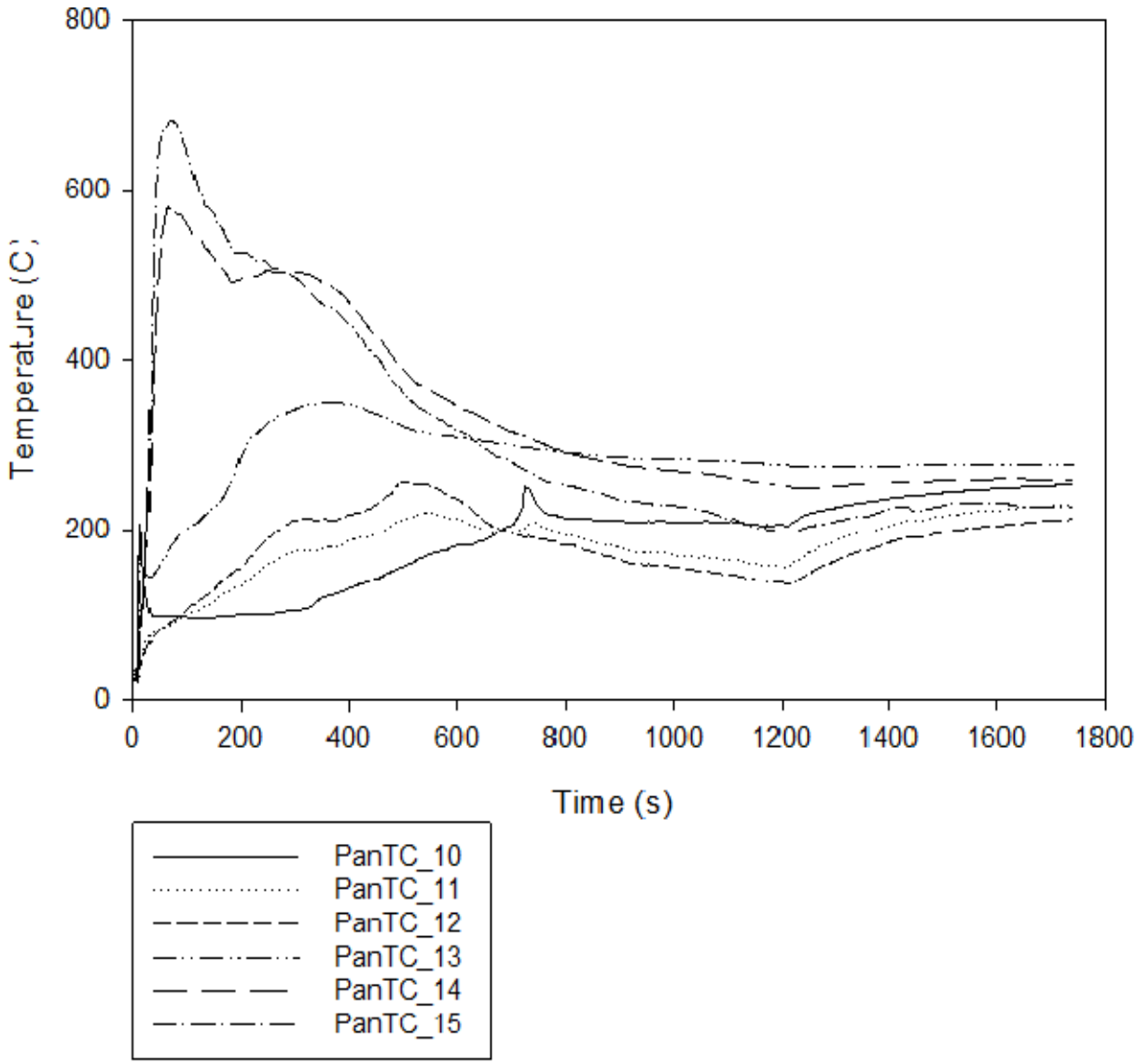

Figure 8-9: Sodium Pool Test 1, Sidewall Pan TC Temperatures versus Time

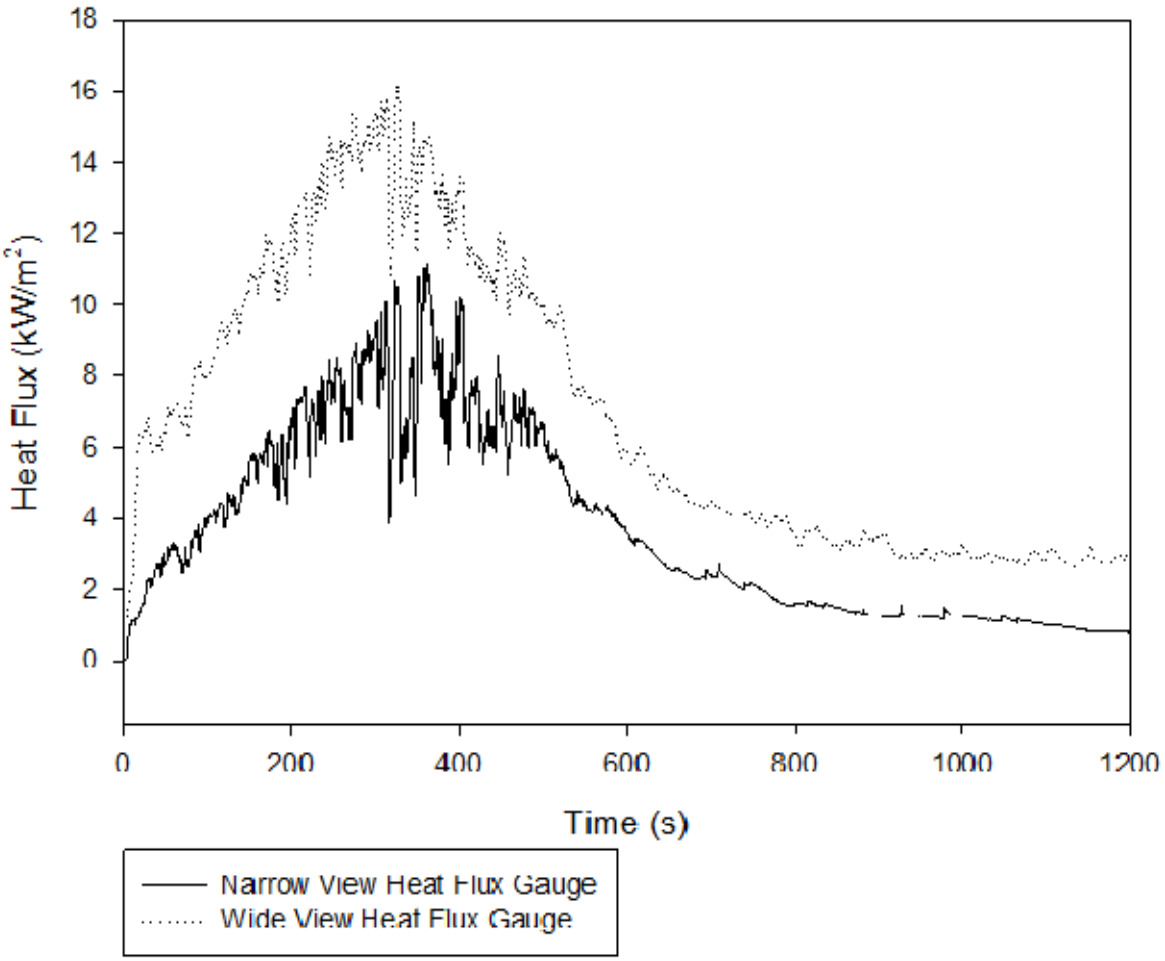

Figure 8-10: Sodium Pool Test 1, Measured Heat Flux versus Time

8.5.2 Sodium Pool Test 2 Measured Data

For instrumentation locations and specifications referred to in the figures of this section please reference Section 8.2. This section displays the measured data from sodium pool test 2.

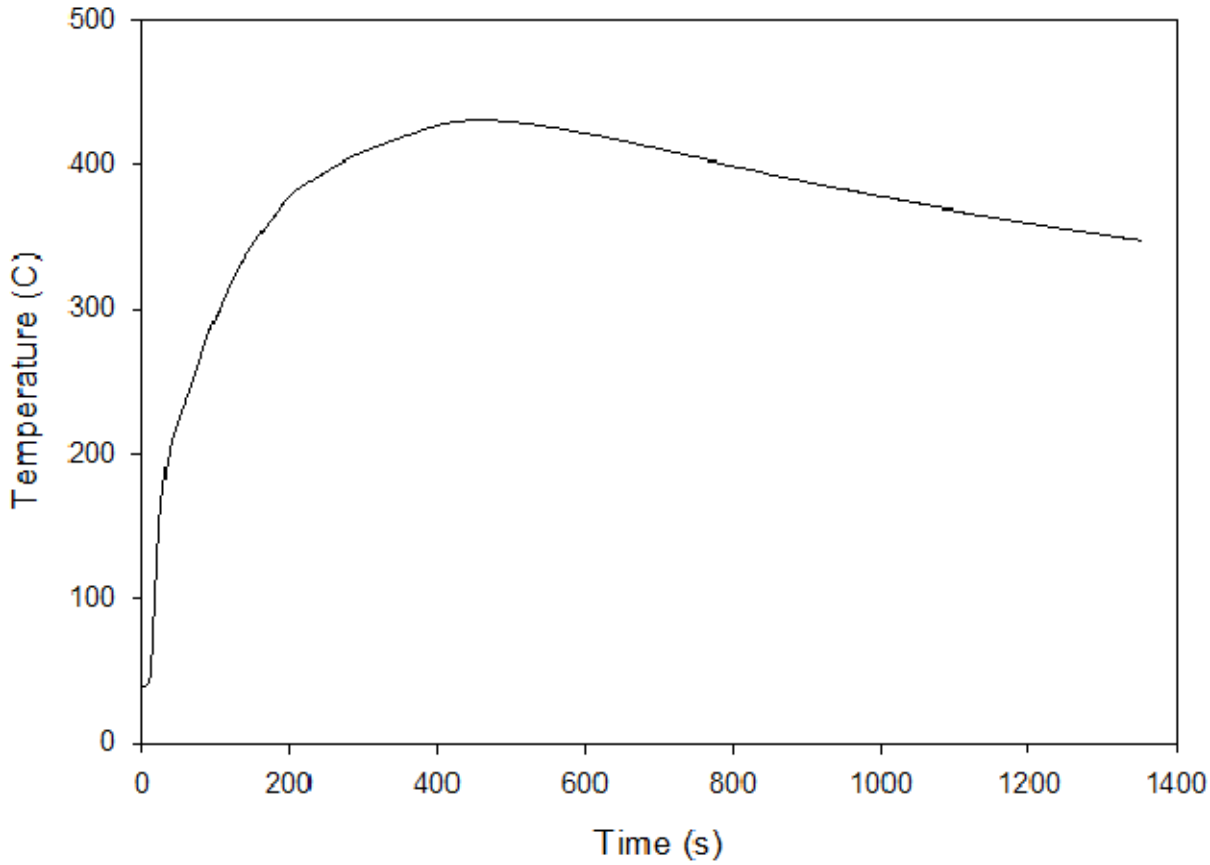

Figure 8-11: Sodium Pool Test 2, Pan Bottom Center TC Temperature versus Time

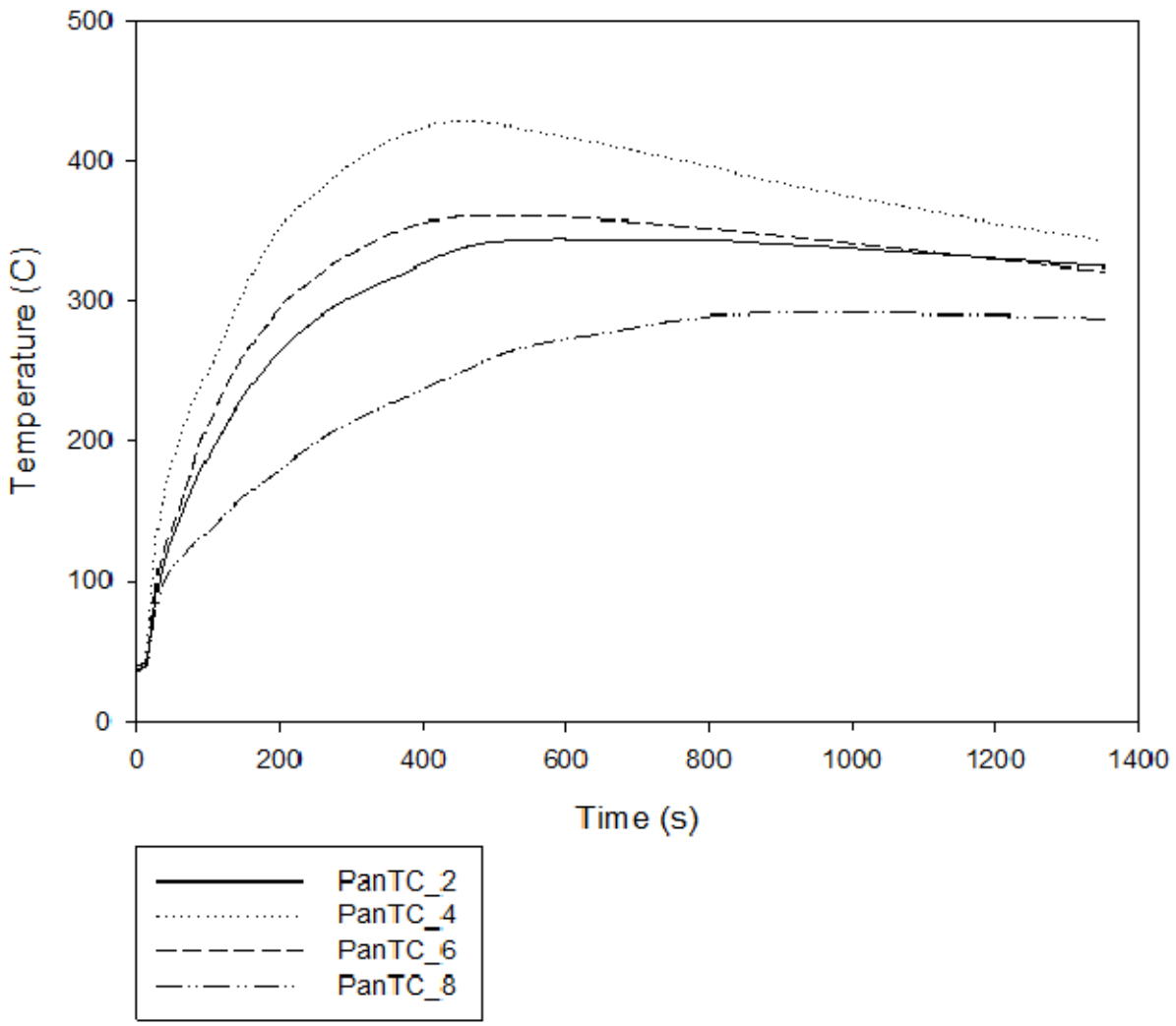

Figure 8-12: Sodium Pool Test 2, Pan Bottom ½ Radius TC Temperatures versus Time

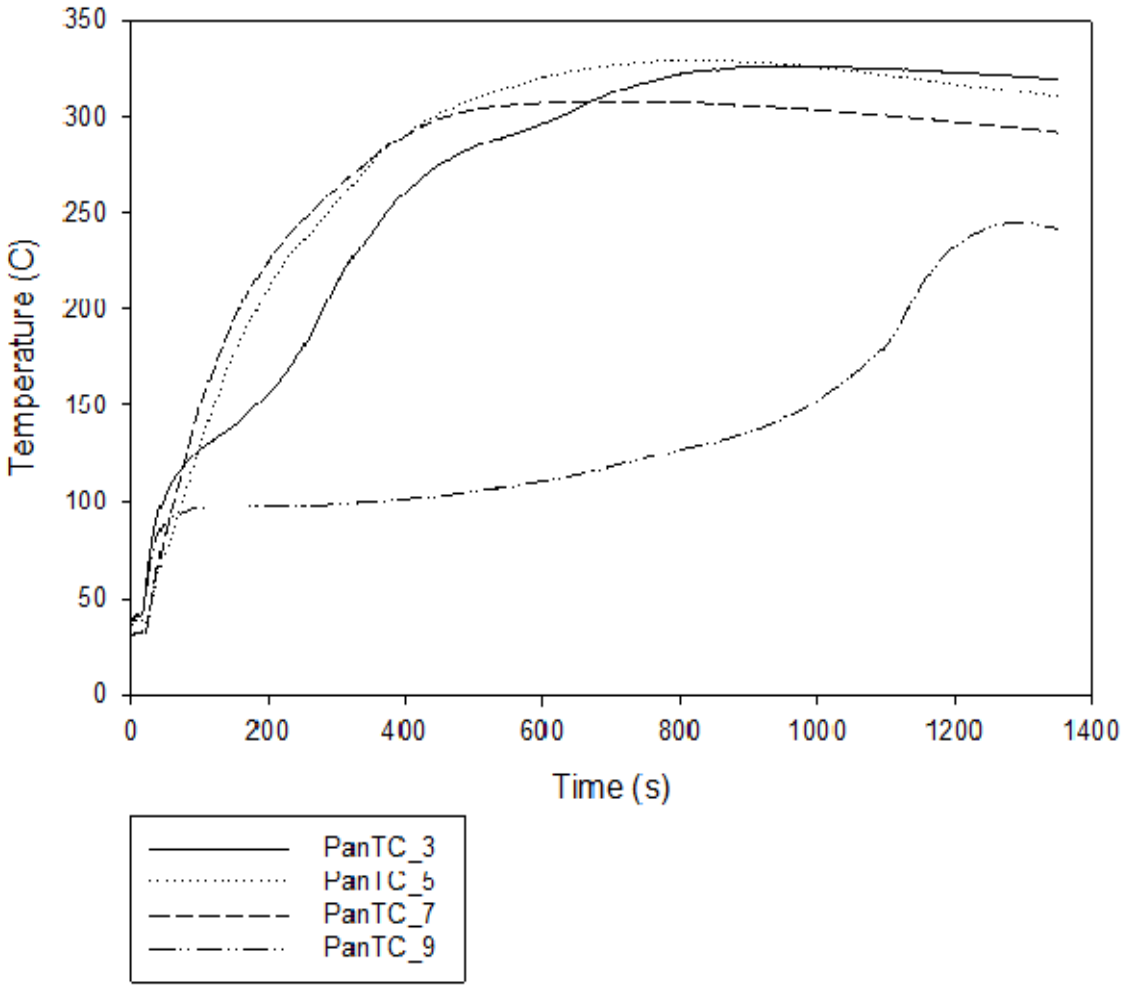

Figure 8-13: Sodium Pool Test 2, Pan Bottom Full Radius TC Temperatures versus Time

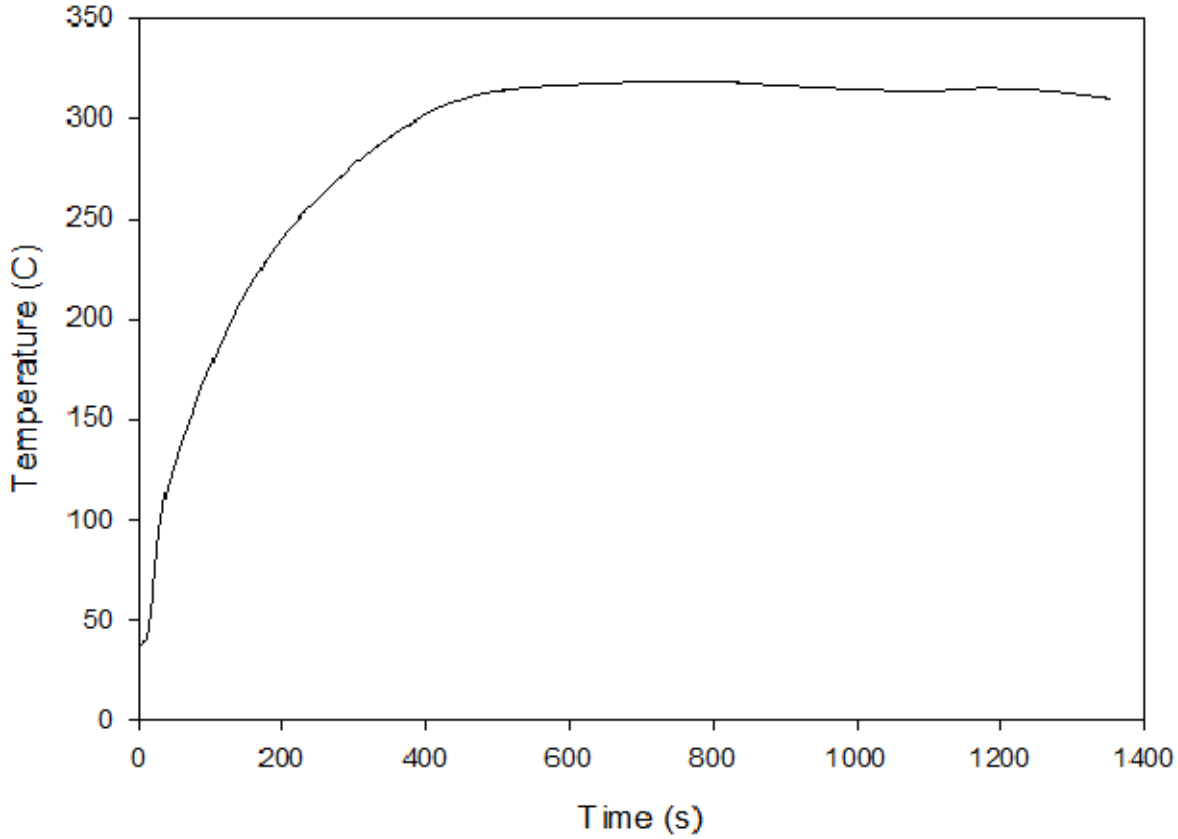

Figure 8-14: Sodium Pool Test 2, Averaged Pan Bottom TCs' Temperatures versus Time

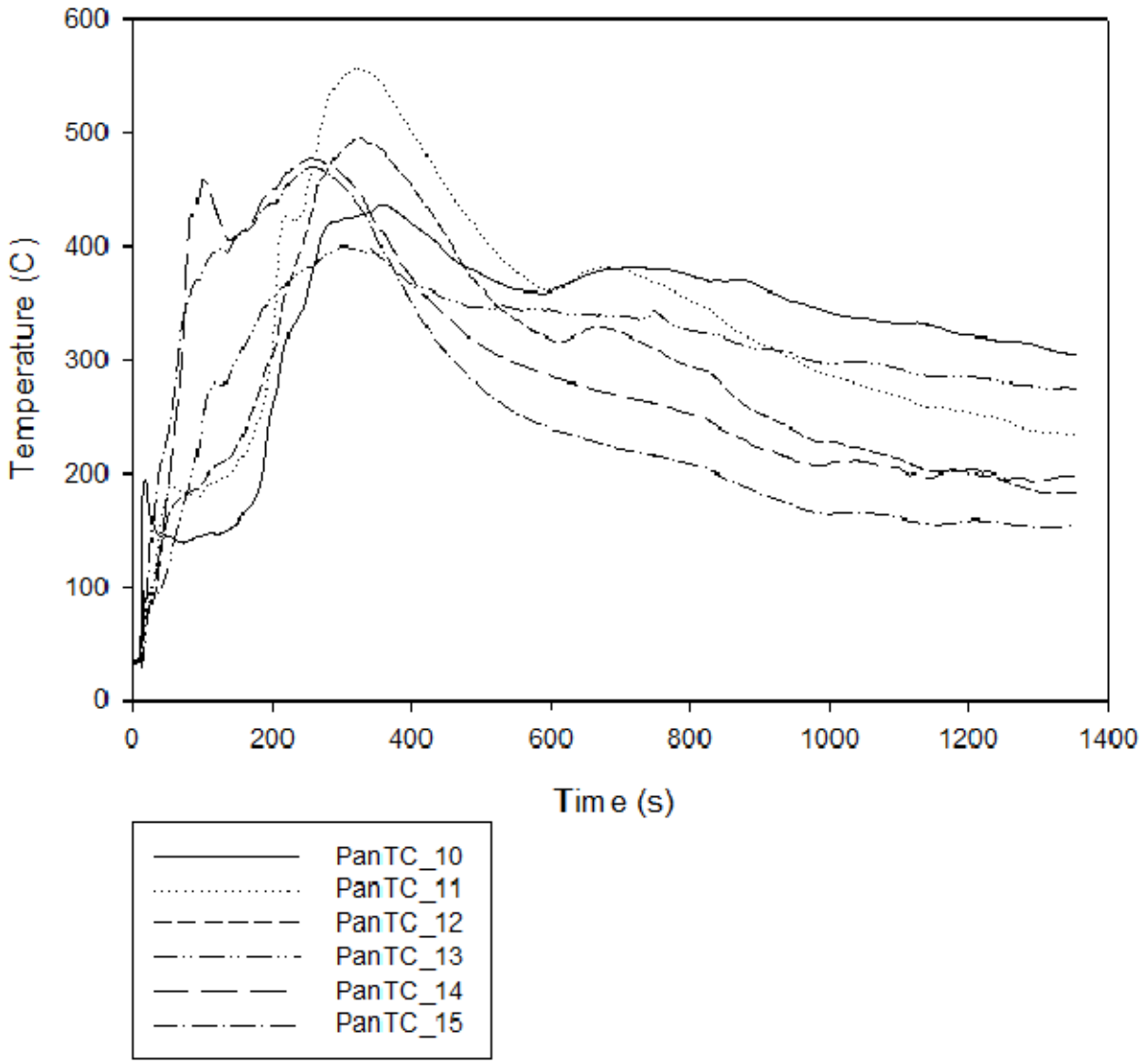

Figure 8-15: Sodium Pool Test 2, Sidewall Pan TC Temperatures versus Time

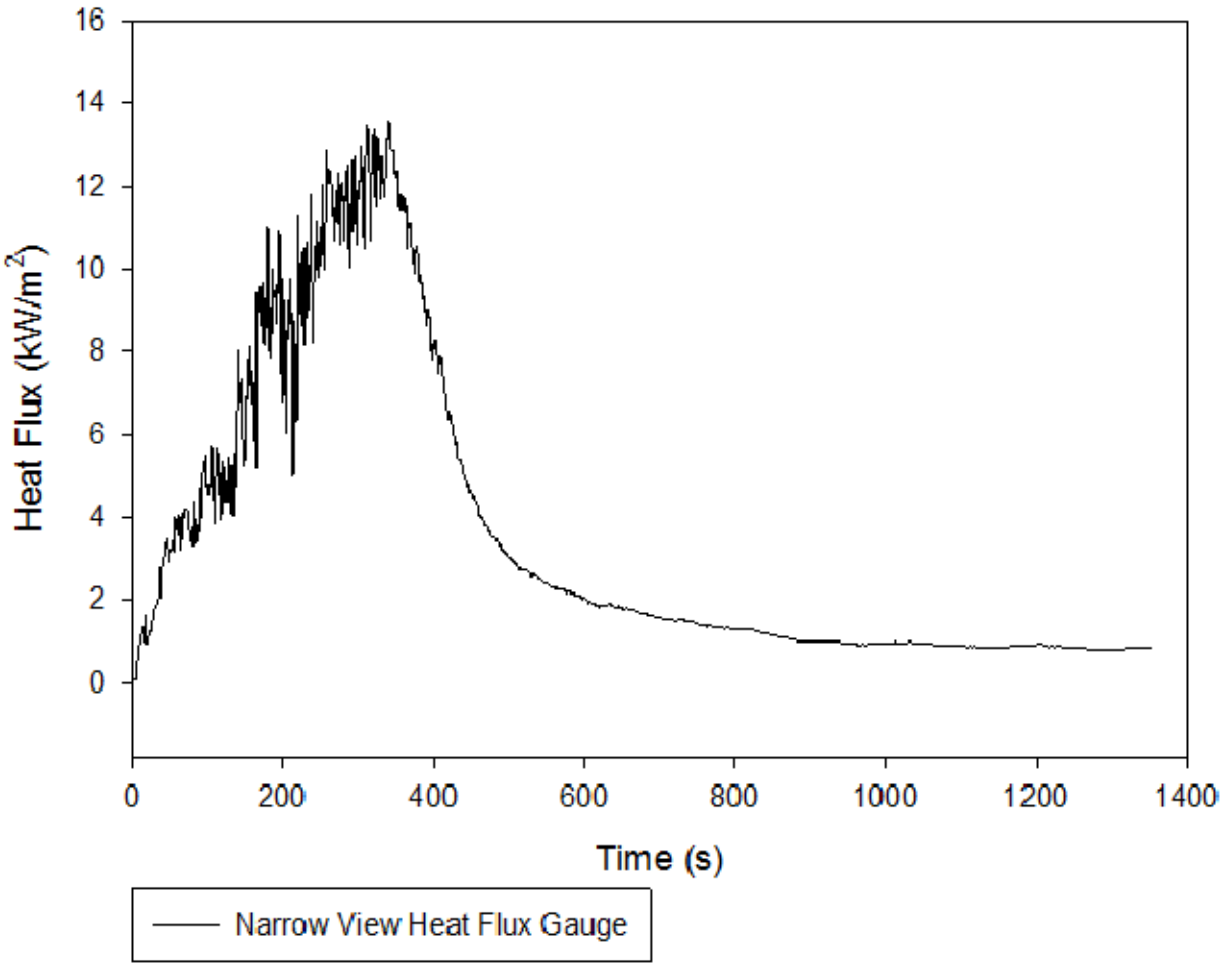

Figure 8-16: Sodium Pool Test 2, Measured Heat Flux versus Time

8.5.3 Sodium Pool Test 3 Measured Data

For instrumentation locations and specifications referred to in the figures of this section please reference Section 8.2. This section displays the measured data from sodium pool test 3.

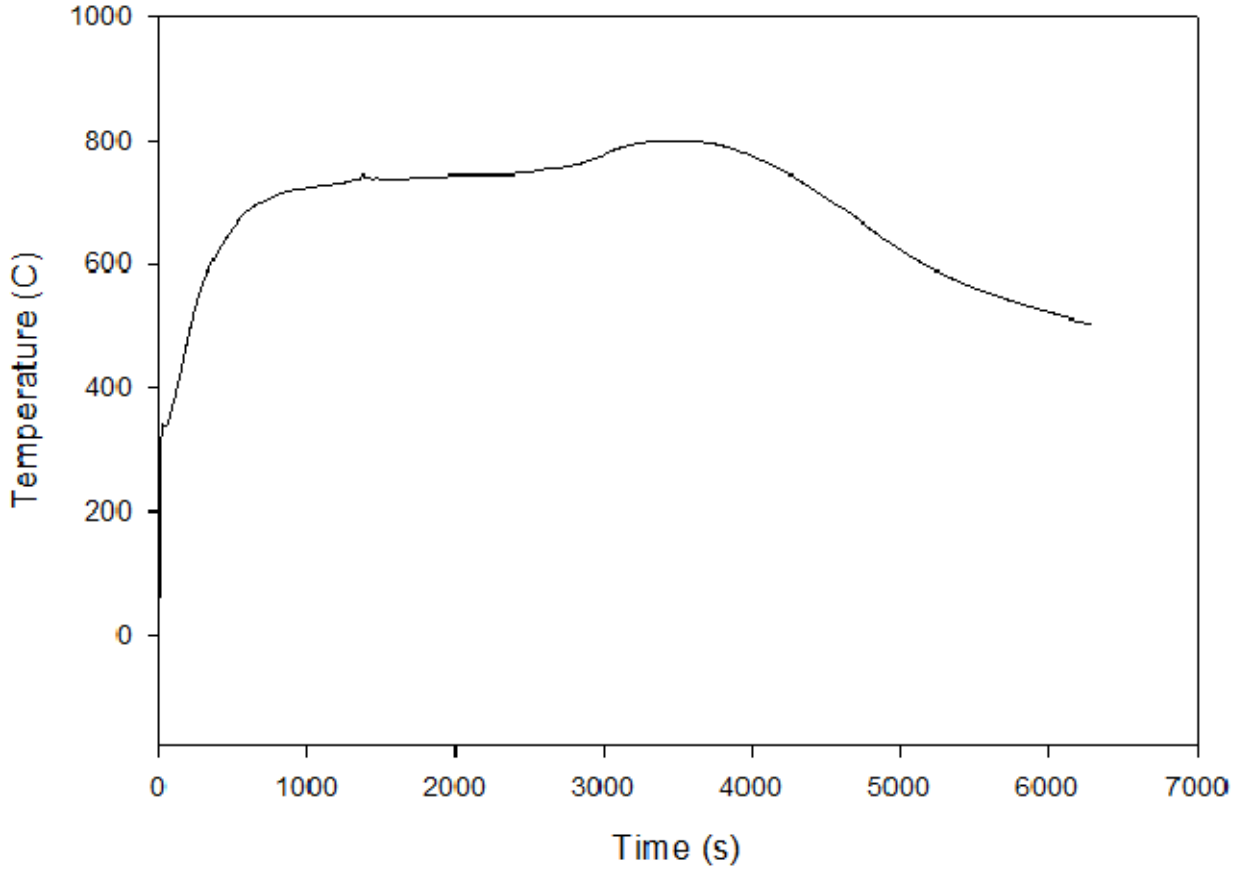

Figure 8-17: Sodium Pool Test 3, Pan Bottom Center TC Temperature versus Time

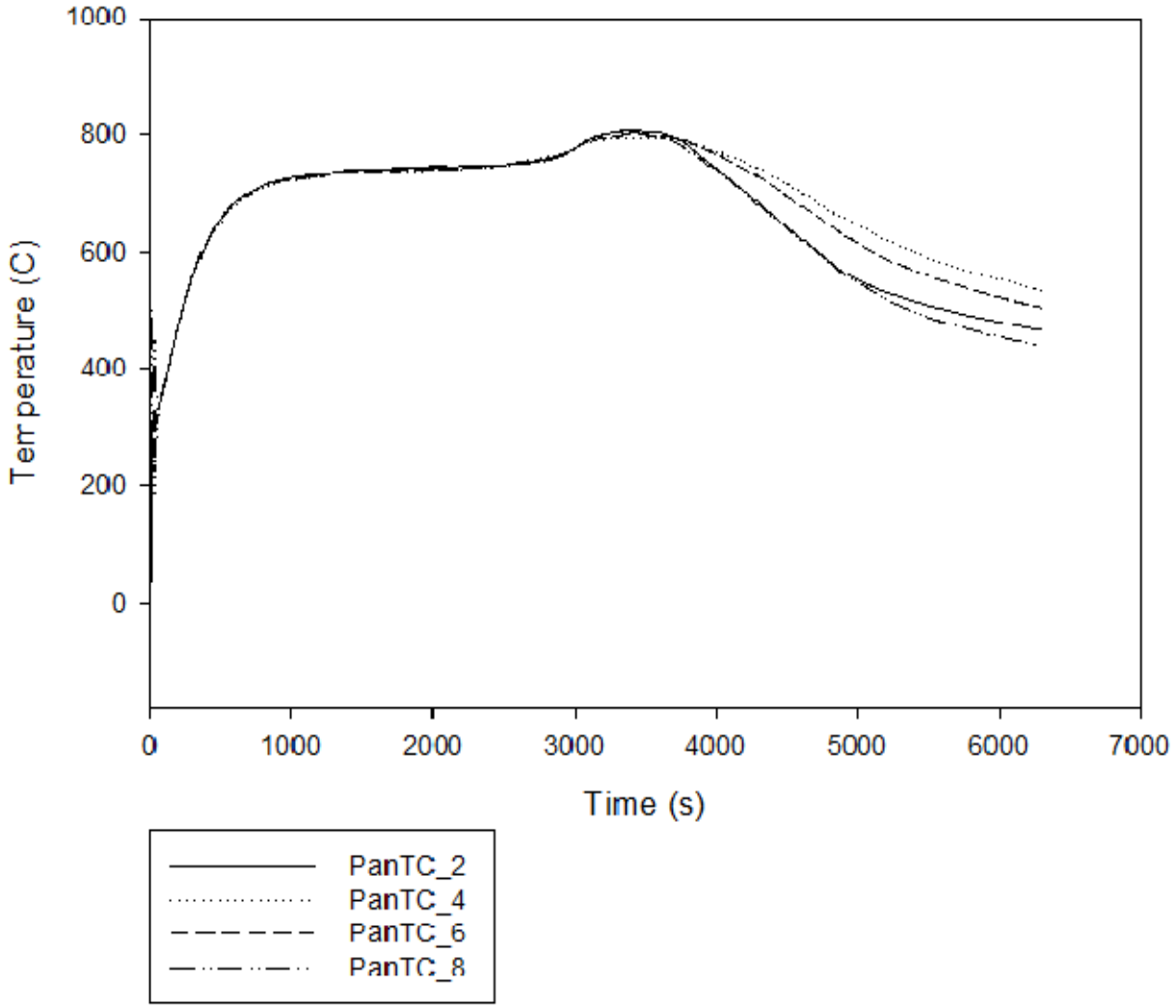

Figure 8-18: Sodium Pool Test 3, Pan Bottom ½ Radius TC Temperatures versus Time

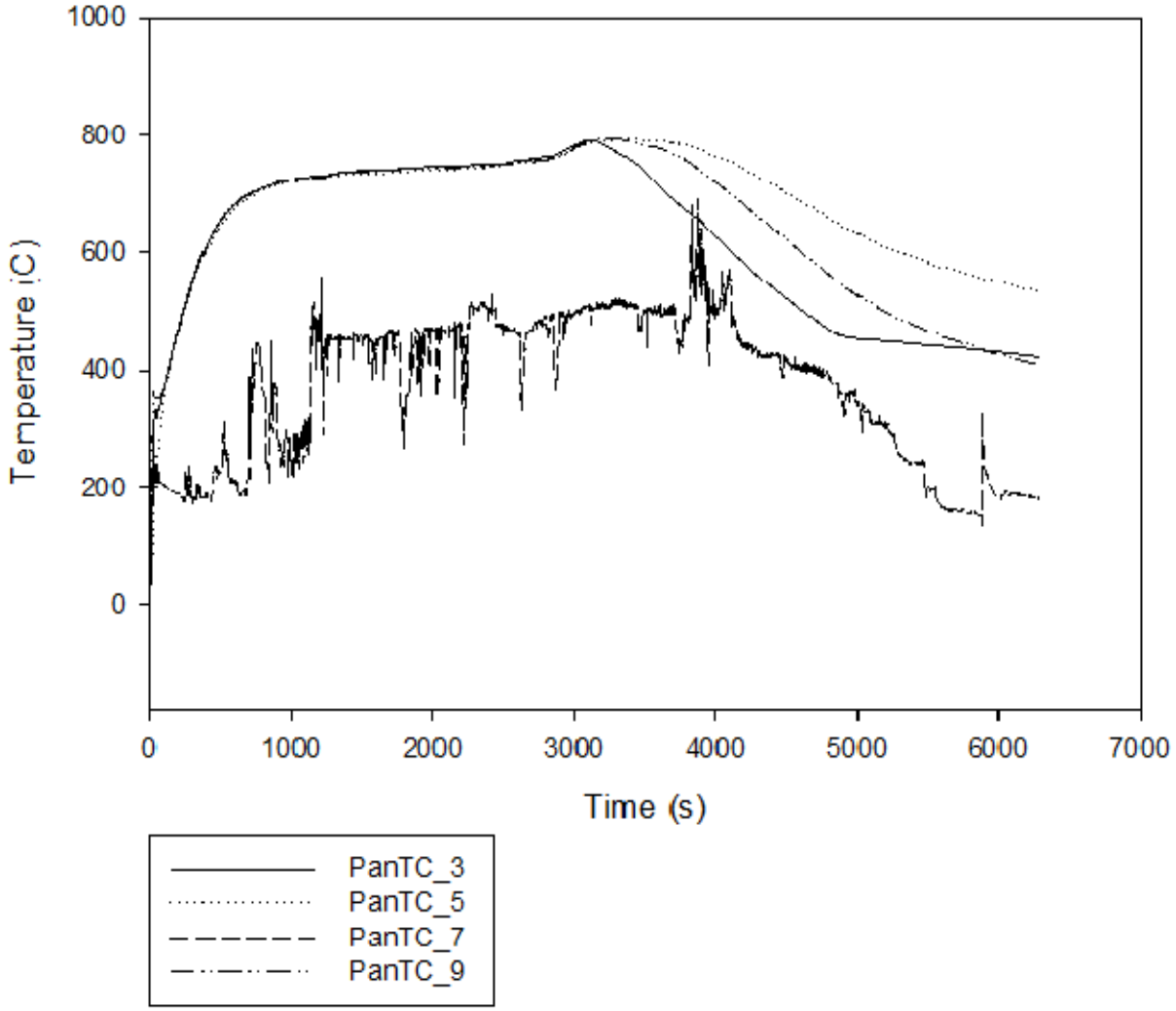

Figure 8-19: Sodium Pool Test 3, Pan Bottom Full Radius TC Temperatures versus Time

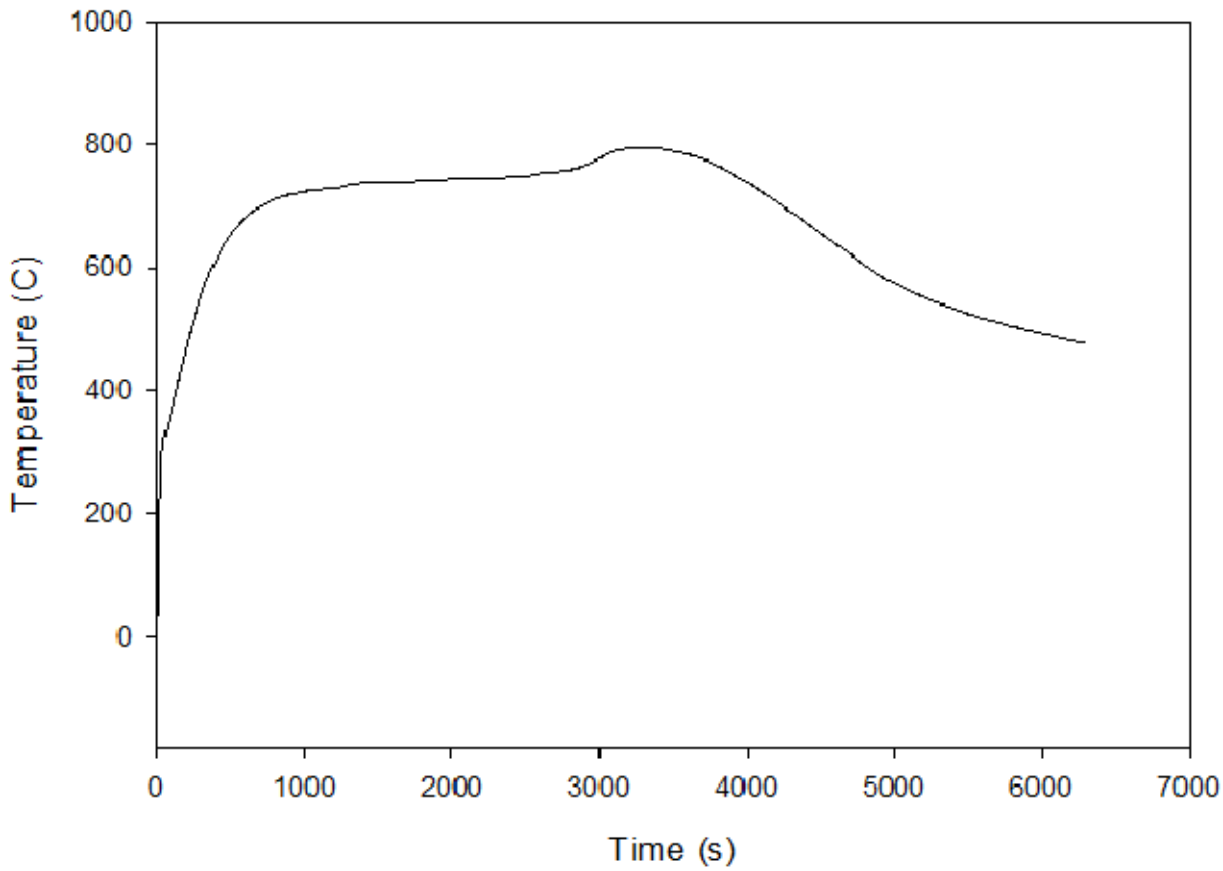

Figure 8-20: Sodium Pool Test 3, Averaged Pan Bottom TCs' Temperatures versus Time (without Pan TC7)

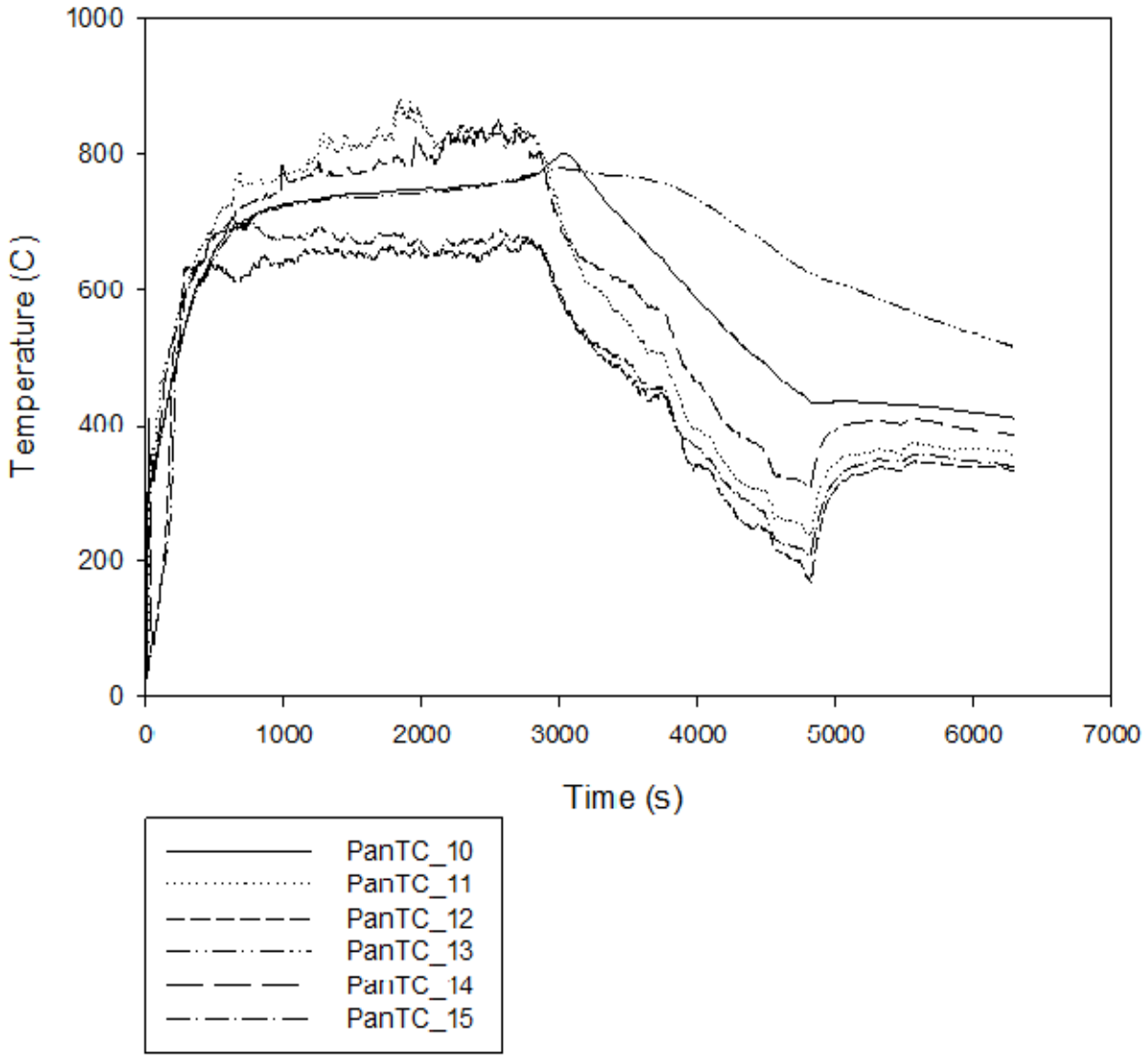

Figure 8-21: Sodium Pool Test 3, Sidewall Pan TC Temperatures versus Time

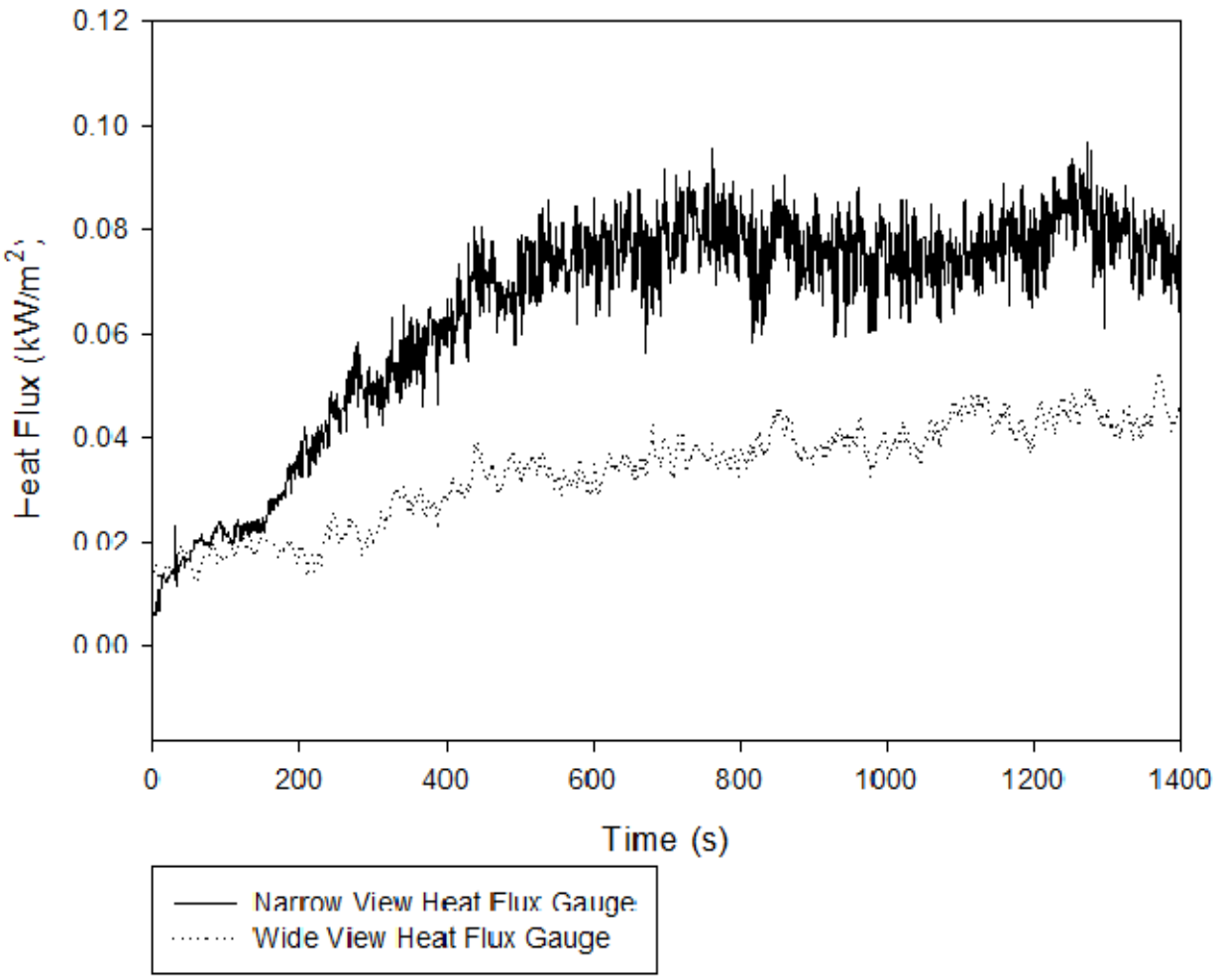

Figure 8-22: Sodium Pool Test 3, Measured Heat Flux versus Time

8.5.4 Sodium Pool Test 4 Measured Data

For instrumentation locations and specifications referred to in the figures of this section please reference Section 8.2. This section displays the measured data from sodium pool test 4.

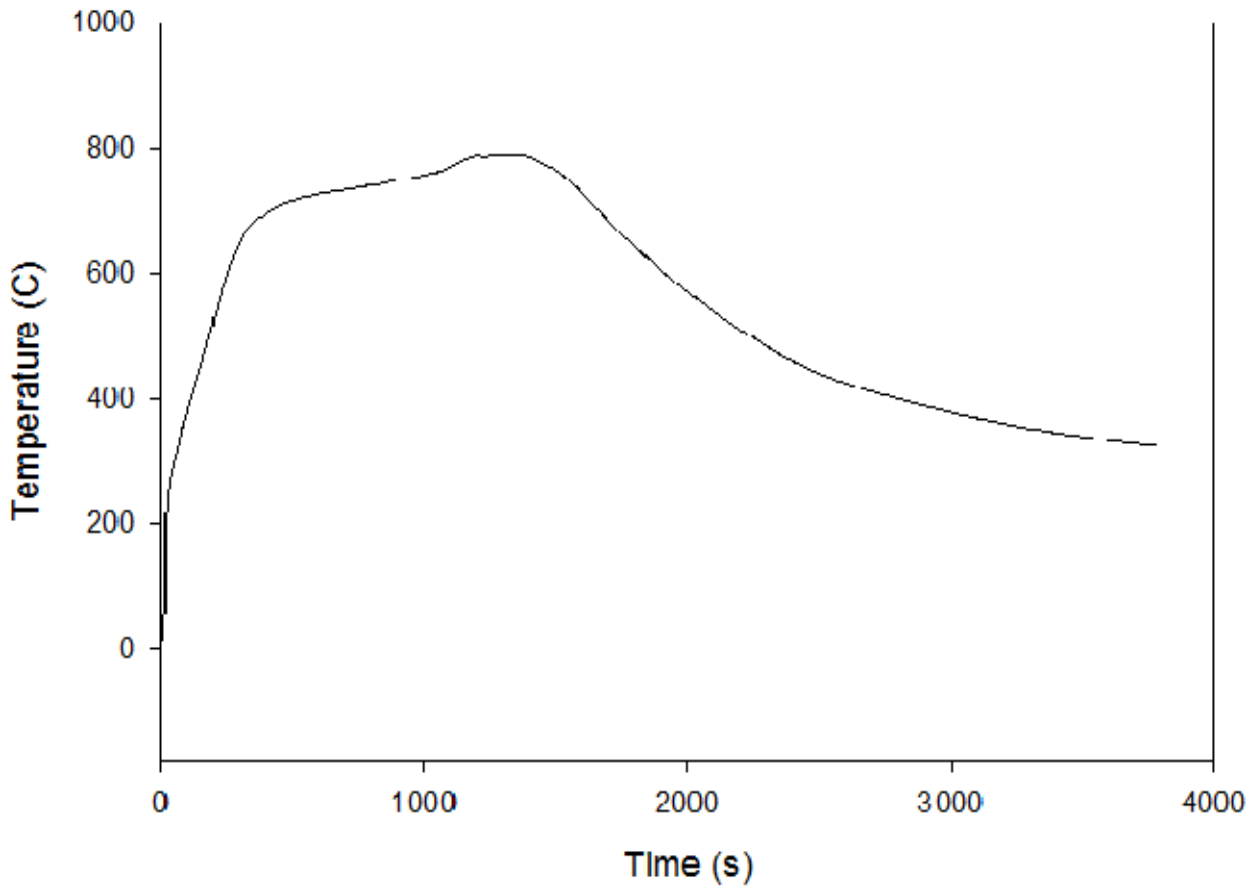

Figure 8-23: Sodium Pool Test 4, Pan Bottom Center TC Temperature versus Time

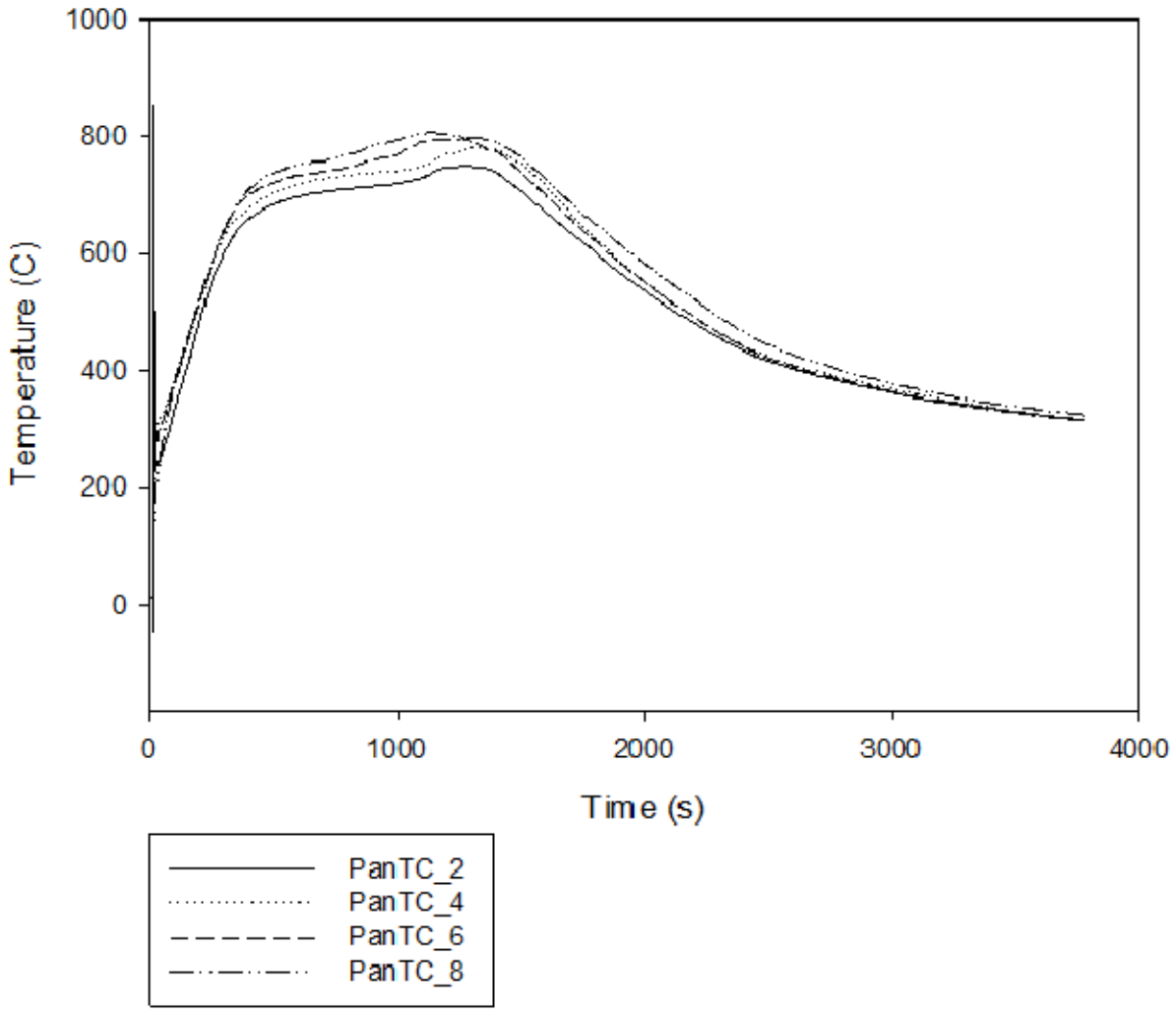

Figure 8-24: Sodium Pool Test 4, Pan Bottom ½ Radius TC Temperatures versus Time

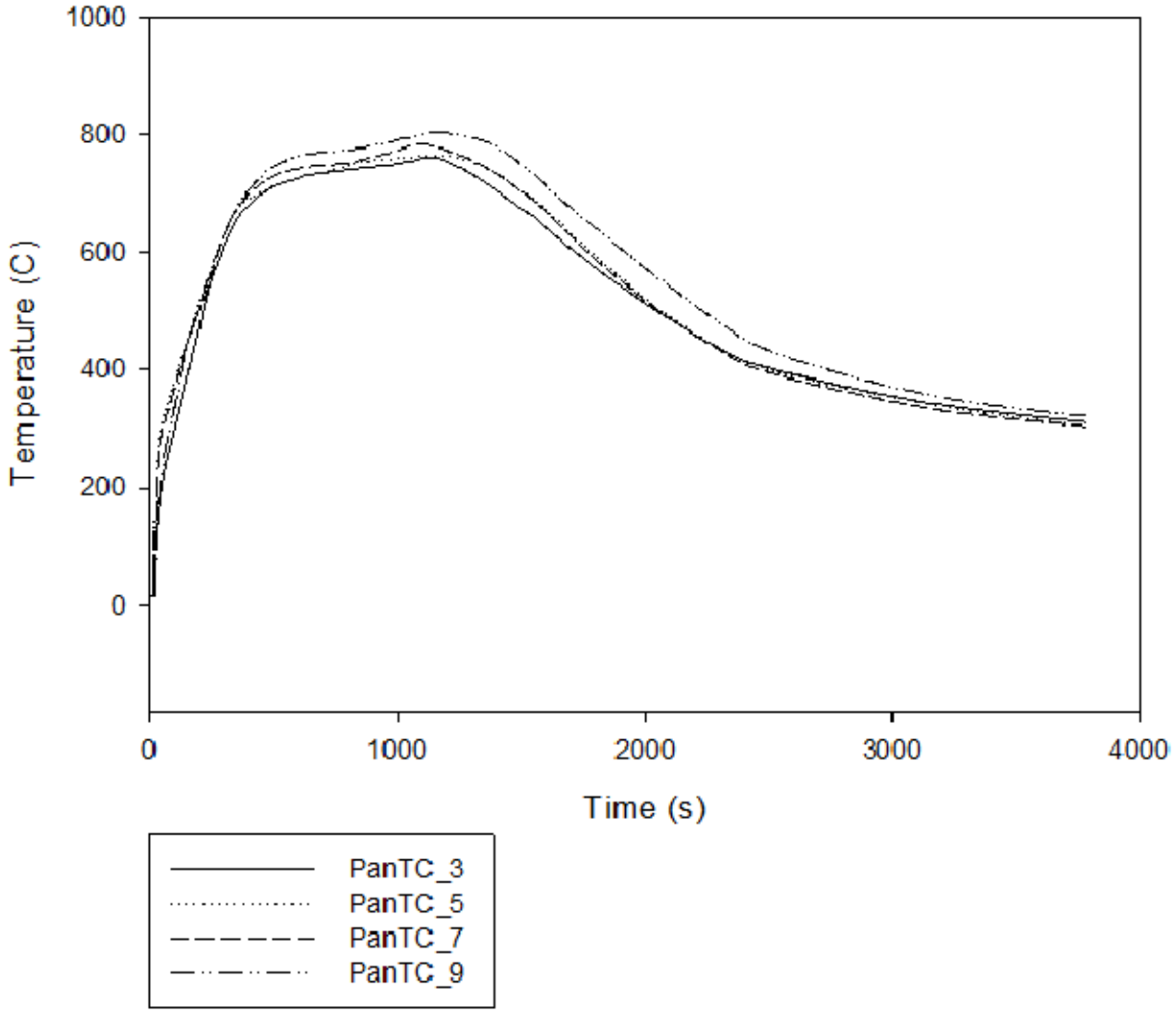

Figure 8-25: Sodium Pool Test 4, Pan Bottom Full Radius TC Temperatures versus Time

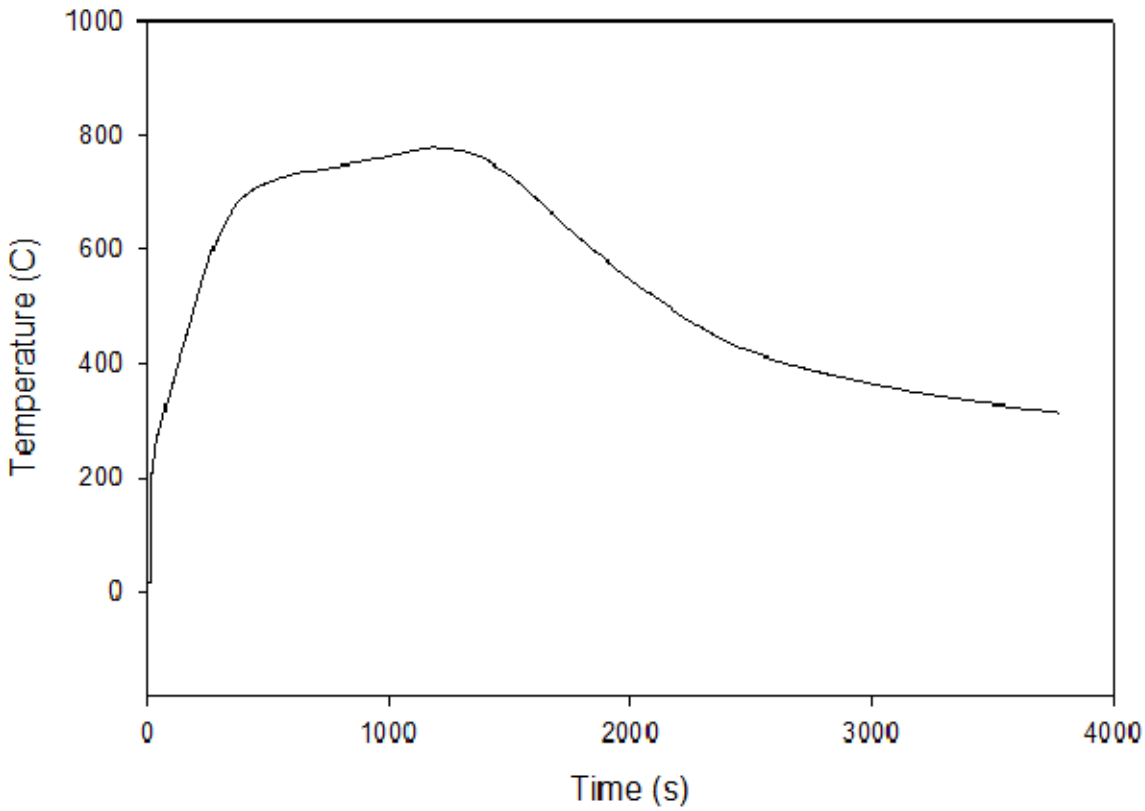

Figure 8-26: Sodium Pool Test 4, Averaged Pan Bottom TCs' Temperatures versus Time

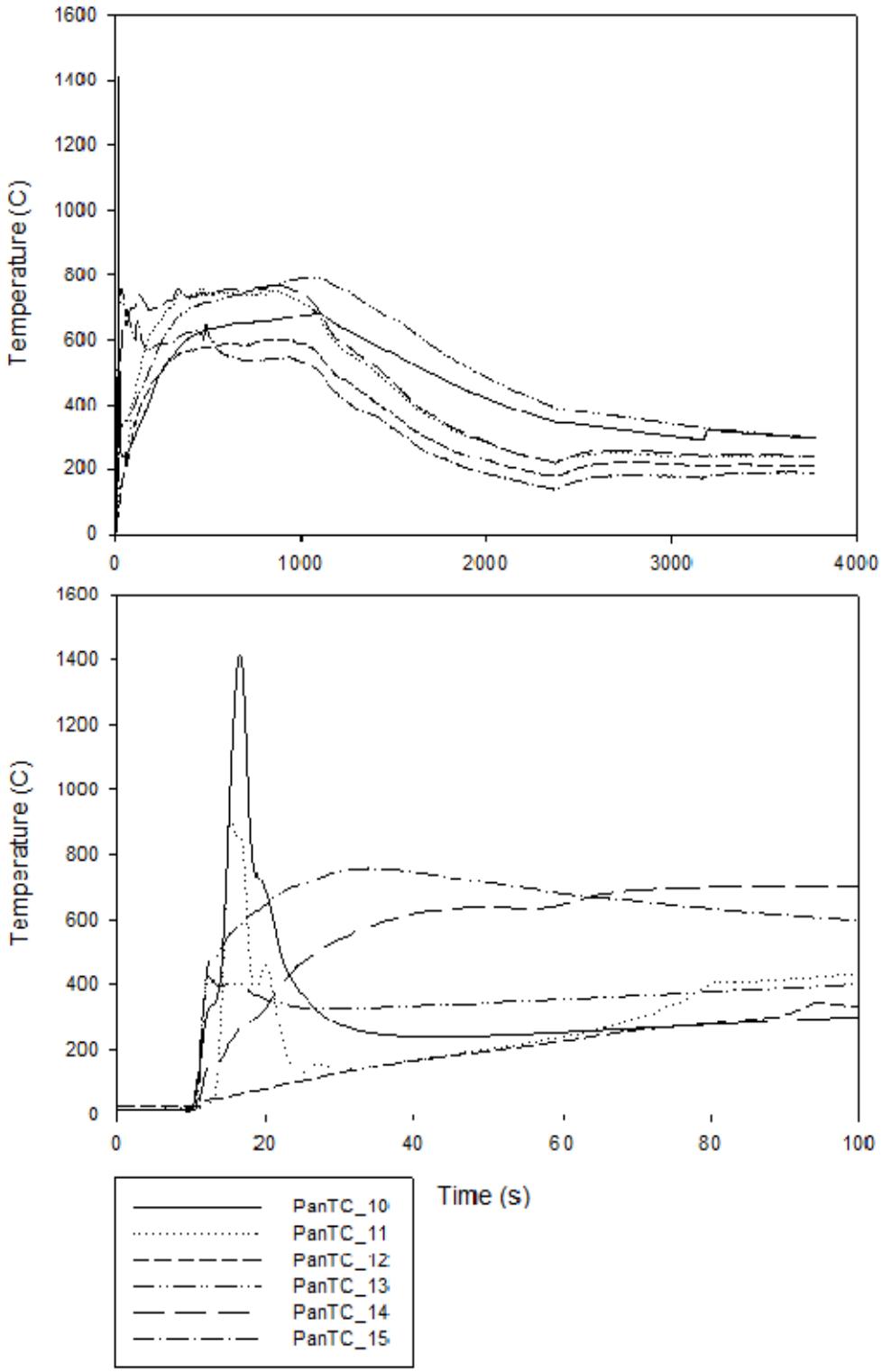

Figure 8-27: Sodium Pool Test 4, Sidewall Pan TC Temperatures versus Time

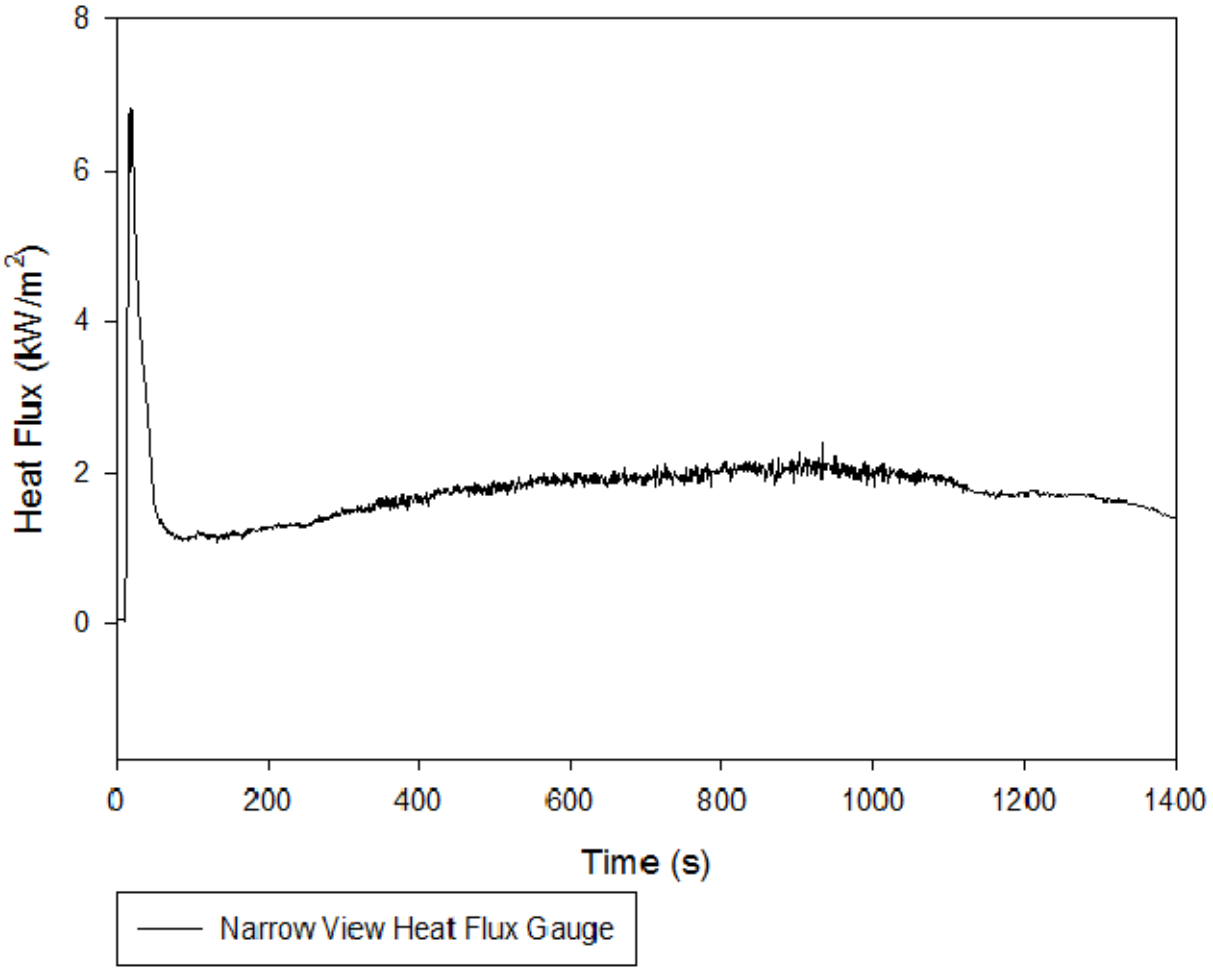

Figure 8-28: Sodium Pool Test 4, Measured Heat Flux versus Time

8.5.5 Sodium Pool Test 6 Measured Data

For instrumentation locations and specifications referred to in the figures of this section please reference Section 8.2. This section displays the measured data from sodium pool test 6.

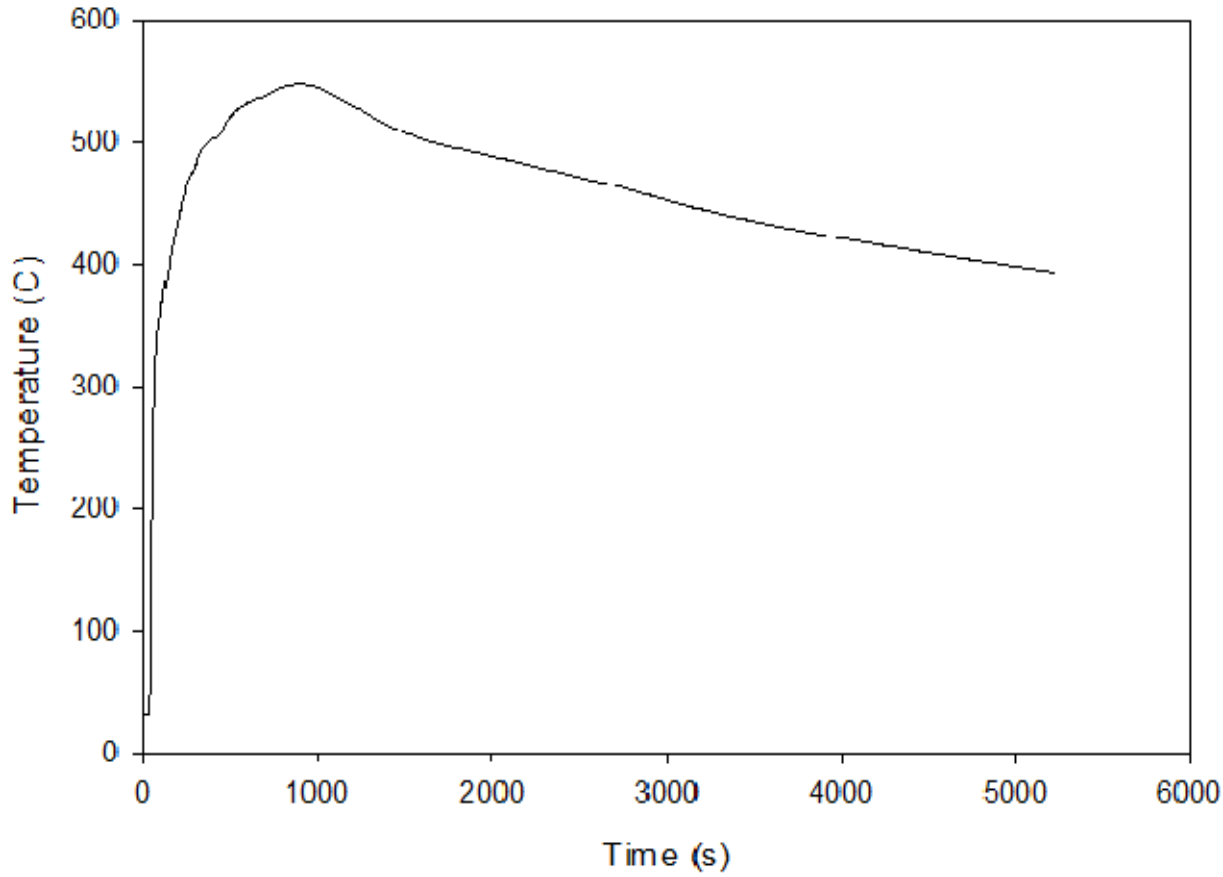

Figure 8-29: Sodium Pool Test 6, Pan Bottom Center TC Temperature versus Time

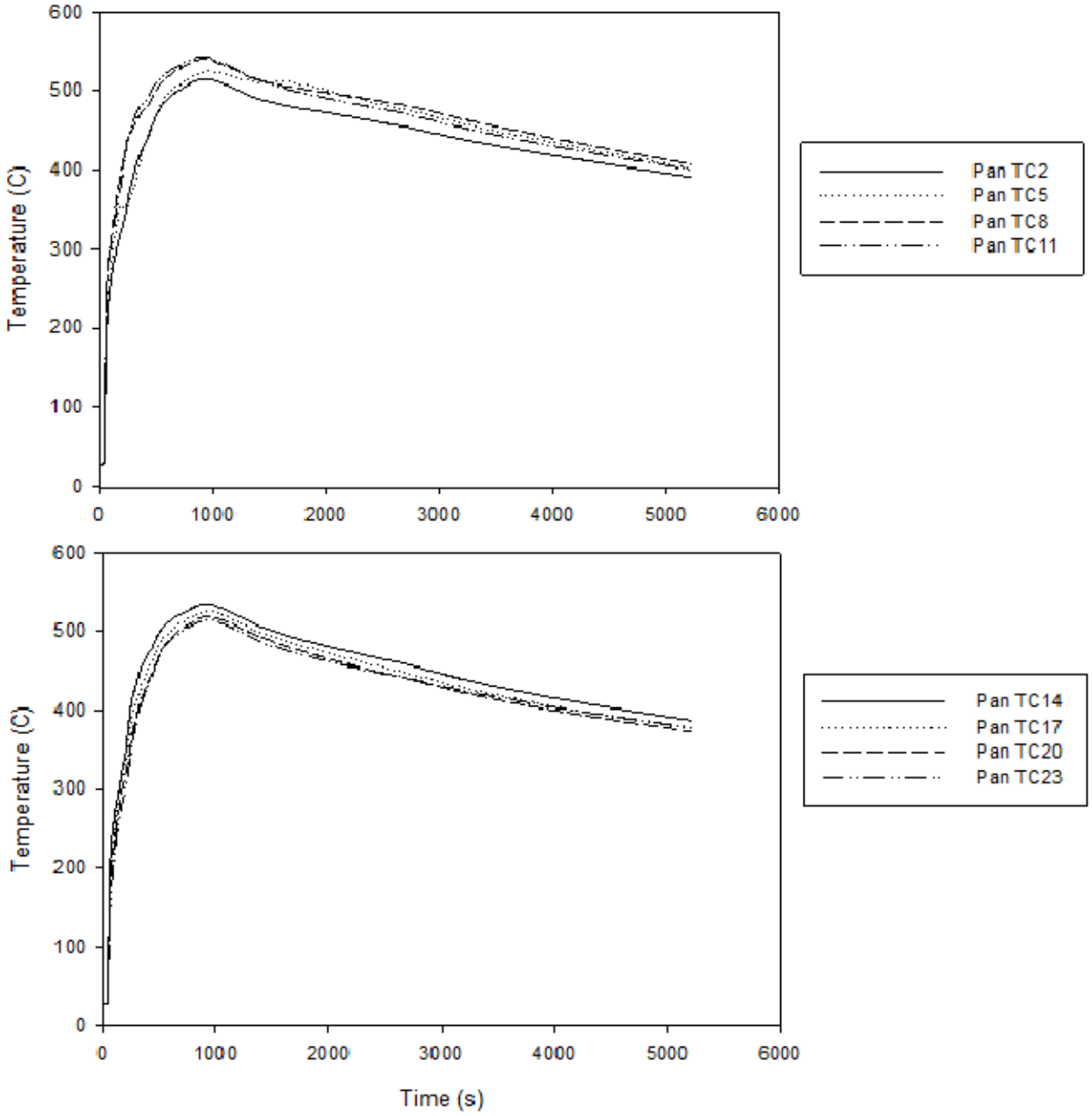

Figure 8-30: Sodium Pool Test 6, Pan Bottom 1/3 Radius TC Temperatures versus Time

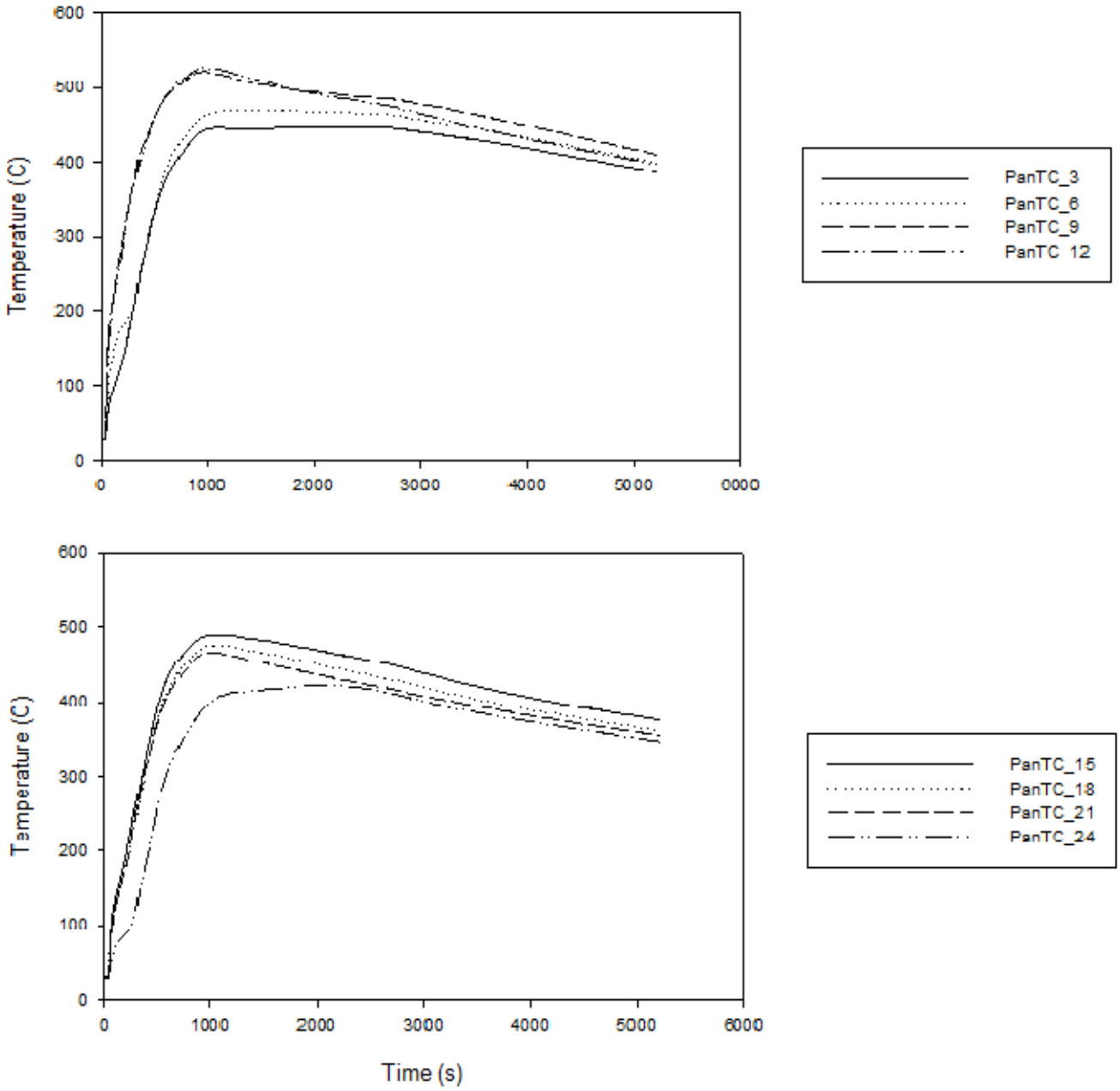

Figure 8-31: Sodium Pool Test 6, Pan Bottom 2/3 Radius TC Temperatures versus Time

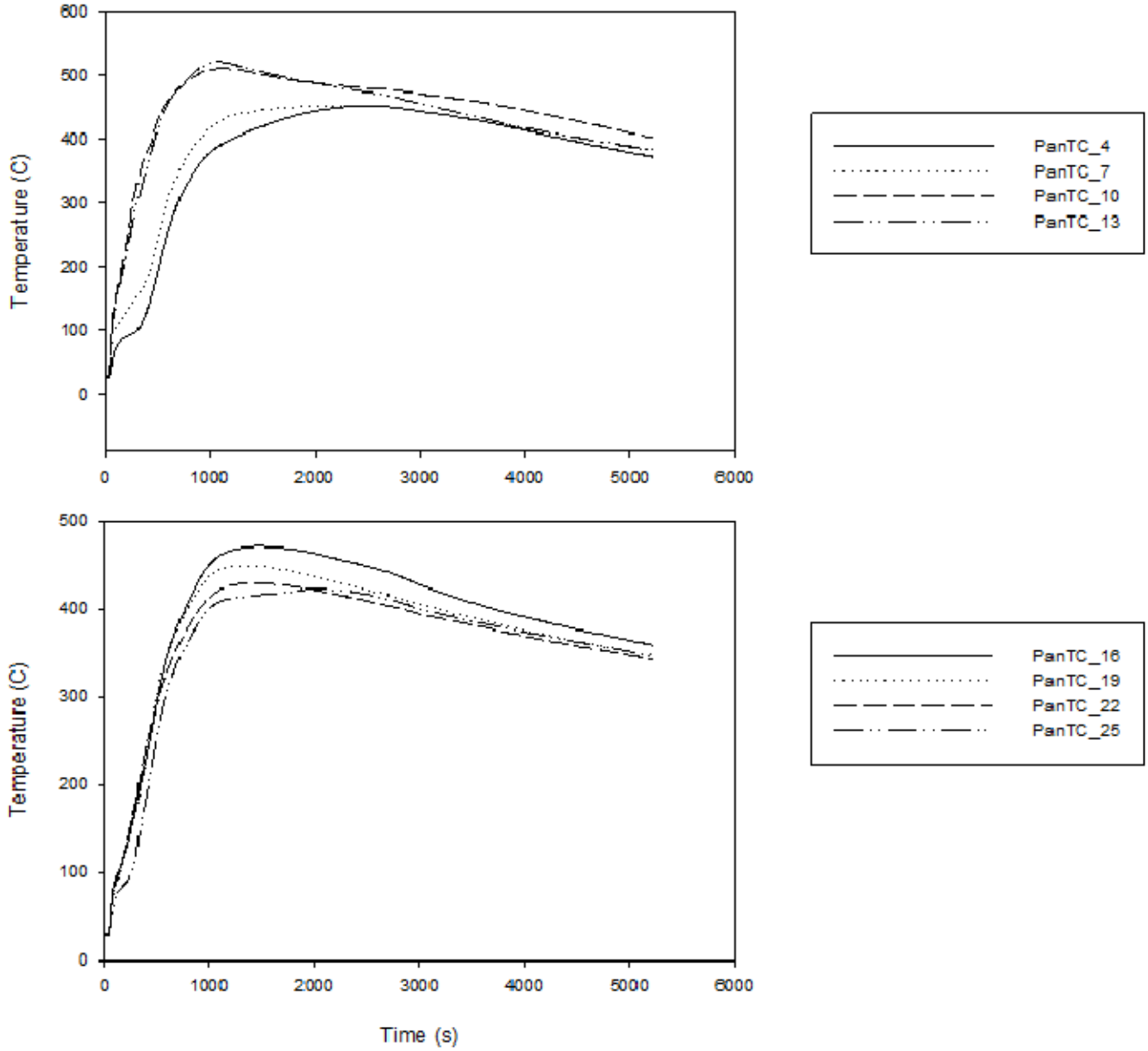

Figure 8-32: Sodium Pool Test 6, Pan Bottom Full Radius TC Temperatures versus Time

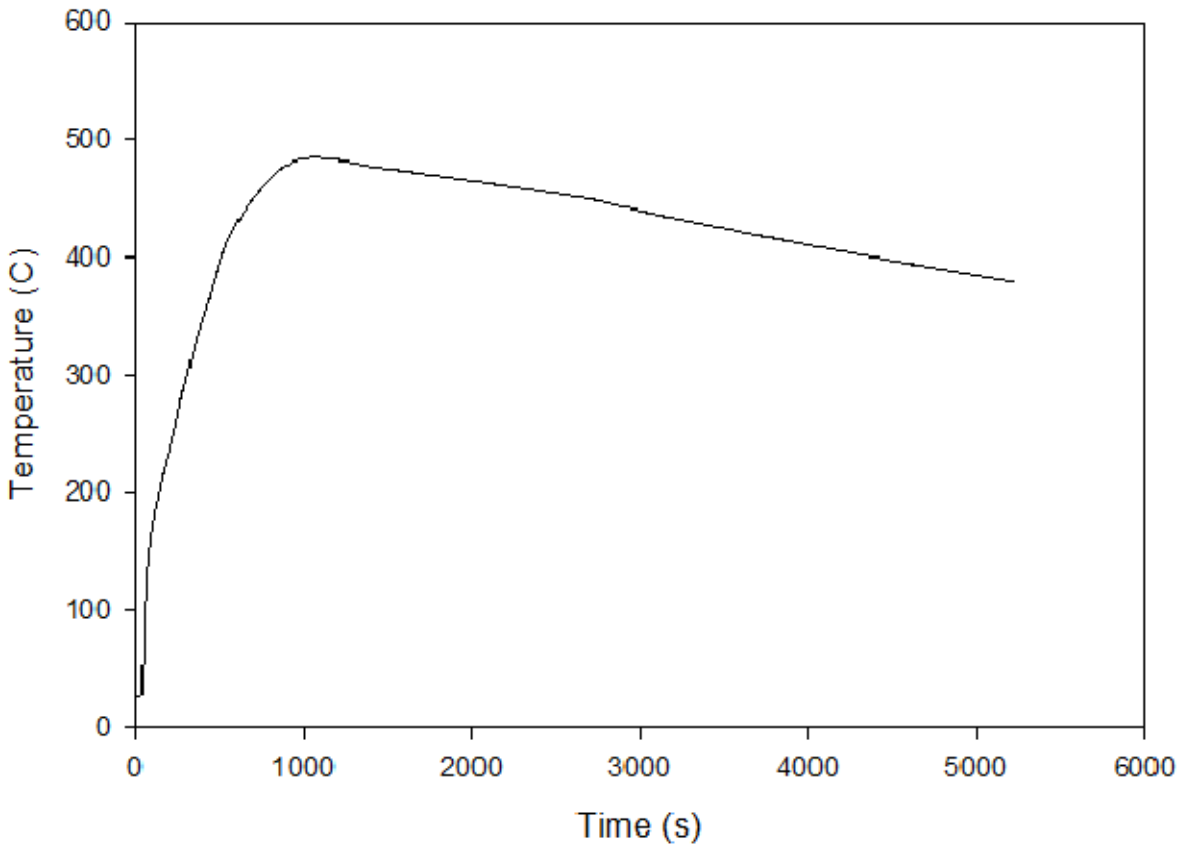

Figure 8-33: Sodium Pool Test 6, Averaged Pan Bottom TCs' Temperatures versus Time

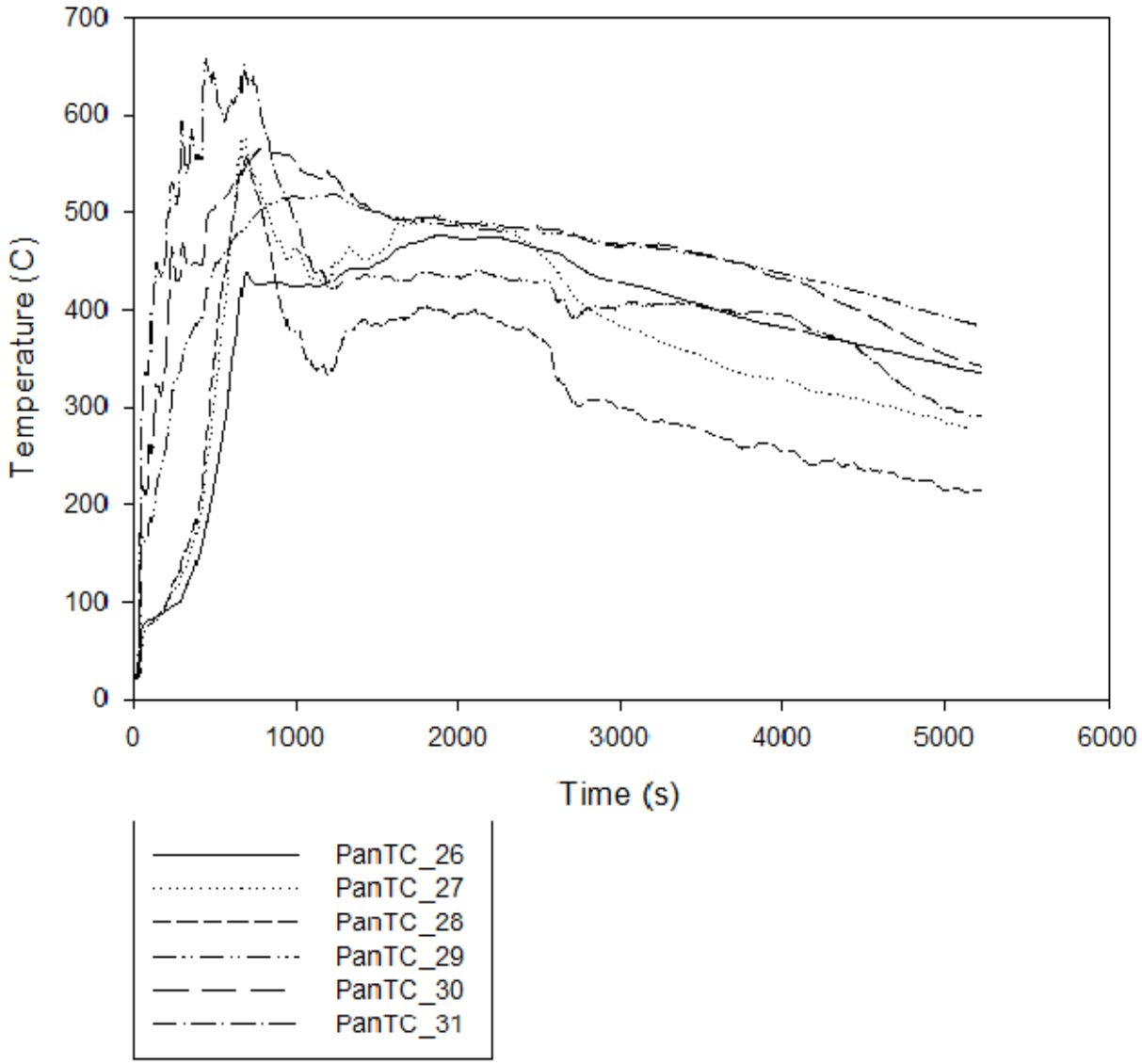

Figure 8-34: Sodium Pool Test 6, Sidewall Pan TC Temperatures versus Time

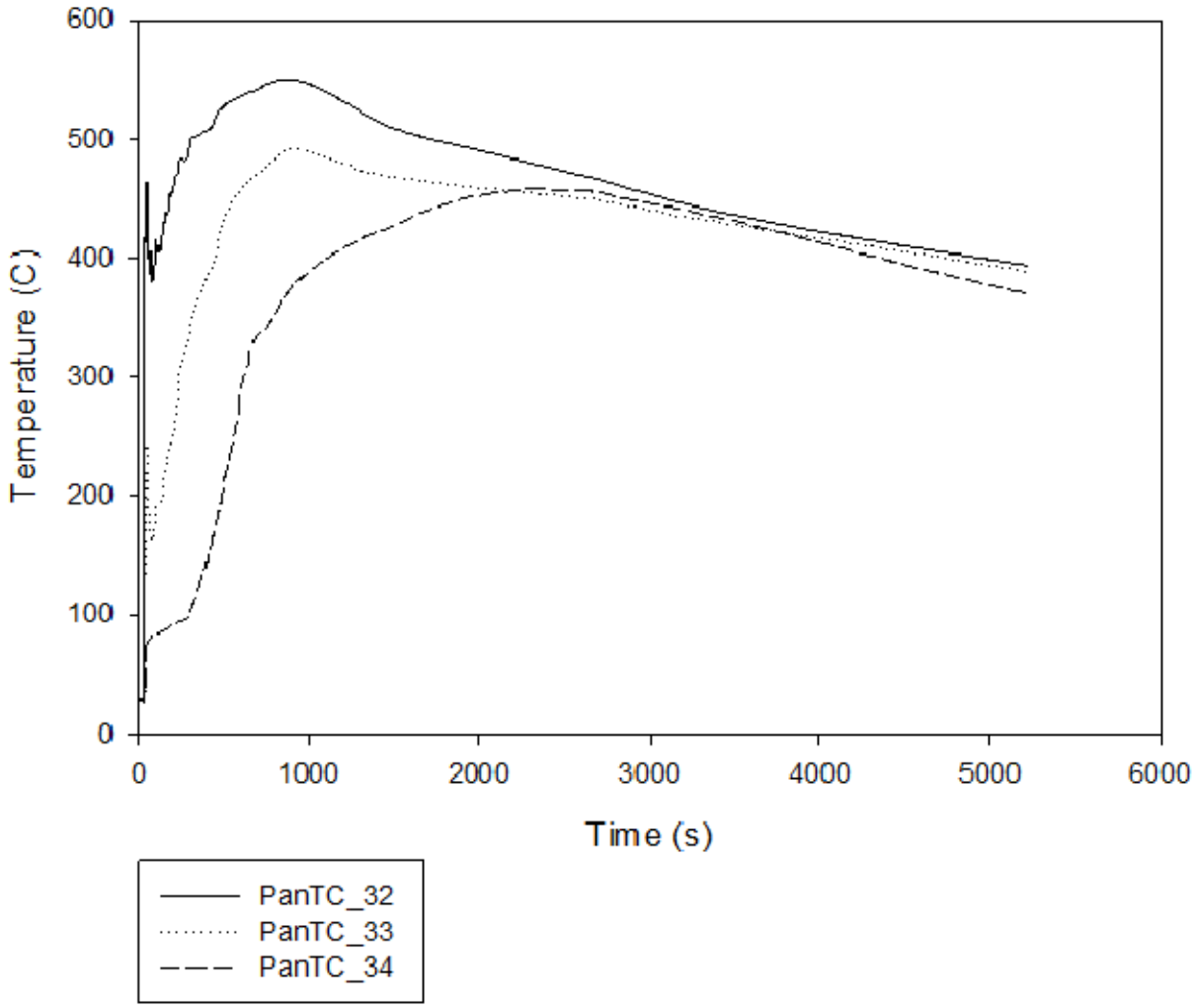

Figure 8-35: Sodium Pool Test 6, Inside Top of Pan TC Temperatures versus Time

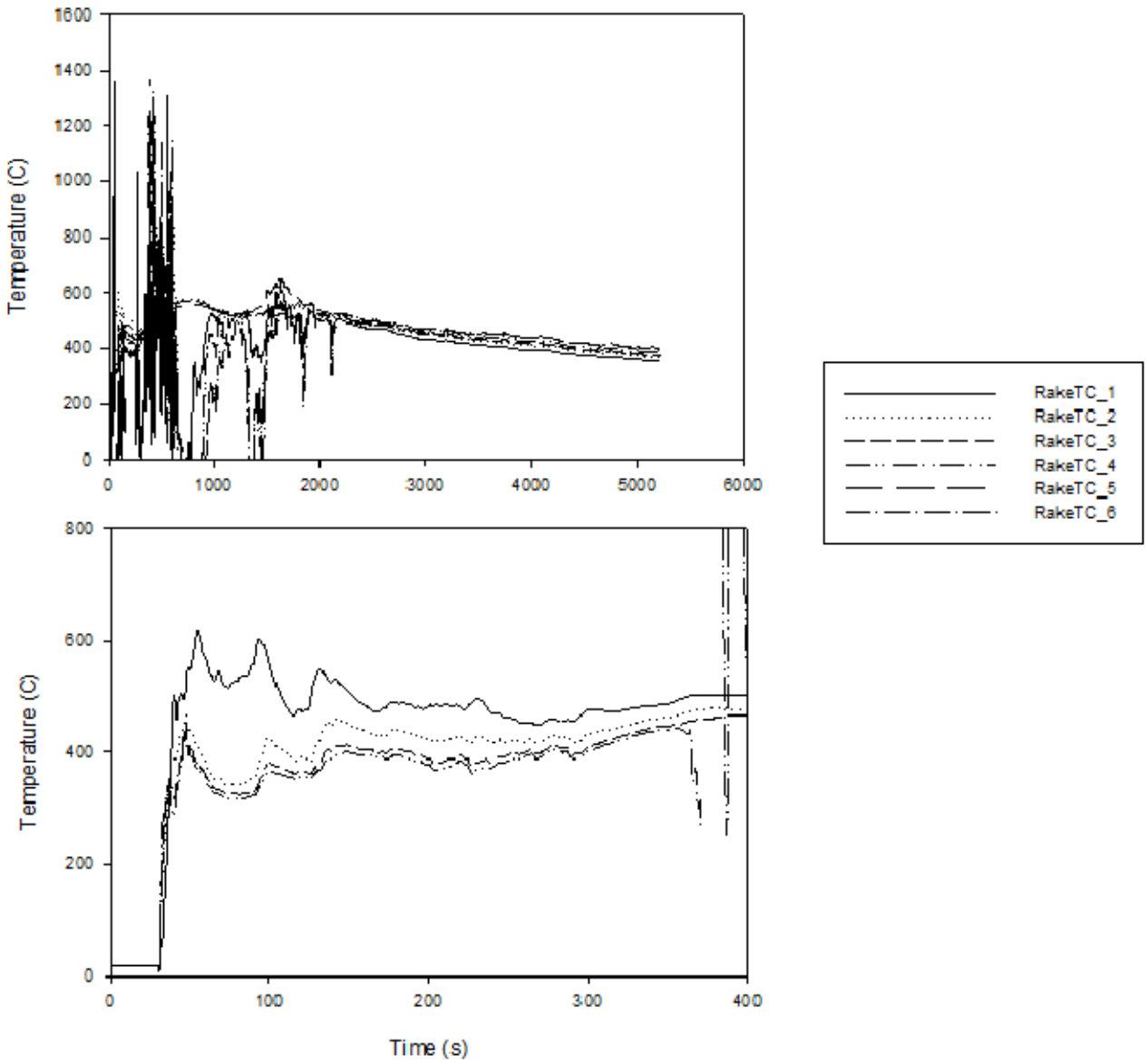

Figure 8-36: Sodium Pool Test 6, Inside Pan Rake TC Temperatures versus Time

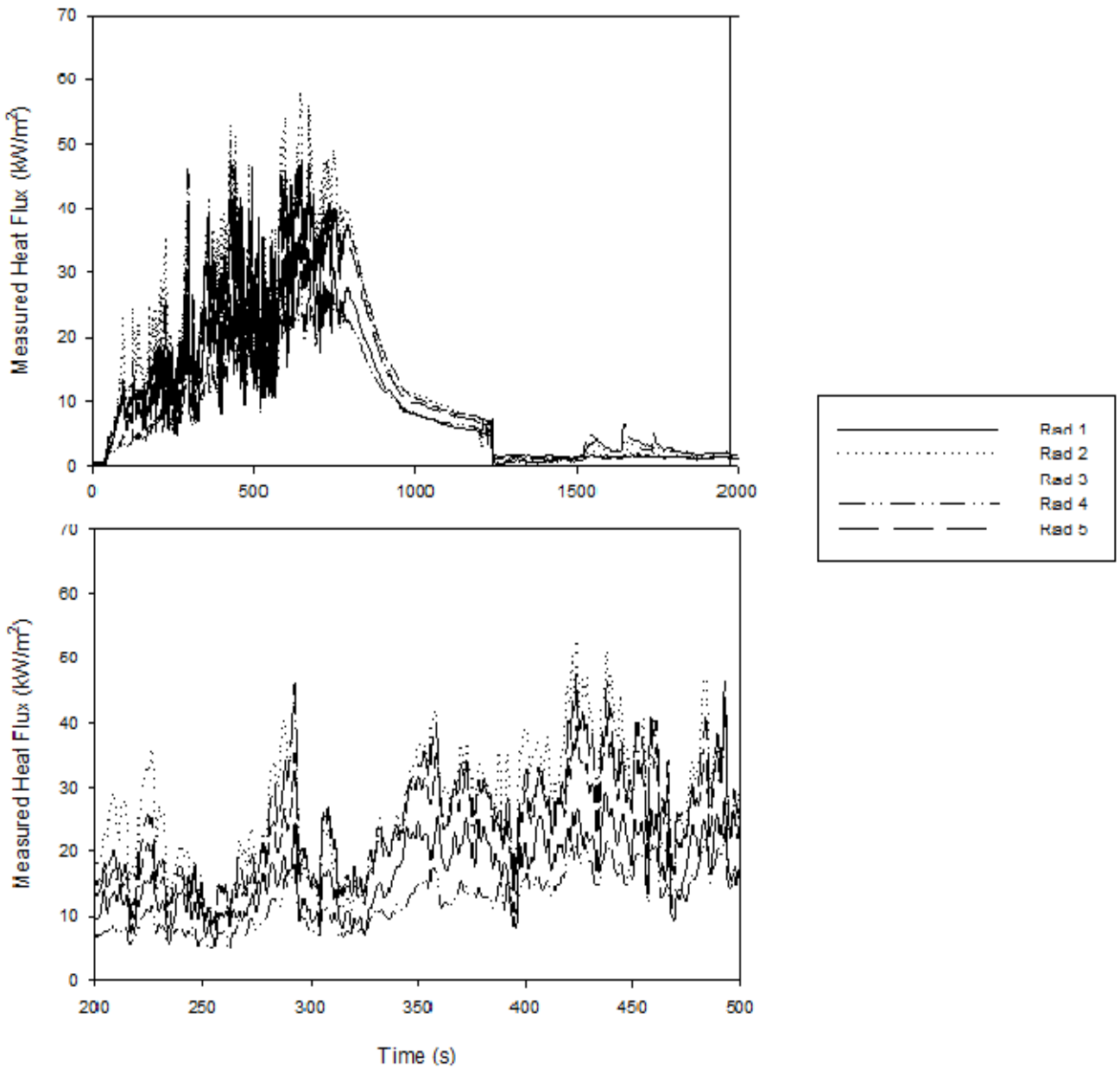

Figure 8-37: Sodium Pool Test 6, Measured Heat Flux versus Time

8.5.6 Sodium Pool Test 7 Measured Data

For instrumentation locations and specifications referred to in the figures of this section please reference Section 8.2. This section displays the measured data from sodium pool test 7.

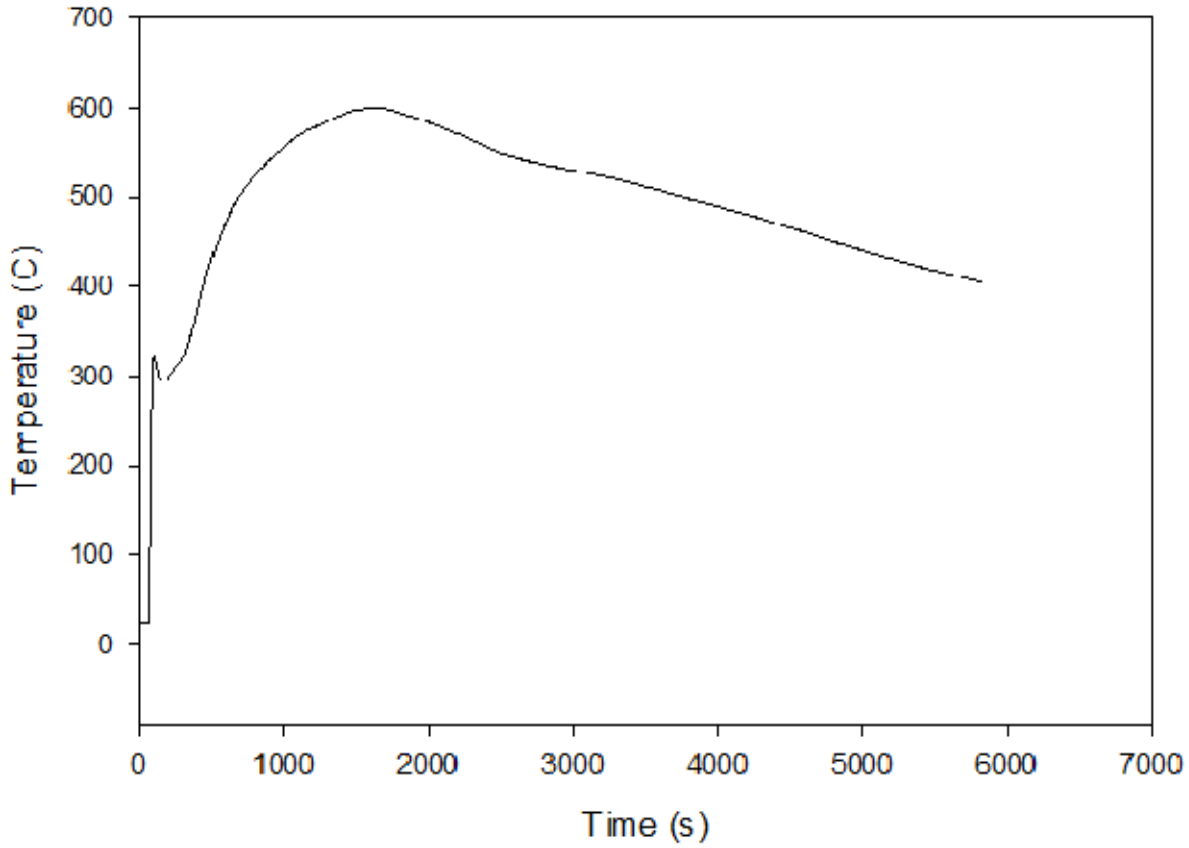

Figure 8-38: Sodium Pool Test 7, Pan Bottom Center TC Temperature versus Time

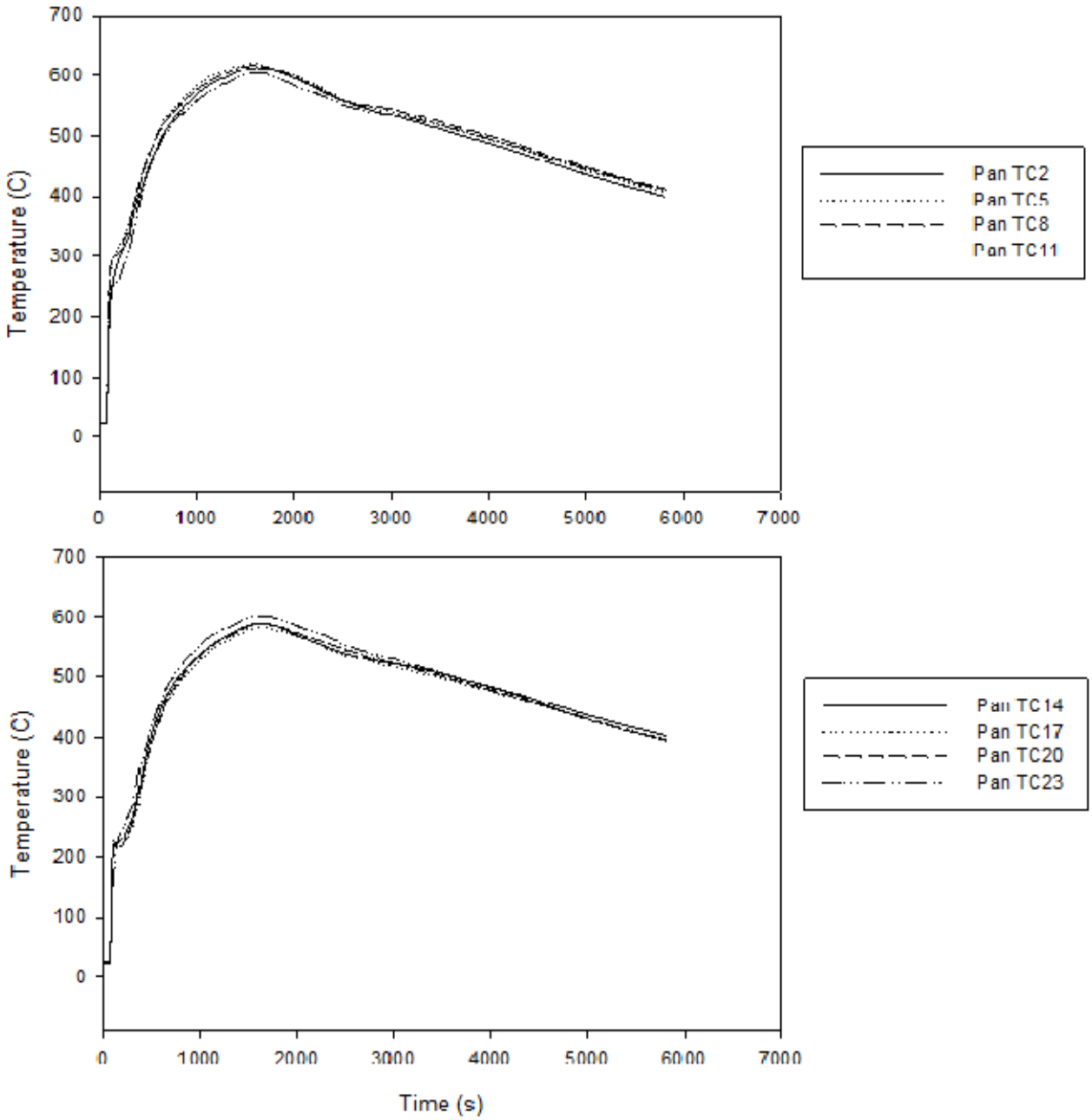

Figure 8-39: Sodium Pool Test 7, Pan Bottom 1/3 Radius TC Temperatures versus Time

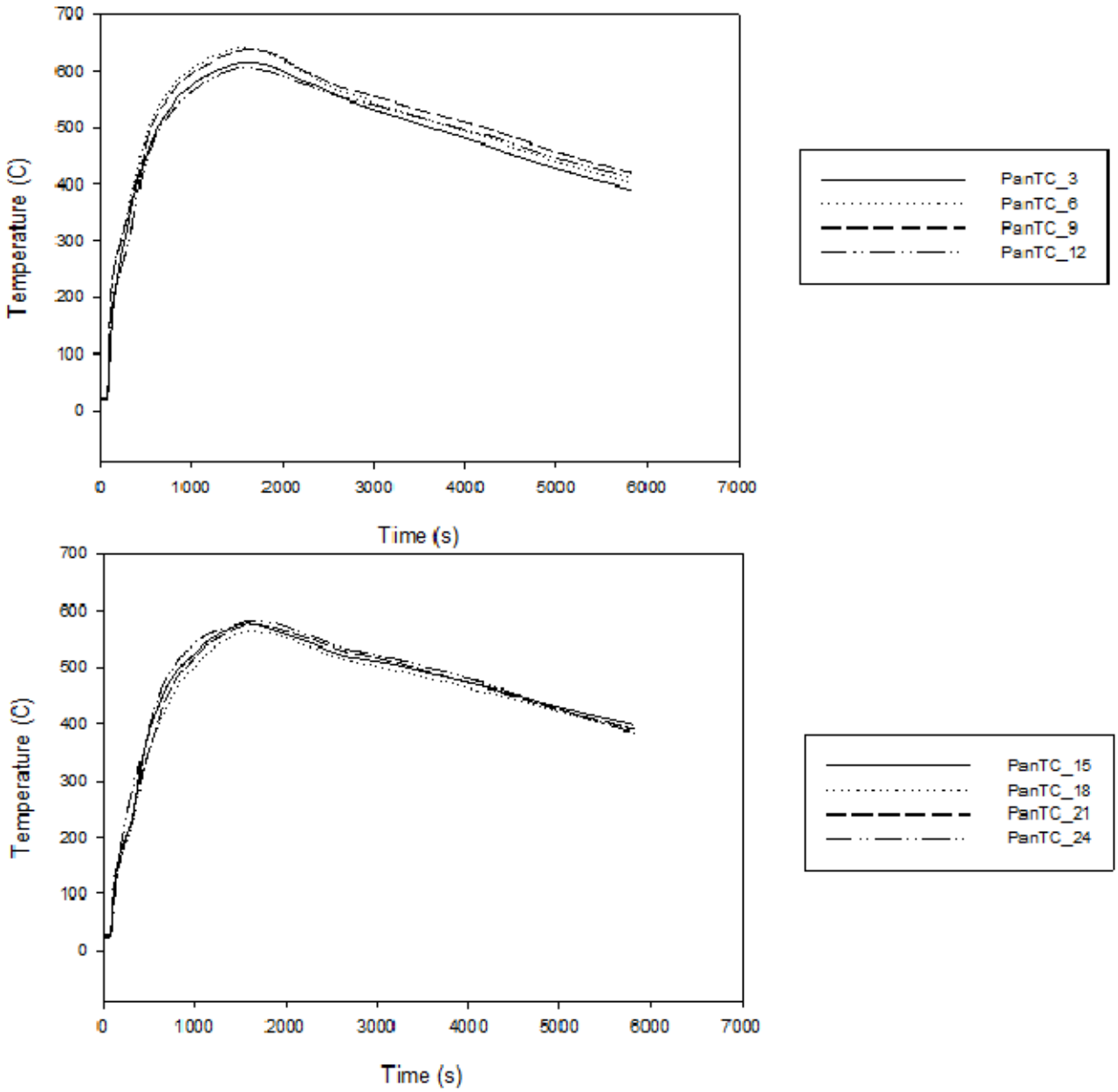

Figure 8-40: Sodium Pool Test 7, Pan Bottom 2/3 Radius TC Temperatures versus Time

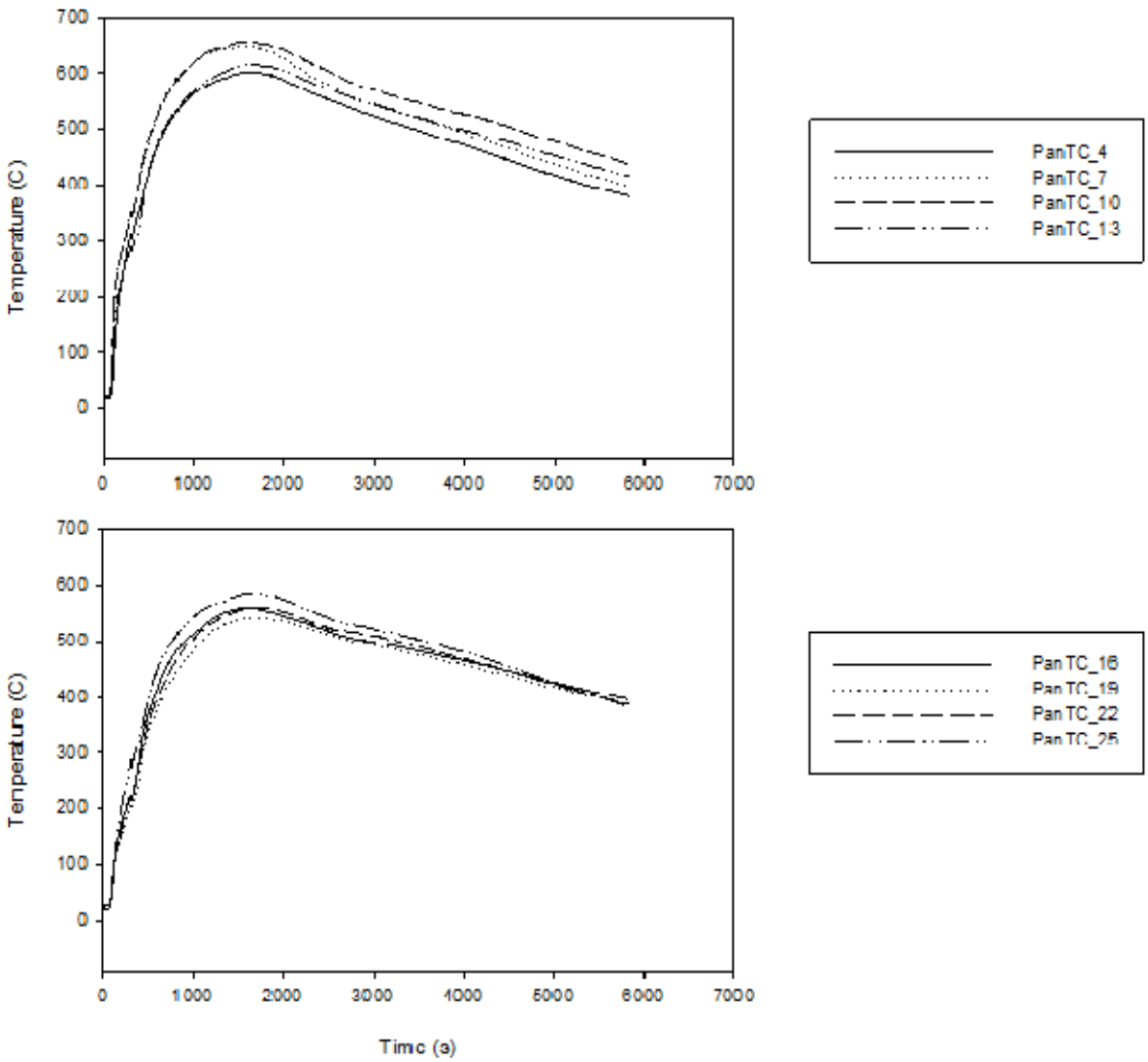

Figure 8-41: Sodium Pool Test 7, Pan Bottom Full Radius TC Temperatures versus Time

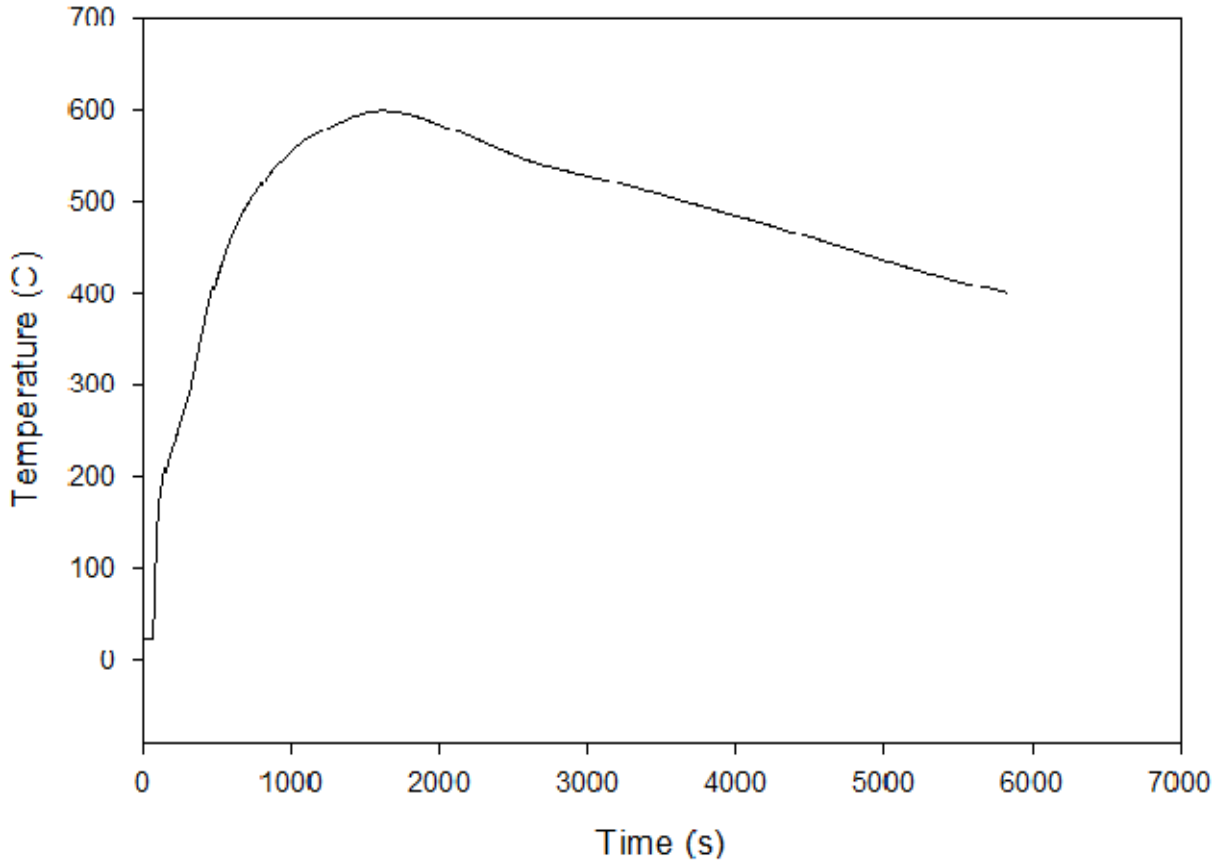

Figure 8-42: Sodium Pool Test 7, Averaged Pan Bottom TCs' Temperatures versus Time

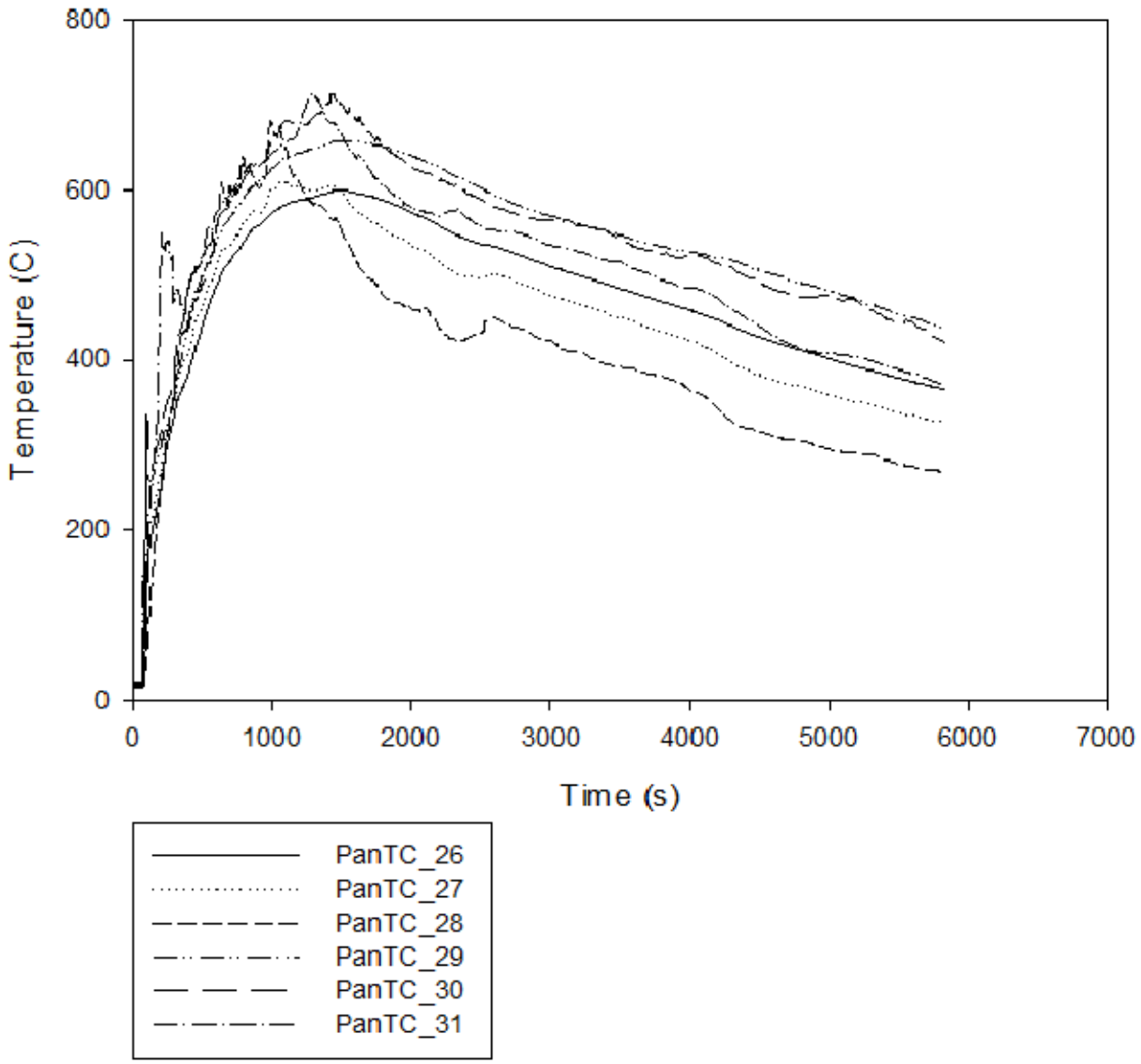

Figure 8-43: Sodium Pool Test 7, Sidewall Pan TC Temperatures versus Time

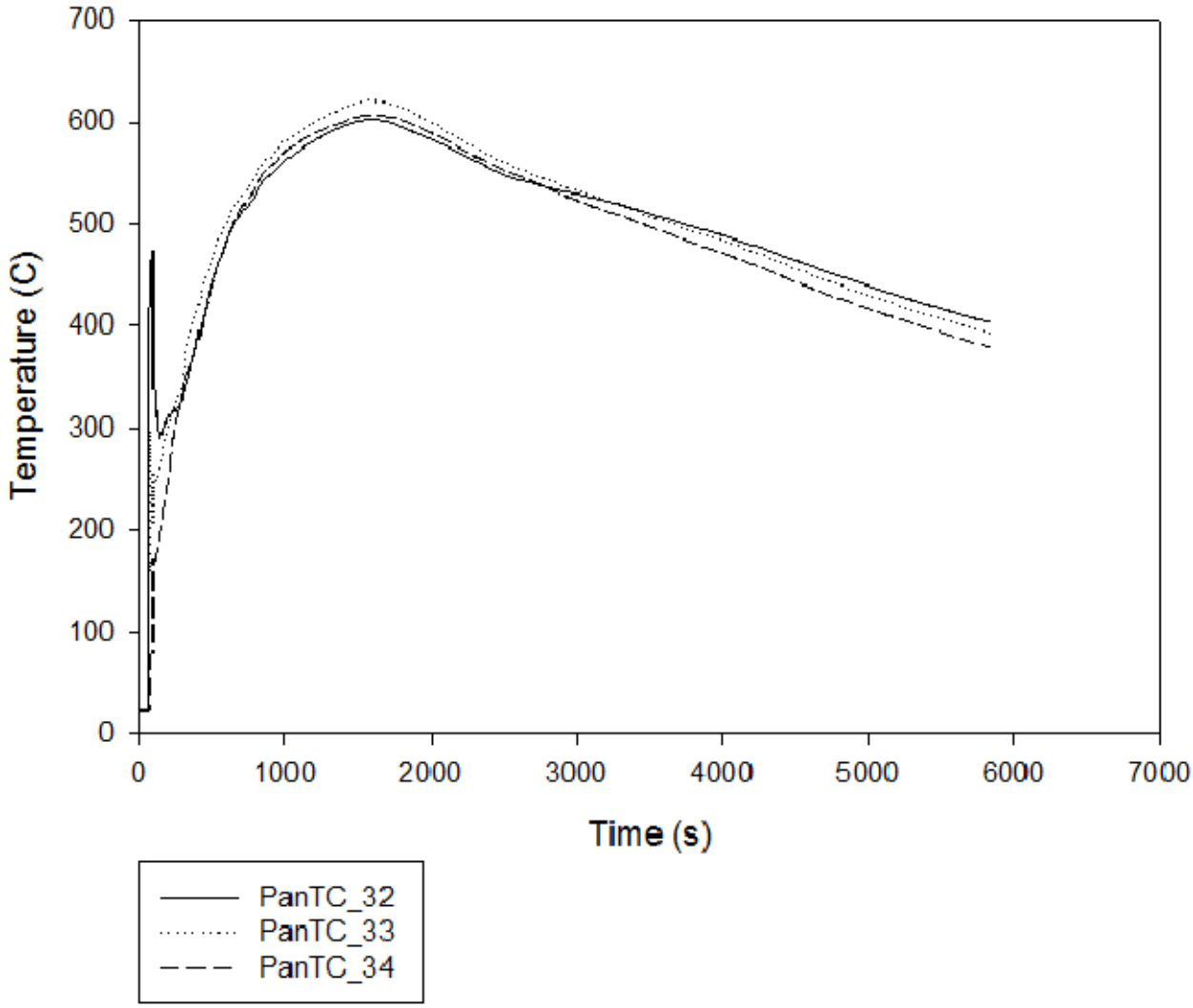

Figure 8-44: Sodium Pool Test 7, Inside Top of Pan TC Temperatures versus Time

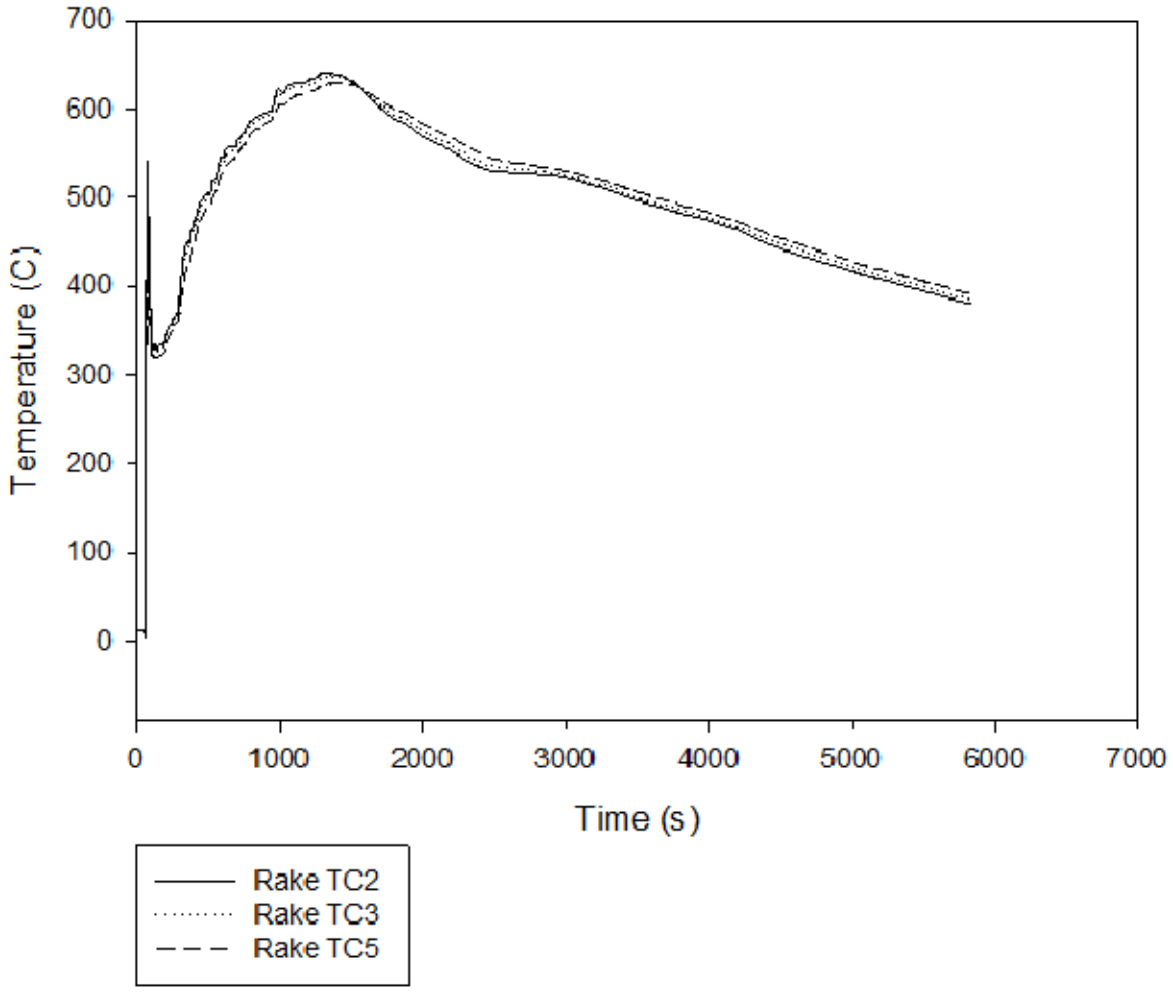

Figure 8-45: Sodium Pool Test 7, Inside Pan Rake TC Temperatures versus Time

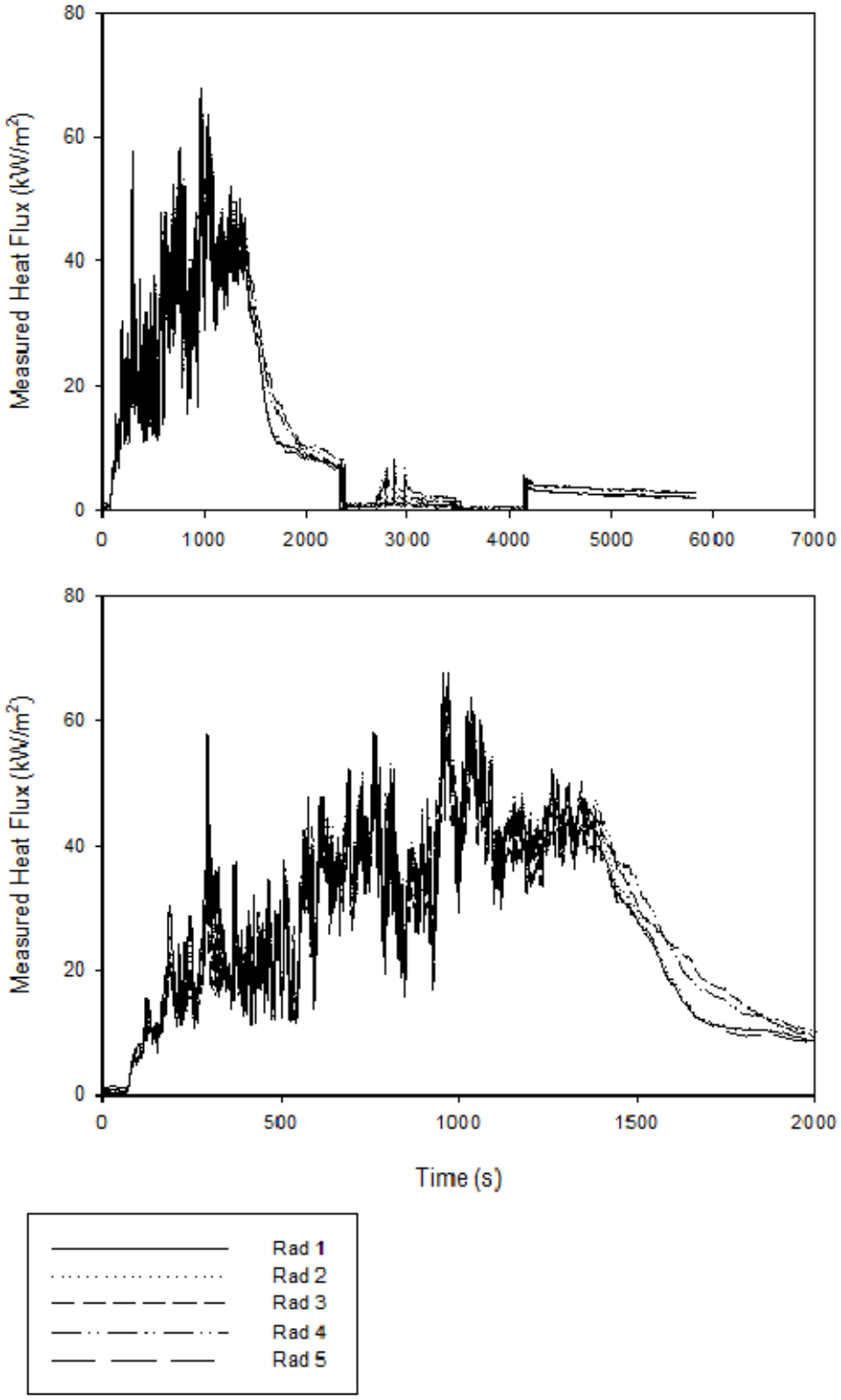

Figure 8-46: Sodium Pool Test 7, Measured Heat Flux versus Time

8.5.7 Sodium Pool Test 8 Measured Data

For instrumentation locations and specifications referred to in the figures of this section please reference Section 8.2. This section displays the measured data from sodium pool test 8.

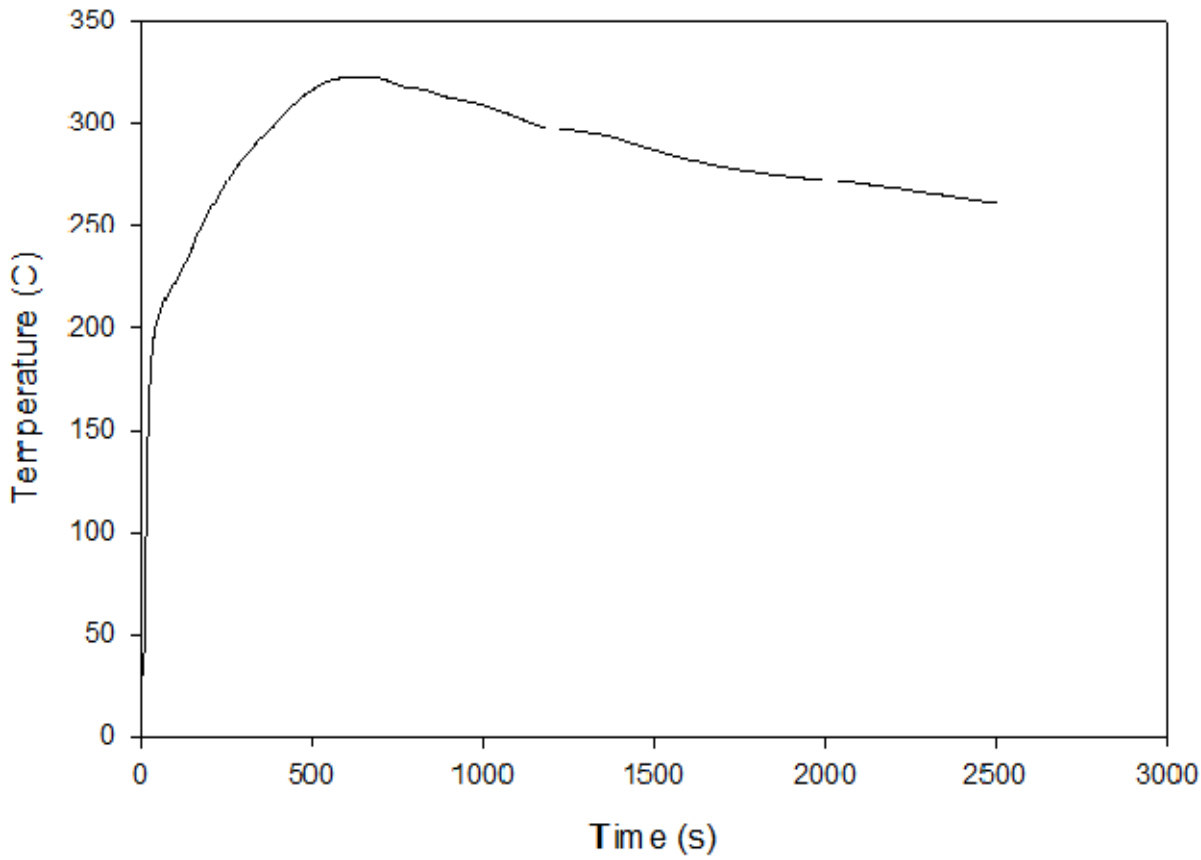

Figure 8-47: Sodium Pool Test 8, Pan Bottom Center TC Temperature versus Time

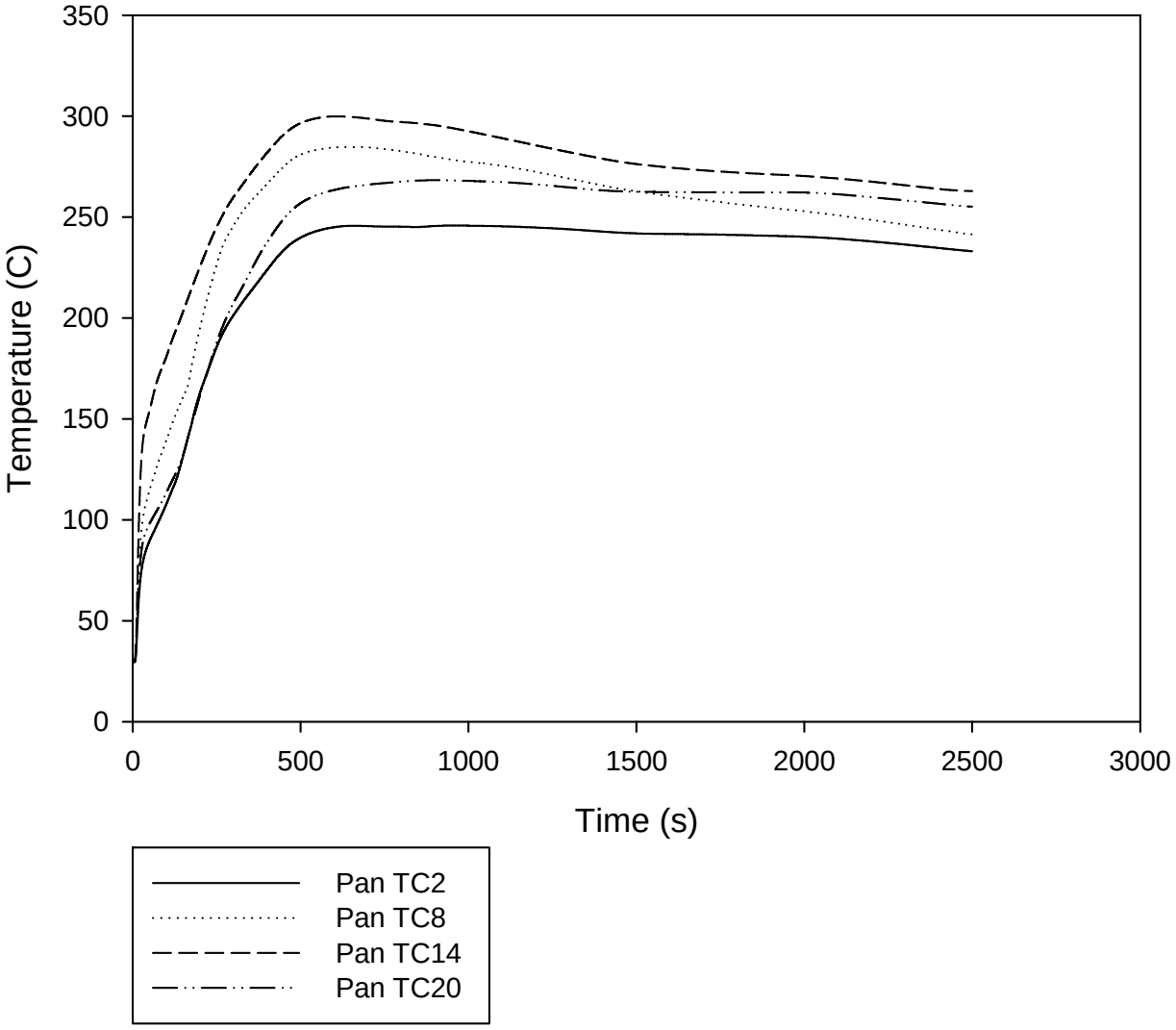

Figure 8-48: Sodium Pool Test 8, Pan Bottom 1/3 Radius TC Temperatures versus Time

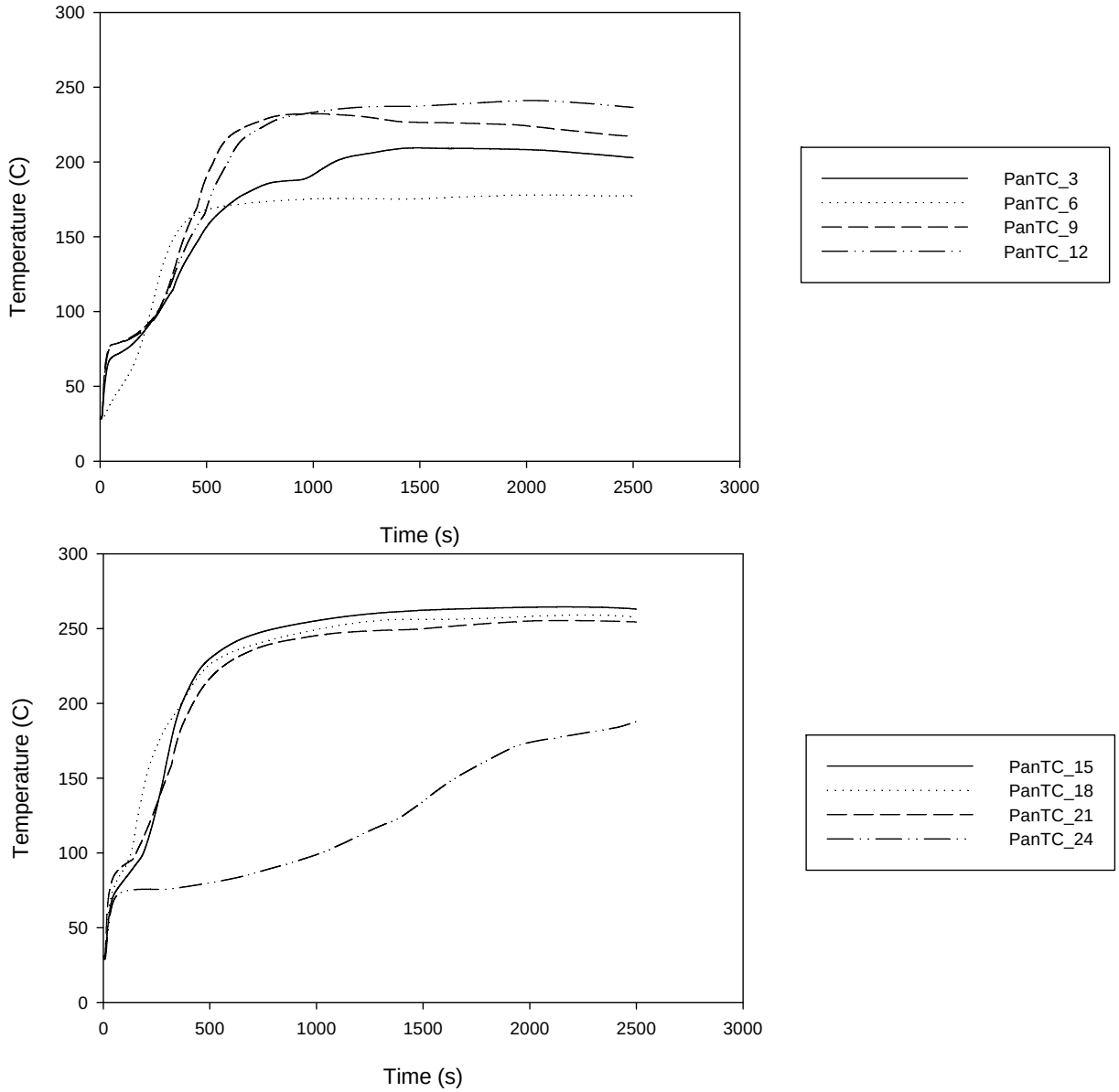

Figure 8-49: Sodium Pool Test 8, Pan Bottom 2/3 Radius TC Temperatures versus Time

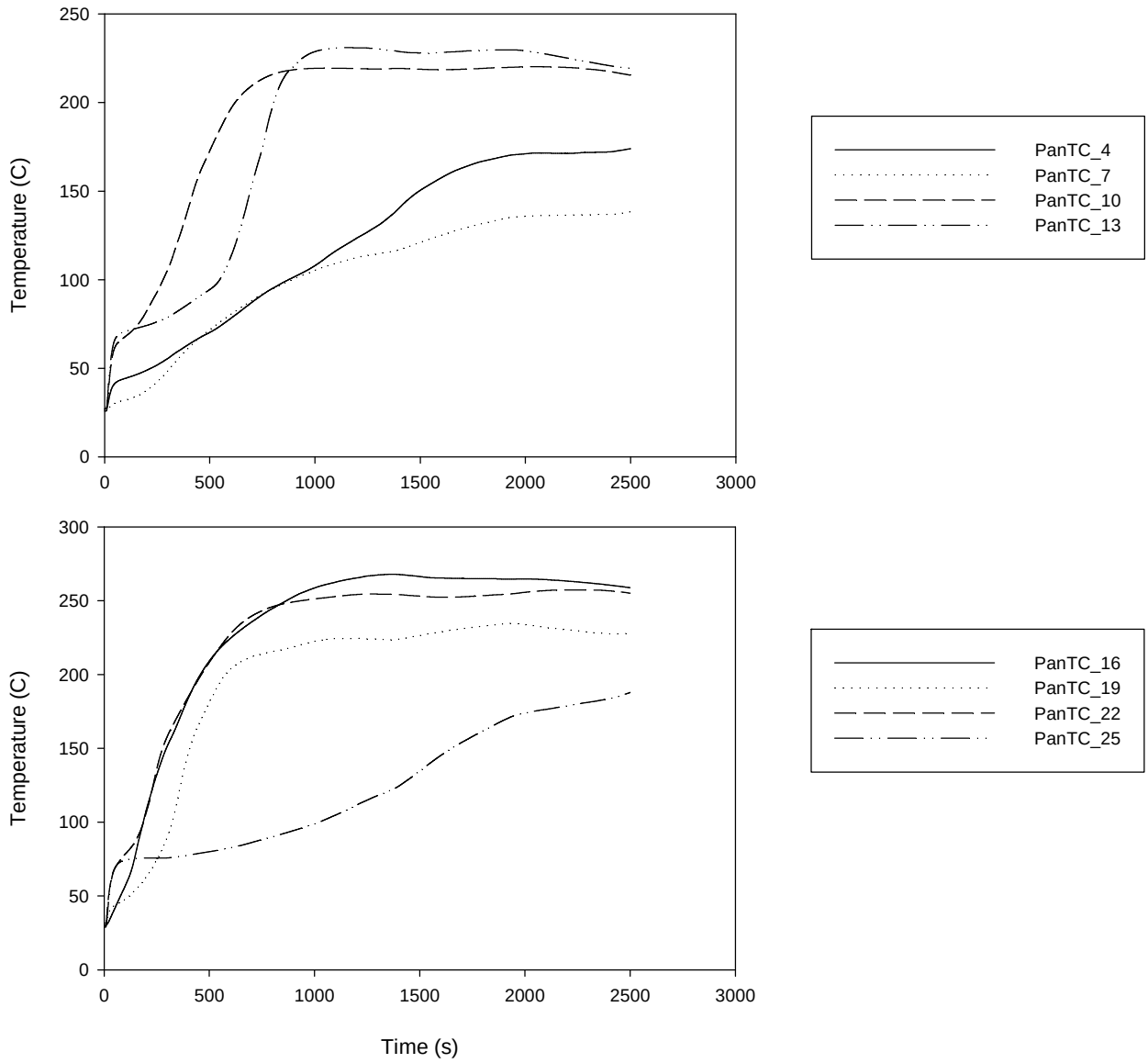

Figure 8-50: Sodium Pool Test 8, Pan Bottom Full Radius TC Temperatures versus Time

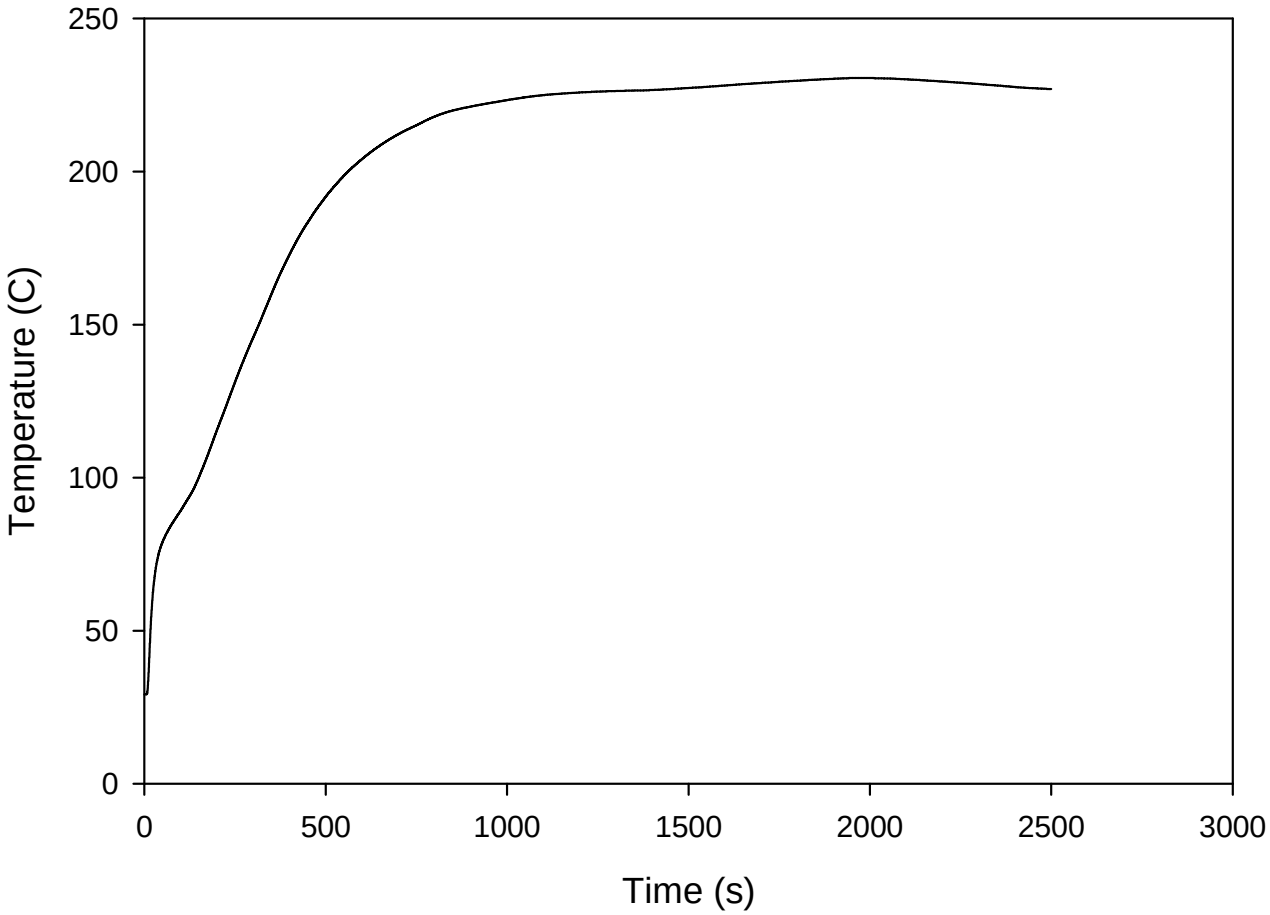

Figure 8-51: Sodium Pool Test 8, Averaged Pan Bottom TCs' Temperatures versus Time

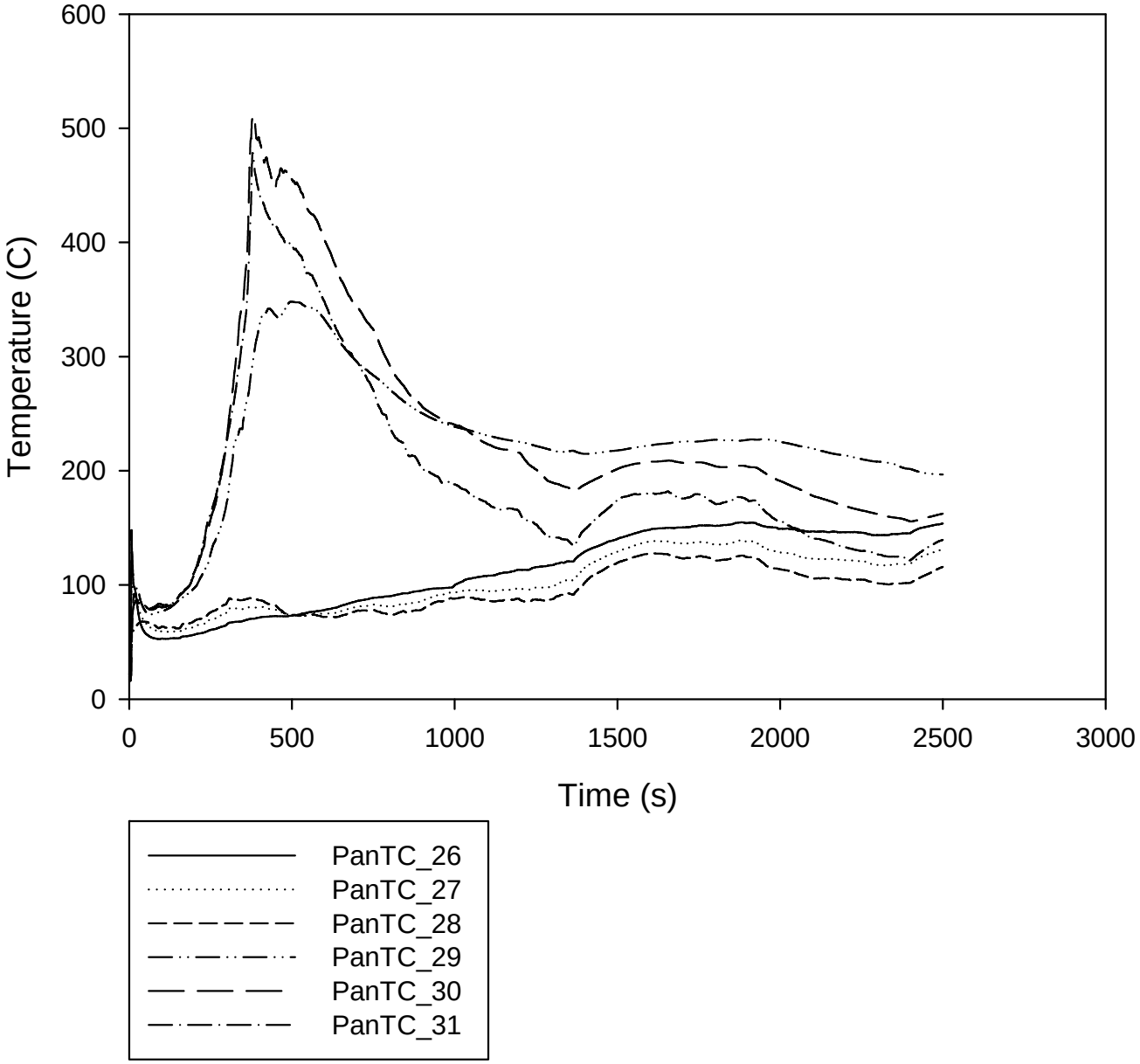

Figure 8-52: Sodium Pool Test 8, Sidewall Pan TC Temperatures versus Time

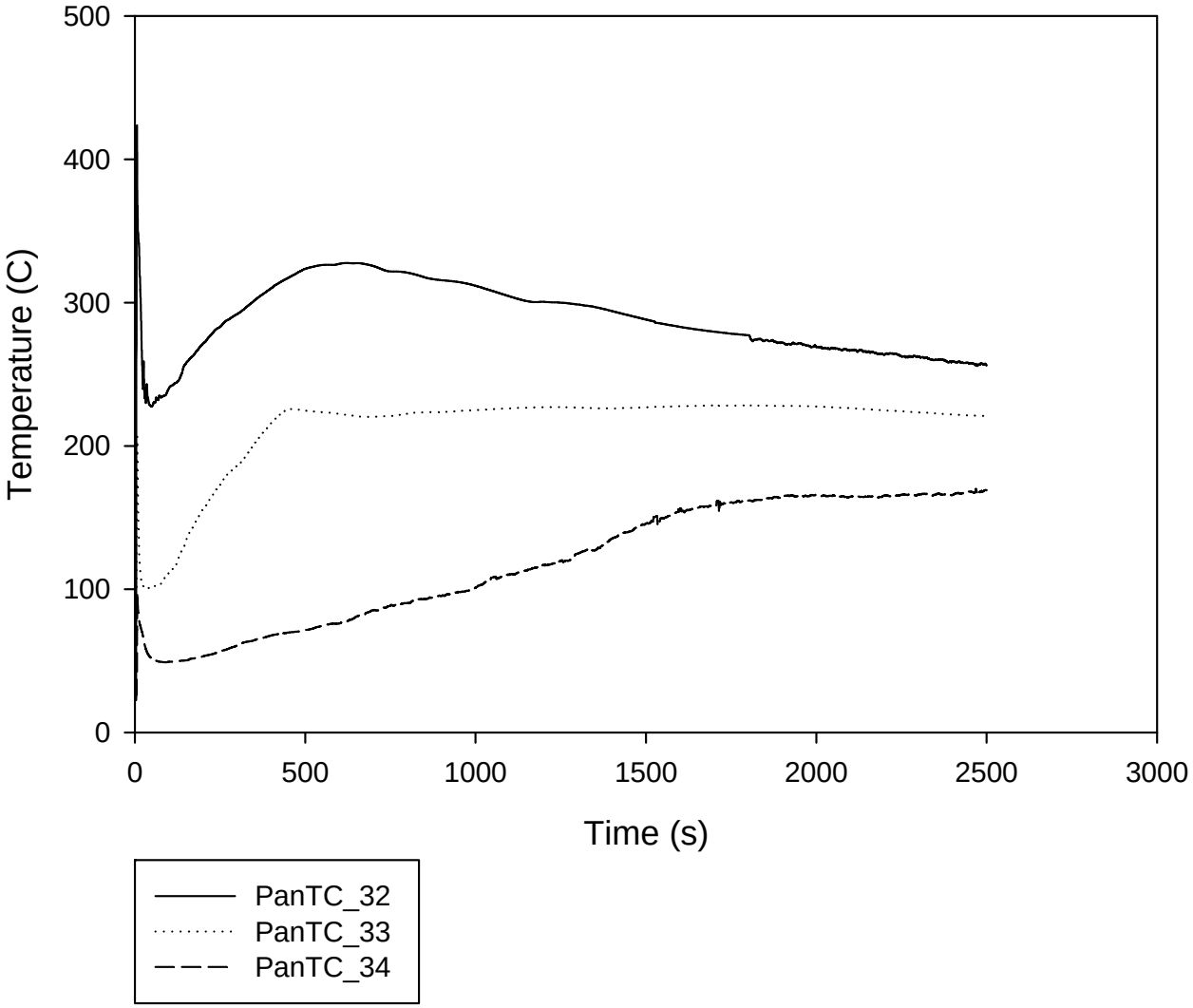

Figure 8-53: Sodium Pool Test 8, Inside Top of Pan TC Temperatures versus Time

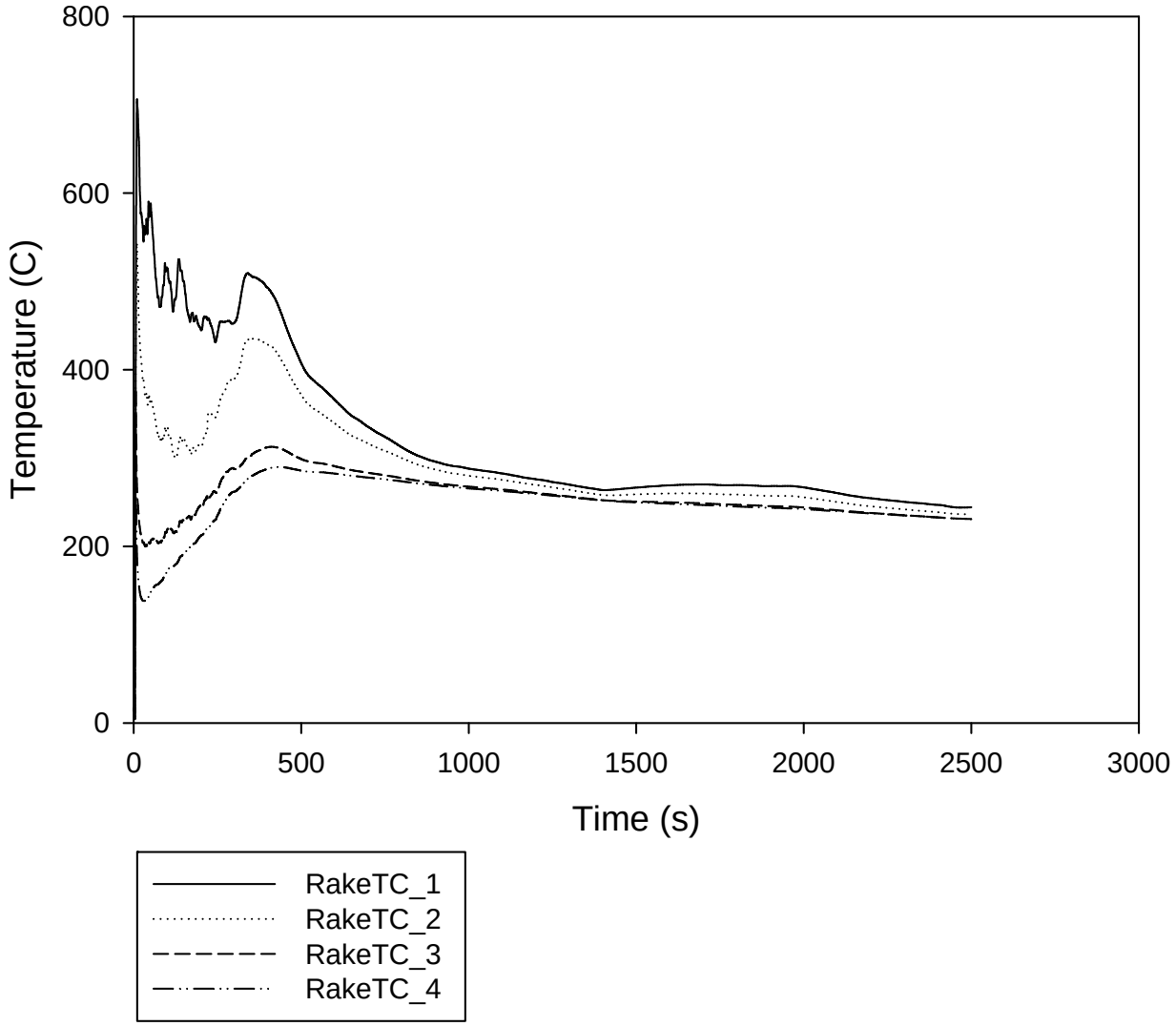

Figure 8-54: Sodium Pool Test 8, Inside Pan Rake TC Temperatures versus Time

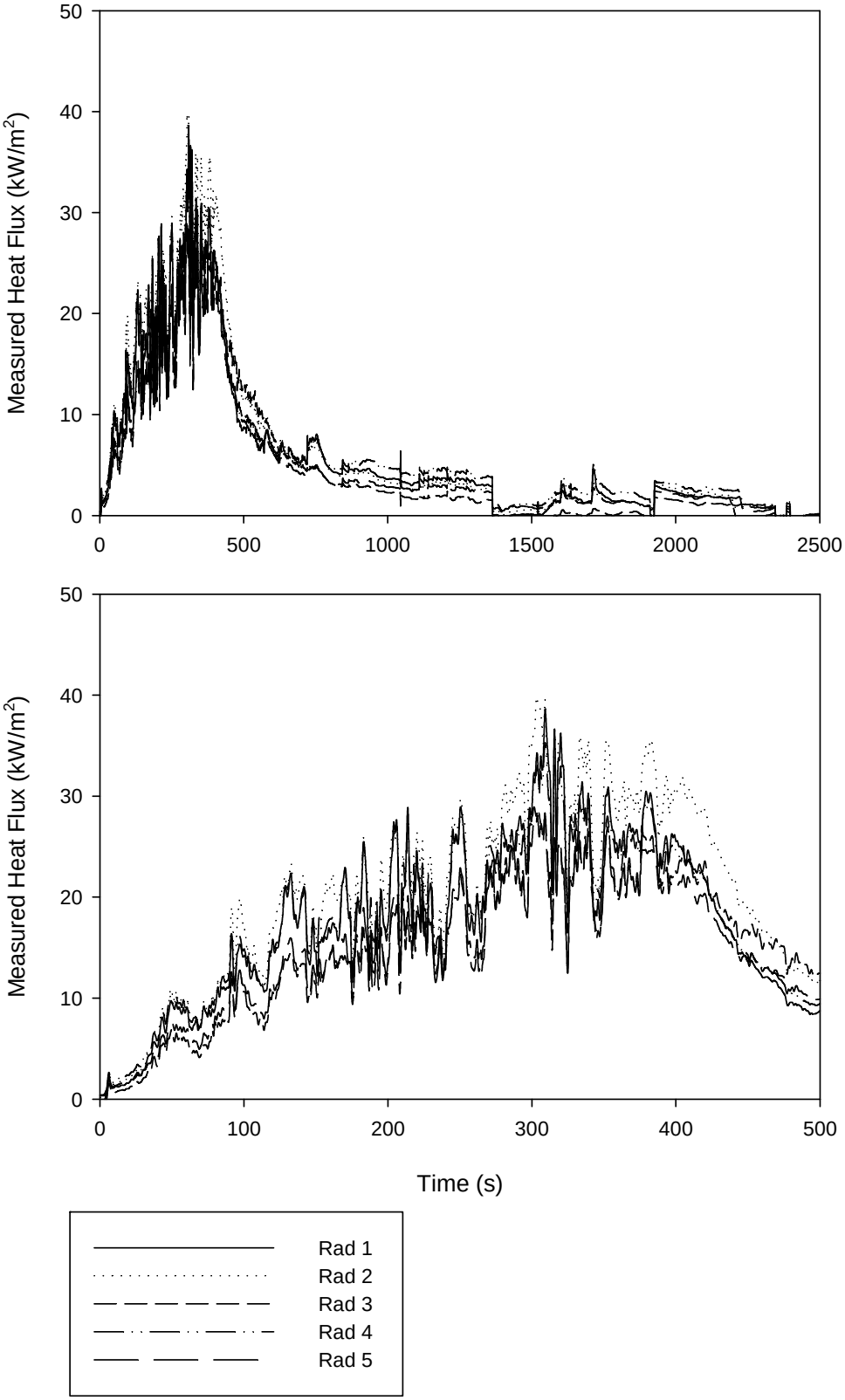

Figure 8-55: Sodium Pool Test 8, Measured Heat Flux versus Time

8.5.8 Sodium Pool Test 9 Measured Data

For instrumentation locations and specifications referred to in the figures of this section please reference Section 8.2. This section displays the measured data from sodium pool test 9.

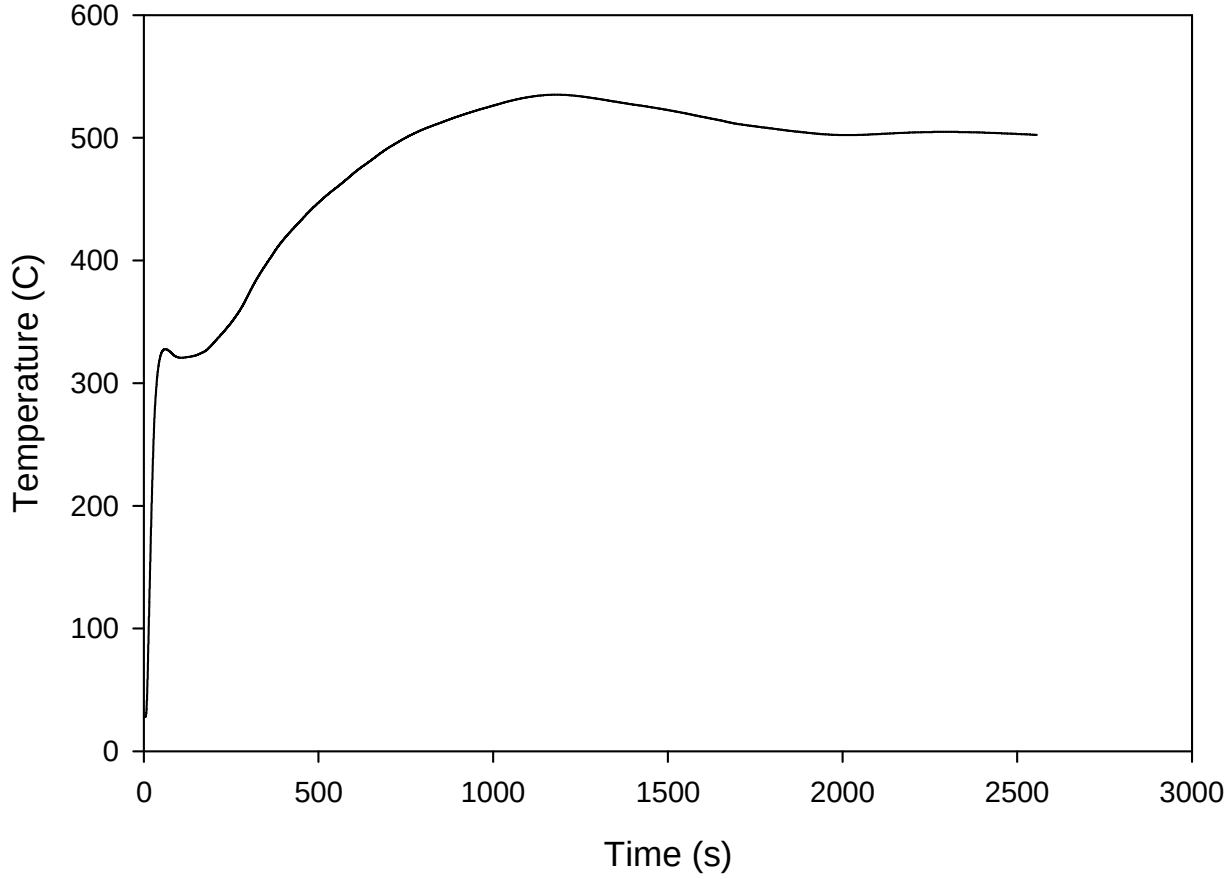

Figure 8-56: Sodium Pool Test 9, Pan Bottom Center TC Temperature versus Time

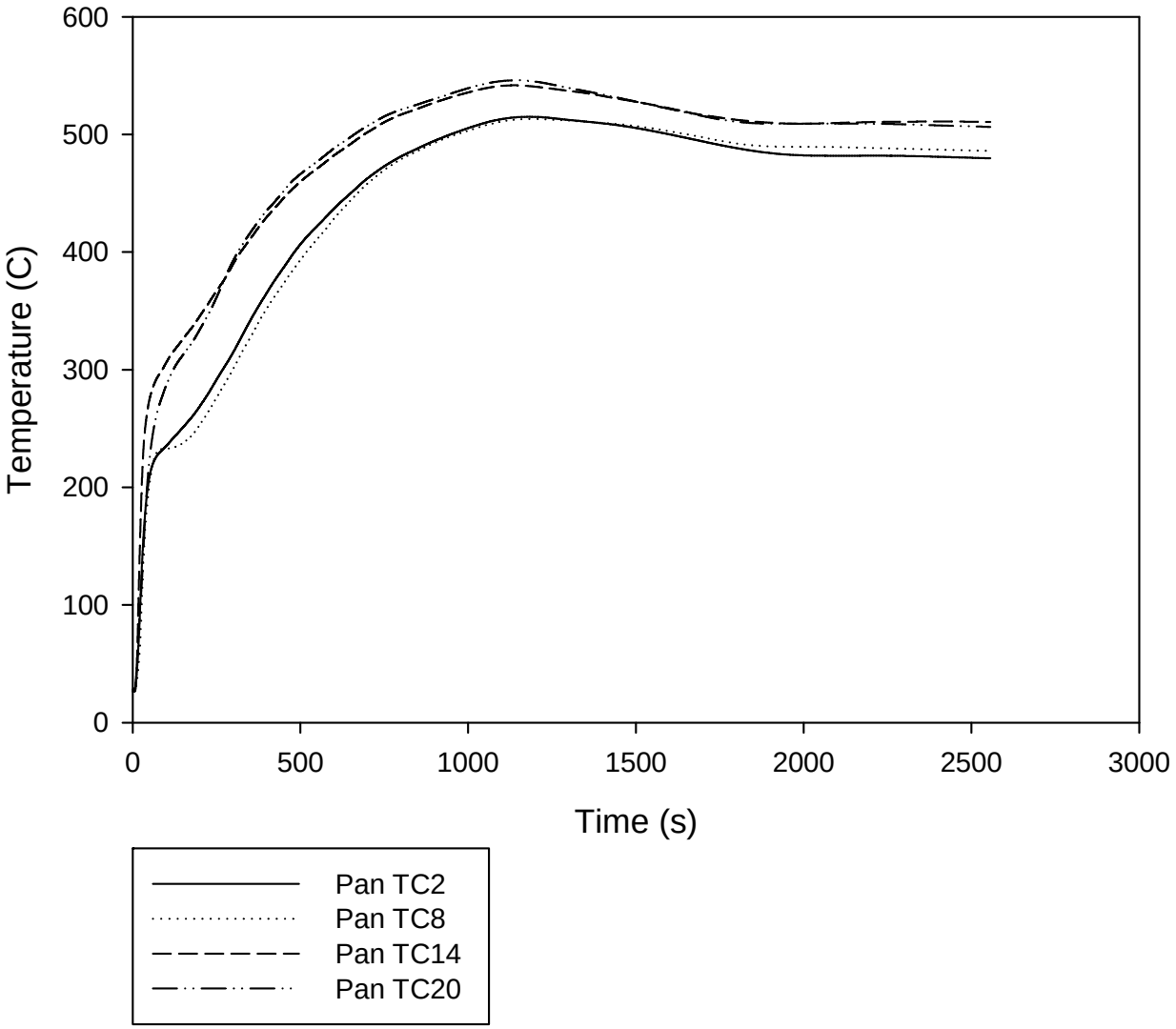

Figure 8-57: Sodium Pool Test 9, Pan Bottom 1/3 Radius TC Temperatures versus Time

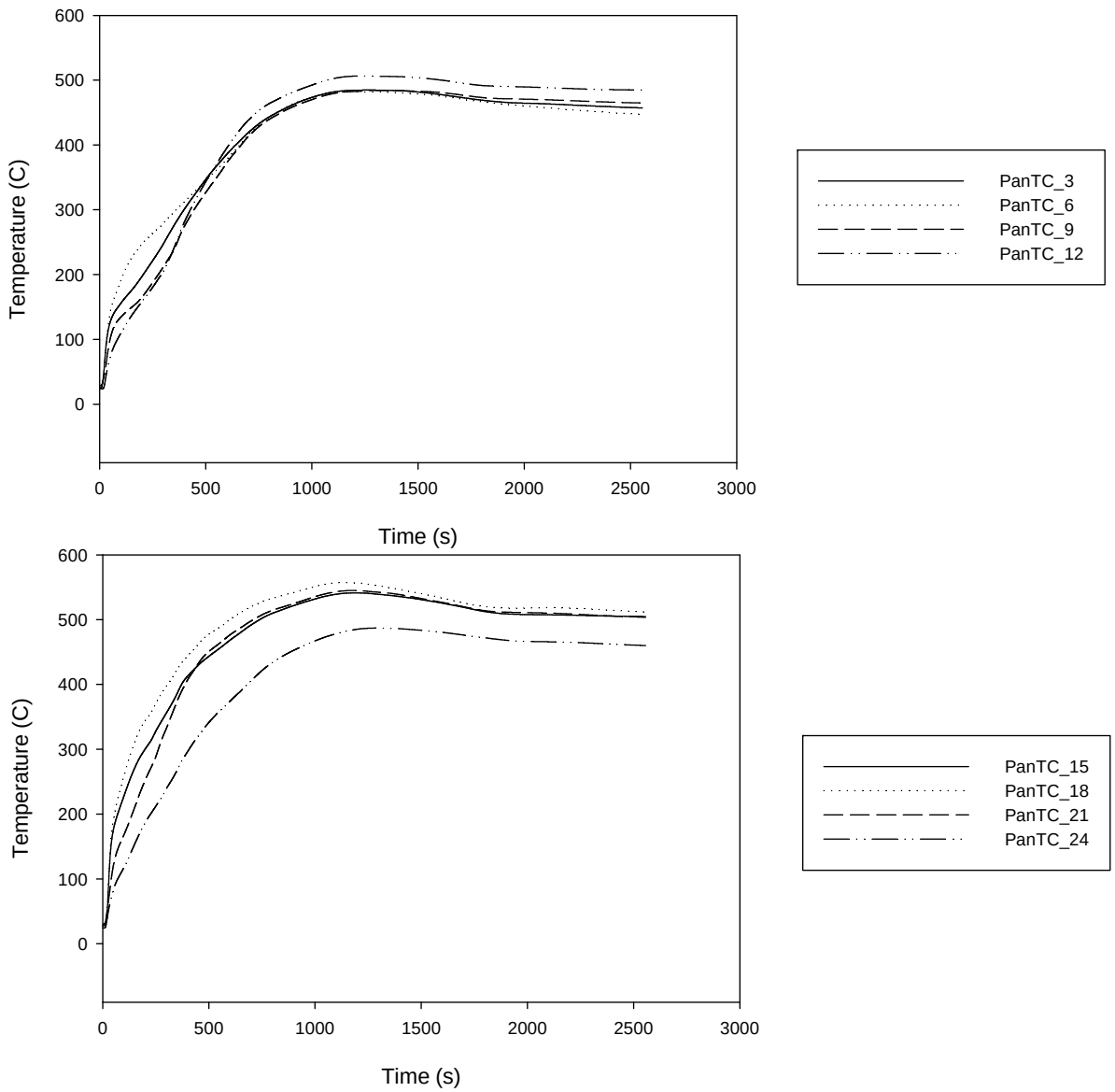

Figure 8-58: Sodium Pool Test 9, Pan Bottom 2/3 Radius TC Temperatures versus Time

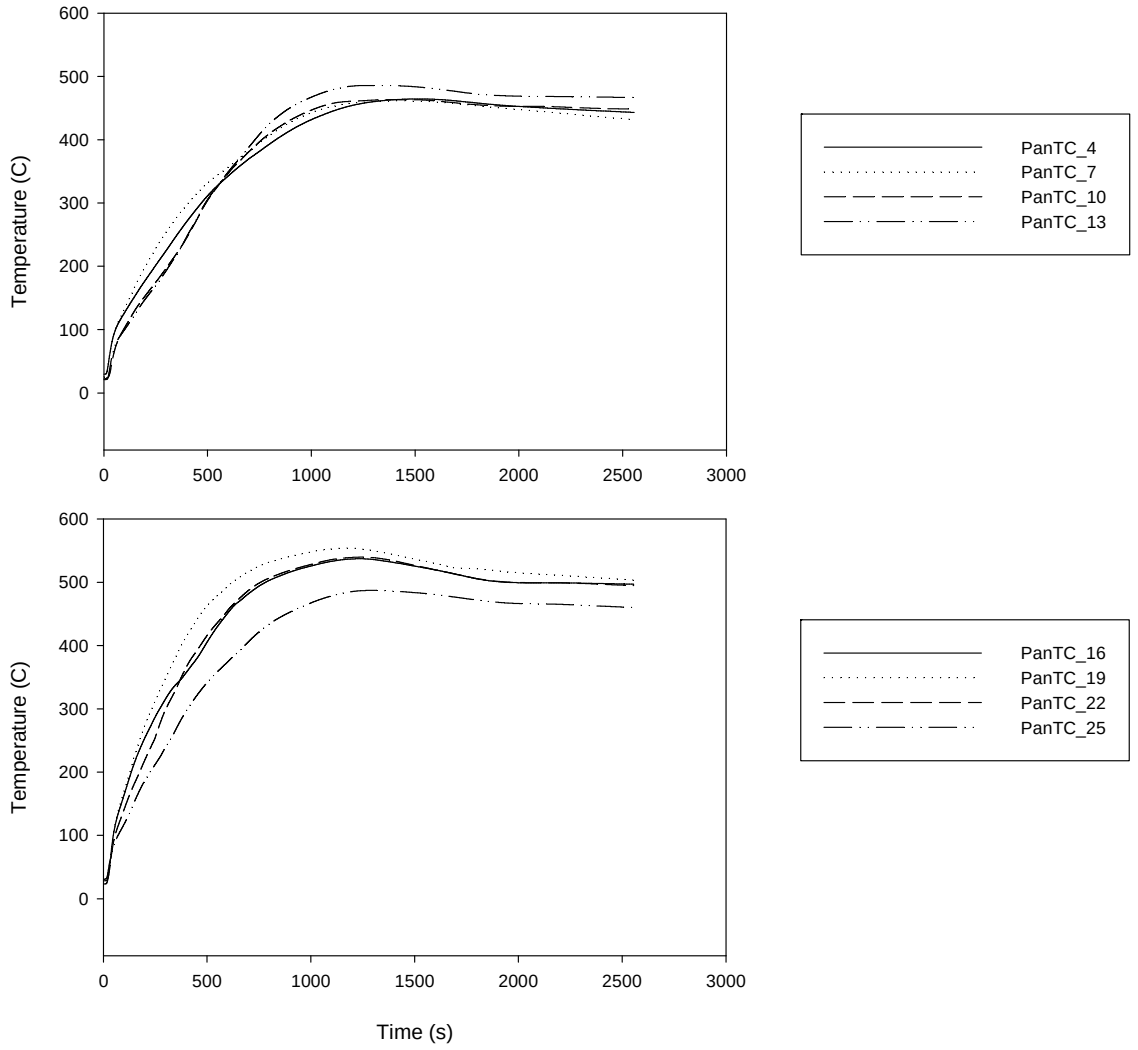

Figure 8-59: Sodium Pool Test 9, Pan Bottom Full Radius TC Temperatures versus Time

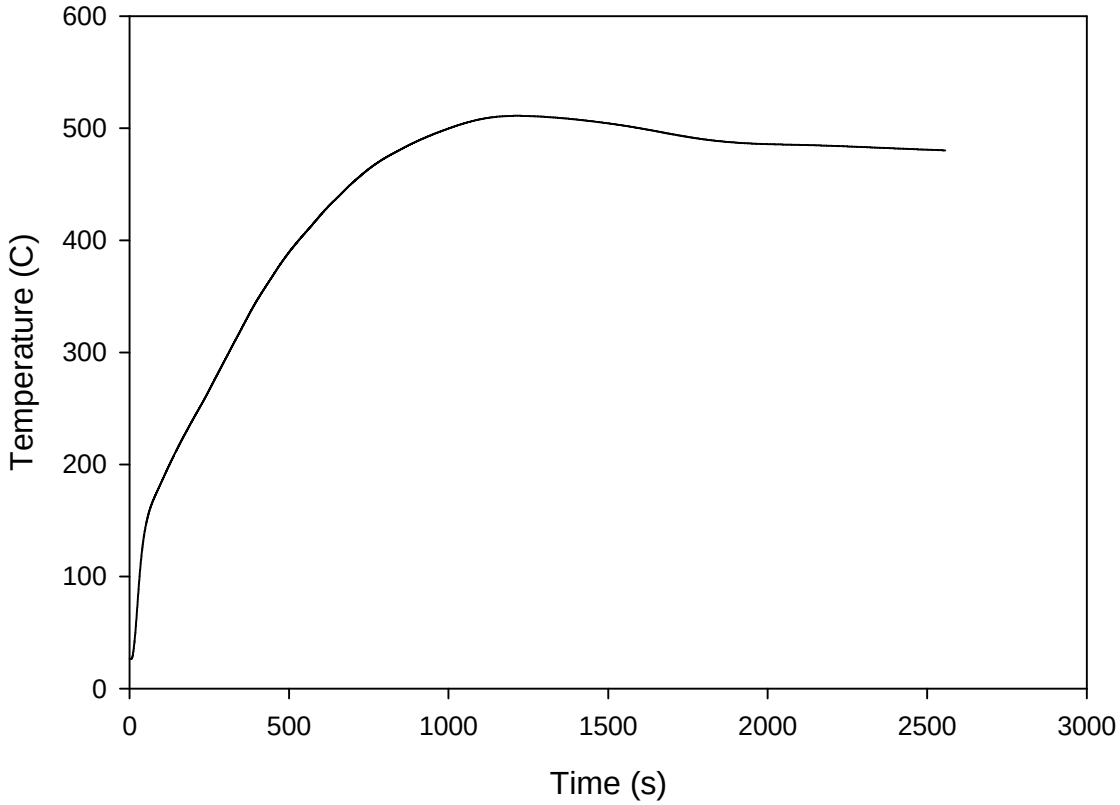

Figure 8-60: Sodium Pool Test 9, Averaged Pan Bottom TCs' Temperatures versus Time

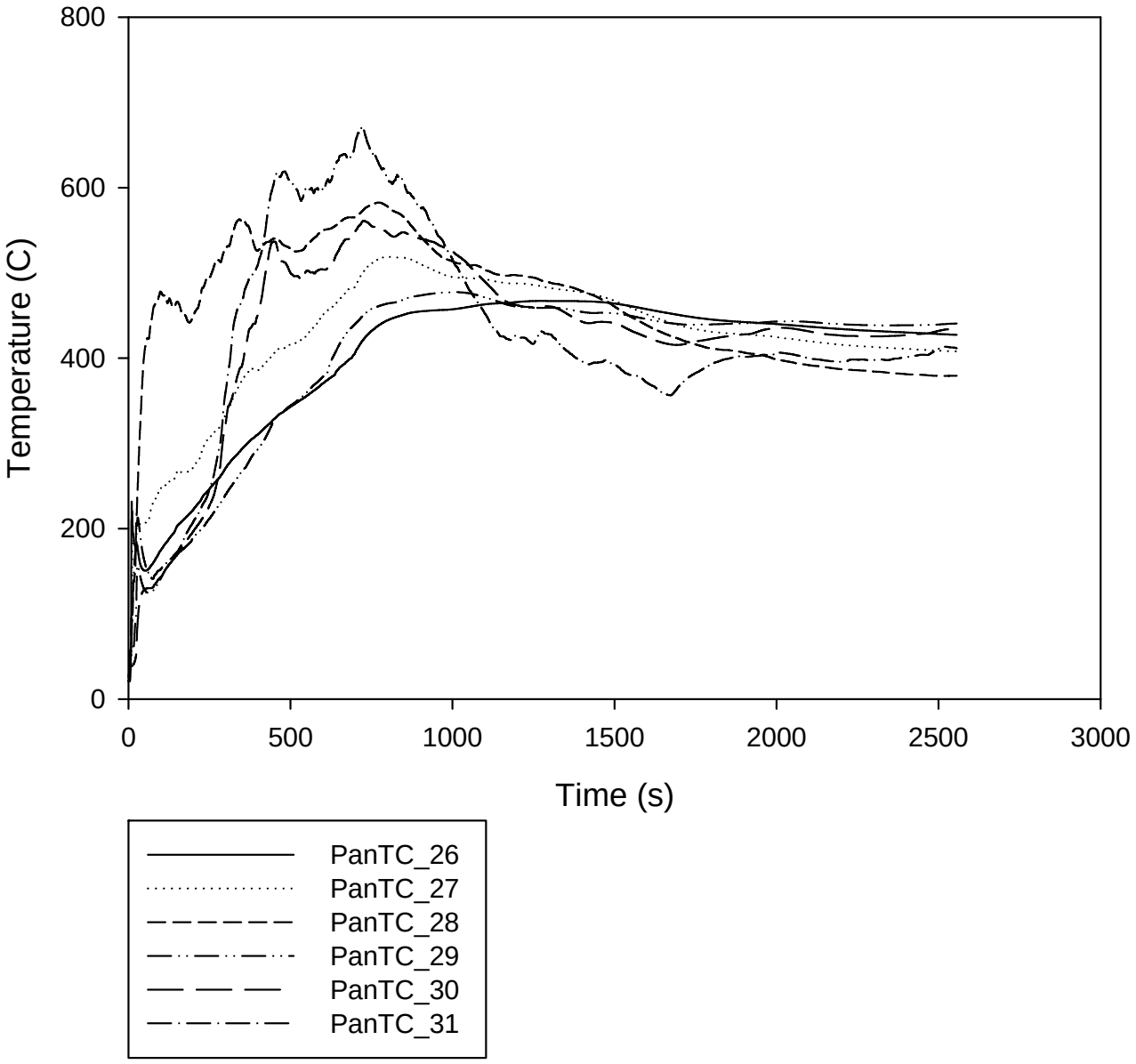

Figure 8-61: Sodium Pool Test 9, Sidewall Pan TC Temperatures versus Time

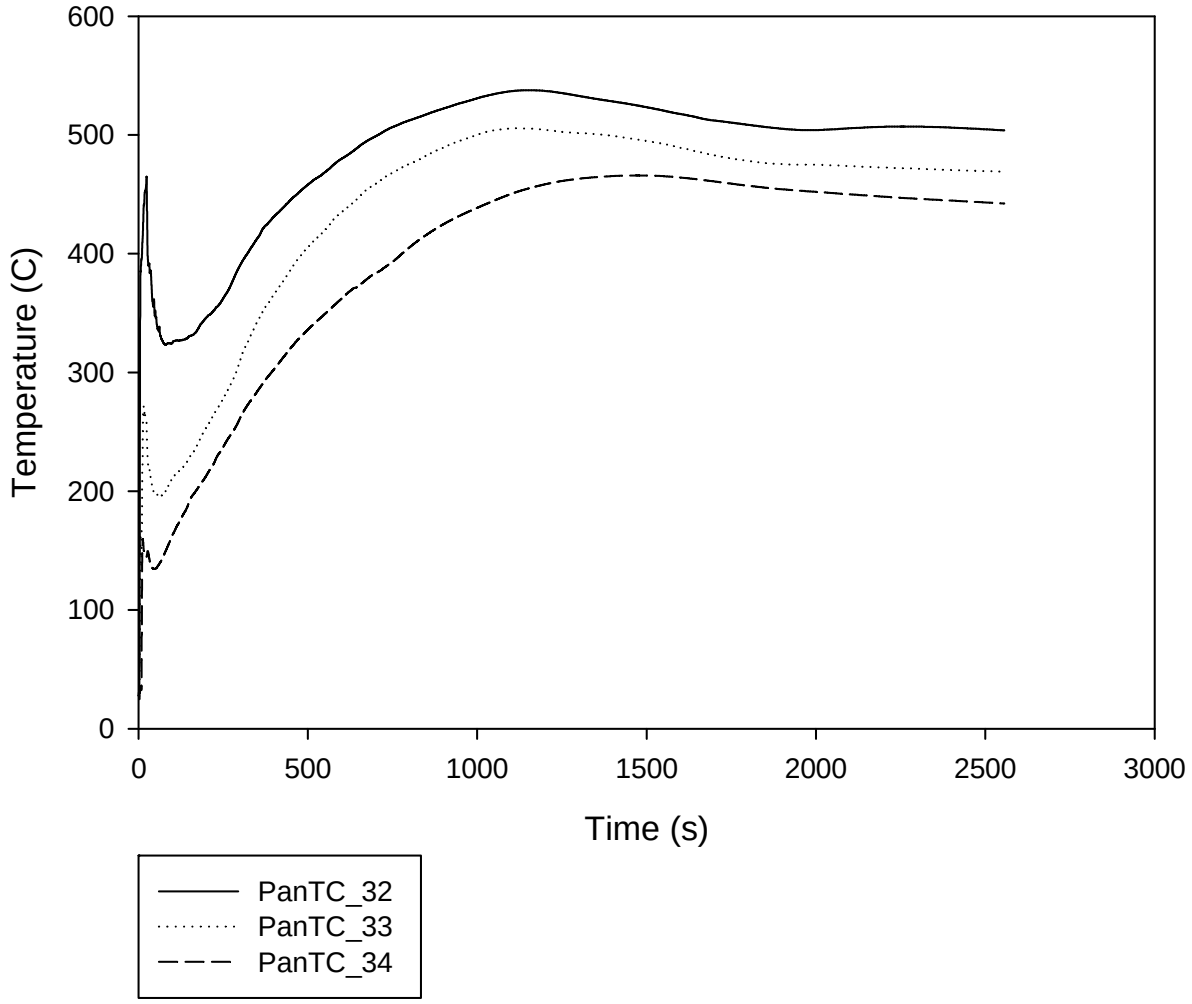

Figure 8-62: Sodium Pool Test 9, Inside Top of Pan TC Temperatures versus Time

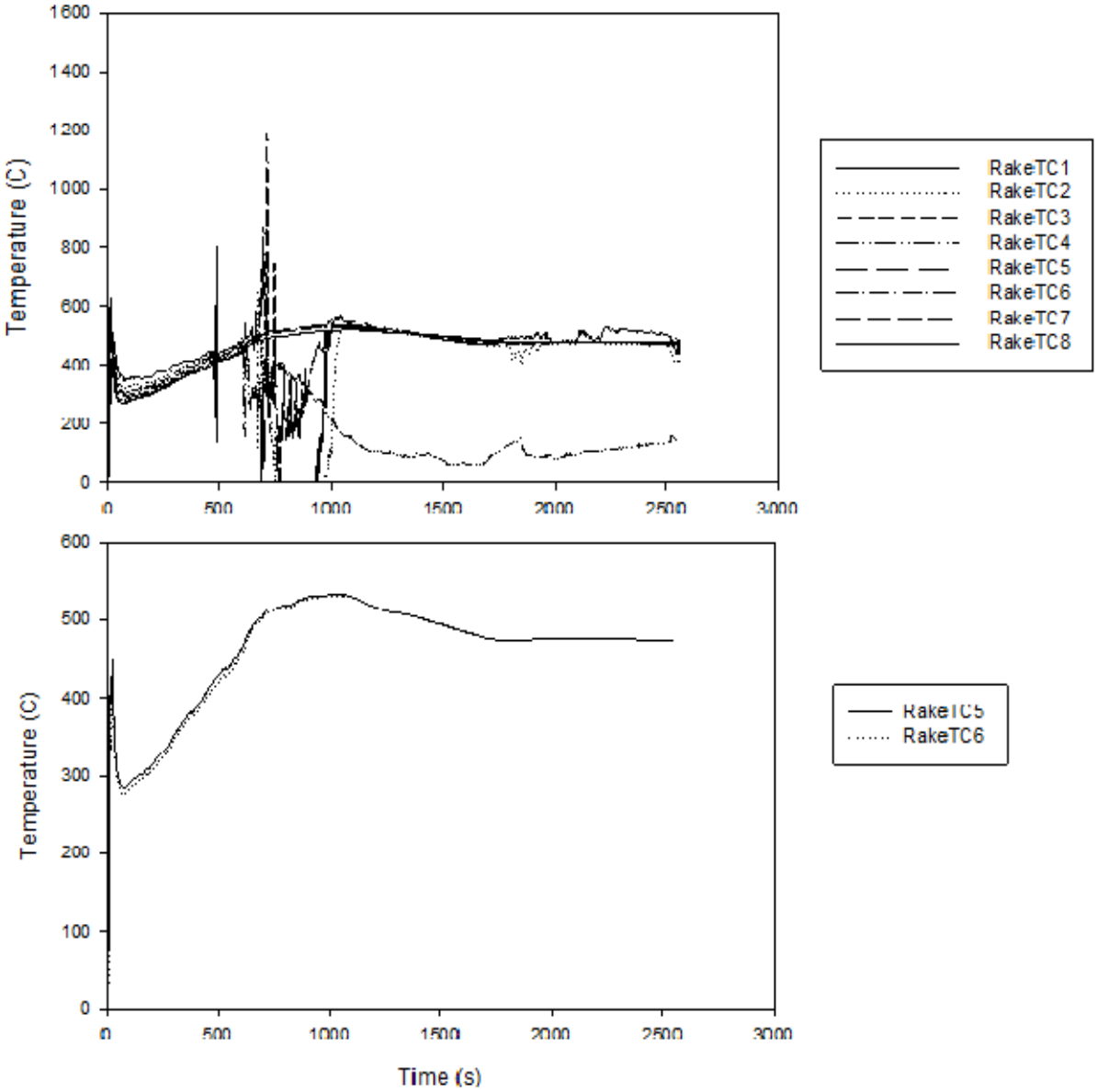

Figure 8-63: Sodium Pool Test 9, Inside Pan Rake TC Temperatures versus Time

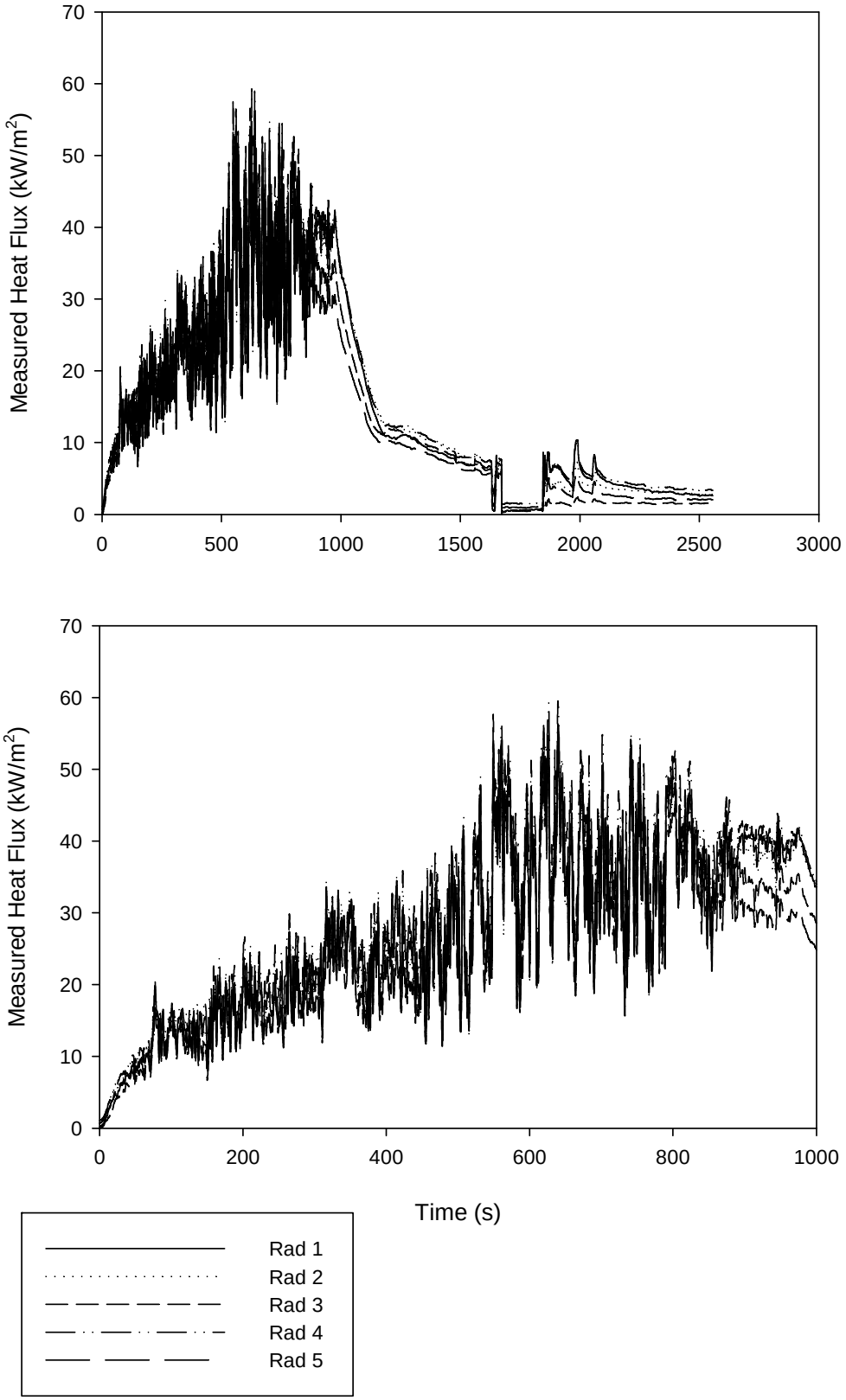

Figure 8-64: Sodium Pool Test 9, Measured Heat Flux versus Time

8.5.9 Sodium Pool Test 10 Measured Data

For instrumentation locations and specifications referred to in the figures of this section please reference Section 8.2. This section displays the measured data from sodium pool test 10.

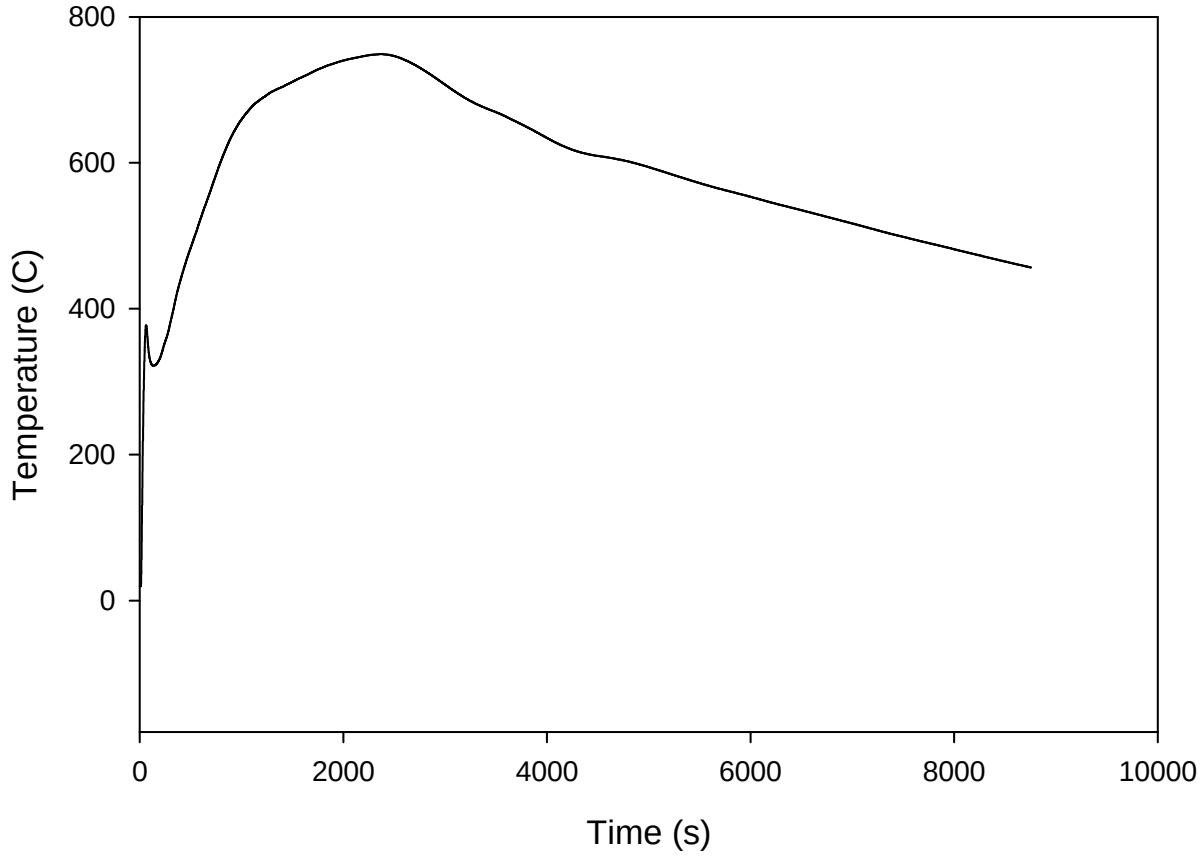

Figure 8-65: Sodium Pool Test 10, Pan Bottom Center TC Temperature versus Time

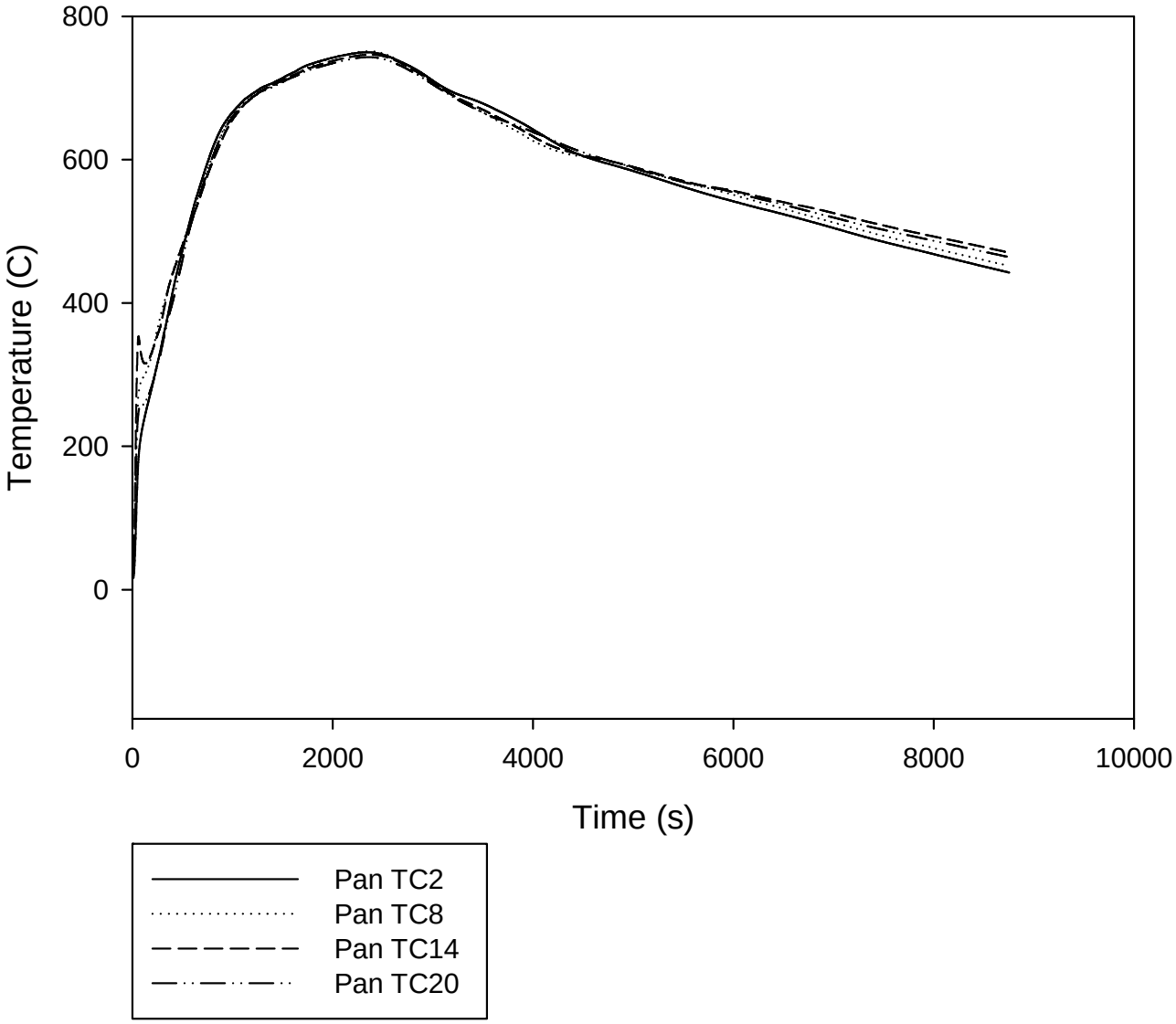

Figure 8-66: Sodium Pool Test 10, Pan Bottom 1/3 Radius TC Temperatures versus Time

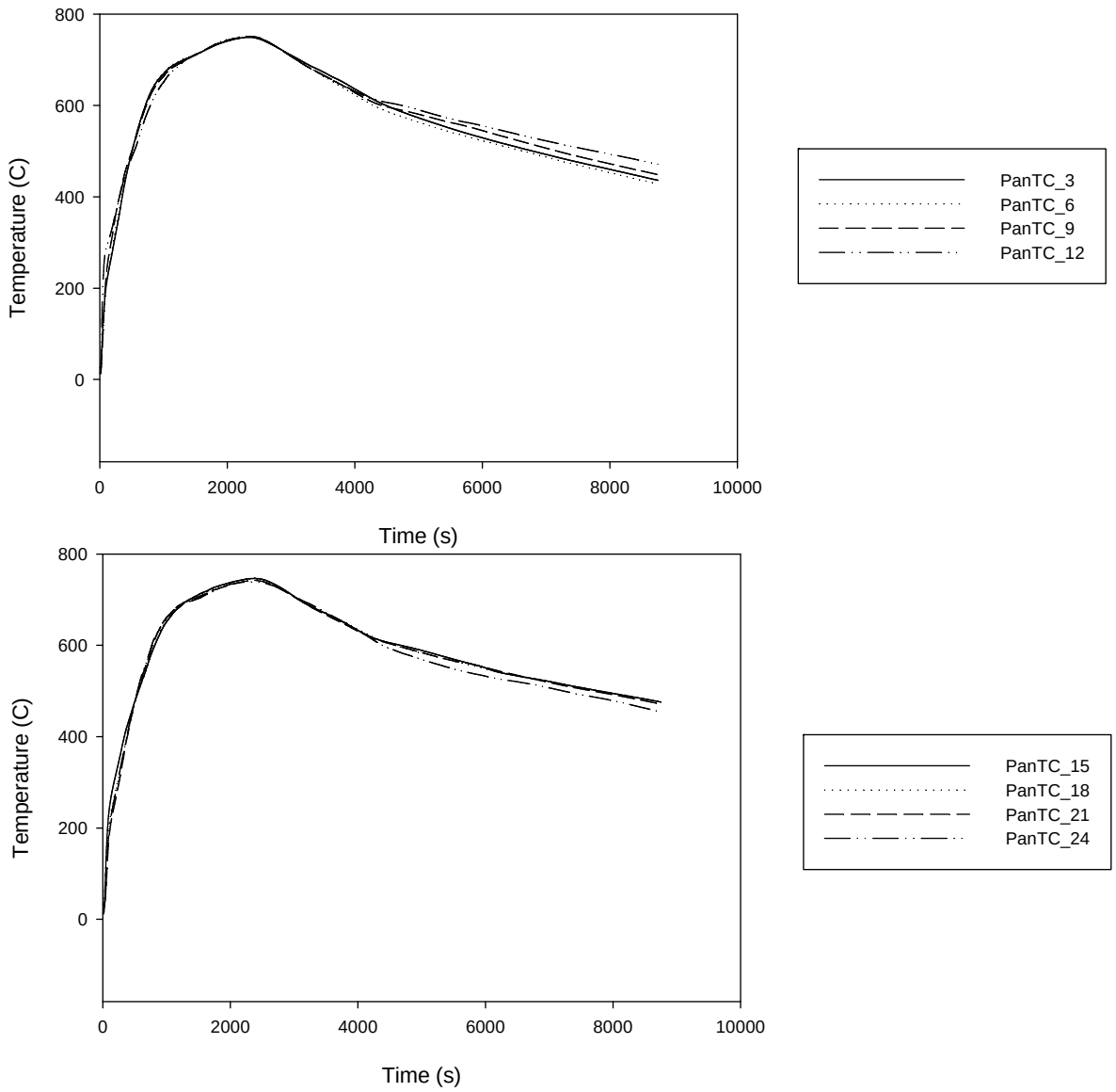

Figure 8-67: Sodium Pool Test 10, Pan Bottom 2/3 Radius TC Temperatures versus Time

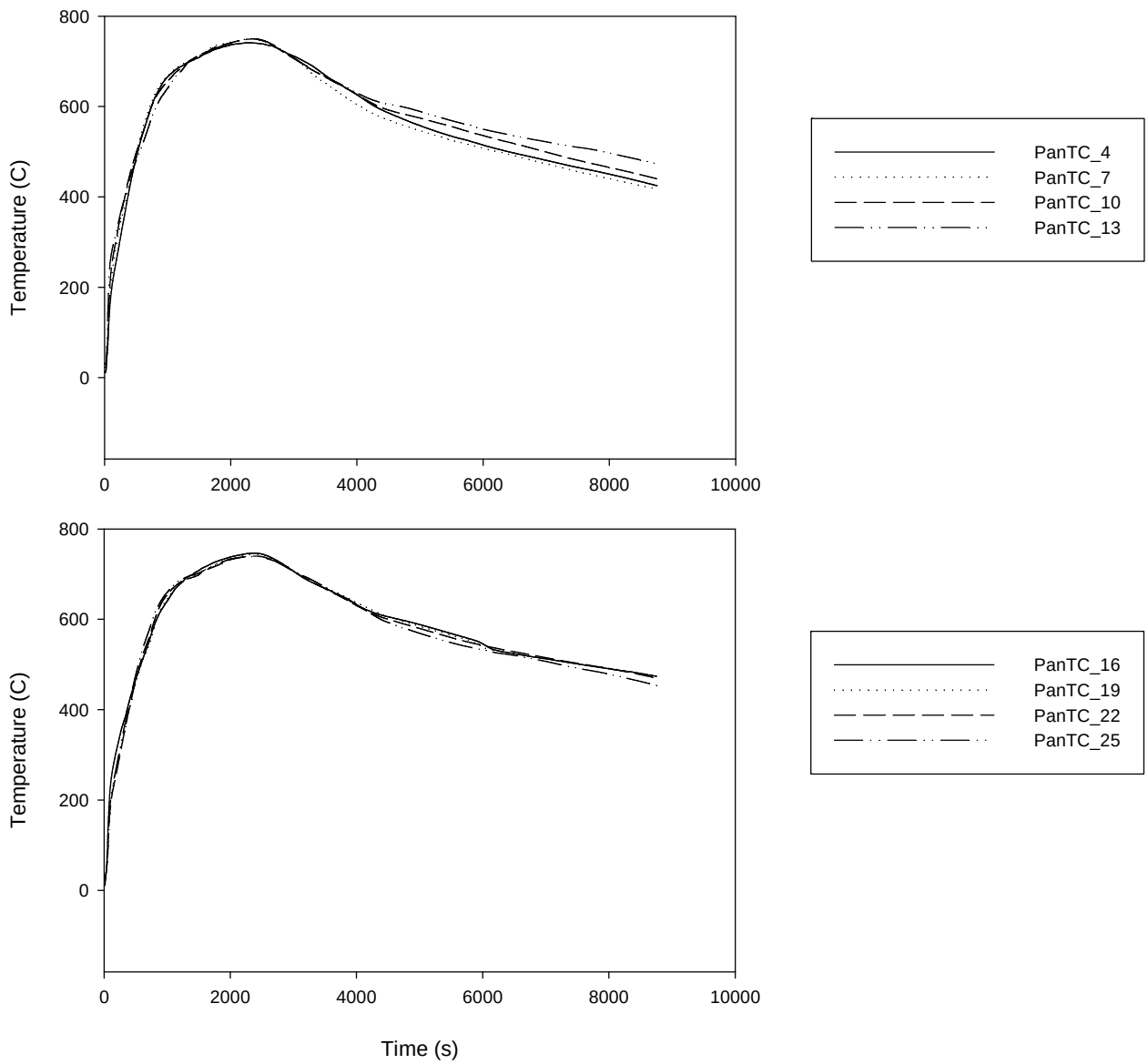

Figure 8-68: Sodium Pool Test 10, Pan Bottom Full Radius TC Temperatures versus Time

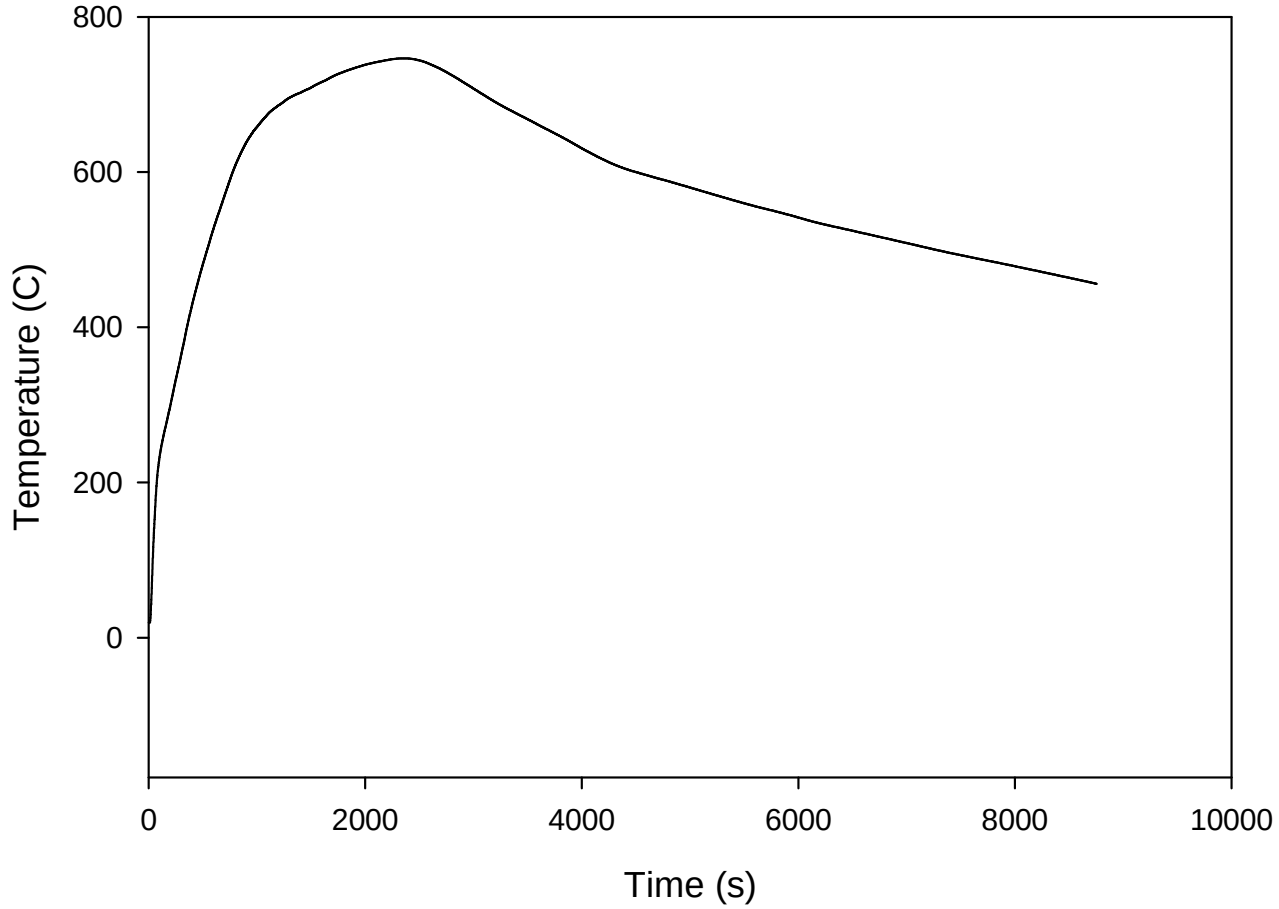

Figure 8-69: Sodium Pool Test 10, Averaged Pan Bottom TCs' Temperatures versus Time

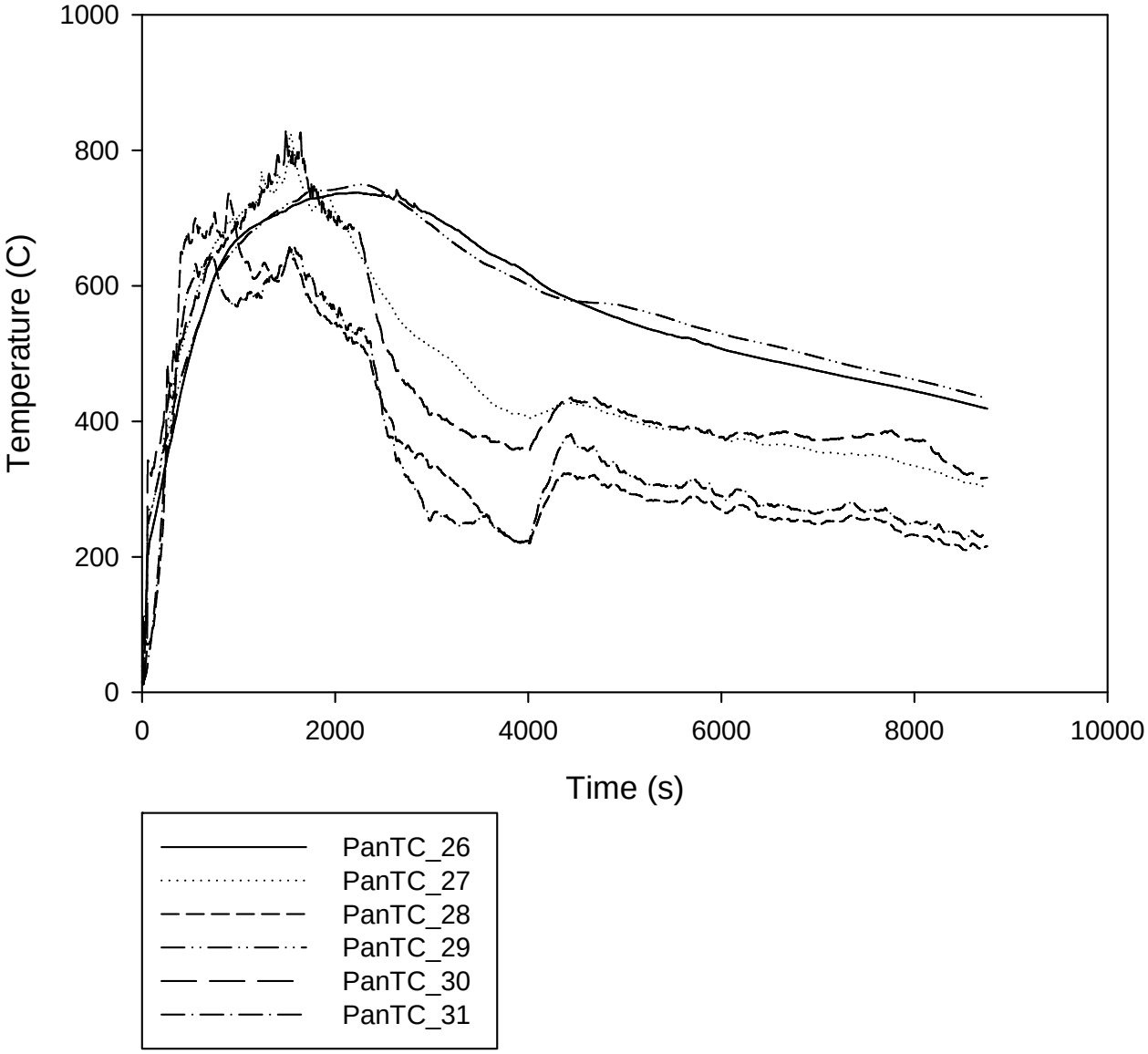

Figure 8-70: Sodium Pool Test 10, Sidewall Pan TC Temperatures versus Time

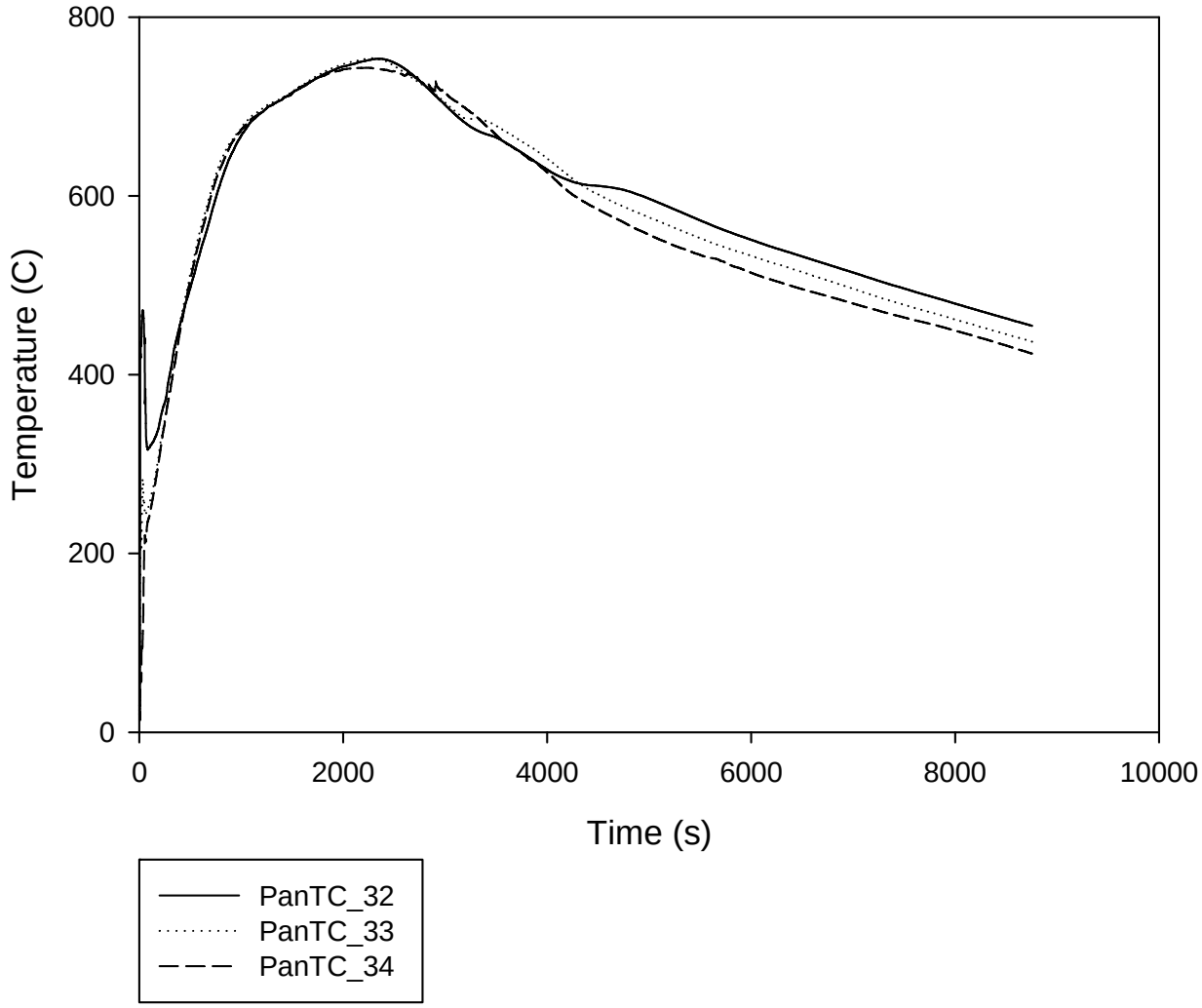

Figure 8-71: Sodium Pool Test 10, Inside Top of Pan TC Temperatures versus Time

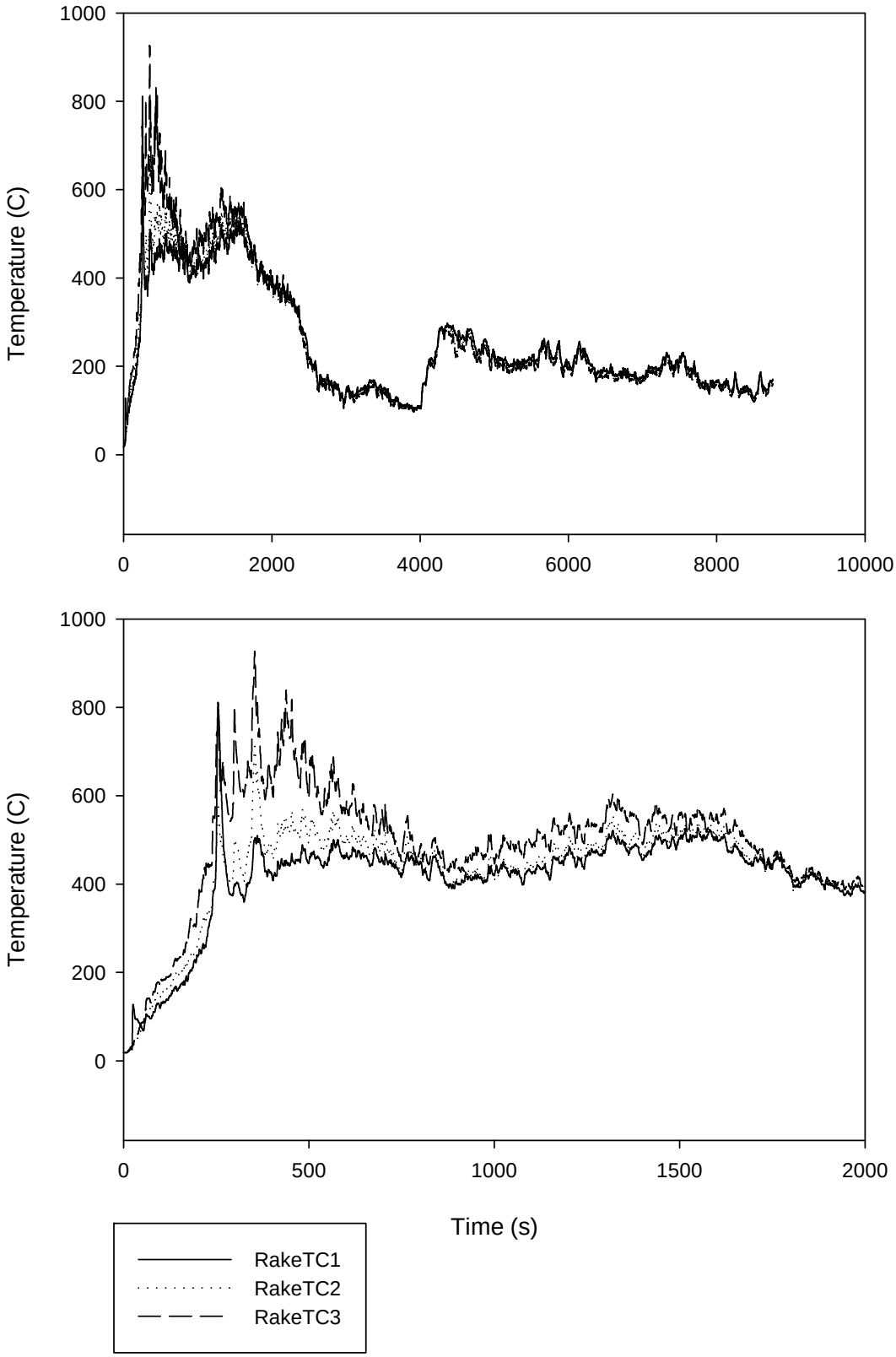

Figure 8-72: Sodium Pool Test 10, Inside Pan Rake TC Temperatures versus Time

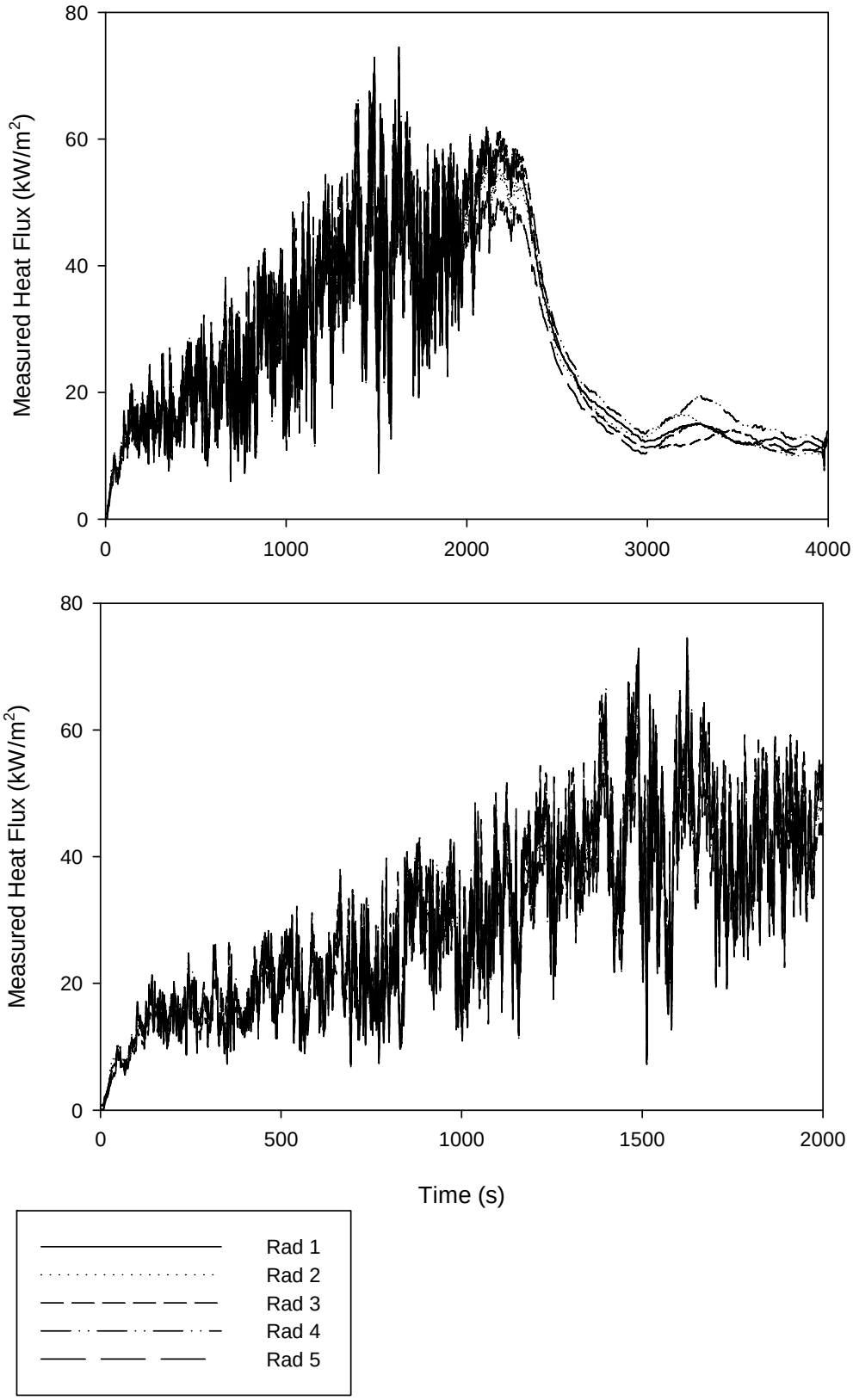

Figure 8-73: Sodium Pool Test 10, Measured Heat Flux versus Time

8.5.10 Sodium Pool Test 11 Measured Data

For instrumentation locations and specifications referred to in the figures of this section please reference Section 8.2. This section displays the measured data from sodium pool test 11. Note none of the inside the pan rake TCs are shown because they all failed during the test.

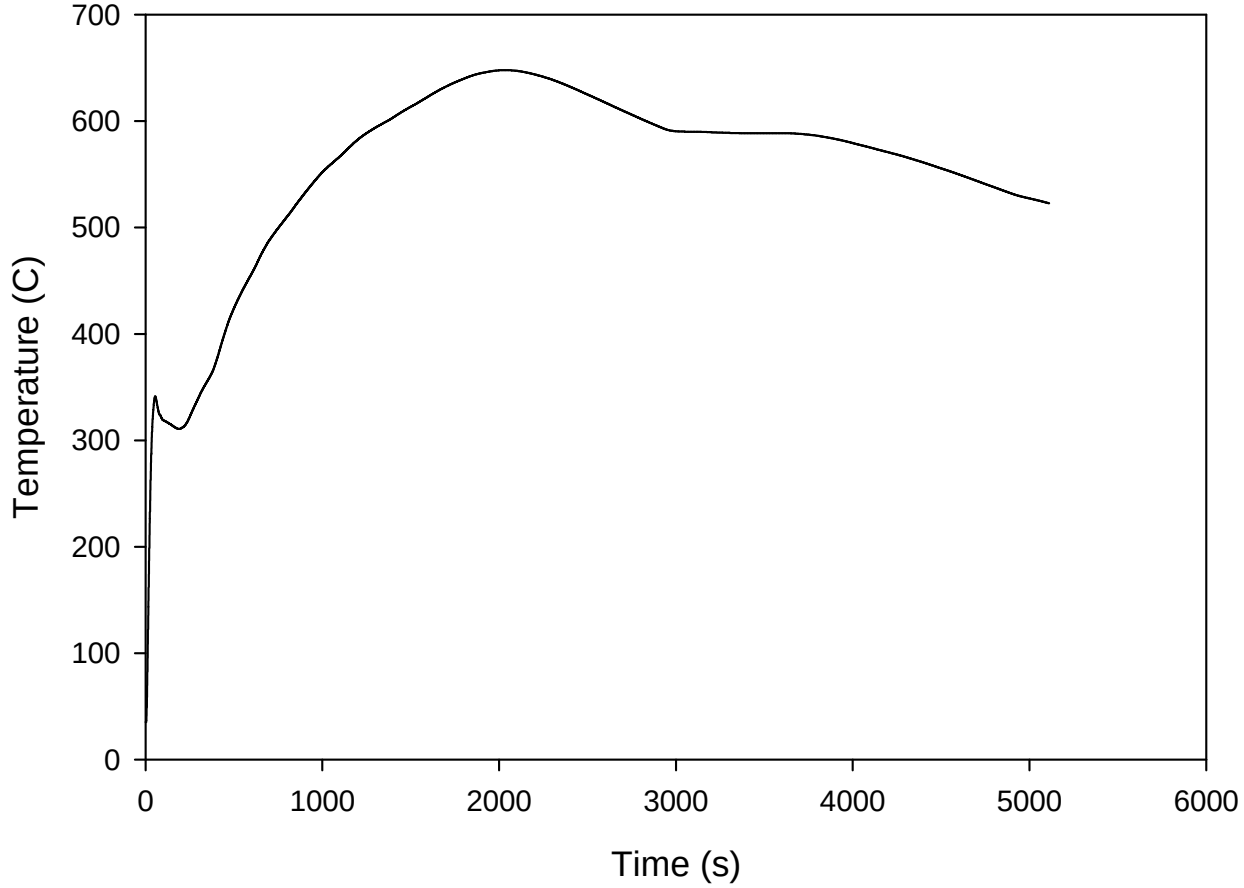

Figure 8-74: Sodium Pool Test 11, Pan Bottom Center TC Temperature versus Time

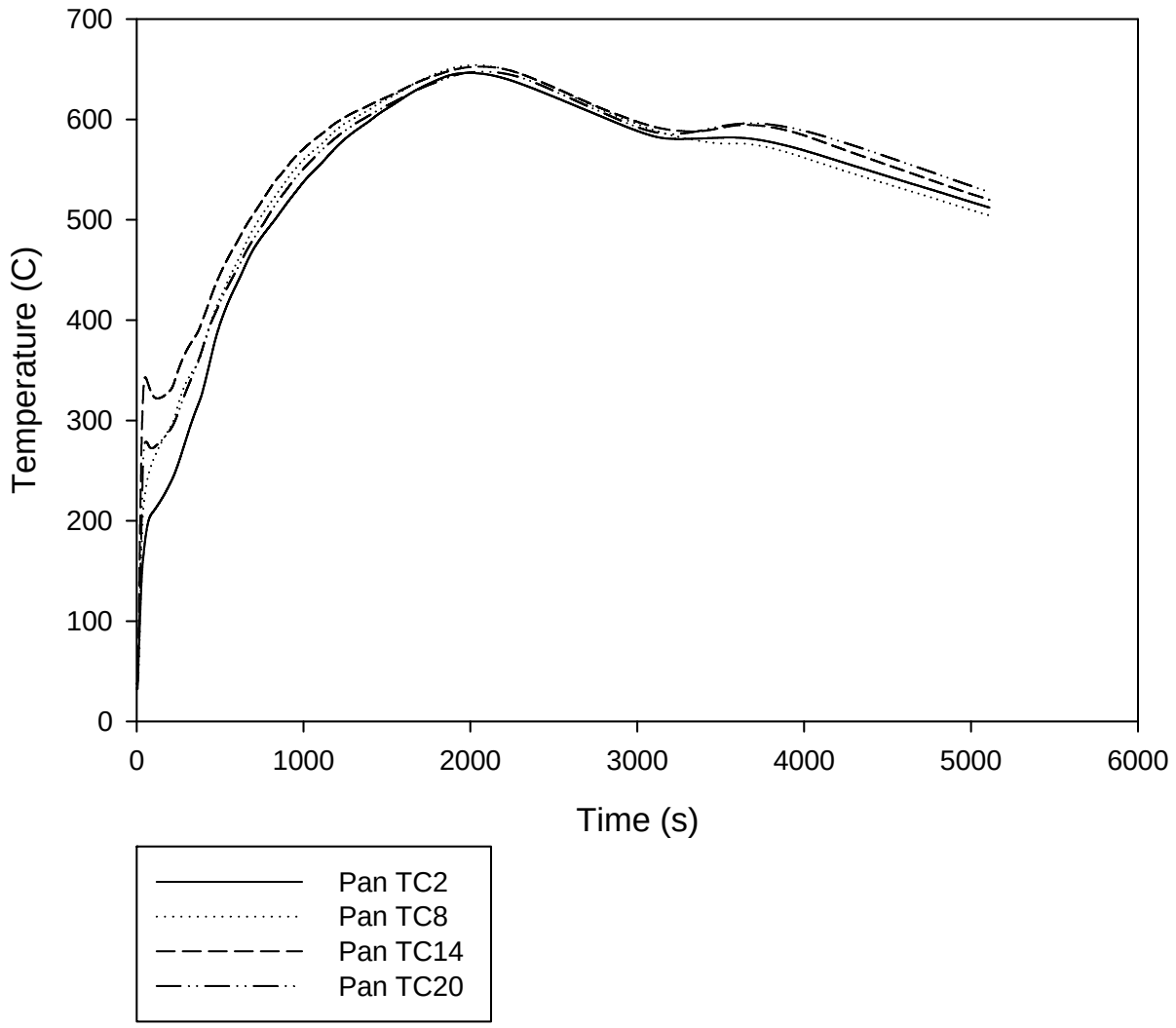

Figure 8-75: Sodium Pool Test 11, Pan Bottom 1/3 Radius TC Temperatures versus Time

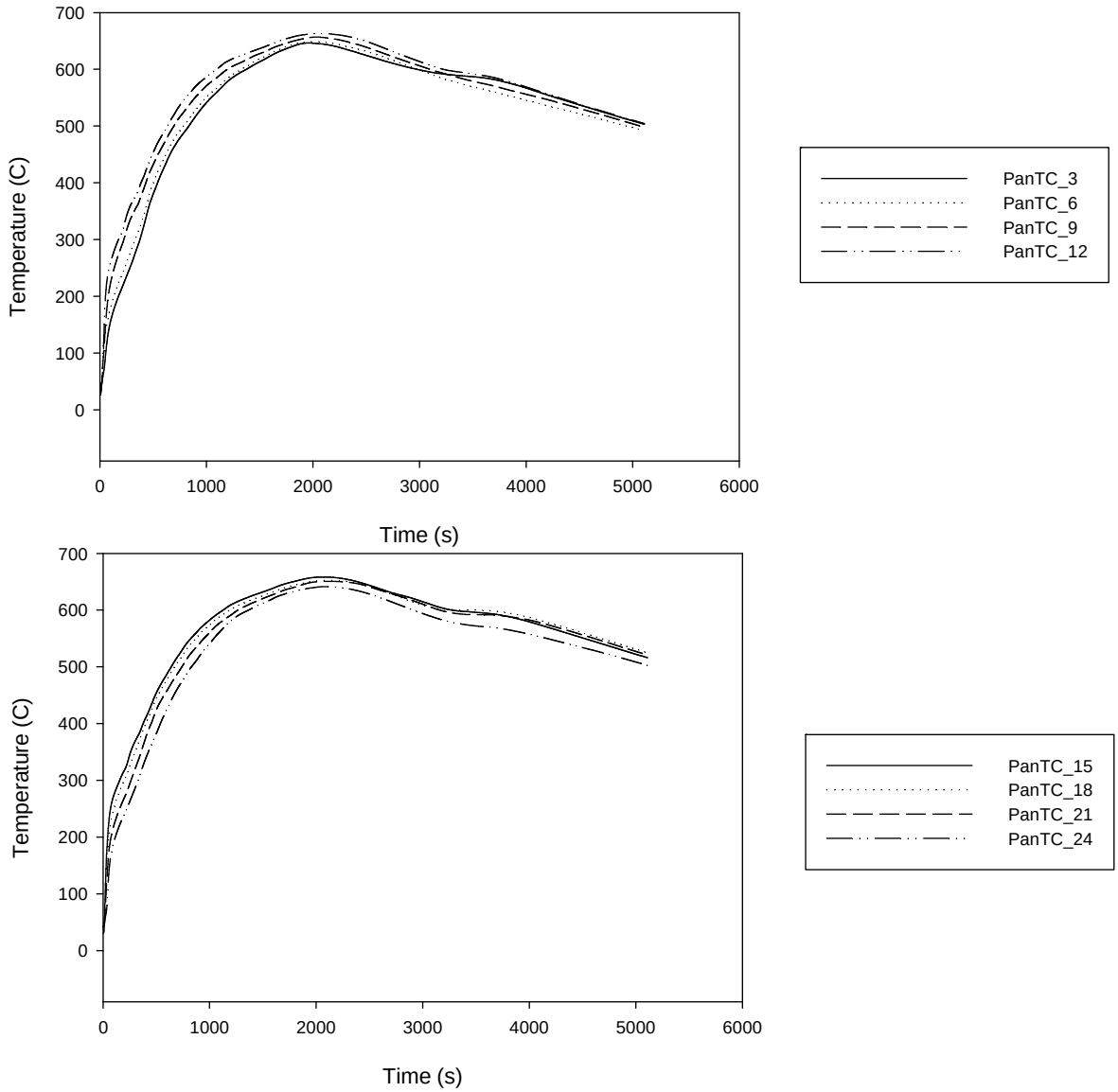

Figure 8-76: Sodium Pool Test 11, Pan Bottom 2/3 Radius TC Temperatures versus Time

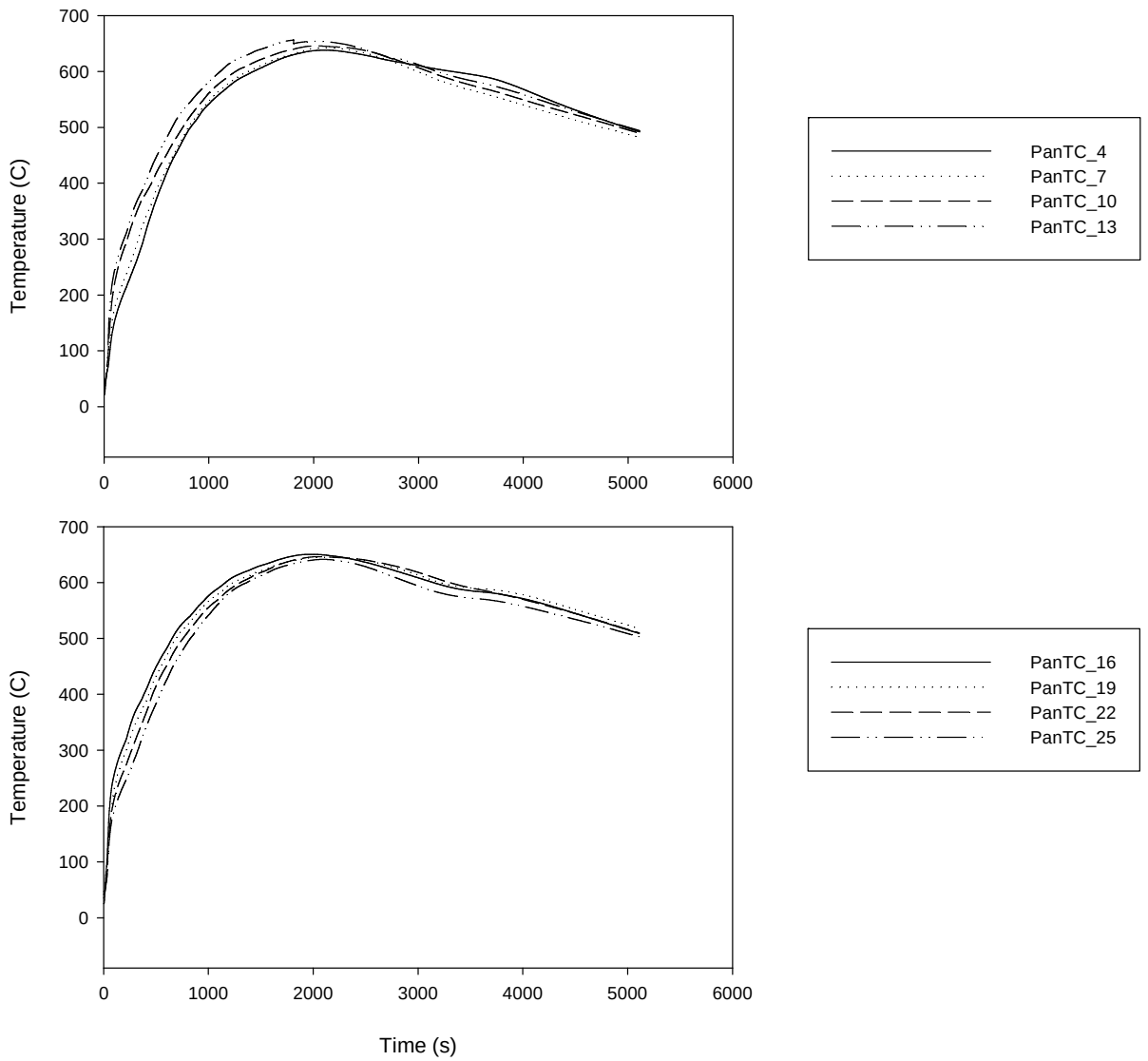

Figure 8-77: Sodium Pool Test 11, Pan Bottom Full Radius TC Temperatures versus Time

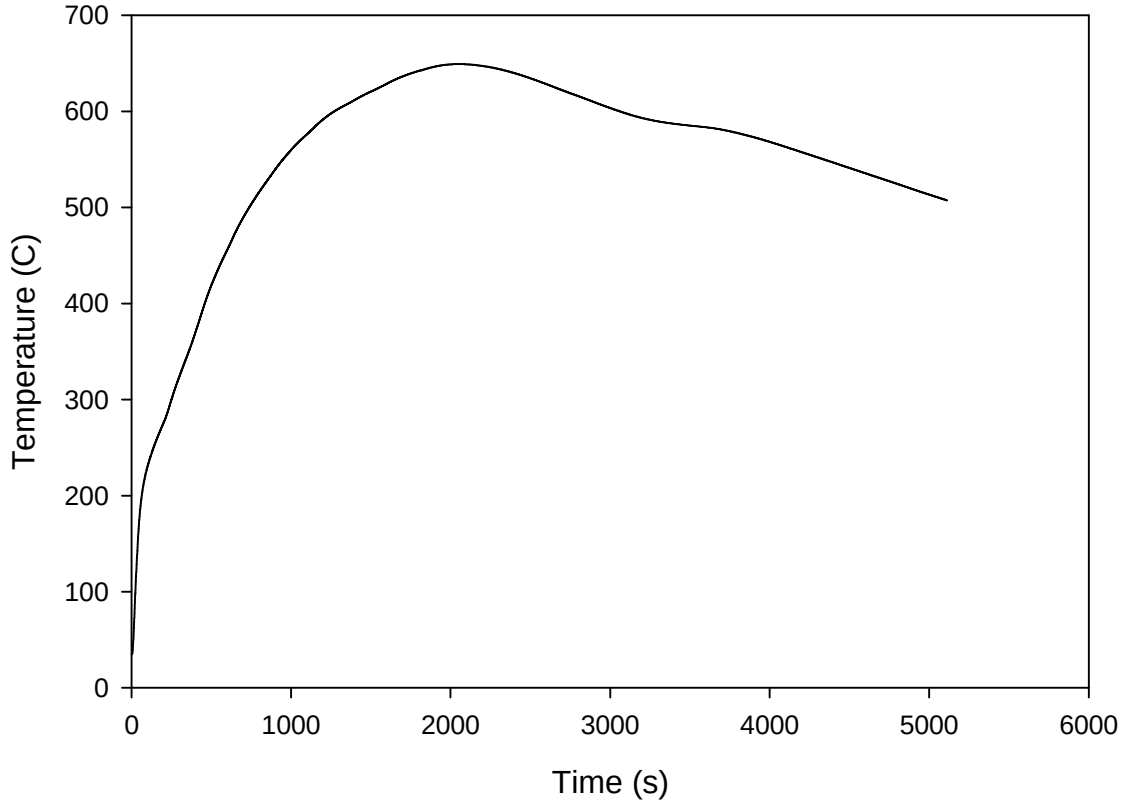

Figure 8-78: Sodium Pool Test 11, Averaged Pan Bottom TCs' Temperatures versus Time

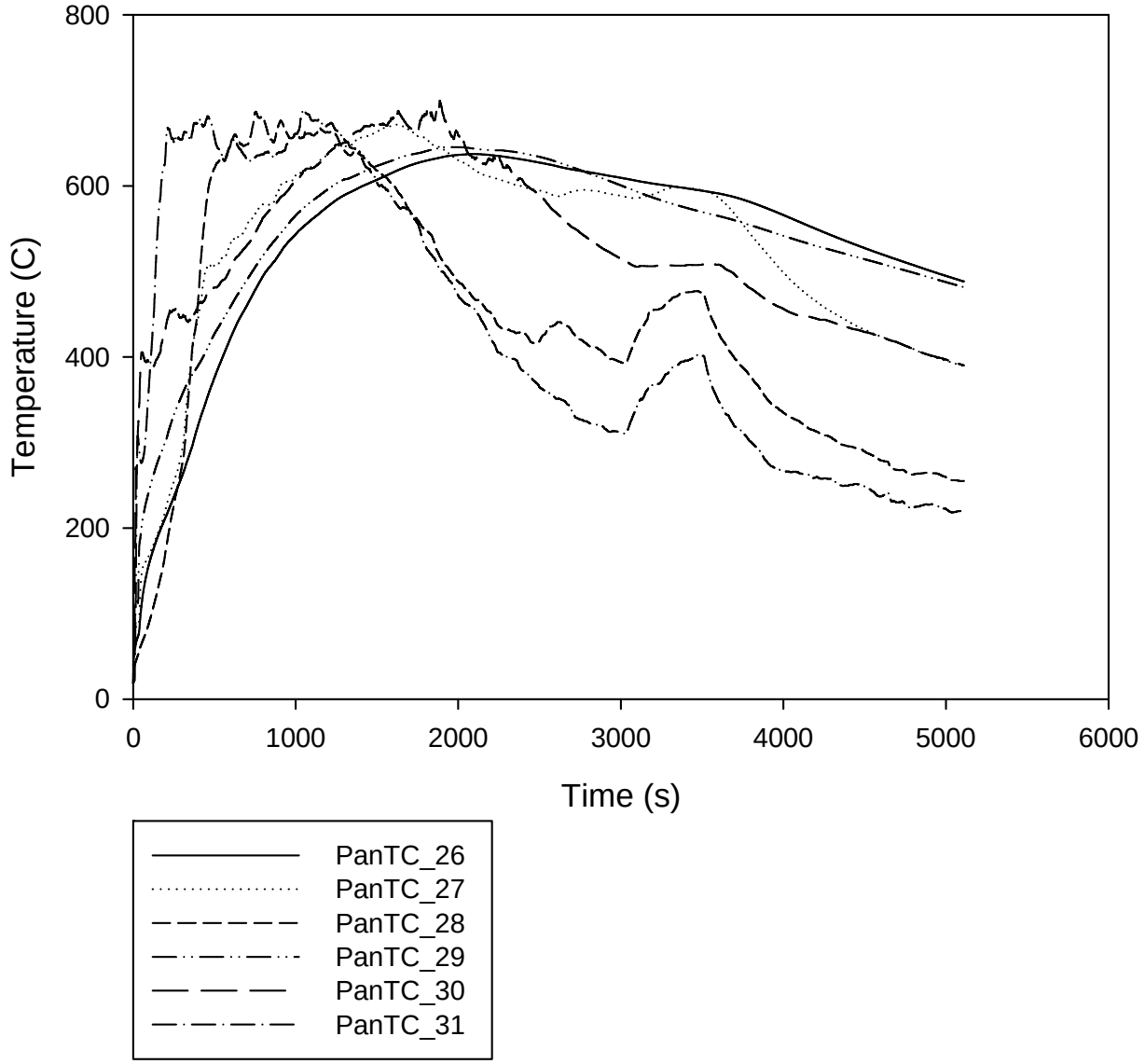

Figure 8-79: Sodium Pool Test 11, Sidewall Pan TC Temperatures versus Time

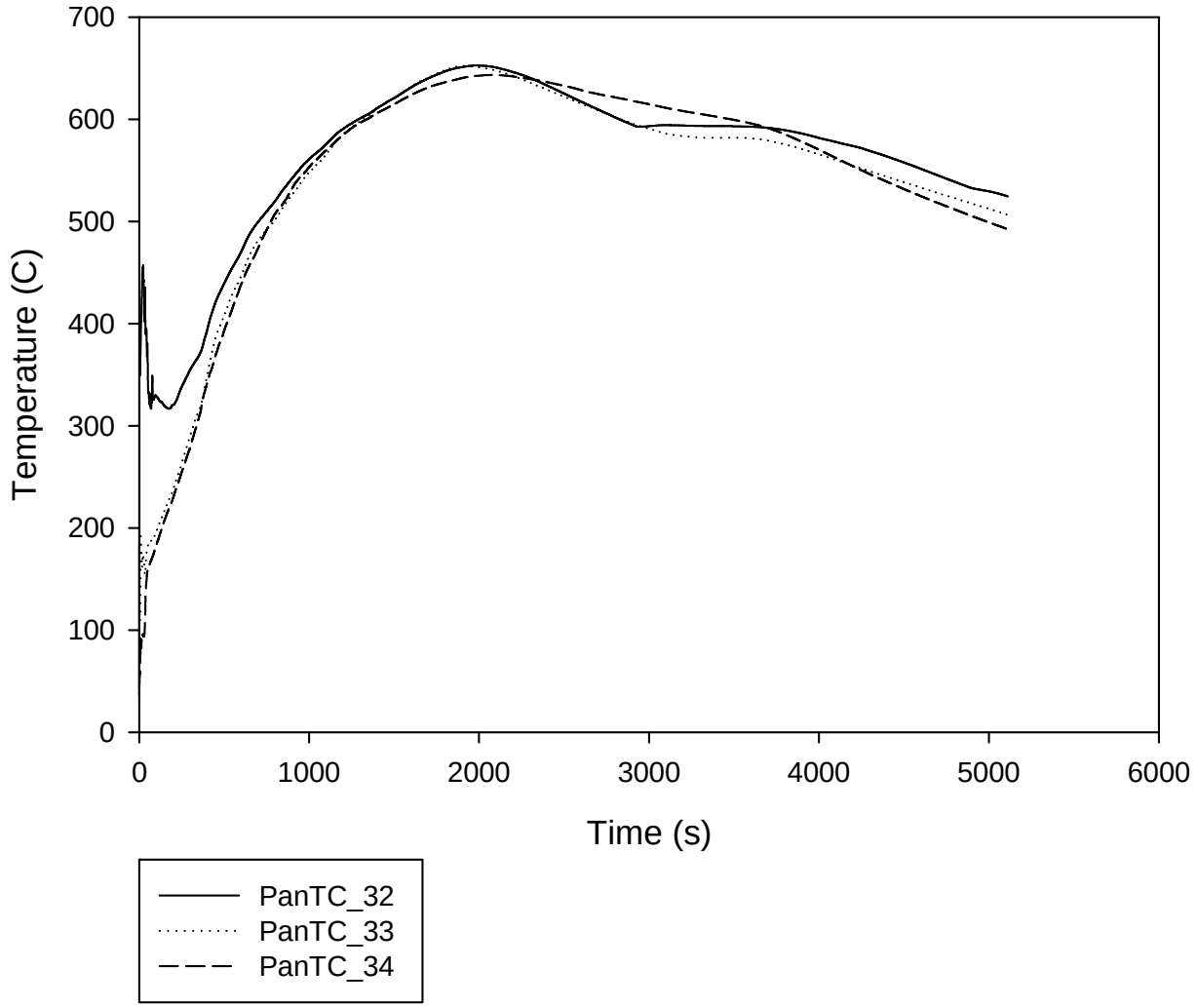

Figure 8-80: Sodium Pool Test 11, Inside Top of Pan TC Temperatures versus Time

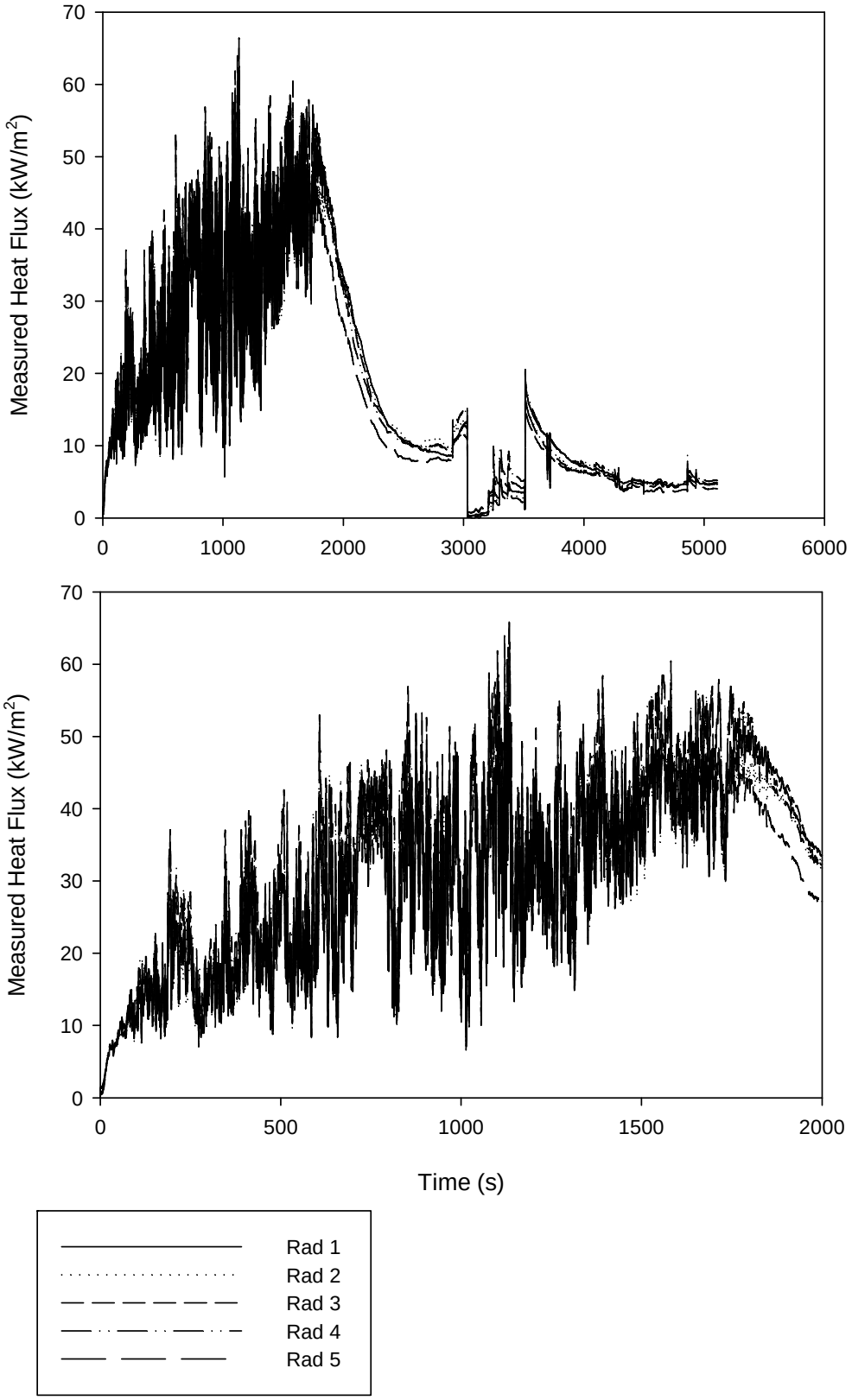

Figure 8-81: Sodium Pool Test 11, Measured Heat Flux versus Time

9 APPENDIX C: REFERENCE PROPERTIES

The below figures and tables are what was used as the reference properties for the model development.

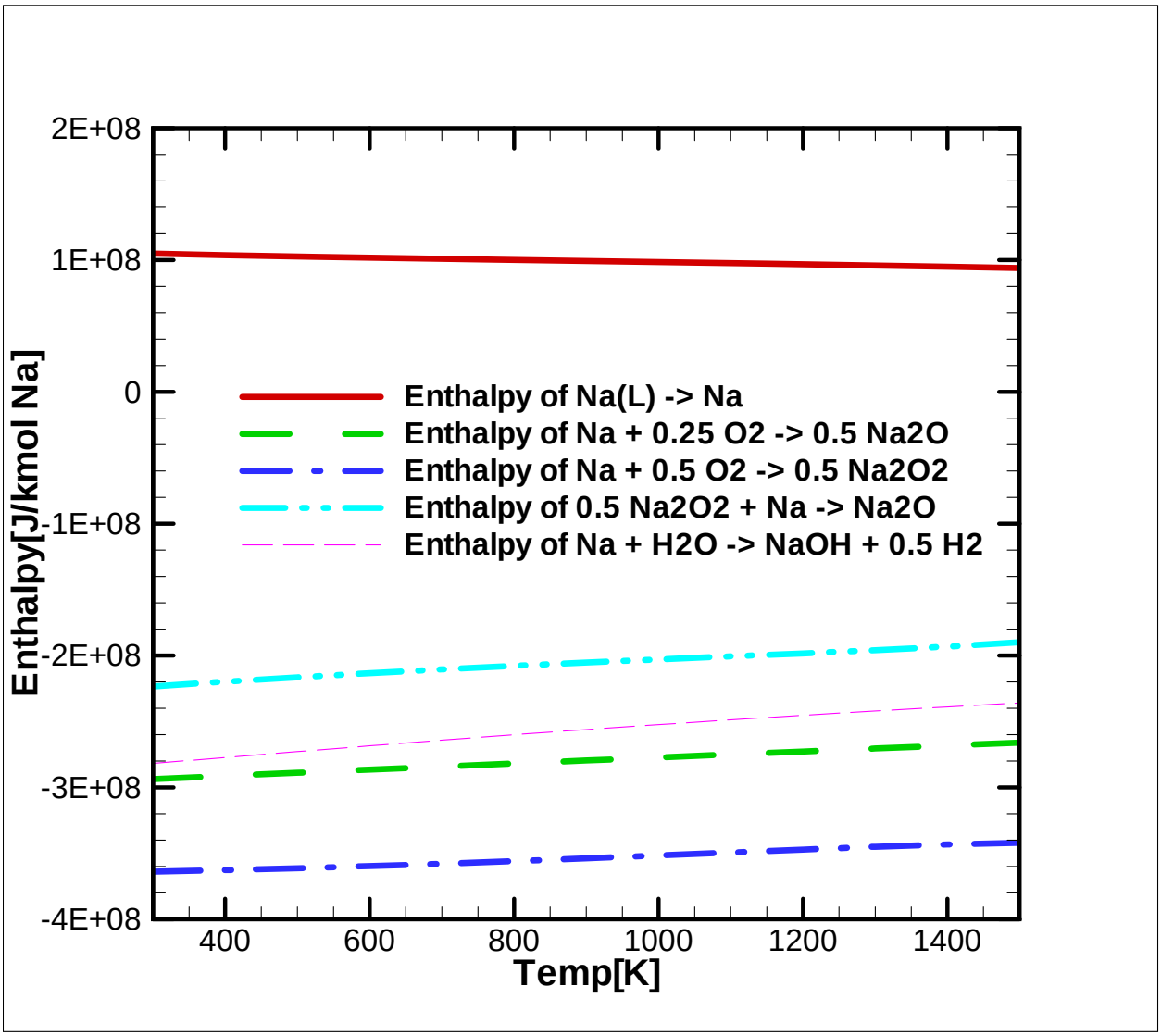

Figure 9-1: Referenced Enthalpy of Reactions

Species	Enthalpy [J/kmol]	Chem Pot [J/kmol]	Gibbs Ref [J/kmol]
H2	-4.3253E+03	-1.7505E+09	-3.8943E+07
O2	-4.4067E+03	-6.5057E+07	-6.1134E+07
H2O	-2.4183E+08	-2.0096E+09	-2.9810E+08
CO	-1.1053E+08	-1.8810E+09	-1.6943E+08
CO2	-3.9351E+08	-2.1688E+09	-4.5722E+08
N2	-4.3686E+03	-5.7740E+07	-5.7099E+07
Na	1.0730E+08	5.1864E+07	6.1492E+07
Na(L)	2.4099E+06	-1.7263E+09	-1.4791E+07
Na2O(L)	-3.7287E+08	-2.1117E+09	-4.0015E+08
Na2O2(a)	-5.1324E+08	-5.5681E+08	-5.4147E+08
NaOH(L)	-4.1639E+08	-2.1508E+09	-4.3924E+08

Table 9-1: Species Properties at 298 K

Temp[K]	Density [kg/m3]	Specific Heat [J/kmol-K]	Viscosity [Pa-s]	Thermal Conductivity [W/m/K]	Diffusivity_O2 [m2/s]	Diffusivity_Na [m2/s]
300	1.1046E+00	2.6790E+04	2.0909E-05	1.6915E-02	3.0568E-05	2.2189E-05
400	8.2844E-01	2.6993E+04	2.5860E-05	3.1931E-02	5.0804E-05	3.6935E-05
500	6.6275E-01	2.7324E+04	3.0250E-05	3.2137E-02	7.4583E-05	5.4319E-05
600	5.5229E-01	2.7752E+04	3.4260E-05	4.9543E-02	1.0162E-04	7.4118E-05
700	4.7339E-01	2.8243E+04	3.7991E-05	5.6544E-02	1.3172E-04	9.6173E-05
800	4.1422E-01	2.8752E+04	4.1509E-05	6.2975E-02	1.6473E-04	1.2036E-04
900	3.6820E-01	2.9231E+04	4.4854E-05	6.9033E-02	2.0051E-04	1.4659E-04
1000	3.3138E-01	2.9624E+04	4.8057E-05	7.4828E-02	2.3897E-04	1.7477E-04
1100	3.0125E-01	2.9959E+04	5.1140E-05	8.0425E-02	2.8002E-04	2.0485E-04
1200	2.7615E-01	3.0262E+04	5.4119E-05	8.5863E-02	3.2358E-04	2.3675E-04
1300	2.5490E-01	3.0535E+04	5.7006E-05	9.1165E-02	3.6958E-04	2.7044E-04
1400	2.3670E-01	3.0776E+04	5.9813E-05	9.6346E-02	4.1795E-04	3.0586E-04
1500	2.2092E-01	3.0986E+04	6.2547E-05	1.0141E-01	4.6864E-04	3.4298E-04

Table 9-2: Gas Mixture Properties near Stoichiometric as a Function of Temperature

108. Distribution

2	MS9018	Central Technical Files	8944
2	MS0899	Technical Library	9536
1	MS0123	D. Chavez, LDRD Office	1011